UNIVERSITY OF SOUTHAMPTON

FACULTY OF PHYSICAL SCIENCES AND ENGINEERING

ELECTRONICS AND COMPUTER SCIENCE

α-Hemolysin Nanopore Sensing of MicroRNA with Electrolyte Gradients

by

Josip Ivica

Thesis for the degree of Doctor of Philosophy

January 2018

Supervisors: **Dr Maurits de Planque**

Dr Philip Williamson

ABSTRACT

Aberrant microRNA expression profiles have been correlated with a range of complex diseases, including specific types of cancer, hence microRNA species are a promising class of molecular cancer biomarkers. Recently, nanopore technology was proposed as a single-molecule methodology to detect and quantify microRNA molecules without amplification or fluorescent labelling. A duplex of microRNA hybridized with a complementary DNA probe is electrophoretically driven to a nanopore, which can be translocated following duplex unzipping at the channel entrance, which is measured as a transient decrease in nanopore electrical current. Nanopore sensing sensitivity is determined by the occurrence frequency of such resistive current pulses, while the specificity is determined by the probe-analyte interaction. This thesis aims to establish the optimal conditions and limitations of nanopore sensing of cancer-related microRNA species with the biological nanopore α-hemolysin as the sensor element. The fragility of aperture-suspended lipid bilayers is one of the main obstacles for sensing with biological pores, hence we first addressed bilayer stability by laser cutting a thin Teflon film to obtain apertures with a tapered wall profile. Nanopore sensing was then investigated with synthetic miRNA 155, overexpressed in lung cancer, in the presence of a complementary DNA probe. Key parameters of duplex nanopore translocation in conventional symmetrical 1 M KCl were in agreement with previous work, including a relatively low pulse frequency, allowing quantification of miRNA 155 down to 10 nM. We then systematically investigated the effect of *cis*/trans KCl gradients across the nanopore. The resistive pulse frequency increased significantly with the salt gradient, indicative of cation-induced field enhancement at the pore entrance, but bilayer and pore stability were reduced. At a 0.5 / 4 M gradient, the pulse frequency was ~60 times higher than for symmetrical 1 M KCl conditions, enabling miRNA quantification down to 100 pM. Additionally, experiments with DNA probes with single and double polynucleotide extensions confirmed the necessity of a double-overhang design under salt gradient conditions, while experiments with NaCl, CsCl and LiCl electrolyte gradients suggested that Li addition can extend the duplex unzipping time. Finally, trials were performed with total RNA extracts from clinical samples. Here, bilayer stability was no limitation but pore clogging precluded nanopore sensing, most likely due to longer mRNA species with secondary structure, necessitating further extract processing. Another consideration for nanopore analysis of microRNAs from clinical samples is to minimize the extract resuspension volume, implying the use of miniaturized bilayer recording methodologies.

Table of Contents

DECLARATION OF AUTHORSHIP

I, Josip Ivica, declare that the thesis entitled α-Hemolysin Nanopore Sensing of MicroRNA with Electrolyte Gradients and the work presented in it are my own and has been generated by me as the result of my own original research.

I confirm that:

1. This work was done wholly or mainly while in candidature for a research degree at this University;
2. Where any part of this thesis has previously been submitted for a degree or any other qualification at this University or any other institution, this has been clearly stated;
3. Where I have consulted the published work of others, this is always clearly attributed;
4. Where I have quoted from the work of others, the source is always given. With the exception of such quotations, this thesis is entirely my own work;
5. I have acknowledged all main sources of help;
6. Where the thesis is based on work done by myself jointly with others, I have made clear exactly what was done by others and what I have contributed myself;
7. Parts of this work have been published as:
    - Josip Ivica, Philip T. F. Williamson and Maurits R. R. de Planque (2016) Quantification of microRNA with α-hemolysin nanopores. Poster presentation at *Membrane Pores: from Structure and Assembly to Medicine and Technology (The Royal Society)*, London, United Kingdom, 27 - 28 June 2016.
    - Josip Ivica, Philip T. F. Williamson and Maurits R. R. de Planque (2016) Optimization of parameters for nanopore resistive pulse sensing of microRNA. Poster presentation at the *60th Annual Meeting of the Biophysical Society*, Los Angeles, United States, 27 February - 02 March 2016.
    - Josip Ivica, Philip T.F. Williamson and Maurits R.R. de Planque (2017) Salt gradient modulation of microRNA translocation through a biological nanopore. *Analytical Chemistry*, 89, 8822-8829.

Signed: .....

Date: .....

Acknowledgements

I would like to start this thesis by sincerely thanking everyone that, directly or indirectly, contributed to this work. Firstly, I would like to express my gratitude and appreciation to my supervisor, Dr. Maurits de Planque for giving me the opportunity to work in his laboratory. I am grateful to him for being so supportive and encouraging through these years and constantly helping with his knowledge and guidance. I would also like to thank my other supervisor Dr. Philip Williamson for the help and valuable suggestions. I owe my gratitude to the University of Southampton for providing funding for this PhD. I would like to thank Shimul Saha for introducing me to the lab and teaching me my first bilayer lessons. I would like to thank Prof Alex Mirnezami and Dr. Rahul Bhome for providing the clinical RNA extract used for experiments. Special thanks to Mrs Shengmiao Zhou for the nanopore measurements with miRNA155 with different probes. Thank you to Marija Miljak for her support and help.

I would like to thank all my friends from Southampton for a good time and all the help I received from them (Carlos Honrado, Kri Müller, Antonio De Grazia, Sumit Kalsi, Hend Alkhammash, Prameen Kalikavunkal, Kai Chang, Yuetao Li, Marios Stavrou, Fabrizio Siracusa, Luke Evans, Billy Anderson, Catarina Moura and Miguel Xavier). Special thanks to Riccardo Reale for his friendship, help when I needed, for all the fun, countless coffees, and for tracking down the magical scotch tape type 550 that was used for machining apertures for the bilayer formation. Thank you to Roel Mingels for his friendship, practical help, for all the laughter and providing a great office and lab environment. I would like to thank Anna Desalvo for love, patience, adventures, shared hopes and help with proofreading this thesis.

Back in Trogir, thanks for all support, good times and constant updates to my friends Marko Šore, Tonko Russo, Kaja Hrabar, Josip Žuvan and Josip Pavković.

Finally, my heartfelt appreciation goes to my sister Marina and parents Ines and Marin, for the endless support and opportunities that I've been given in my entire life.

.

Definitions and Abbreviations

αHL	Alpha hemolysin
AeL	Aerolysin
Ago-2	Argonaute 2 protein
ALD	Atomic layer deposition
DPhPC	1,2-diphytanoyl-sn-glycero-3-phosphocholine
C	Capacitance
cDNA	Complementary DNA
ClyA	Cytolysin A
DGCR8	DiGeorge syndrome critical region 8 (nuclear protein)
Dicer	RNAse III enzyme
ds	double-stranded
ssDNA	Single-stranded deoxyribonucleic acid
Dosha	Protein enzyme
dsDNA	Double-stranded deoxyribonucleic acid
DSN	Duplex-specific nuclease
dsRNAp	Double-stranded RNA-binding proteins
DVP	Differential pulse voltammetry
ECL	Electrochemoluminescence
EDTA	Ethylenediaminetetraacetic acid
EOF	Electroosmotic flow
FRET	Forster resonance energy transfer

f_{on}	Capture frequency
I	Current
I_B	Blocked current
I/I_0	Residual current
Ji	Current flux of ions
LNA	Locked nucleic aminoacid
MspA	Mycobacterium smegmatis porin A
miRNA	MicroRNA
mRNA	Messenger RNA
NaPSS	Sodium polystyrene sulfonate
NGS	Next-generation sequencing
NRPS	Nanopore resistive pulse sensing
nt	Nucleotide
OmpG	Outer membrane protein G
P	Permeability
PCR	Polymerase chain reaction
PEG	Polyethylene glycol
PMMA	Poly(methyl methacrylate)
Pre-miRNA	Precursor microRNA
Pri-miRNA	Primary microRNA
PolII	RNA polymerase II
qRT- PCR	Quantitative reverse transcription polymerase chain reaction
Rc,bar	Barrier limited capture rate of DNA
Rc,diff	Diffusion limited capture rate of DNA

RISC	RNA-induced silencing complex
RMS	Root mean square
RNA	Ribonucleic acid
SDA	Strand displacement amplification
ss	Single-stranded
SiN	Silicon nitride
SiO_2	Silicon dioxide
SPR	Surface plasmon resonance
SS	Solid-state
TEM	Transmission electron microscopy
τ_{on}	Mean interevent time
τ_{off}	Mean dwell time

Chapter 1: Introduction

This overview Chapter explains the biomedical significance of microRNA and introduces appropriate analytical techniques, conventional methodologies as well as nanopore resistive pulse sensing. The majority of nanopore studies was performed with solid-state pores. Section 1.2 presents the aims and scope of this project on microRNA sensing with the biological nanopore α-hemolysin. The novelty of the obtained results is briefly summarized in Section 1.3, after which the structure of the dissertation is outlined in Section 1.4.

1.1 Context

MicroRNAs (miRNA) are class of short, ~18-22 nucleotides, non-coding RNA molecules that can regulate protein expression by binding to messenger RNA (mRNA), which modulates the translation process [1, 2]. As regulators of protein expression, miRNAs play an important role in many biological processes. Aberrant expression profiles of specific miRNAs were found in many disorders such are cardiovascular, neurodegenerative, inflammatory diseases and cancer [3]. Their disease-specific alternations, remarkably stable form and presence in the body fluids make miRNAs promising non-invasive biomarkers for a variety of diseases [4, 5]. Hence, the detection and quantification of specific miRNAs in body fluids can be used to monitor, screen and early diagnose diseases such as cancer. However, the main challenge for the quantification of miRNA molecules is their extremely low concentration, thought to be in the low or sub-picomolar range [6, 7]. It was estimated that miRNAs constitute only 0.01% of a total RNA extract [8].

The gold standard protocol for miRNA quantification is the quantitative reverse transcription polymerase chain reaction (qRT-PCR). Other common molecular techniques are microarray and next-generation sequencing technology. The qRT-PCR method requires two opposing primers to synthesize cDNA and dsDNA, which is challenging task because of the short length of miRNA sequences. Moreover, the sequence of various miRNAs can differ in only one nucleotide which complicates their discrimination and the primer design for PCR [2]. The existence of their precursors, primary miRNA (pri-miRNA) and precursor miRNA (pre-miRNA), in the total RNA extract can lead to erroneous estimation of mature miRNA concentration [2].

The biosensor-based detection of miRNAs is a rapidly growing field. Any biosensor consists of a biological part and a transducer or physicochemical part. The transducer component converts the interaction between the biological part and the biomarker into a signal that can be measured and analysed [9]. An attomolar limit of detection of miRNAs was achieved with various electrochemical and optical biosensors [10]. The main advantages of biosensor techniques over the classical molecular techniques are their low cost, short assay time and small sample volume.

Other desirable metrics for miRNA detection include: label-free operation, wide dynamic range, minimal target amplification, multiplexing potential (simultaneous detection of more miRNAs within the same sample) and ease of implementation [11].

Nanopore resistive pulse sensing (NRPS) is an electrical single-molecule technique with the potential to realize sensitive detection of miRNAs at low cost because there is no requirement for optical detection [12, 13]. Nanopore sensors consist of a pore in a biological or synthetic membrane between two compartments filled with electrolyte solution. Each compartment has an electrode to apply a voltage across the nanopore. The potential difference between the two compartments causes a steady ionic flow, in the pA to nA range, through the nanopore, which can be measured with a high impedance amplifier. Analyte molecules in solution interacting or passing through the pore cause an obstruction in the ionic current through the nanopore; this is called a *resistive pulse*. Based on the resistive pulse characteristics it is possible to gather information about the size and concentration of the analyte. There are two types of nanopores available for experiments: artificial solid-state nanopores and biological nanopores. The biological nanopores are a class of transmembrane proteins secreted from bacteria as toxins. The main advantage of biological pores is their reproducible self-assembly into a well-defined multimeric nanopore structure. However, they require a fragile lipid membrane, their biological target, as a matrix material for pore formation. Solid-state nanopores do not require a biomembrane environment, which simplifies NRPS experiments. The usual materials of choice for their fabrication include silicon nitride (Si_3N_4), silicon dioxide (SO_2), graphene and aluminium oxide (Al_2O_3) [14]. They are mechanically and chemically more robust and durable than their biological counterparts. The main drawbacks of solid-state nanopores are the requirement for nanofabrication methods, which are not necessarily highly reproducible, and a high electrical noise contribution, which is detrimental to sensitivity.

The most commonly used biological pore is α-hemolysin (αHL), a toxin from *S. aureus*, which has a diameter of about 1.4 nm at its narrowest point [15].The dimensions of this protein are very convenient to detect single molecules such as RNA or DNA since their diameter is ~1 nm. This pore was recently used as a biomolecular sensor for circulating miRNA [13]. The previously mentioned molecular techniques for miRNA detection require fluorescent labelling and/or amplification, while αHL-based detection of a specific miRNA species requires only its complementary DNA probe. This is because single strand DNA or RNA can pass freely through a nanopore with the dimensions of αHL, but a DNA-miRNA duplex cannot pass through the pore without first dissociating into two separate oligonucleotide strands. The DNA probe was modified with single-strand $(dC)_{30}$ overhangs in order to facilitate the capture of the duplex [13, 16, 17]. Unzipping of a DNA/miRNA hybrid at the pore channel entrance causes a specific pore current blockage, that is longer and deeper compared to the blockage produced by single-stranded DNA or miRNA molecules.

The capture frequency of DNA/miRNA hybrid by the nanopore is linearly correlated to the miRNA concentration. Therefore, to calculate the concentration of miRNA in the sample one needs to determine capture frequency. However, the extremely low concentrations of miRNAs in the biological sample reduce the capture frequency by the nanopore, which decreases the estimation accuracy of the concentration. Increasing the capture rate of miRNA-DNA duplex within the sample of constant miRNA concentration would be beneficial for both accuracy and sensitivity of the nanopore technique. The capture rate can be enhanced by increasing the applied voltage, by DNA probe modifications, by applying a salt gradient and by engineering the αHL nanopore [12, 18].

However, to date, there are no clear guidelines about either DNA probe modification, voltage application or salt gradient conditions for miRNA detection with αHL nanopores. Even though salt gradients have been previously established across biological pores to enhance miRNA capture rates [13, 19], there is no literature discussing their influence on resistive pulse parameters produced by miRNA-DNA probe duplexes. Moreover, the stability of lipid bilayers and nanopore biosensors under salt gradient conditions has not been reported.

1.2 Aims and scope

The aims of this work are to establish the optimal conditions and limitations of nanopore sensing of cancer-related miRNA species with wild-type αHL nanopores, and to apply optimized assay parameters to microRNA analysis of a clinical mRNA extract.

The main objective is to achieve a high resistive pulse frequency without compromising lipid bilayer and pore stability to such an extent that a statistically meaningful number of duplex-pore translocation events cannot be obtained. However, any strategy that enhances assay sensitivity should not come at the expense of sacrificing specificity. For example, it should remain possible to distinguish a probe-miRNA duplex unzipping event from single-strand DNA probe or single-strand miRNA translocation. Using synthetic microDNA as a model for (biochemically less stable) microRNA, key results obtained with miDNA-DNA probe duplexes should be verified with miRNA-DNA duplexes. Probe specificity should be evaluated with a non-target sequence.

The effect on NRPS parameters of increasing the applied potential, of introducing KCl salt concentration gradients over the nanopore, and of using electrolytes other than KCl under gradient conditions will be investigated with the miDNA155 - P155 probe duplex at 100 nM concentration as a reference sample. Lower duplex concentrations will be employed to assess assay sensitivity under specific conditions. To investigate any preferential interactions of the 3' or 5' oligonucleotide extension with the αHL pore, the effect of probes with an extension only on the

3' or only on the 5' side of the complementary DNA sequence should be compared with the NRPS characteristics of duplexes with the conventional double-extension design.

Clinical mRNA extracts will be provided by Prof. Alex Mirnezami and Dr Rahul Bhome (Faculty of Medicine, University of Southampton). It should be established whether the lipid bilayer membrane remains stable in the presence of mRNA extract, after dilution in a KCl solution to obtain a defined electrolyte concentration. The next question is whether extracts spiked with synthetic miDNA155-P155 duplex give resistive pulses. For a final test, diluted extract should be incubated with a DNA probe against a microRNA species that is expected to be present in the sample, and it will be evaluated whether resistive pulses corresponding to probe-hybridized target miRNA can be observed.

1.3 Summary of main achievements

This work, for the first time, showed how the resistive pulse parameters of miRNA-DNA probes can be modified in various *cis/trans* KCl gradients. The capture frequency exponentially increased with the salt gradient, but the dwell time of the miRNA-probe duplex considerably decreased. However, this work showed that by replacing the KCl from the *cis* chamber with LiCl or NaCl dwell time increases without significant reduction of the capture frequency.

Although the ability of αHL nanopores to detect at which side DNA/RNA molecules are translocating through the pore has been previously shown, this striking feature was not observed in the case of miRNA detection with DNA probes in any earlier published work. In this work was initially observed that the double overhang DNA probe produced a bimodal amplitude upon translocation through the αHL nanopore. Following, it was proved that modifying the probe to have single-side overhangs, enabled to distinguish between duplex nanopore entry by the 3’ or 5’ probe overhang. Moreover it was showed that, in salt gradient conditions, the double overhang modification is crucial for miRNA detection with αHL nanopore, since it does not produce long-lasting blockages characteristic of the single-side overhangs.

In this work, the different characteristics of DNA-DNA and DNA-RNA duplexes upon interaction with αHL pore were observed. The RNA-DNA duplex unzipped faster than the DNA-DNA duplex, as shown in previous work. However, it was showed that this feature depends on the voltage and possibly on the oligonucleotide sequence that is used in the experiment.

Although the salt gradient was proposed as an enhancing mechanism for improving the capture rate of the miRNA-DNA probe duplex, none of the existing studies did implement the salt gradient conditions in nanopore experiments with a biological extract. In this work, long-lasting pore clogging was observed in the presence of RNA extracted from clinical samples when salt

gradient conditions are used, hence the present work pointed out to the necessity of further processing of the RNA extract.

1.4 Thesis structure

This thesis is divided in 7 Chapters. Following this Introduction, Chapter 2 describes the importance of microRNA molecules for gene regulation and the possibility to use them as novel molecular biomarkers for a variety of diseases. Currently used conventional methods for miRNA detection are reviewed. Subsequently, biosensor-based methods for the detection and quantification of miRNA are outlined. The nanopore resistive pulse sensing technique and its various applications are then described in detail. Chapter 3 outlines the experimental techniques for the single-channel recordings, and shows the preliminary results obtained with nanopore resistive pulse sensing of homopolymers. Chapter 4 describes the results of nanopore resistive pulse sensing of miRNA155, miDNA155 and miDNA21 in symmetrical 1 M KCl solution. Chapter 5 investigates the influence of salt gradients across the nanopore on resistive pulses produced by miDNA-DNA probe duplex. In Chapter 6, preliminary results with clinical mRNA extracts are shown. Finally, conclusions can be found in Chapter 7.

Chapter 2: Literature review

This chapter outlines the importance of miRNA molecules in biological processes and the possibility to use miRNA species as novel molecular biomarkers for a large variety of diseases, especially specific types of cancer. Current conventional methods as well as biosensor methods for the detection and quantification of miRNA in clinical samples are described. The nanopore resistive pulse sensing technique and its diverse applications are then explained in more detail. The existing nanopore literature on miRNA detection and quantification is reviewed with an emphasis on miRNA detection with the αHL nanopore.

2.1 MicroRNA importance and biological pathway

MicroRNAs (miRNA) are groups of short non-coding RNA molecules (18-24nt) that are involved in many biological and pathological processes. It is believed that they regulate 30-60 % of human protein encoding genes by binding to specific messenger RNA (mRNA) inside a cell [1, 20]. The first miRNA was discovered in *C. elegans* in 1993, and miRNA sequences have been found in other animals and plants ever since. Today we know more than 2500 human miRNA sequences, and their number is constantly increasing. MicroRNA biogenesis begins with the transcription of primary miRNA (pri-miRNA) inside a cell, driven by RNA polymerase II (pol II). Pri-miRNA is several kilobases long, has a cap and 30 polyadenyl tail. Following, pri-miRNA is processed by Drosha and DGCR8 protein complexes, giving 60-100 nucleotides long precursor miRNA (pre-miRNA). Exportin 5 protein recognises pre-miRNA and transports it from the nucleus into the cytoplasm, where it binds to a multi-protein complex composed of Dicer, double-stranded RNA-binding proteins (dsRNAp) and Argonaute-2 proteins (Ago-2). Dicer along with dsRNAp generates a miRNA:miRNA* duplex, where the first strand presents the mature (guide) miRNA, while the second strand is called passenger miRNA*. This RNA duplex is then transferred to the pre-RNA silencing complex, where the passenger miRNA* is degraded while the guide miRNA binds to the Ago-2 proteins and generates the mature RNA-induced silencing complex (RISC), that is able to bind the mRNA in the cytoplasm. Target mRNA is recognized by the so-called seed region of the miRNA, that is located at its 5' end, from the 2^{nd} to the 7^{th} nucleotide. This seed region binds to 3' untranslated region of mRNA[1]. An interesting fact is that one miRNA can target several mRNA sequences; it is believed that this is due to the short seed region.

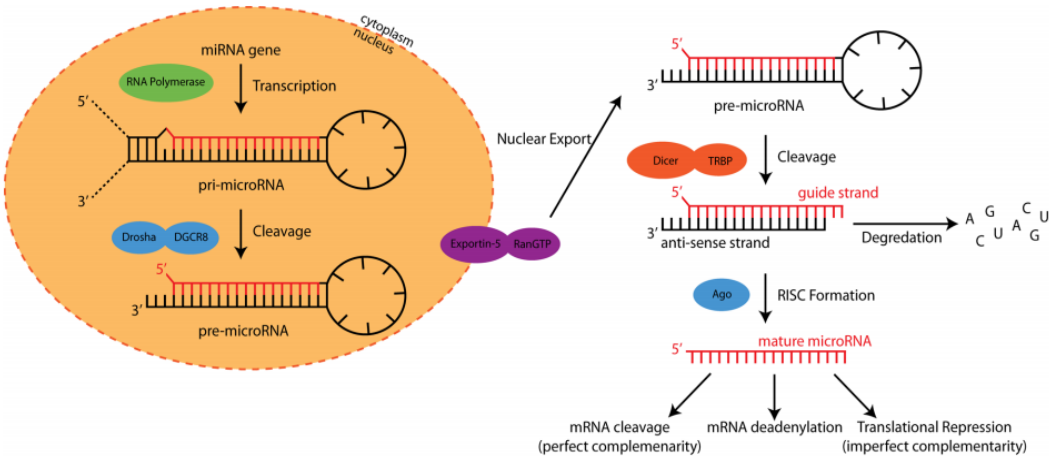

Figure 2.1. Biogenesis pathway of miRNA. The miRNA transcription starts in the cell nucleus while its maturation occurs in the cytoplasm, where the mature miRNA sequence interacts with target mRNAs, thus affecting protein expression. Taken from [10]

The miRNA-mRNA interaction usually triggers an inhibition of the protein expression. For this reason, miRNAs play an important role in many biological processes, such as cellular development, proliferation, differentiation, metabolism and homeostasis [21].

2.1.1 MicroRNAs role in disease-potent disease biomarkers

Considering their great importance in the gene expression, it is not surprising that abnormal miRNAs expression profiles were found for various diseases. Calin *et al.* were the first to report that an irregular expression of two miRNAs is related to chronic lymphocytic leukaemia [22]. The miRNAs that enhance cell proliferation, angiogenesis and reduction of tumour suppressor mRNAs are called *oncogenic miRNAs*. For example, miRNA21 belongs to the group of oncogenic miRNAs being involved in the downregulation of several tumour-suppressing genes [23-25]. It was found to be overexpressed in many cancer types including breast, stomach, liver and colon cancer [26, 27]. On the contrary, miRNAs that enhance cell death, differentiation and enhance tumour suppressor genes are called *tumour suppressor* miRNAs [28]. For example, the tumour suppressor miRNA family such as let -7 was found downregulated in lung cancer [29]. Hence, in cancer tissues, either oncogenic miRNAs are upregulated or tumour suppressor miRNAs are downregulated. Their irregular expression profiles in cancer tissue are found to be tissue-specific and significantly different from expression profiles in healthy tissues [3, 30]. Abnormal miRNA expression profiles were reported for cardiovascular diseases, neurodegenerative diseases and inflammation processes [1, 31]. MiRNAs were found in stable form in 12 bio-fluids including saliva, urine, plasma and serum [32]. They can enter into blood circulation either passively after cell death or by active secretion [31]. Despite being short RNA sequences, they have proven to exist in a remarkably stable form encapsulated in exosomes, in microvesicles and mostly co-fractioned with Ago-2 proteins, that are believed to protect them from RNAse activity [33]. It was found that their expression levels in blood were altered in many diseases, including cancer [34].

The existence of these cell-free, circulating miRNAs in easily accessible sources such as body fluids makes them a promising, non-invasive biomarker for prognostic and diagnostic purposes [34].

2.1.2 Current methods for miRNA quantification

Detection and quantification of specific miRNAs is a challenging task due to their small size, a similarity between sequences, extremely low levels in samples and heterogeneity of their origin [35]. Both the above-mentioned pri-miRNA and pre-miRNA contain the mature sequence of miRNA, so the presence of this longer intermediate in the sample can influence the accuracy of the miRNA detection [36]. The amount of expected miRNA amount varies significantly with the sample origin and can span several orders of magnitude (Table 2.1). Moreover, it is estimated that each miRNA represents only a small fraction of the total RNA extracted ~0.01%[8]. MiRNAs extracted from bio-fluids are more desirable biomarkers, as samples can be obtained more easily and with less discomfort for the patient compared to biopsies.

Table 2.1. MiRNA concentration range in different samples [35].

Sample	Sample size	Total RNA (µg)	Amount of each mature miRNA
Cell cultures	10^5 cells	0.2-3	0.3 amol to 30 fmol
Tissues	50-100 mg	>5	0.3 amol to 30 fmol
Serum-plasma	200-400 µl	0.01-1	7 zmol to 3 amol
Other body fluids	200-400 µl	0.027-14	-

The three main methods for miRNA detection in biological samples are quantitative reverse transcription polymerase chain reaction (qRT- PCR), microarrays and next-generation sequencing (NGS). The protocols to detect circulating miRNAs are the same ones that are used for the detection of tissue/cell miRNAs, but the amounts of starting material are significantly lower [37]. Every technique has its own advantages and disadvantages in the detection and quantification of miRNAs.

2.1.2.1 qRT-PCR detection of miRNA

The polymerase chain reaction (PCR) is a method for detection and amplification of desired nucleotide sequences. This technique uses repeated heating and cooling cycles of a buffer solution containing the sequence of interest, DNA polymerase enzymes and free single nucleotides. Heating the solution to 95 °C denatures double-stranded DNA (dsDNA) and is followed by cooling it down to 55 °C with a complementary binding of primers to the target nucleotide sequence. The solution is subsequently heated to app 70° C to initiate the activity of taq polymerase which adds nucleotides to the primer sequence [38]. This cycle is repeated many

times, resulting in exponential amplification of the desired nucleotide sequence. The qRT-PCR is a modification of PCR, where an RNA sequence is firstly converted into its complementary DNA (cDNA) by reverse transcription. This can be achieved with two main strategies: stem-loop primer method and poly A tailed PCR [39]. qRT-PCR is the current gold standard technique for miRNA detection, with reported detection range spanning from 0.1 aM to 10 fM [40]. cDNA is usually quantified at the end of each thermal cycle by measuring the fluorescence intensity, thus this method requires an addition of fluorescently labelled probes (SYBR Green and TaqMan, Figure 2.2) which bind to cDNA [41, 42]. Extraction efficiency is usually assessed by addition of a known amount of non-human miRNA in the sample prior extraction, which is used to normalize the data. However, small miRNAs are difficult to amplify with qRT-PCR since the usual primers used for PCR are in the same size range as miRNA molecules. Therefore, the main drawback of this method is the need to design specific primers for short miRNAs. Moreover, various miRNA sequences might differ in one or two nucleotides only, which makes the primer design even more complicated. Another disadvantage of qRT-PCR is its inability to detect multiple miRNA targets in the volume of a single sample [43]. In addition, the detection can be altered by DNA contamination of the sample, so removal of DNA molecules from the sample is a mandatory step to add prior to miRNA detection.

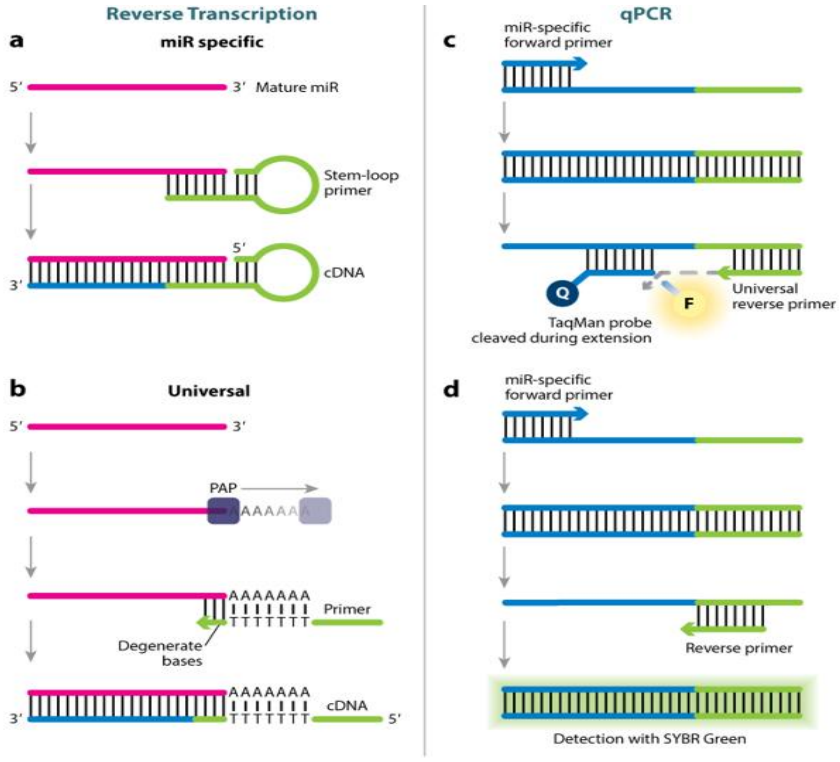

Figure 2.2. Two methods for creating cDNA sequence from mature miRNA a) with stem-loop primer and b) PAP universal primer. Fluorescent detection of qPCR of miRNAs using c) TaqMan fluorescent probe or d) SYBR green fluorescent probe for miRNA detection. Taken from [43].

2.1.2.2 Microarray based detection

Microarrays allow high-throughput detection of multiple miRNAs simultaneously in one sample and constitute a suitable method for miRNA screening. The detection is based on the hybridization of fluorescently labelled miRNAs with DNA probes immobilised on microarray plates (Figure 2.3). The probes in microarray detection have a linker and a capture sequence. The linker sequence is situated at the 5' end, and consists of either poly A or poly T; it has a modified amine so it can bind to the amine-reactive glass slide. The capture end instead is a complementary sequence to the specific miRNA [44]. After extraction from the biological sample, miRNAs are fluorescently labelled and hybridised with the DNA probes on the microarray plate. Microarrays can contain thousands of different probes that can span large melting temperature intervals. Since hybridization efficiency depends on the melting temperature T_m, it needs to be normalized [44]. Normalization can be achieved by altering the DNA probe length, but because of short miRNA length, this method is not suitable for normalization. It was shown that locked nucleic amino acids (LNA) can be used to enhance thermal stability of miRNA/DNA probes and were reported to increase both sensitivity and selectivity of miRNA detection [45]. Recently the ligase assisted sandwich hybridization was used for label-free detection of synthetic miRNA131, with a limit of detection of 30 fM, that is comparable to the detection limits found with the qRT-PCR method [46]. However, the common microarray assays are lacking sensitivity, since different probes have different hybridization preferences. Most of the literature reports limits of detection in the nM-pM range, that is lower compared to the qRT-PCR resolution. Other disadvantages of microarrays miRNA detection are the requirement of a relatively high amount of total RNA extract as an input (ng- µg), and the long time to result of the experiment, which can exceed 24 hours [11].

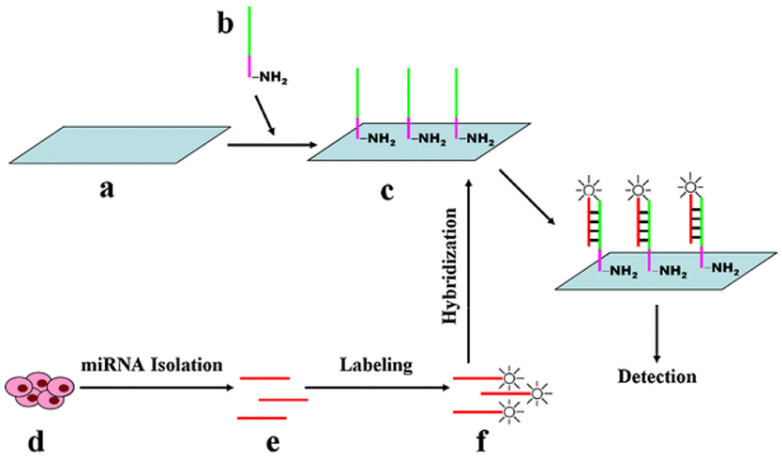

Figure 2.3. Microarray-based detection of miRNA. a) Amine-reactive glass slide b) DNA probes with linker part (purple) and capture sequence (green) c) microarray plate with DNA capture probes d) miRNA isolation from a biological sample. e) Labelling miRNA with fluorescent dye f) hybridization of miRNA and DNA capture probe followed by fluorescence detection. Taken from [44].

2.1.2.3 Next-generation sequencing

Development of next-generation sequencing (NGS) made possible to comprehensively study miRNAs expression profiles. This technique relies on new next-generation sequencing machines that are able to process millions of sequence reads in parallel over short periods of time. The common scheme of miRNA profiling with NGS technique is shown in Figure 2.4. The first step of NGS sequencing is the construction of a cDNA library, prepared from the RNA sample of interest. Extracted RNA is firstly run on an agarose gel, so the bands corresponding to sizes of miRNAs can be cleaved, and subsequently modified with sequencing linkers on both 5' and 3' miRNAs ends. They are then reversely transcribed to cDNA [47-49]. Another run on agarose gel can be made to cut the bands with the length that correspond to miRNA with added adapters. The next step is a large-scale parallel sequencing of individual cDNA molecules from the library, and quantification of their expressions by a density of accumulated reads profiles, which is done with bioinformatical tools. Some of the limitations of this technique include the high cost, high amount of initial RNA required (10 µg) and the need for special equipment and highly skilled bioinformaticians.

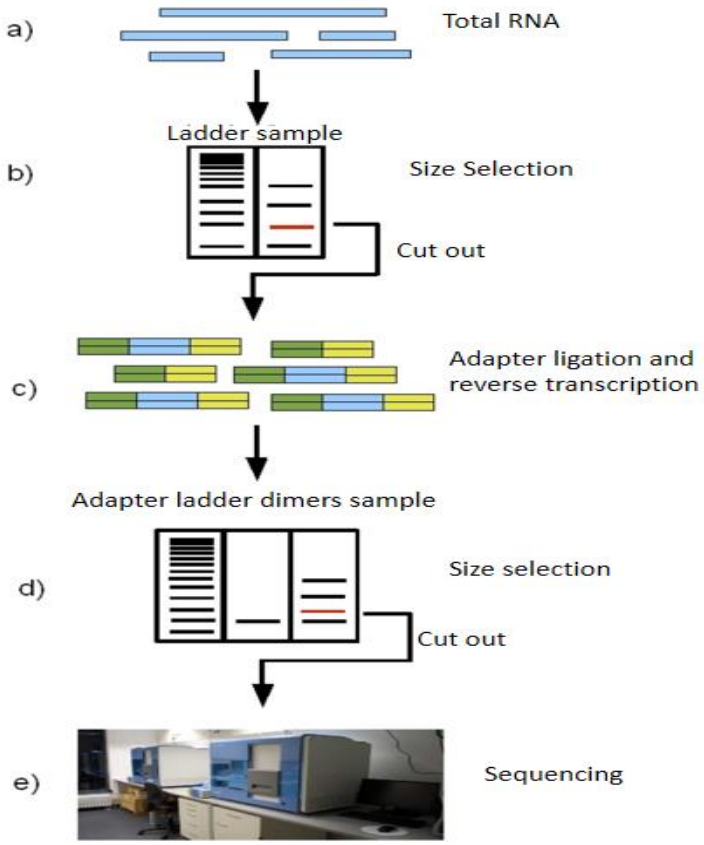

Figure 2.4. The scheme of Illumina strategy for miRNA detection. a) Total RNA is extracted from the sample. b) Size selection of only short RNAs from the agarose gel. c) Adapter ligation and reverse transcription. d) Size selection of only miRNAs sequences from the agarose gel. e) Sequencing. Taken from [49].

2.2 Biosensor methods for miRNA detections

Biosensors are devices able to detect and quantify biological analytes by converting their presence and concentration into a signal that can be detected and analysed [50]. They consist of a biological component (enzymes, proteins, nucleic acids, antibodies, receptor proteins) and a transducer, or physicochemical detector. Based on the type of transducer, biosensors can be divided into several categories, such as optical, electrochemical, magnetic, ion sensitive, calorimetric, piezoelectric etc. Biosensors play an important role for cancer diagnostics thanks to their ability to detect various cancer biomarkers (such are DNA, RNA fragments and proteins) before a diagnosis can be done with clinical techniques [9]. A vast amount of work has been done recently on miRNA detection and quantification, using various types of biosensors. The new materials and the development of nanotechnologies resulted in excellent limits of detection and increased dynamic range.

2.2.1 Detection of miRNA with optical biosensors

Optical biosensors detect variations in fluorescence, absorbance and refractive index. The miRNA detection is based on hybridization with DNA probes that are usually modified with optical reporters. The miRNA detection with optical biosensors relies on fluorescence, electroluminescence or plasmonic and photonic approaches [10]. The limit of detection of miRNA reported with optical biosensors is in the nM – aM range [10].

Fluorescent assays use fluorescent molecules to bind with miRNA via detection probe. Specificity of the detection might be achieved by constructing molecule complexes that will have an ‘off’ fluorescent signal in the absence of miRNA in the sample, while the fluorescent signal will switch ‘on’ in the presence of miRNA. Detection of off and on states can be done with FRET (Forster Resonance Energy Transfer) imaging technique. In order to detect fluorescence with FRET technique, the energy needs to be transferred from a fluorophore donor to a fluorophore acceptor molecule. Wu *et al.* detected miRNA 141 with a DNA displacement scheme, where the DNA probe for miRNA 141 was labelled with fluorescent FAM tag at the 5' end and hybridized with 12 nt long output probe which contained ((Dabcyl)-labelled) quencher at the 3' end, forming a DNA probe-quencher molecular beacon [51]. In the absence of miRNA in solution, there was no fluorescence observed because of the close position of the quencher to the fluorophore probe. However, in a presence of miRNA 141, the quencher tag was displaced with the fully complementary target miRNA sequence. This resulted in emittance of fluorescence signal [51]. The intensity of fluorescence signal could be correlated with the target miRNA concentration. By using this approach miRNA sequences were detected with the limit of detection of 1 fM [51]. Molecular beacons can be constructed in a way that it is initially an open mode and the fluorescence is decreasing upon addition of miRNA to the sample. Larkey *et al.* detected miRNA

let 7 with DNA displacement technique with a limit of detection of 10 nM [52]. Reporter molecule was modified with fluorescent Cly3 and Cly5 molecules at both ends and hybridizes with DNA probe. Upon addition of miRNA let-7-c, the reporter molecule was replaced with miRNA strand, which led to its folding and to the moving of the quencher closer to the fluorophore. This resulted in a decreased emittance of fluorescence [52].

Different FRET pairs were used to improve the assay sensitivity. For example, fluorescence quenching graphene oxide (GO) was used to absorb the fluorescent DNA probe [53]. Without the miRNA in the solution, no fluorescence was observed. When miRNA126 was introduced in solution and hybridized with DNA probe, the exonuclease cleaved the miRNA:DNA probe hybrid from graphene oxide quencher, which increased the fluorescence signal. Tu *et.al* reported a limit of detection of miRNA126 as low as 3 fM [53].

Electrochemiluminescent (ECL) detection is another optical method used to quantify and detect miRNAs. It requires the ECL reporter molecule that is able to emit light as a result of electrochemical excitation. Liu *et al.* used (2,2'-bipyridyl) ruthenium (II) $[Ru(bpy)_3]^{2+}$ labelled probe to detect miRNA21 in three cell lines, and were able to detect up to 100 pM without any amplification or sample recycling [54]. With the target sample recycling strategy and enzymatic amplification, the ELC detection was vastly improved [55, 56]. Chen *et al.* reported an ECL biosensor for miRNA21 detection based on a target-induced cycling strand displacement amplification (SDA) mediated by Phi29 [56]. The dynamic range of detection was 10 aM – 10 pM, with the limit of detection as low as 3.3 aM.

Surface plasmon resonance technique (SPR) is an optical method that can be employed to detect low levels of miRNAs. The surface plasmon resonance detects changes in the optical properties caused by hybridization of target miRNA with the probe. Qui *et al.* coupled the enzyme DSN activity with SPR technique to detect and quantify miRNA21 in the blood RNA extracted from cancer patients. They reported the miRNA21 limit of detection of 3fM [57]. The DNA probe was immobilised on reduced graphene oxide (rGO) SPR biosensor. After miRNA21 hybridization, the DSN enzyme cleaved miRNA21:probe duplex from the rGO, thus displacing the DNA probes from the rGO surface, which caused a decrease in signal [57].

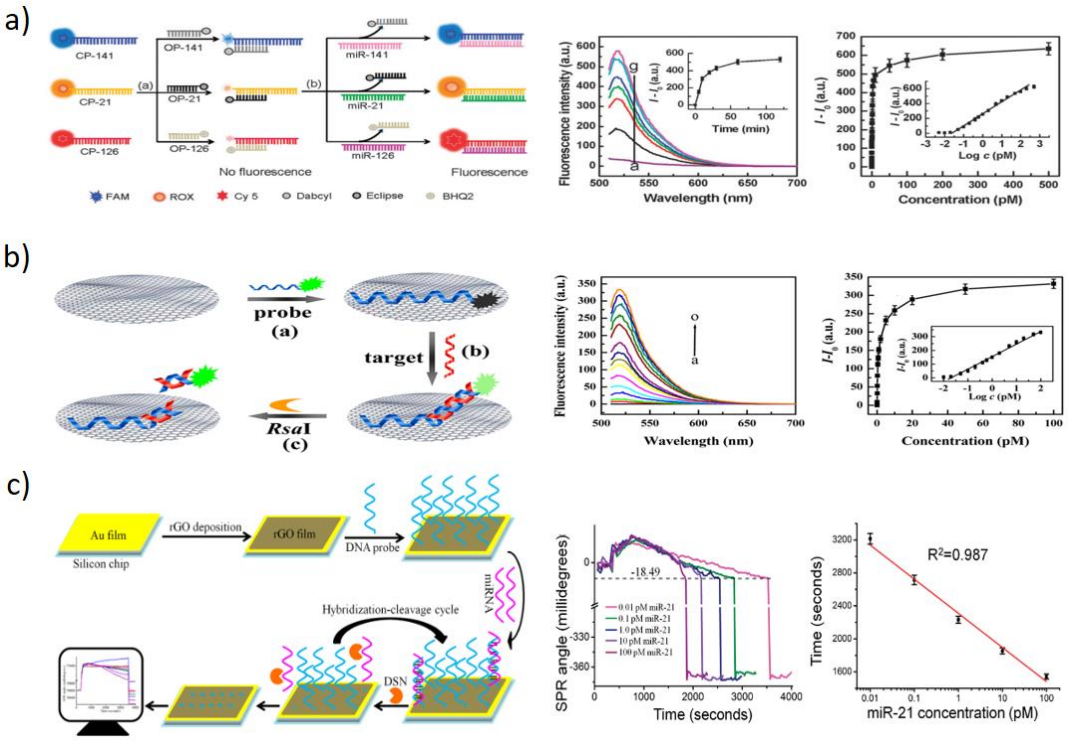

Figure 2.5. a Multiplex detection of miRNAs by FRET detection. Without miRNA presented in the sample the, there is no fluorescence signal because of the close proximity of the fluorophore and quencher on DNA probe. The fluorescence intensity is increased by with miRNA141 concentration. Taken from [51] b DNA probe labelled with a fluorophore is quenched with graphene oxide (GO). After hybridization with miRNA, the target sequence is cleaved from GO resulting in an increase of fluorescent signal (right panel). Taken from [53]. c) Surface plasmon resonance detection of miRNA. The DNA probes are immobilized on reduced graphene oxide surface. After hybridization with target miRNA the DSN cleaves the miRNA:DNA probe duplex which induces SPR angle shift. Taken from [57].

2.2.2 Electrochemical detection of miRNAs

Electrochemical sensors are a great tool for a cheap, rapid and simple bioanalysis. The electrochemical detection is based on the hybridization of a target miRNAs with immobilized DNA capture probes on a solid electrode surface. The redox signal or the change in capacitance or impedance are measured [58-63]. With this method, it is possible to detect miRNA in the ranges of aM – nM levels [64]. The detection of miRNAs can be achieved by label-free, label based and enzyme-based methods [10]. Later one allowed ultrasensitive miRNA detection. Ren *et al.* detected miRNA let – 7b with immobilized thiolated DNA capture probes on a gold electrode (Figure 2.6 a) [60]. After hybridization, the target miRNA:capture probe complex was cleaved from the gold electrode with a duplex-specific nuclease (DSN). The concentration of let – 7b was determined by measuring the impedance changes between control and DNS cleaved biosensor. The limit of detection with this enzyme-based electrochemical biosensor was reported to be 1 fM [60]. Miao *et al*. were able to detect 1.6 fM of miRNA21 by measuring the electrochemical signal reduction of methylene blue (MB) [65]. The capture probe for miRNA21 was immobilised on the gold electrode, while guanine-rich detection probe was modified with MB and immobilized on gold nanoparticle (Figure 2.6 b). Addition of miRNA21 lead to the creation of a DNA complex

composed of miRNA21, capture probe and detection probe. In the presence of K^+ ions, the detection probe adopted a quadruplet structure able to interact with the iridium complex. Li *et al*. detected miRNA24 by monitoring the oxidation signal of guanine [66]. They used multi-walled carbon nanotubes on which DNA probes complementary to miRNA24 were immobilized by cross-linking. After hybridization of miRNA24 to the DNA probes immobilised onto the carbon nanotubes, the difference in guanine oxidation was measured by differential pulse voltammetry (DPV). The limit of detection of miRNA24 by this technique was reported to be 1pM [66]. Tran *et al.* used quinone polymer on the functionalized electrode surface[67]. In the absence of miRNA in the sample, DNA probes were captured on the electrode, which resulted in a differential current output, whereas in the presence of target miRNA the current output was linear. The limit of detection of this technique was reported at 650 fM [67].

An even higher sensitivity (0.76 aM) was reported by Cheng *et al*. [68]. They used streptavidin-functionalized titanium phosphate nanoparticles with incorporated Cd^+ ions (Figure 2.6 c). The thiol-modified DNA probe was attached to the gold nanoparticle modified graphene. The titanium nanoparticles bound to biotin labelled capture probe: miRNA21 hybrid. Electrostatic attachment of $[Ru\text{-}(NH_3)_6]^{3+}$ to DNA probe served as an electron mediator between titanium phosphate nanoparticles and electrode surface [68]. The electrochemical current of Cd^+ ions was used to determine the concentration of miRNA21 sequence. The current – miRNA21 concentration was linear over 7 orders of magnitudes, from 10^{-10} M –10^{-18} M [68].

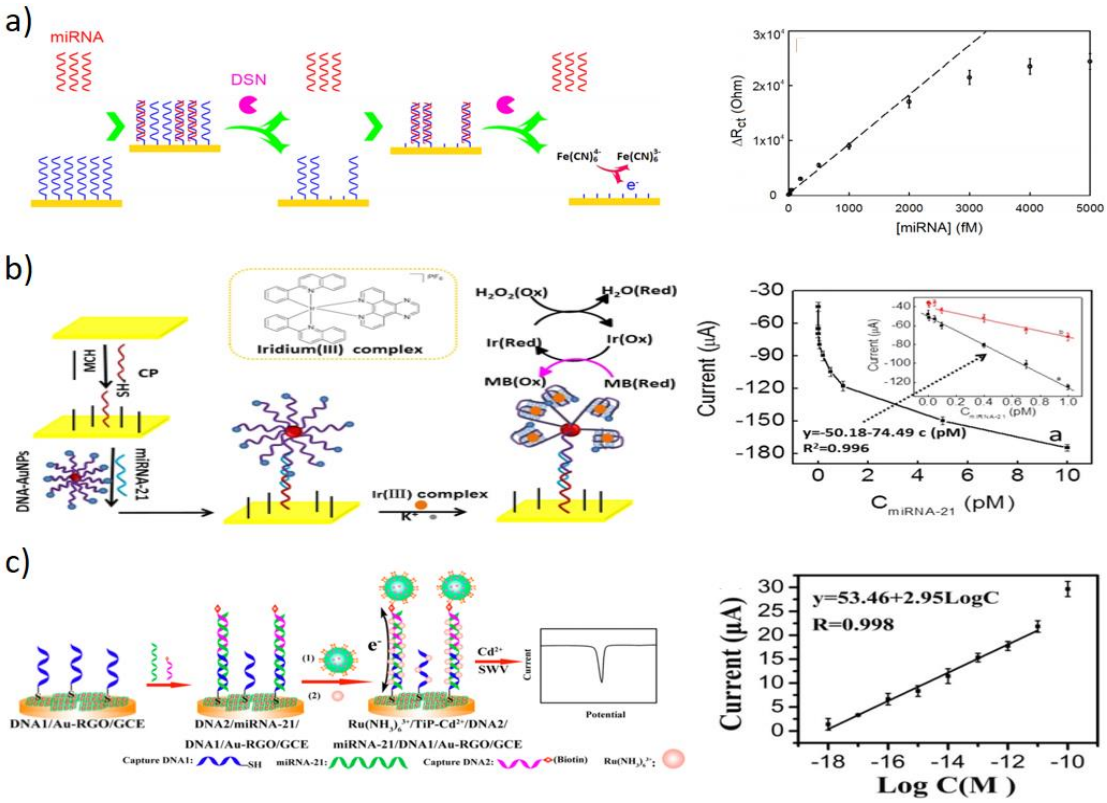

Figure 2.6. Electrochemical detection of miRNAs. a) Scheme of impedimetric detection of miRNA assisted with a duplex-specific nuclease. Taken from [60]. b) Electrochemical detection of miRNA21 by using iridium (III) complex. Taken from [65]. c) Electron transfer mediated electrochemical biosensor for microRNAs detection. Taken from [68].

2.3 Comparison of miRNA detection with biosensors and common molecular methods

When compared to the conventional molecular techniques for miRNA detection, where the time to result can be longer than one day, the biosensor detection methods are significantly faster (results can be obtained from ~1 to 2 hours [11]). Another advantage of biosensors is the existence of label-free methods that do not require labelling of miRNA targets. This simplifies the sample preparation and decreases times and costs of the detection [11]. Molecular techniques such are microarrays, qRT-PCR and next-generation sequencing usually require a large amount of RNA for miRNA detection, while biosensor techniques require much lower amounts of total RNA extract [11].

On the other hand, the multiplex detection of different miRNAs is one of the main challenges for biosensors, since the sequences of miRNAs can differ in only one nucleotide and the expression levels can vary more than five orders of magnitudes for different miRNAs. The multiplex detection would require parallel analysis and the use of more complex instrumentation, like multiple electrode configurations and different potentiostats [11].

2.4 Nanopore sensing

During the last two decades, the nanopore technology showed exceptional ability to detect, quantify and characterise a large variety of biomolecules. The technique was proposed as a potential low cost technique for DNA sequencing. Moreover, nanopores are a great candidate for many point of care applications *ie.* detection of DNA damages, heavy ion detection and lately miRNA quantification. This section will introduce the nanopore resistive pulse sensing technique with its applications. Since the biological nanopore αHL will be used as a miRNA sensor in this work, the various applications of this pore will be detailed.

2.5 Nanopore resistive pulse sensing working principle

Nanopore resistive pulse sensing (NRPS) is a technique able to detect molecules based on the decrease in ionic current or resistive pulse that a molecule is producing upon its interaction with the nanopore channel. This method is similar to the classical Coulter counting used for detecting bacteria, viruses and prokaryotic cells in electrolytes [69]. The Coulter counter consists of two electrodes placed across an orifice separating two electrolyte solutions and electrometer measuring the conductivity of electrolyte [70]. The conductivity of the orifice would decrease upon passing of erythrocytes, cells or bacteria presented in solution [70].

With the development of electrophysiology techniques that are able to measure ionic currents through nanoscopic structures such as ion channels and nanopores, the concept of Coulter cell detection was extended to single molecule sensing [71-73]. The common nanopore setup is consisting of two electrolyte-filled compartments (*cis* and *trans*)[1] which are separated by an insulating membrane containing either machined, artificial or biological pore [74]. The pore in the insulating membrane serves as the only connection between compartments providing passage of ions and analyte molecule across the insulating membrane. The potential difference in the nanopore system is applied via two electrodes placed in each compartment. Usually, the *cis* compartment holds the ground electrode, while the *trans* compartment contains the working electrode that applies the potential to the system [74, 75]. When a steady potential is applied to nanopore system it causes electrophoretic movement of ions through the pore that results in the generated ionic current that can be measured by low-noise, high-impedance amplifier. Nanopores have usually linear current-voltage response, which gives a steady DC current signal when a constant voltage is applied across the nanopore (Figure 2.7 a). Once analyte enters the pore, the

[1] Cis and trans names are taken from electrophysiological ion channel recording where *cis* is associated with extracellular side and *trans* is associated with an intracellular side of the membrane.

ion current flux through the pore reduces. These current blockages are called resistive pulses and can be measured and characterised by amplitude and duration of the block. After interaction is over the pore current restores to its open value current until another analyte molecule occupies the channel again. The occurrence of resistive pulses is correlated with the analyte concentration in solution i.e. larger number of pulses means higher analyte concentration [76]. Hence, characterization of analyte interaction with a pore is measured by three parameters: duration of analyte-pore interaction or dwell time (τ_{off}), inter-event time between two resistive pulses (τ_{on}) and amplitude of pulse $I_{RES} = I_B/I_0$, where I_0 is open pore current while I_B is blocked current. The dwell time (τ_{off}) and current amplitude of resistive pulse are specific for a target molecule and are concentration independent [77]. The concentration of the analyte molecule can be determined by measuring capture frequency (f_{on}) that can be calculated as the inverse of the interevent time $f_{on} = 1/\tau_{on}$ [78]. The resistive pulses associated with analyte-pore interaction occur randomly hence the nanopore is usually described as a stochastic sensor. Consequently, the dwell time and interevent intervals have a stochastic nature and follow a statistically exponential distribution. The mean duration of dwell time and interevent interval are determined as time constants of their exponential distributions.

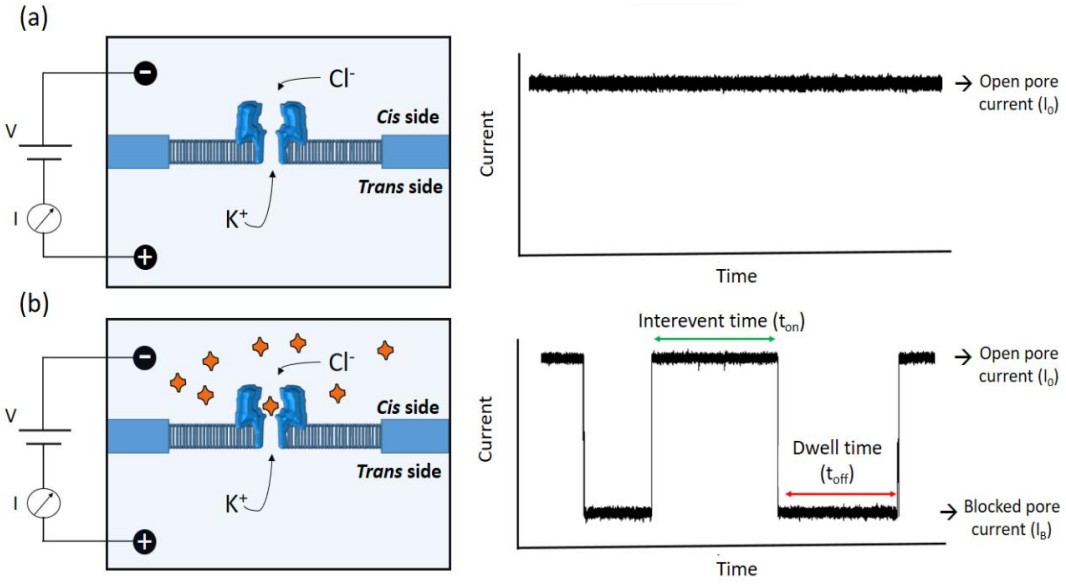

Figure 2.7. The principle of nanopore resistive pulse sensing experiments. A biological pore is reconstituted in the membrane separating two chambers filled with KCl electrolyte. Two electrodes immersed in solution are used to apply a voltage and measure the ionic current flowing through the pore. (a) Open pore current ionic current as a response to the applied voltage when no analyte molecules are presented in the solution (b) Modulation of ionic current through the pore as a result of analyte occluding the pore. Parameters that can characterize resistive pulses are time between two adjacent pulses or inter-event time (t_{on}), block duration or dwell time (t_{off}) and current block amplitude I_B.

Detection of molecules with nanopore is based on modification of ionic current hence, the nanopore needs to be wide enough to accommodate both molecule of interest and ions in their hydrated form e.g. 2 nm for double-stranded DNA (dsDNA). Resolution of nanopore detection

theoretically depends on the hydrated dynamic size of ions (~0.1 nm) thus; nanopore should be able to distinguish two molecules whose difference is in range of hydrated ion size [71].

2.6 Types of nanopores

Nanopores can be divided into two groups: biological and solid-state. The insulating membrane for biological pores is lipid bilayer since it is necessary to restore their functionality while the solid-state nanopores can be fabricated with great precision in materials such are silicon nitride (SiN), silicon oxide, alumina or graphene. Both of the nanopore technologies were used for broad single molecule sensing with a DNA as a most common molecule of interest.

2.6.1 Biological nanopores

The majority of biological nanopores used in nanopore technologies are secreted by bacteria and belong to the family of pore-forming toxins [79]. Since they are transmembrane proteins, they require a biological membrane environment in order to restore their functionality. The common substrates where biological pores are reconstituted are planar lipid bilayers, liposomes and other polymer films [80-83]. The main advantages of biological nanopores are their high reproducibility and well-defined geometry [14]. Moreover, the features of biological nanopores can be changed by bioengineering, hence they can be customized in order to improve the sensing of specific analytes [84].

To date, the most common biological pore in nanopore sensing experiments is alpha hemolysin (αHL). Commercial availability, resolved atomistic structure, well-defined conductance and stability over a range of physicochemical conditions make αHL the most reasonable choice for nanopore detection. αHL is a bacterial toxin secreted by *Staphylococcus aureus* as 293 amino acids. These water-soluble monomer associates as a heptamer in the membrane [85]. When αHL assembles in eukaryotic cell membranes it yields strong haemolytic activity via disturbing the membrane potential by providing non-selective passage of K^+, Ca^{2+}, ATP and low molecular weight molecules through the membrane [86, 87]. This protein is 10 nm long when inserted in a phospholipid bilayer (Figure 2.8). The transmembrane part is 5.5 nm long and 2.6 nm wide. The cap of the protein has a diameter of 10 nm and comprises of 2x7 antiparallel beta strands from each monomer. The crystallographic structure revealed that the cap opening has a diameter of 2.6 nm, which widens to 3.8 nm in the vestibule of the protein [15]. The lysine ring at 147, situated in the beginning of the transmembrane stem, is responsible for the narrowest constriction of the protein, being about 1.4 nm [15].

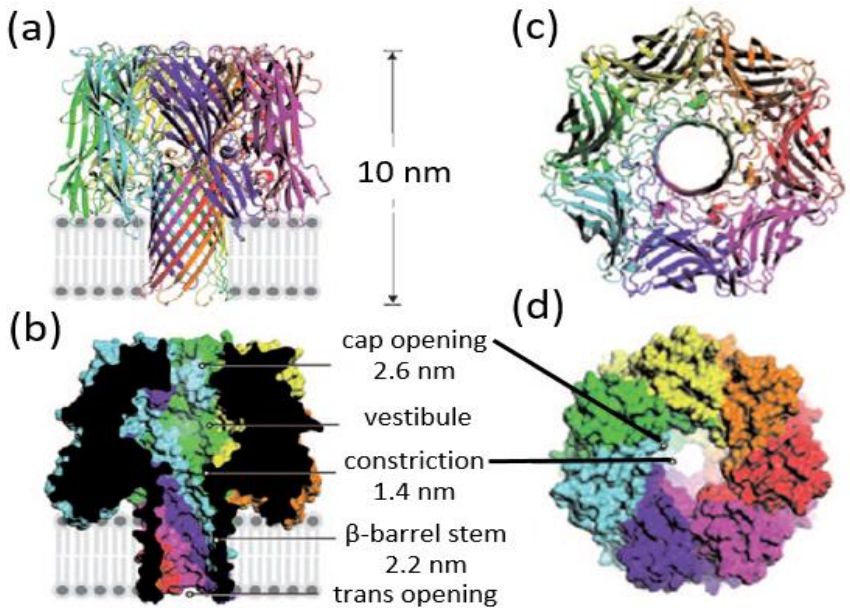

Figure 2.8. (a) Side view of the αHL in a lipid membrane. Both length of the protein and its diameter of the cap are 10 nm long (b) The cross-sectional view of the αHL nanopore. The diameter of the pore is changing from *cis* side to the *trans* side. Narrowest constriction is 1.4 nm wide. (c)(d) Top view of αHL channel from cap domain. Each colour presents different subunit of the pore. Taken from [78]

The constriction of αHL is of great importance for molecular detection because molecules with a diameter larger than 1.4 nm cannot translocate through the pore. For example, double-stranded DNA (dsDNA) cannot translocate through αHL pore since it has a diameter of 2 nm, while single-stranded DNA ssDNA is able to pass since its diameter is about 1 nm [88].

The conductance of αHL in a solution of 1M KCl with pH ranging from 7.4 to 8 is well defined and has a constant value of ~ 1 nS, which makes the nanopore detection of molecules passing through the channel straightforward [89]. Moreover, it is stable over a broad temperature range, spanning from 4 ºC to 93 ºC [90], and can be used in a wide pH spectrum ranging from acidic pH 4 to alkaline pH 11 [91]. It does not show gating events, although misfolded monomers can lead to different structures and to unpredicted current levels produced by the protein in the membrane [92].

Although the vast majority of nanopore sensing experiments with biological pores was done with αHL, its dimensions of 10 nm and constriction of 1.4 nm can be a limiting factor for specific analyte sensing [74]. There are several alternative biological nanopores with different pore characteristics that can be used for more specific analyte detection (Figure 2.9). For example, **MspA** (*Mycobacterium smegmatis* porin A) has a constriction that is 1.2 nm wide and only 0.6 nm long, which makes this pore suitable for DNA sequencing applications [93, 94].

Phi29 motor. Bacteriophage phi29 motor consists of 12 subunits that assemble in the channel. This protein is 3.6 nm wide and 7.5 nm long and allows the detection of larger analytes compared

to αHL nanopore. The conduction of phi29 in 1 M KCl was found at 4.8 nS, that is almost five times higher compared to αHL [95]. This pore was used for detection of dsDNA [95, 96].

Cytolysin A (ClyA) is a toxin secreted from *Salmonella typhy* and it is assembled from twelve monomeric subunits. This pore is 13 nm long and it has two openings. The narrower opening is 3.3 nm wide while the larger is ~6.4 nm wide. This makes ClyA pore more suitable for larger analytes, such as proteins and ds DNA [97-100].

Aerolysin is an hexameric pore toxin from *Aeromonas hydrophila*. Compared to αHL, having the narrowest constriction of about 1.4 nm, aerolysin is only around 1 nm wide in its extracellular part [101]. The smaller constriction makes this pore convenient for sensing of narrower molecules such as ssDNA, peptides and sugars [102-104]. Moreover, the lumen of the pore is believed to contain ~91 charged amino acids, which makes this pore strongly anion selective [101]. The charged pore lumen is also believed to slow down the DNA translocation, thus enhancing the sensitivity of the system. Aerolysin was demonstrated to separate poly (dA) from 2-10 nt based on the current block amplitude [104]. Baaken *et al.* showed that this pore has better resolution for discriminating polyethylene glycol (PEG) polymers compared to αHL pore [105].

Outer membrane protein G (OmpG) from E. coli assembles as a monomer in the membrane. Its channel is made of 14 beta barrels with a pore dimension of ~1.3 nm, similar to αHL pore [106]. An engineered form of OmpG pore was used to detect proteins via not translation mechanism [107, 108].

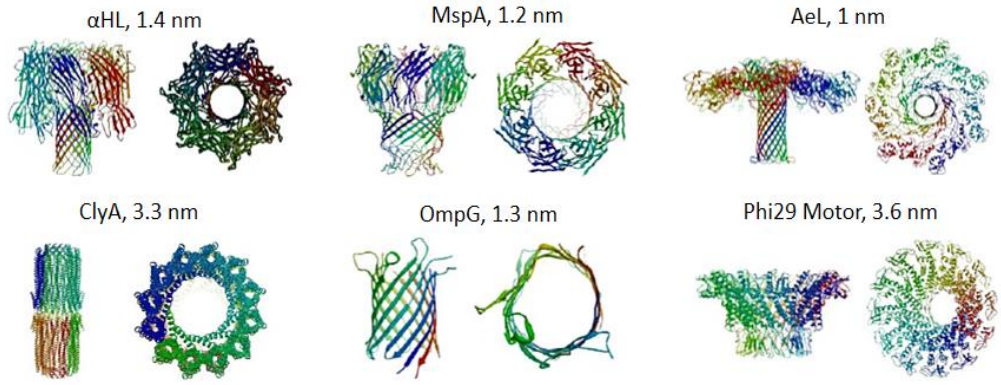

Figure 2.9. Structures of common biological pores used in nanopore sensing along with their critical constrictions. Modified from [84].

2.6.2 Solid-state nanopores

Although they have a superior atomistic resolution, biological pores present some disadvantages. Their main limitation is the requirement of a mechanically fragile lipid bilayer in which the protein pore needs to be assembled in order to become functional, which can be a long and tedious process [83]. The narrow pore-size range limits the detection of analytes. As they are biological

structures, they are sensitive to physicochemical conditions such are ion concentration, lipid bilayer composition and pH of the solution [109]. After single pore insertion, there is a certain probability that other pores will insert, which can lead to instability of the bilayer and complications in the data analysis. It is not surprising that a lot of effort was put in developing solid-state nanopores, which would overcome the previously mentioned problems associated with biological pores [110]. Solid-state nanopores are inexpensive and more robust compared to biological nanopores. Their diameters and thicknesses can be tuned with sub-nanometre precision, which enables a broader size range compared to biological nanopores. Common materials for solid-state nanopore fabrication are silicon nitride SiN and silicon dioxide SiO_2, due to their excellent chemical and mechanical resistance [111]. Apertures with diameters ranging from 2 to 20 nm can be fabricated in silicon-based membranes by using transmission electron microscope (TEM) [112].

By using atomic layer deposition (ALD) it is possible to produce nanopores in Al_2O_3 material with angstrom-level control. These nanopores can be produced with electron beam irradiation in a size ranging from 2-30 nm in 45-60 nm thick Al_2O_3 and are more robust compared to silicon-based nanopores [113]. Moreover, Al_2O_3 nanopores possess positive surface charge, unlike their silicon-based counterparts whose surface is negatively charged.

Graphene nanopores were firstly fabricated by Drndić and co-workers in 2008 [114]. Graphene has excellent mechanical, electrical and thermal properties. The thickness of graphene monolayers is similar to the distance between two nucleotides in DNA strands (~0.4 nm), which makes these nanopores suitable for DNA sequencing technology [115-117]. The nanopores are produced in this material with focused electron beam had a diameter from 2-25 nm.

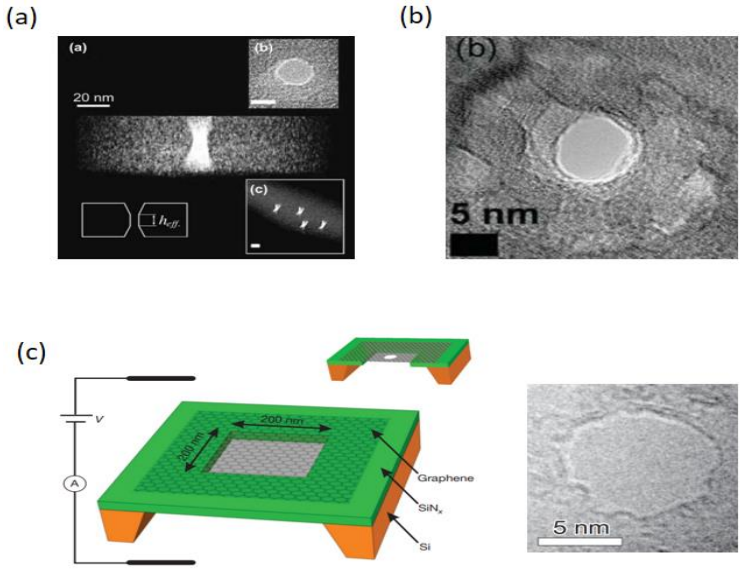

Figure 2.10. a) 7 nm nanopore in 50nm thick Si_3N_4 membrane fabricated with the electron beam of field emission TEM. Taken from [112] b) the 8 nm nanopore produced with ion beam sculpting in Ag_2O_3. Taken from [113] c) 7 nm pore fabricated in single layer graphene membrane. Taken from [116].

Because of their tuneable diameter size, they are addressed as possible DNA sequencing tool. However, the translocation speed of DNA in solid-state nanopores is still too fast to achieve necessary base resolution. The ideal DNA speed upon translocation through nanopore should be 0.01-1 ms per nucleotide [118] which is far slower than 27 bases/μs for silicon based nanopores and 1.4 bases/μs achieved for Ag_2O_3 nanopore [113, 119]. Although the fabrication processes development enabled sub-nanometre manipulation of solid-state nanopore dimensions, their resolution is still far from the atomic precise biological pores. Another advantage of biological pores is the better signal to noise ratio, being the noise in solid-state nanopores significantly higher compared to biological proteins.

2.7 DNA/RNA sensing with nanopore

As previously mentioned, DNA/ RNA molecules are the common molecules of interest for nanopore sensing applications. This is not surprising knowing that DNA is probably the most important biological macromolecule since it holds genetic information stored in the sequence of nucleotides, (adenine (A), thymine (T), cytosine (C) and guanine (G)), along a nucleic acid chain. Sequencing of the genetic code is the process to precisely determine the position of every nucleotide along the DNA strand, and it is of great importance for understanding the genetic risk factors associated with complex human diseases [120]. The whole human genome has approximately three billion bases and was first sequenced in 2001 by International Human Genome Sequencing Consortium and Celera Genomics [121, 122]. The major drawbacks of early sequencing techniques were the high cost (10 million dollars for human genome) and the long time that was required for genome sequencing, that exceeds several months [123]. It is not surprising that great effort was put to resolve the primary DNA sequence faster and cheaper. In 2003 the National Institute of Health (NIH) introduced the '1000 $' genome project with the goal to sequence the whole human genome in less than 24 hours for less than 1000 $ [124]. The nanopore technology has a potential to sequence the complete human genome at a cost of less than 1000 $, perhaps as low as 100 $ [14]. The low cost, high throughput, and low amount of required material without the need for amplification make nanopore technologies a promising DNA sequencing tool [125]. In solution, DNA/RNA polynucleotides are behaving as negatively charged polymers because of their phosphate group at each nucleotide. This feature allows DNA/RNA molecules to be driven through nanopores using an electric field. Nanopore-based DNA sequencing primarily relies on the assumption that each of the four nucleotides (A,T,C,G) causes a specific blocking event, so it could be possible to monitor the specific current blockages while DNA translocates through the pore, and to obtain the whole DNA sequence [77, 124].

In 1996 Kasianowicz *et al.* demonstrated for the first time that ssDNA (~1nm wide) can be electrically pulled and translocated through the αHL nanopore whereas wider (~2nm) dsDNA cannot [126]. For their experiments, they used polyuridylic acid (poly U) with an average length

of 210 nucleotides and ssDNA in 1M KCl with pH =7.5. The applied voltage was held to +120 mV (*trans* side positive) and polynucleotides were added in the opposite (*cis*) side. In absence of polynucleotides, the current across the pore was +120 pA and there were no transient events. After adding poly U, translocation events occurred with current reduction of 85-100% [126]. When the *trans* side was set to -120 mV there were no observed translocations, suggesting that polynucleotides were driven through the nanopore purely by electrophoretic force. A potential use of αHL nanopore as a new DNA sequencing tool was demonstrated by Akeson *et al.*, that used this protein to discriminate poly A, poly U and poly C RNA homopolymers (~150 nt long) [127]. Since then, the research mainly focused on developing cheap and rapid DNA sequencing technology using nanopores [128, 129]. They were able to detect the differences between resistive pulses produced by three homopolymers. It was shown that poly A produced three types of current pulses by interacting with the αHL pore: an initial 200 μs blockage with I/I_0 from 0.4 to 0.55, a second blockage with intermediate length and an I/I_0 of 0.45 (referred to as vestibule block) and a third 1-4 ms blockage with residual amplitude I/I_0 of 0.15. It was later shown that only the last of those pulses represented an actual translocation of poly A homopolymers through the channel since the first two were unspecific blockages caused by the interaction of the homopolymers with the vestibule of the αHL channel, and not an actual translocation [130]. The residual amplitude of poly U was found to be 0.15 I/I_0, a similar value to the poly A blockage, but with a shorter translocation time and lacking the 0.45 I/I_0 blockage shoulder that was observed in poly A blocking events. Poly C had a distinct current blockage pattern since its transient time was substantially shorter than poly A, and it lacked the multiple blockage levels [127]. Interestingly, although poly C was smaller than poly A (since C is a pyrimidine), it had deeper current amplitude. The reason for this is the 1.34 nm wide helical formation that poly C adopts at room temperature, so it can easily translocate through the 1.4 nm constriction of αHL [127]. On the other hand, poly A has a helical structure that is 2.1 nm wide, so it can translocate through the pore only when its helical structure is partially unwound and it adopts an extended structure [127]. Moreover, the blockages produced with poly C polymer have bimodal residual amplitude I/I_0 values of 0.09 and 0.05.

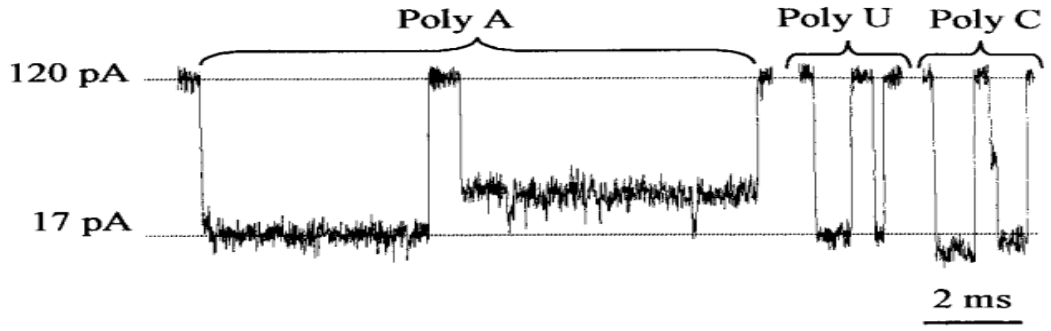

Figure 2.11. Duration and amplitude differences between three distinct RNA homopolymers upon interaction with αHL nanopore. Taken from [131].

The double I/I_0 residual amplitude block of 0.09 and 0.05 for the poly C translocation through the αHL pore observed by Akeson *et.al.* was suggested to be linked to the side at which homopolymeric strands were entering the αHL pore [127]. Mathe *et al.* confirmed this speculation by attaching poly $(dA)_{50}$ overhang from either 5' or 3' end of DNA hairpin [132]. In their work, the I/I_0 produced by poly dA tail entering from 3' end was 0.09, showing a deeper block compared to 5' end entries (that generated a I/I_0 of 0.13) [132]. Purnell *et al.* used a different method for discriminating 5' and 3' DNA orientation, by modifying the sides of the poly A, poly C and poly T with biotin [133]. After hybridization with streptavidin, the biotinylated sides of the polynucleotide chains were not able to enter αHL, allowing only unmodified strands to thread the αHL pore. They reported bimodal amplitude for all three polynucleotides: poly A, poly C and poly T depending on the side of polynucleotide interactions [133]. They also showed that the poly A strand caused a deeper current block when its 3' end entered the pore first compared to the 5' end. On the contrary, poly C and poly T displayed deeper amplitude levels for 5' end entries compared to 3' end Figure 2.12.

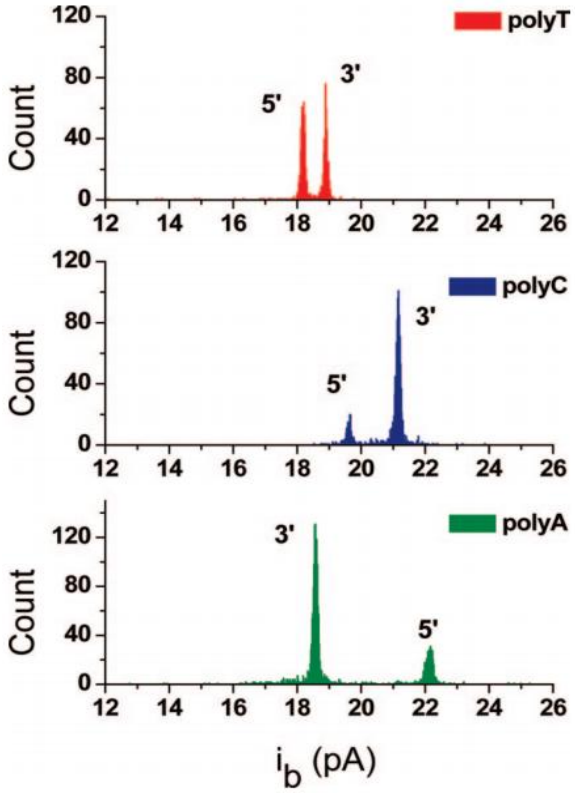

Figure 2.12. Bimodal amplitude blocks depending on DNA side orientation in αHL pore. For poly T and poly C, the deeper block amplitude corresponds to the entrance of the polynucleotide in the αHL channel from its 5', whereas for poly A the amplitude block is greater when poly A threads the αHL from its 3' end. Taken from [133].

The threading of the polynucleotides starting from 3' end was more frequent and faster compared to blockage events starting from the 5' end [134]. A possible explanation for the higher capture rates of 3' ends with αHL pores was given by molecular dynamic simulations that revealed that nucleotide bases are tilted towards 5' end in the narrow αHL channel (Figure 2.13). Therefore,

any polynucleotide strand that is captured from its 3' end would experience less friction and this event is more likely to occur compared to threading from 5' end.

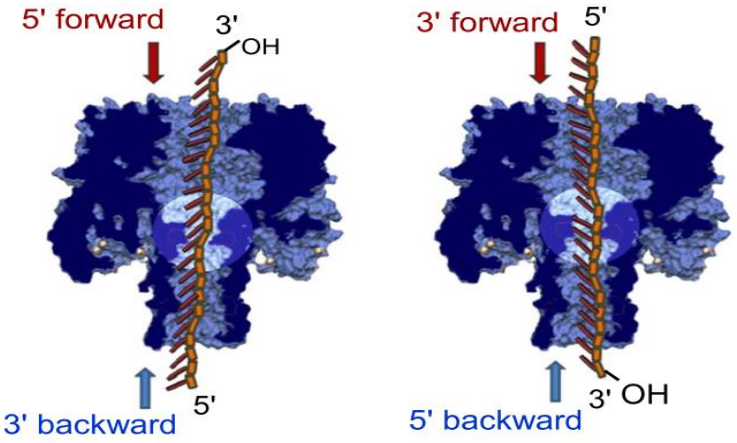

Figure 2.13. The difference of the polynucleotide base tilting with the respect of the polynucleotide orientations. Taken from [134].

These experiments demonstrated the ability of wild-type αHL pore to detect the differences between RNA and DNA homopolymers, and the side at which they enter the pore. However the speed at which nucleotides traverse the αHL pore is ~1 μs/base what requires ultrasensitive high-speed detection of DNA which is currently beyond spatial and electronic resolution of existing techniques [14]. It is estimated that 10- 15 nucleotides can fit inside the 5 nm long stem of the αHL nanopore and they all contribute to a single current level block [135]. Ideally, the current level block should be generated from only one nucleotide at a time. For this reason, wild-type αHL is not the best nanopore of choice for sequencing. To solve this limitation, Hagan Bayley's research group bioengineered αHL nanopore to obtain pores with sensing region shorter than 5 nm [136, 137]. Moreover, in order to prolong DNA interaction with the protein, the DNA was immobilized inside the channel by using streptavidin. This approach was adopted by Stoddart *et al.*, that managed to detect the position of four adenine nucleotides in a poly C sequence [136].

The DNA speed can be modified by using DNA processing enzymes such are exonuclease and polymerases. Clarke *et al.* used modified αHL with positively charged β-cyclodextrin, am7βCD, to capture mononucleotides cleaved by exonuclease from *E.coli* [125]. The nucleotides produced different current levels upon interacting with αHL that could be distinguished with more than 90 % of accuracy [125]. Polymerases are another group of DNA processing enzymes that have been recently employed for DNA sequencing with nanopores. Phi 29 DNA polymerase (phi29 DNAP) can add nucleotides to the ssDNA template from 5' to 3' direction in the presence of magnesium ions and dNTPs at a rate of ~1 nt per millisecond. Akeson *et al*. showed that this DNA processing enzyme remains attached to the DNA template and can pull it in the opposite direction of the electric field. They modified the DNA template with a blocking oligomer sequence in order to

avoid that the polymerase starts the synthesis before the DNA is captured by the nanopore [138]. After the ssDNA is secured to the pore, the template is slowly pulled forward in the *cis-trans* direction inside the protein. At the same time, at the other end the blocking oligomer sequence is unzipped from the DNA-phi29 DNAP complex [138]. During the unzipping of the blocking oligomer sequence, the current trace of each nucleotide base in the template passing through the pore in the forward direction is obtained. Once the blocking oligomer is completely unzipped, the 10 mM MgCl can be added along with the dNTP in order to initiate the polymerization. In order to detect the moment at which the blocking oligomer is unzipped, the DNA template was modified with abasic sites. These reduce significantly the current through the pore compared to the passage of nucleotides. Once phi 29 DNAP starts processing the DNA template, it pulls it backwards in *trans-cis* direction (opposite of electric field). Therefore the same DNA template can be read two times (in *cis –trans* entering the pore and in *trans-cis* direction when pulled by the polymerase). This increased the technique resolution [138]. The ssDNA is pulled through the αHL pore at a rate of 2.5-40 nt/second, 4 orders of magnitude slower comparing to free-DNA translocation speed. The same principle was implemented on an engineered MsPA pore by Manrao *et al*., who got an even higher resolution, detecting the C-A-T trimer repeat in the DNA template sequence [139].

In 2014, Oxford Nanopore Technology (founded by Hagan Bayley and Gordon Sanghera) released MiniION, the first commercial nanopore sequencer platform [140]. This device weighs only 90 g and, with dimensions of 10 x 3 x 2 cm, is the smallest DNA sequencer currently available. It is simply connected and controlled by any laptop computer having its corresponding software [141]. The core of MinION is a fluidic cell that has 2048 individual protein nanopores embedded in separate membranes. Prior analysis of the DNA sample, the hairpin is added to one of the ends of dsDNA. The helicase enzyme unwinds the dsDNA into ssDNA that is captured by the nanopore. Upon translocating through the pore, the DNA sequence produces a continuous current-time signal. After the helicase passes through the hairpin, the nanopore reading of complementary DNA strand begins. This uninterrupted current recoding of two complementary DNA strands is called 2 D read, and is processed with algorithms for nanopore sequencing. In 2015, the complete genome from *E. coli* was assembled *de novo* using the MinION sequencer [142]. In 2016, MinION sequencer was used as a diagnostic tool for detecting genome mutations of Ebola virus outbreak in West Africa [143].

2.7.1 Voltage dependable capture rate of negatively charged polynucleotides

Experiments with DNA/RNA homopolymers and the αHL pore showed that only a small fraction of molecules was captured by the pore. It is estimated that only 1 in 1000 polymer-pore interactions ends up in DNA capture [144]. The reason for this low capture rate was explained by the energy barrier that DNA needs to overcome to be captured by the pore [145]. If the DNA

capture is governed by the energy barrier, the barrier limited capture rate ($R_{c,bar}$) can be estimated as:

eq 1

$$R_{c,bar} = \omega \cdot e^{\left[\frac{-(U^* - \Delta U)}{kT}\right]}$$

Where ω is the threading attempt rate of DNA, U^* is the energy barrier for DNA capture, ΔU is the reduction of activation energy of DNA with the applied potential, T is the temperature (K) and the *k* is the Boltzmann constant.

The energy barrier U^* for ssDNA for αHL pore was found in the range 8 kT [145]. By applying the potential across the pore, the energy barrier for the DNA capture reduces of the factor $\Delta U = q_{eff}\, \Delta V$, being q_{eff} the effective charge of the DNA chain in the pore channel and *V* the applied potential. It is estimated that around 12-15 nucleotides occupy the 5 nm beta barrel of the channel [135]. The effective charge of the *n* nucleotides of DNA inside the αHL has a considerably lower value than $-ne$, since the charge of DNA is strongly shielded in confined pore environment [146]. The effective charge per nucleotide is estimated to be ~0.1 value of *e* [146, 147]. The electrophoretic force on a 15 DNA nucleotide inside the channel can be estimated as $F = neq_{eff}V/l$, where *l* is the channel length. For a voltage of 120 mV and l = 5 nm, this gives F~ 6 pN.

Henrickson *et al*. investigated the capture of poly $(dC)_{30}$ with αHL nanopore in a voltage ranging from 50 to 120 mV [145]. The minimum voltage required for translocation of poly $(dC)_{30}$ was found to be around 60 mV. In the 50 -120 mV voltage range they observed an exponential increase of the capture rate with the voltage, supporting the theory of the barrier limited DNA interaction with the αHL channel. At zero voltage the capture rate was estimated at a neglectable value of 0.015 min^{-1} [145]. Meller and Branton determined the capture rate of 2.6 μM and 0.9 μM poly $(dC)_{40}$ with αHL nanopore in the extended voltage range from 60 to 250 mV at a temperature of 2 °C [148]. They observed an exponential increase of capture rate with the voltage with two regimes. In the first regime (60-140 mV) the capture rate increased with a slope 6 times higher than the second regime (150 -250 mV) [148]. Nakane *et al*. used poly $(dA)_{50}$ and extended voltage range from 100 to almost 300 mV, and showed that at high voltages (>200 mV) the capture rate linearly depends on voltage [149]. Hence, at higher voltages, the capture depends on the rate at which DNA diffuses towards the pore entrance. The diffusion limited capture rate of DNA (R_{cdiff}) is given by

eq 2

$$Rc_{diff} = (\pi d^2 \mu / 4l)\, V$$

Where μ is the electrophoretic mobility of DNA and it is independent of the DNA length, *d* is the diameter of the pore, *l* is its length and *V* is the applied potential [150].

Wanunu *et.al* showed that the capture rate of short and medium DNA (400 and 3500 bp) with a SiN nanopore increased exponentially while the capture rate of long DNA (>8000) linearly depended on the voltage [151].

2.7.2 Geometric and electrostatic influence of αHL on DNA capture

Henrickson *et al.* demonstrated that the capture rate of poly $(dC)_{30}$ was 6 times higher when poly dC_{30} were added to the *cis* side compared to the *trans* side [145]. The lower DNA capture rate from *trans* side might come from geometrical constraints of the αHL channel, because the wider *cis* side entry (2.6) might be energetically more favourable compared to the narrower *trans* side entry (2.2 nm) of the pore [145]. Another reason for the significantly lower capture rate for the *trans* side was proposed to come from electrostatic repulsions between the negatively charged amino acids in the vicinity of the *trans* side opening of the αHL channel [145, 152]. At the vicinity of the *trans* opening of the αHL pore there are two negatively charged aspartic acids: D127 (0.18 nm from *trans* entry) and D128 (0.05 nm from *trans* entry) and one positively charged lysine K 131 (0.15 nm from *trans* entry). At neutral pH~7, aspartic acids are negatively charged while lysine is charged positively, hence when all the charges in the vicinity of *trans* entry of αHL channel are summed up, we get a net charge at the *trans* opening of αHL of -7e, that acts repulsively on negatively charged polymers [152]. The maximal distance at which charged polymer would feel the electrostatic effect of the pore can be estimated with the Debye length (κ^{-1}) that is given by the equation:

eq 3

$$\kappa^{-1} = \sqrt{\frac{\varepsilon_0 \varepsilon_r kT}{2 n_B e^2}}$$

Where ε_0 is permittivity of vacuum, ε_r is the dielectric constant of water, *k* is the Boltzmann constant, *T* is the absolute temperature on the Kelvin scale, n_B is the bulk concentration of electrolyte and *e* is the elementary charge.

The usual electrolyte of choice for nanopore recordings is 1 M KCl in which the Debye length is ~0.3 nm thus the repulsion between negatively charged DNA and negatively charged *trans* entrance of the pore can be significant in a 2 nm wide channel [152].

Interestingly, the same amino acids D127 and D128 were found as main attributors to the αHL current rectification. This means that the pore current is not symmetrical when comparing the

positive and negative voltages values. In conventional electrolytes, such are1 M NaCl and 1 M KCl, and neutral pH~7, the current ratios I (+V) / I (-V) were found in the range from 1.3-1.4. Several theoretical and experimental studies showed that D127 and D128 are one of the main contributors for observed current rectification of αHL [145, 153-155]. The point mutations D127C and D128 C decreased the αHL current rectification to ~1.2 and 0.95 respectively [156]. The αHL current rectification was shown to depend on the cation type. Bhattacharya *et al*. found that current rectification I(+V)/ I (-V) has its smallest value of 1.1 in LiCl, and increases to 1.4 in CsCl [155]. The reason for the small current rectification in LiCl was explained with the strong affinity of Li^+ ions to D127 and D128 amino acids, hence screening their negative charge. The KCl, RbCl and CsCl showed lower ability to screen negatively charged D127 and D128 amino acids, hence their current asymmetry ratio I(+V)/ I (-V) was found at ~1.4. It was shown that αHL pore became nonselective when high concentrations of KCl (>3M) were used, suggesting that charges along the pore channel might be well shielded in high KCl concentrations [157].

Table 2.2. The distance of charged amino acids along the αHL pore from the cis entrance. Taken from [153].

Amino acid	Distance from cis entrance (nm)	pK_A
Lys^{8} (K8)	1.13	10.5
Asp^{13} (D13)	1.84	3.9
Glu^{111} (E111)	5.06	4.1
Lys^{147} (K147)	5.10	10.5
Asp^{127} (D127)	9.82	3.9
Lys^{131} (K131)	9.85	10.5
Asp^{128} (D128)	9.95	3.9

At low pH (~4), aspartic acid becomes protonated which neutralizes its negative charge. It was shown that the asymmetry ratio of the αHL pore in 1 M NaCl decreased from 1.3 to 1.08 when the pH was lowered from 7.4 to 4.5 [153]. Wong and Muthukumar measured I (+120mV)/ |I(-120mV)| ratio and got 1.06 value in 1 M KCl where the pH of *cis* side was 7.4 while pH of *trans* side was 4.5 [152]. Moreover, they showed that the capture rate of negatively charged 16 kD sodium polystyrene sulphonate (NaPSS) increased two times when the pH in *trans* side was lowered from 7.5 to 4.5 [152]. The increased capture rate was explained by the weaker electrostatic repulsion between NaPSS polymer and negatively charged t*rans* beta barrel of the pore [152].

The single amino acid mutations on αHL were shown to vastly improve DNA capture. Maglia *et. al.* examined several αHL mutants that were engendered in a way that the charge in the vestibule was positively increased [18]. On the other hand, Tian *et al.* made the αHL *trans* side even more negative with K131D mutation and showed that capture rate of positively charged TAT peptide by K131D-αHL increased 200 fold compared to WT-αHL [158].

2.7.3 Increasing the capture rate of negatively charged molecules with salt gradient

Wanunu *et al.* proposed an alternative way to increase nanopore capture rate of DNA by establishing a salt gradient across the nanopore in a way that KCl concentration in *cis* side is lower than KCl concentration in *trans* side [151]. By using *cis/trans* salt gradient of 0.2 / 4 M KCl, the capture rate of 8000 bp dsDNA increased almost 30 fold compared to conventional symmetrical 1 M KCl *cis/trans* solution [151]. Furthermore, the dwell time of dsDNA in presence of salt gradient increased 3-fold compared to symmetrical conditions, enhancing the sensitivity of the technique. The improved capture rate of dsDNA with silicon nitride nanopore under salt gradient condition was attributed to an locally increased electric field near the *cis* entrance of the pore Figure 2.14 [151].

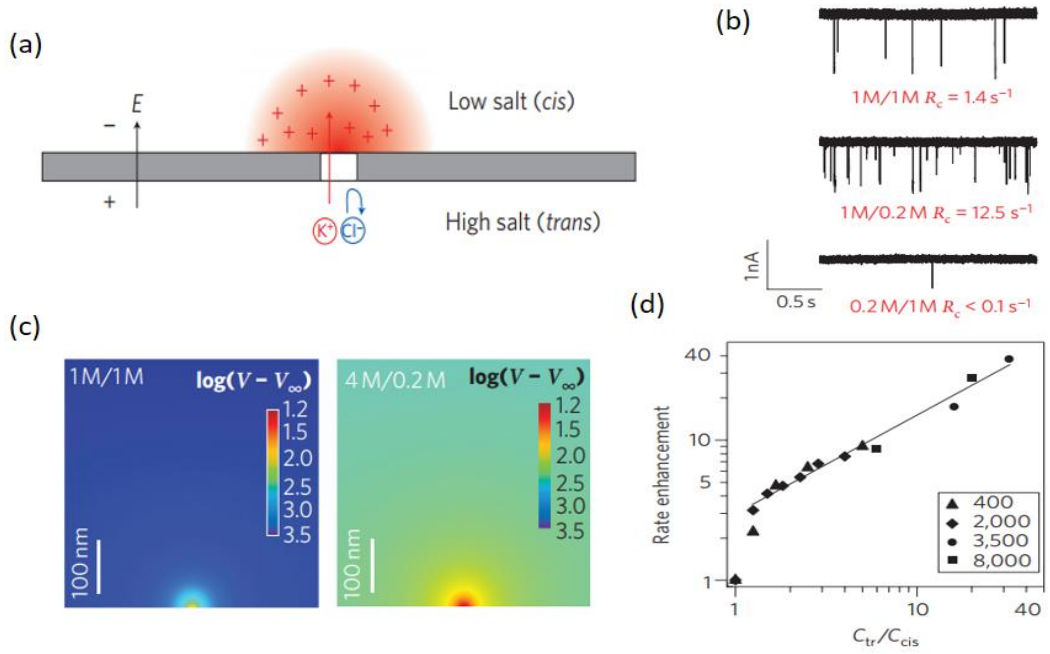

Figure 2.14. (a) Scheme of creating a salt gradient across the pore. The positive ions (K^+) are pumped from the high salt compartment in the direction of the electrical potential gradient. As a result, the vicinity of cis side nanopore is polarised because of the localised concentration of K^+ ions, which attracts the negative DNA macromolecules near the pore. (b) Current traces through the 3.5 nm SiN nanopore in the presence of 400 bB DNA under various *trans / cis* KCl concentrations (c) The electrical potential maps in the cis side of the pore in symmetric KCl conditions (left panel) and asymmetric 0.2 / 4 M KCl *cis/trans* conditions. (d) the capture rate of 400 – 8000 bp DNA increases with the salt gradient when $c_{trans} > c_{cis}$. Taken from [151].

He *et al.* showed the existence of charge accumulation around the pore mouth by numerical simulation (Figure 2.15) [159]. The localized accumulation of K ions around the cis entrance of the pore under salt gradient is necessary to maintain the constant current flow through the pore [151, 159]. The current flux of ion *i* (j_i) through the nanopore under applied electric field is given by:

eq. 4

$$j_i = \mu_i \, c_i \, z_i \, F \, E$$

Where the μ_i is the mobility of the ion *i*, F is the Faraday constant, E is the electric field, and c is the ion concentration. In the salt gradient conditions, the concentration of salt and electric field are changing along the longitudinal pore axis z (Figure 2.15 b), but their product E (z)*c(z) should be independent of the z coordinate to satisfy the current continuity. The conductivity decreases along the pore z-axis from *trans* to *cis* side because the higher salt concentration in *trans* compartment solution has a higher conductivity than the salt solution in *cis* compartment. Hence, in order to keep the continuous current flow through the pore axis, the potential gradient needs to increase along the pore axis towards *cis* side. The system can achieve the increase of E (z) towards *cis* side by locally accumulating the K^+ ions near the *cis* side entrance [159].

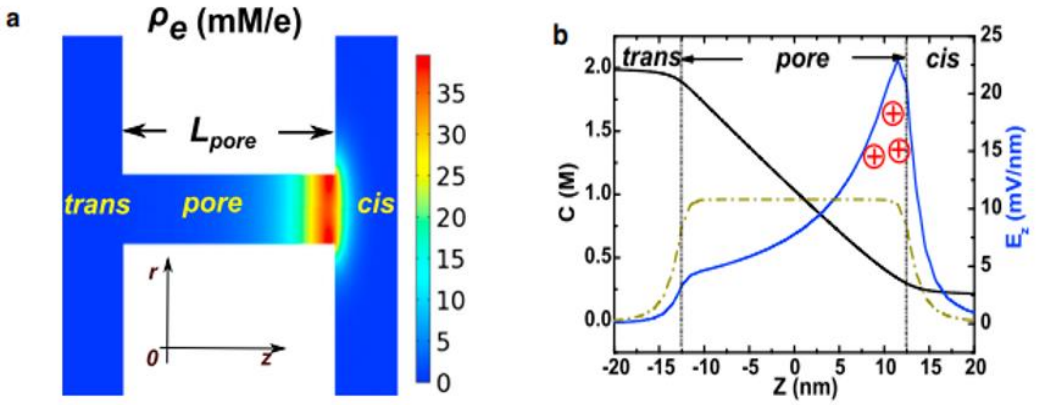

Figure 2.15. a) Distribution of charge density p_e along the pore z axis. b) the change in salt concentration (black line) and electric field (blue line) along the z axis of the 25 nm long pore. The concentration of KCl in *trans* chamber was 2 M while in *cis* chamber it was set at 0.1 M. Taken from [159].

Wanunu *et al.* hypothesized that protrusion of potential into cis side significantly increases with c_{trans}/c_{cis} ratio (Figure 2.14 c) [151]. The enhanced electrical field near the pore was expected to increase the DNA speed through the nanopore thus reducing the resolution. On the contrary, experiments showed that translocation times of 400 bp and 2000 bp DNA increased 1.6 and 3.5 times when KCl concentration in *cis* chamber decreased from 1 to 0.2 M while the concentration of KCl in *trans* was held at 1 M [151]. They proposed that this increased dwell time was the result of an electroosmotic flow (EOF) inside the SiN nanopore with opposite direction to the DNA motion passing through the protein [151]. The EOF is a movement of fluid through the pore under the applied potential. The silicon nitride nanopores have uniformly distributed negative charge ~ -35 mC/m^2 [160], thus the number of positively charged counter-ions is higher in the proximity of the pore wall and lower in the bulk solution. When an electric potential is applied, the counter ions will move away from the anode, carrying solvent molecules along with them. This induces the plug flow of solvent inside the nanopore, which is in opposite direction to the DNA

translocation in the pore. Several theoretical and experimental studies confirmed the hypothesis of Wanunu *et al.* that EOF can be strong enough to slow down the DNA translocation speed through the nanopore [151, 159, 161-163]. Hence, the salt gradient can be finely tuned across the solid-state nanopore to control the speed of DNA upon translocation through the pore. In a recent work by Shin *et al.,* the dwell time of 90 bp dsDNA through the Mo_2S nanopore was 100- fold prolonged in 0.6 / 3 M KCl (*cis/trans*) compared to 10 µs dwell time in the symmetrical 1 M KCl solution [164].

2.7.3.1 Salt gradient modulation of interaction of negatively charged polymers with biological pore

The majority of salt gradient studies were performed on solid-state-nanopores with different properties from biological nanopores. On the other hand, there are only a few studies on salt gradient across biological pores. Jeon and Muthukumar studied the translocation properties of negatively charged sodium polystyrene sulphate NapSS through the αHL under asymmetric pH conditions and KCl gradient [165, 166]. They investigated both *cis* and *trans* influence of KCl concentration on capture rate and dwell time on 16 and 35 kD NaPSS at various voltages. The influence of the [KCl] concentration in the cis chamber on the dwell time of 16 and 35 kD NaPSS was determined by varying $[KCl]_{cis}$ from 0.5 to 1.5 M while keeping $[KCl]_{trans}$ constant at 1 M KCl [166]. The dwell time of 35 kD NaPSS at 140 mV reduced 2-fold from 2.35 ms in 1.5 / 1 M KCl *cis/trans* to 1 ms in 0.5/1 M KCl *cis/trans*. Furthermore, they observed 10-fold increase of capture rate for 16 kD NaPSS when $[KCl]_{trans}/[KCl]_{cis}$ was increased from 1 to 10. They demonstrated that effective charge of the polymer is increasing with decreasing concentration of KCl in *cis* chamber (lower salt concentration-less screening) [166]. Therefore, the negatively charged polymer feels larger electrophoretic force upon translocating the pore leading to shorter dwell time and higher capture rate.

The same approach was taken to determine the influence of $[KCl]_{trans}$ on dwell time of 35 kD NaPSS at 160 mV and pH = 7.4 where the concentration $[KCl]_{trans}$ was varied from 0.75 to 1.5 while the $[KCl]_{cis}$ was kept at 1 M KCl. Interestingly, the dwell time was found constant at ~1.2 ms for all three gradients when pH of the solutions was 7.5 [166]. The dwell time of 16 kD NaPSS reduced with increasing the $[KCl]_{trans}$ only when the pH of solution was lowered to 4.5. The dwell time decreased from 2.5 ms in 1 / 0.25 M KCl (*cis/trans*) to 0.85 in 1 / 1.5 M KCl (*cis/trans*) at 120 mV. The electrostatic repulsion between negatively charged beta barrel entrance of αHL and NaPSS was proposed as the main contributor to the capture rate and dwell time of NaPSS polymer[166]. At neutral pH~7 there is electrostatic repulsion between the negatively charged polymers and αHL channel. Lowering pH to 4.5 the electrostatic interactions became attractive since negative amino acids become protonated at pH~4. Hence, decreasing the concentration in

$[KCl]_{trans}$ at pH = 4.5 resulted in enhanced polymer-pore interactions which slow down the NaPSS transport through the pore [166].

These experiments showed that capture rate of negatively charged polymers can be vastly improved by establishing the salt gradient across the αHL pore, that has similar features to the for SiN nanopore employed by Wanunu *et al*. [151]. However, Jeon and Muthukumar observed decreasing of dwell time with an increasing salt gradient across the pore [166]. That observation was in contrast with the work on SiN nanopores, where dwell time of dsDNA was increasing with the magnitude of $[KCl]_{trans}$ / $[KCl]_{cis}$ gradient [151, 159]. As previously mentioned, the EOF inside negatively charged SiN nanopore increased with the salt concentration gradient, in the opposite direction to the DNA translocation. Unlike solid-state nanopores, that have uniformly charged walls, the pores have heterogeneous charge distribution. Because of this, most of the biological pores are ion selective, meaning that certain ions pass through the channel more easily compared to others. The net water flow through biological nanopores can be calculated from the ion selectivity (P_+ / P_-) of the pore, where P_+ and P_- are permeabilities of cations and anions into the pore. At the neutral pH~7 and in 1 M KCl electrolyte, αHL pore has a permeability ratio P_+ / P_- ~ 0.7, meaning that Cl^- ions pass through the pore more easily compared to K^+. Therefore, when a positive potential is applied across the αHL pore, the net flow of water will orientate from *cis* to *trans* due to the anion selectivity of the pore. It was shown that EOF can contribute to the capture rate of small molecules such are β-cyclodextrin and small peptides [167, 168], but its contribution to the capture rate of negatively charged polymer NaPSS was shown to be negligible [166]. Therefore, in biological nanopores the EOF is not sufficiently strong to oppose the electrophoretic movement of negatively charged polymers inside the nanopore, which is further enhanced by the salt gradient.

2.8 Nanopore mass spectrometry

Superior resolution of biological nanopores in detection and characterization of microscopic differences between molecules was demonstrated with αHL and aerolysin nanopores by using polyethylene glycol (PEG) polymer [169-171]. PEG has the structure $H - (O - CH_2 - CH_2)_n - OH$, hence its molecular weight is increasing by 44.05 g/mol with the n repeating units. Robertson *et al.* and Baaken et *al.* demonstrated αHL capability to detect differences between single PEG monomers in polydisperse PEG powder with average molecular weight of 1500 by measuring current block amplitude [169, 170]. Robertson and co-workers used single αHL nanopore and highly purified PEG with 29 repeating units (r.u) (M_w = 1294 g/mol) to obtain the characteristic level of current blockage [169]. After that, the polydispersed PEG with an average Mw of 1500 g/mol was dispersed in *trans* side solution bathing singe αHL channel. The PEG 1500 produced multilevel blockages whose amplitudes were clearly distinguished. The single level amplitude obtained with PEG with 29 r.u. was used as a reference amplitude to determine other PEG

monomers in solution [169]. The αHL nanopore demonstrated capability do distinguish PEG monomers from 24 to 48 repeating units. Baaken and co-workers performed a similar experiment with purified PEG with 28 r.u and a chip- based nanopore microarray that enabled the collection and analysis of large data set [170]. The same group demonstrated that another biological pore, aerolysin, has potential to discriminate the PEG monomers from 17 to 47 repeating units, with a broader resolution range compared to the αHL nanopore [171].

These experiments showed the capability of the nanopore to discriminate monomers of PEG in polydisperse powder with high precision. Neighbour peaks of conductance in event histogram could clearly be separated and had one to one correspondence with the results obtained with MALDI-TOF spectra (Figure 2.16).

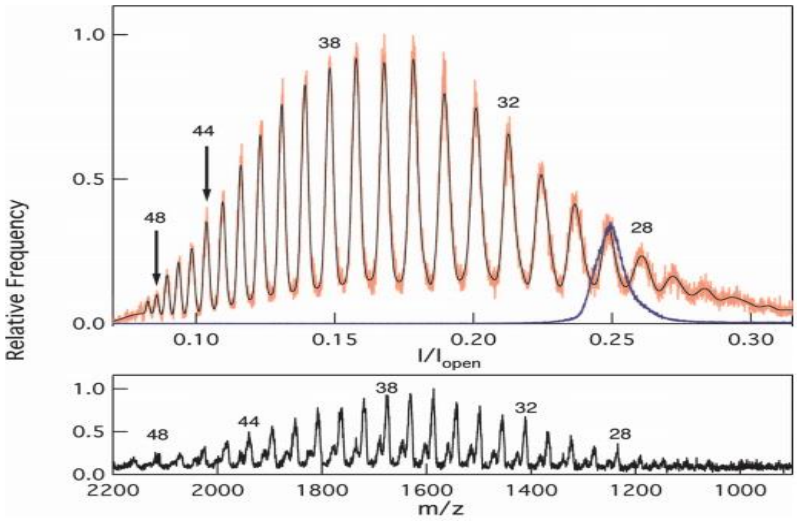

Figure 2.16. The upper graph presents PEG distribution amplitudes with the assigned number of repeating units for each monomer. Blue peak corresponds current amplitude of purified PEG with 29 r.u. The lower graph presents mass spectrometry obtained by using MALDI-TOF mass spectra. Taken from [169].

2.9 Peptide and protein detection with nanopores

The nanopore sensing of proteins and peptides is somewhere more challenging compared to ssDNA since polynucleotide chain is linear and with homogenous distribution of charge, whereas polypeptides and proteins have strong secondary structures and the charge that is not uniformly distributed [172]. Because of their various sizes and secondary structures, many proteins are not able to translocate through biological nanopores such is αHL. The influence of charge, length and structure of the helical and beta hairpins polypeptides was examined with αHL nanopore. On a case of beta-hairpin peptide, it was shown that folded peptide structures have a higher barrier to translocate the αHL nanopore compared to unfolded peptides [173]. The unfolded peptide beta hairpin was shown to translocate through the pore producing fast transient current blockage, whereas folded beta hairpin produced long lived current blockages [173]. Oukhlend *et al*. showed

that maltose binding protein from *E. coli* translocated αHL pore only with unfolded structure in guanidium chlorine (Gdm-HCl). In absence of denaturant, the MBP could not produce current blockages through αHL pore. On the contrary, when the concentration of Gdm-HCL increased to 0.8 M, short transient spikes, representing unfolded MBP translocations, were observed [174].

The constriction of αHL of 1.4 nm limits the detection by translocation of larger analytes such as proteins. However, it was shown that proteins and peptides can be detected without translocation through the pore, but it is necessary to chemically modify either the αHL pore or the protein target. Movileanu *et al.* modified the αHL pore adding 3.4 kD polyethylene glycol (PEG) with a biotin tail, able to bind streptavidin in solution [175]. The beta barrel of αHL was engineered in a way to contain electrostatic traps that could bind to proteins labelled with electrostatic peptide tag [176].

Because of the size-related limit in the detection of the αHL pore, other biological pores with larger diameters, such is ClyA pore, were investigated and showed potent capabilities of protein detection. ClyA pore was used for detection of folded and unfolded proteins since its large extracellular entrance (~6 nm) was sufficient to accommodate various proteins [99]. On the other hand, solid – state nanopores can be finely tuned enlarging their diameters sufficiently to accommodate large analytes such are proteins. Solid – state nanopores were also used to detect proteins in their fully folded state and to detect conformational changes of proteins such are folding and unfolding [177-179].

2.10 Nanopore technology for medical application

The majority of nanopore research is focused on DNA sequencing and optimization of the experimental parameters that would make it possible. Since nanopores are extremely sensitive to the physiochemical characteristics of molecules, they are suitable for detection of proteins, RNA, DNA, antibiotics etc. This makes the technology suitable for medical applications. For example experiments with αHL shown that this nanopore can be used to detect various DNA damages, such are abasic sites, oxidative damage and base mismatches [180-182]. Other examples include detecting specific target molecules with DNA/RNA aptamers that are single-stranded nucleic acids able to bind specific targets with great activities. Kawano *et al.* reported cocaine detection with DNA aptamer by using αHL channel [183]. Once bonded to cocaine, the cocaine-aptamer complex folded into a "Y" shape and was captured by an αHL pore [183]. By measuring the time necessary to block the pore with the complex, they were able to determine 300 ng/mL of cocaine in solution. Detection of heavy metals that are able to damage DNA such are Pb, Ba and Hg was also reported with αHL nanopore [184, 185]. Moreover, nanopore technology provides a promising application for detection and quantification of miRNA molecules [186]. As previously mentioned, the number of resistive pulses produced by an analyte in solution can be correlated

with its concentration. This convenient feature of NRPS was used for miRNA quantification with the solid-state and biological nanopore.

2.10.1.1 MicroRNA detection with biological nanopore

The detection of cancer related miRNA molecules with nanopores is a challenging task since the length and cross-section of the miRNAs have dimensions of ~7 nm and 2.5 nm respectively [12]. Being single-stranded molecules their translocation speed through the αHL pore would be too fast for the detection of the target miRNA in a sample. For example, the average speed of RNA translocation through the αHL was estimated to be 3-22 μs per base [127, 187]. Hence, the detection of specific miRNAs based on their short (~100 μs) resistive pulses would be too complicated for the αHL pore. On the contrary, the dsDNA cannot pass freely through the αHL pore because of the ~1.4 nm pore constriction. The studies undertaken on the larger biological structures such are DNA hairpins showed that those structures have to unzip before translocation through the αHL nanopore which resulted in the prolonged analyte – pore interaction and a specific current signature [147, 188, 189]. The duplex unzipping approach was used by Wang *et al.* for the detection of lung cancer associated miRNA 155 with αHL nanopore [13]. Their strategy was based on hybridization of the miRNA 155 with its complementary DNA probe [13]. By doing so, they created a larger and wider miRNA-DNA probe duplex compared to the non-hybridized miRNAs in solution. In order to facilitate the capture of miRNA-DNA probe duplex, the DNA probe was extended with a single-stranded overhang $(dC)_{30}$ at 5' and 3' ends of the probe (Figure 2.17 a) [13]. Moreover, they reported that the miRNA-DNA duplex created a specific, multilevel resistive pulse signature upon interaction with αHL pore (Figure 2.17 c), that could be easily separated from the resistive pulses created by single-stranded miRNA155 and P155 sequences (Figure 2.17 e). Level 1 was the longest, and correlated to the unzipping of the miRNA155 from its DNA probe. In level 2, unzipped miRNA-155 temporarily blocked αHL channel vestibule with I/I_0 value of 0.42. Finally, level 3 expressed the short-lived miRNA translocation through channel, with I/I_0 = 0.08 [13]. On the contrary, when only ssDNA probe P155 or miRNA155 translocated through the pore, they created resistive pulses with a duration of only ~0.2 ms , about three order of magnitude shorter compared to level-1 blockages associated with hybridized DNA probe-miRNA duplex.

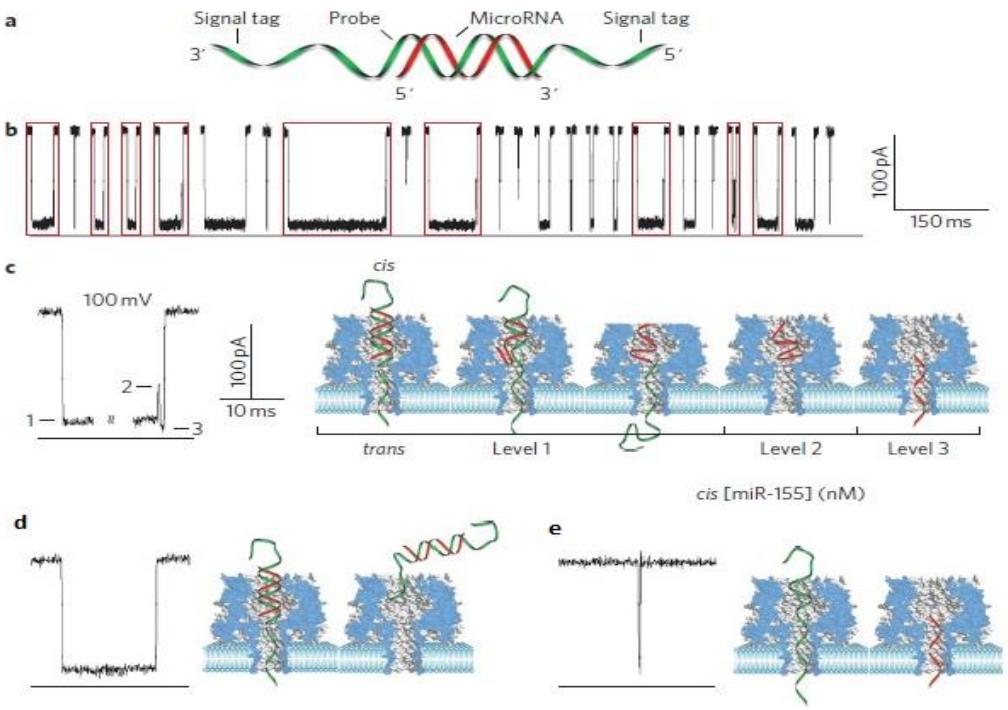

Figure 2.17. a) miRNA with DNA probe and signal tag. B) current trace showing blocking events with miRNA-DNA complex, c) characteristic blocking levels caused by miRNA-DNA complex, Level 1 presents capturing of DNA probe and unzipping of Probe/miRNA complex. In Level 2 unzipped miRNA shortly stays in vestibule causing partial blocking of pore, in level 3 miRNA is translocated through pore, d) single level block with no translocation event, e) short blocking of pore caused by translocation of miRNA without DNA probe (270μs). Taken from [13].

In order to quantify the concentration of target miRNA molecules with nanopore resistive sensing, the frequency of resistive pulse events should be correlated with the duplex concentration. The miRNA concentration in the solution can be quantified by the frequency of signature events of miRNA-DNA duplex as $f_{on} = k_{on}$ [duplex], where $f_{on} = 1/t_{on}$ (events per second) represents the capture frequency, [duplex] presents the miRNA-DNA probe duplex concentration and k_{on} ($M^{-1}s^{-1}$) presents the occurrence rate constant of duplex capture events [13]. Therefore, the capture frequency of miRNA-DNA probe duplex determines the sensitivity and limit of quantification of the nanopore assay. For example, the capture frequencies of miRNA155-P155 duplex observed by Wang *et.al* were 0.2 s^{-1} for 100 nM duplex and 0.033 s^{-1} for 10 nM duplex [13].

Since the capture frequency is calculated from the interevent interval between the stochastic current blocks, large numbers of pulses are required to determine the capture rate with a good accuracy. As argued by Zhang *et al.* in their work on detection of miRNA with αHL, about ~200 events are required to limit the relative error to ~5 %, while 70 events are enough for an error of 10 %. Wanunu *et.al,* in the work on miRNA detection with a solid-state nanopore, stated that ~200 events are enough to determine concentration with 93% accuracy [17, 190]. This implies that recordings with a single αHL nanopore in 1 M KCl at 100 mV should last at least 17 minutes

in presence of 100 nM miRNA155-P155 duplex to collect 200 events and ~ 100 min for collecting the 200 pulses in presence of 10 nM miRNA155-P155 duplex.

As previously mentioned, the electrophoretic force acting on DNA increases with potential which results in higher capture frequencies. Wang *et al.* demonstrated that the capture frequency of 10 nM miRNA155- P155 duplex increased 6 fold from 0.033 s^{-1} to ~ 0.19 s^{-1} when the voltage increased from 100 mV to 180 mV [13]. Hence, the capture frequency at 180 mV of 10 nM miRNA155-P155 duplex became similar to the capture frequency of 100 nM miRNA155-P155 duplex at +100 mV [13]. The same group reported a linear increase of capture rate (Figure 2.18) from 0.2 s^{-1} to 0.8 s^{-1} of 100 nM miDNA155-P155 duplex for the voltage range from 100 to 180 mV [16]. The drawback of using high voltages for miRNA detection with DNA probe is the reducing the dwell time of duplex. The dwell time of miDNA155-P155 duplex decreased exponentially from 430 ± 70 ms at 100 mV to only 1 ± 0.3 ms at 180 mV [16]. Reduced dwell time decreases the sensitivity of the nanopore assay since it would be difficult to distinguish duplex translocation from nonspecific polymer pore interactions. Moreover, higher voltages can destabilise the lipid matrix in case a biological pore is used for the experiment. The maximum potential used for miRNA sensing with αHL pore is 180 mV, due to the limited stability of lipid bilayer matrix with higher voltages [111].

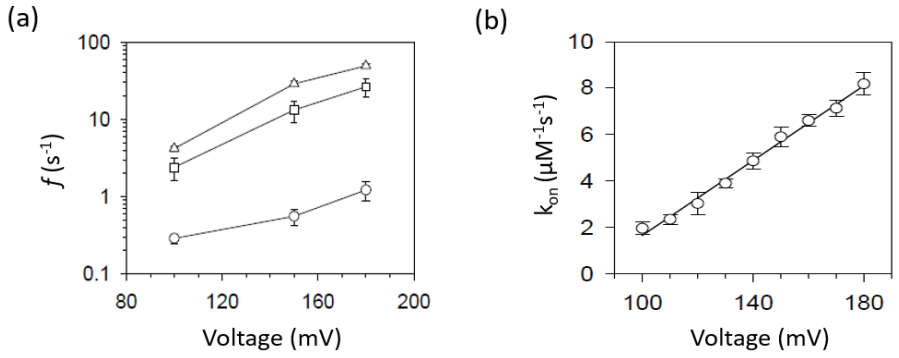

Figure 2.18. (a) Capture frequency dependence on voltage for 1 pM (circle), miRNA155-P155 10 nM (square) miRNA155-P155 and 25 nM miRNA155-P155 (triangle) duplex. Taken from [13]. (b) The capture rate dependence on voltage for 100 nM miDNA155-P155-dC_{30} duplex. The linear dependence of capture rate on voltage suggests diffusion limited capture rate. Taken from [16].

Wang *et al.* reported detection and quantification of cancer-related miRNA155 in biological samples from lung cancer patients with αHL nanopore in 1 M KCl at 100 mV [13]. They measured the frequency of miRNA155-P155 signature blocks after probe P155 was introduced in RNA extract from both healthy donors and lung cancer patients (Figure 2.19 a-d) [13]. The frequency of miRNA155-P155 duplex signatures was about two times higher in samples from lung cancer patients compared to samples from healthy donors Figure 2.19 e.

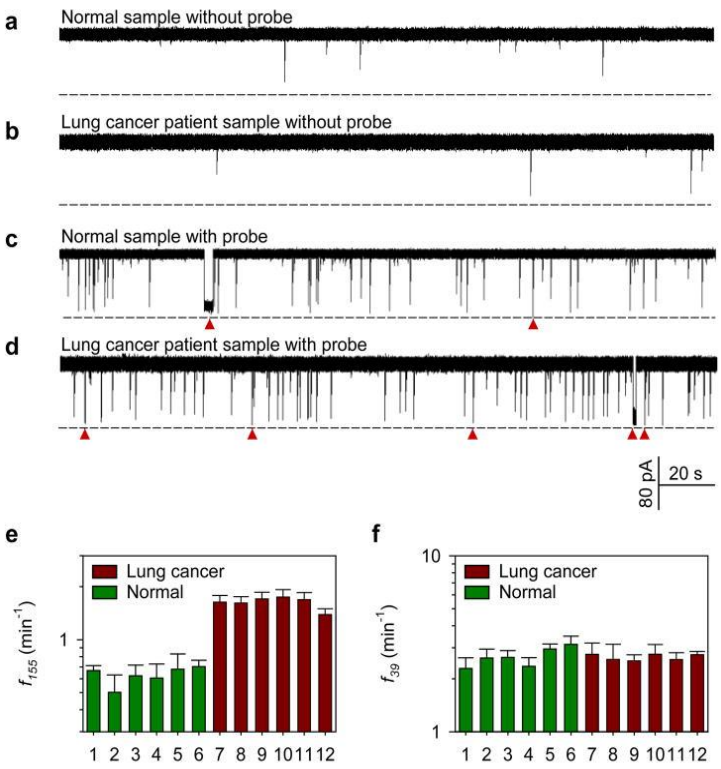

Figure 2.19. Single αHL current traces in 1 M KCl at 100 mV for: a) normal sample without the P155 probe, b) sample from lung cancer patient without probe, c) normal sample with the probe P155 d) Lung cancer patient sample with the P155 probe. e) Capture frequency of miRNA155-P155 duplex for healthy donors and lung cancer patients f) Capture frequency of miRNA39-P39 introduced as a positive control in both samples from healthy donors and lung cancer patients. Taken from [13].

The capture frequency for miRNA155-P155 for the lung cancer sample was found at ~0.03 s^{-1} which was similar to the capture frequency of the 10 nM miRNA155-P155 duplex from synthetic miRNA155 in 1 M KCl at 100 mV [13].

2.10.2 DNA probe design for miRNA detection with αHL nanopore

DNA probe design plays an important role both in selectivity and sensitivity for miRNA detection with the nanopore. Considering the number of known miRNAs and their similar size ~22 nt, it would be difficult to distinguish between different miRNAs in solution with nanopore sensing based just on their short translocation time. The DNA probe has the task to selectively bind only to target miRNA and ideally not to interact with other miRNAs in solution. As mentioned previously, more than 2500 miRNAs molecules were identified, some of them having sequences that can differ in only one nucleotide. Wang and co-workers demonstrated that αHL was able to discriminate between two miRNAs (let-7a and let-7c) with sequences differing in only one nucleotide, based on the duration of the signature event [13]. The unzipping duration of the fully hybridized let-7a*P_a in 1 M KCl at 100 mV was 2.4 times longer than let-7c*P_a. Similarly, the duration of let – 7 c*P_c was 2 times longer than the let-7a*P_c duplex. The presence of a mismatch

in the duplex reduces the duplex stability, which results in a shorter signature duration compared to the fully hybridized duplex [13].

In the work of Xi *et al*., the sensitivity of the technique was further increased by introducing the locked nucleic acid (LNA) modification of the probe [19]. LNA is a nucleic acid analogue in which the ribose moiety contains a bridge between 2' oxygen and 4' carbon atoms, which enables enhanced base stacking and backbone reorganization. As a result, the DNA probe with LNAs has increased hybridization properties (*i.e.* melting temperature). In their work, they used three miRNA sequences from let-7 family: let-7a, let-7b and let-7c. The DNA probe complementary to let -7b was modified with locked nucleic acid (LNA) and with capture overhang dC_{30} attached to 5' end of the probe [19]. They measured dwell times of let-7 b, let 7-a and let 7- c hybridized with DNA probe LNA-P_{22b} in the standard electrolyte solution,1 M KCl, pH = 7.8 at 180 mV (*trans* side positive) [19]. The unzipping duration of let 7b- LNA-P_{b22} was 916 ms, about 10 and 30 times longer when compared to block durations produced by let-7c/LNA-P_{b22} and let-7a/LNA-P_{b22} [19].

DNA probe design was shown to be important in the capture rate of miRNA. Capture rate can be increased with modification of the DNA probe. Extending the probe with capture overhang is necessary since single-stranded tail guides the duplex towards the pore, which is proceeded by unzipping of the duplex with electrophoretic force. The force acting on DNA-miRNA duplex is proportional to the length of the capture overhang. Wang and co-workers modified the DNA probe from its 3' end with different poly (dC) overhangs and showed that the capture frequency increased with the length of poly (dC) capture overhang. They showed that the capture rate of poly $(dC)_{30}$ was three times higher than the one with the probe having capture tail $(dC)_8$. Experiments were performed in symmetrical 1M KCl at 150 mV(Figure 2.20 b) [16]. The side of DNA probe at which the capture tail is attached also matters, since capture tail at 3' end of DNA probe at +100 mV in 1 M KCl solution had 20 times higher capture rate compared to poly $(dC)_{30}$ overhang attached to 5' of the DNA probe (Figure 2.20 a) [13].

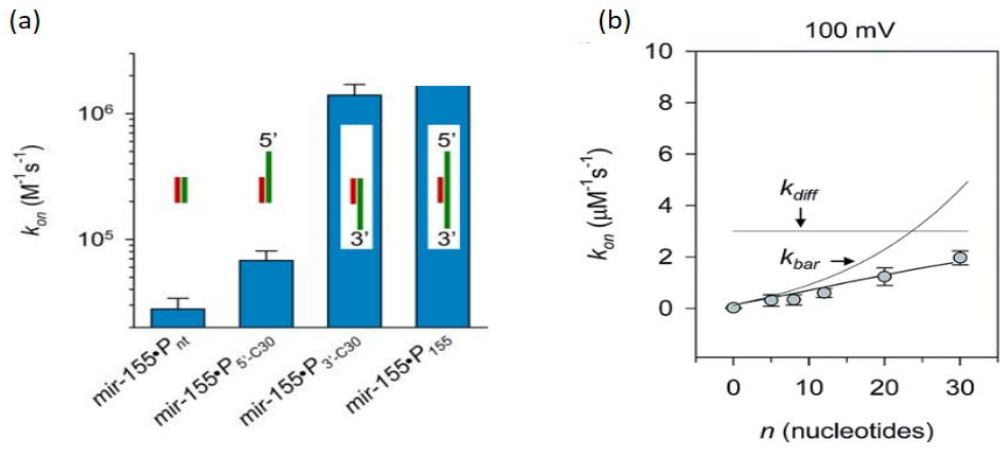

Figure 2.20. (a) Influence of capture overhang dC_{30} position in the DNA probe on capture rate of miRNA155 in 1 M KCl at 100 mV. Taken from [13]. (b) Dependence of the capture rate on dC overhang length at 100 mV in 1 M KCl. Taken from [16].

2.10.3 Multiplex detection of miRNAs with αHL nanopore

The detection and quantification of multiple miRNA sequences in the same sample is a highly desirable feature that is still lacking in most of the previously discussed biosensor technologies [11]. Multiplexed detection of miRNAs would be a useful tool for diagnosis of diseases where more miRNAs have irregular expression. Zhang *et al.* showed that capture overhang of DNA probe can be modified with PEG polymer with different numbers of repeating units, which enabled them to discriminate among 4 different miRNAs [17]. They extended the DNA probes from 3' end with familiar dC_{30} overhangs modified by PEGs of various lengths (3, 8 and 24 r.u.). The current blockage was the deepest for the probe containing dC_{30} overhang modified with the longest PEG molecule (24 r.u.) and gradually shallower for the overhangs modified with shorter PEGs. Capture overhang without PEG modification produced the shallowest current blockages (Figure 2.21).

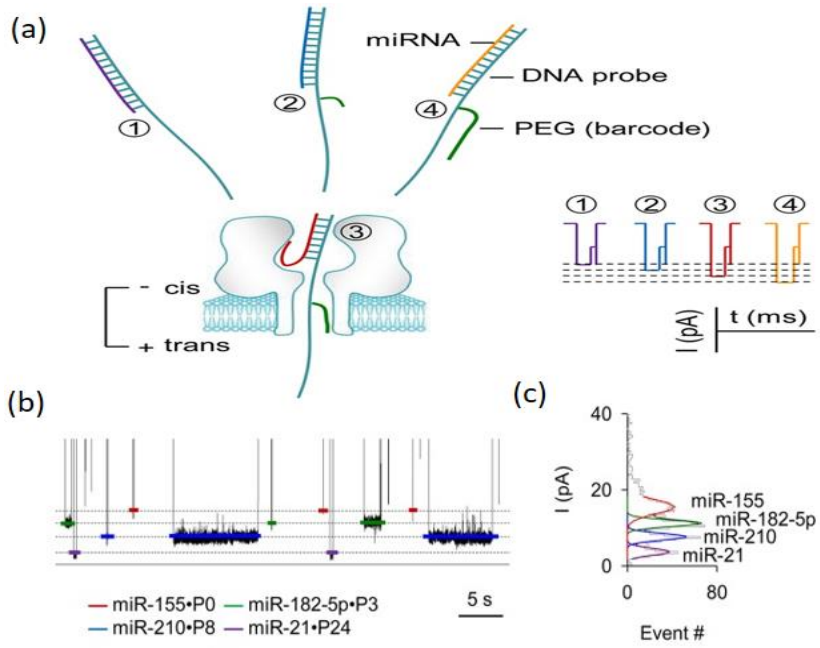

Figure 2.21. a) Four miRNA labelled with DNA probe further modified by PEG. b) Real-time current blockages produced with four different miRNA-Probe duplexes depended on PEG size. c) Amplitude histogram produced with four different miRNA-Probe duplexes. The shallower amplitude was observed for miRNA155-P155 without PEG modification while the deepest amplitude was observed for miRNA21-P21 with the longest PEG (24) modification of the probe. Taken from [17].

The capture frequency of each of the four miRNAs increased linearly with their concentration[17]. Moreover, the capture frequency of three miRNA-Probe duplexes (all fixed at 75 nM) remained constant when only the concentration of the fourth miRNA (miRNA155) was varied from 75 to 500 nM, demonstrating no interference between the molecules [17].

2.10.4 Probe design for nanopore detection of miRNA in complex solution

The complexity of the real clinical samples presents a problem for nanopore detection of miRNA because the other RNA/DNA macromolecules such are tRNA, mRNA extracted from the sample might produce nonspecific long blockages of the αHL pore[158]. To overcome nonspecific molecule interference with αHL pore, Tian *et al.* constructed the DNA probe modified with polycationic HIV-1 TAT peptide [158]. Unlike the 'conventional' experimental conditions, where DNA analytes are placed cis side of αHL channel and pulled through the pore by applying a positive voltage from *trans* side, the miRNA/DNA probe was dispersed in *trans* solution facing transmembrane part of αHL channel (Figure 2.22) [158]. Therefore, when positive voltage was applied so *trans* side was positive to cis side, negatively charged molecules were electrophoretically pulled away from the pore towards the positive electrode, while the target miRNA hybridised with peptide modified DNA probe moved towards the pore and produced transient current modification [158]. In order to improve the capture rate of the polycationic probe, αHL was modified with K 131 D mutation, where positively charged lysine (K) was replaced with negatively charged aspartic acid (D) [158]. The negative charge in *trans* entrance of αHL pore

was thus increased from -7e to -21e, which resulted in an improved electrostatic attraction between the positively charged peptide and the αHL pore entrance. The capture rate of the TAT peptide increased 200- fold from 4.1 $\mu M^{-1}s^{-1}$ with wild-type αHL to 880 $\mu M^{-1}s^{-1}$ with K121 D αHL mutant pore [158].

The electrolyte solution used in experiments was 1M KCl, 10mM Tris (pH =7.2) and the applied voltage was 180 mV (*trans* side positive). Concentrations of miRNA and matching probes used in experiments were respectively 100 nM and 300 nM [158].

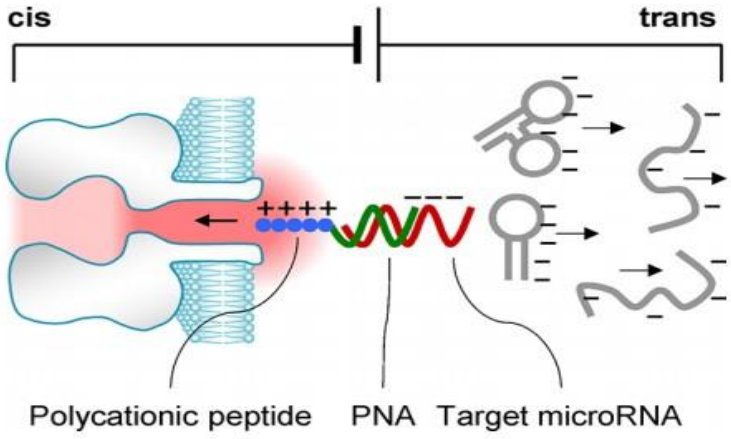

Figure 2.22. Schematic principle of capturing peptide modified DNA probe and its miRNA. Unlabelled miRNA, tRNA and mRNA are attracted to positive (*trans*) electrode and not detected by nanopore. Taken from [158].

2.10.5 Nanopore detection of enzymatic amplified miRNA

Recently Zhang *et al.* demonstrated detection of miRNA- 20a with αHL nanopore by using isothermal amplification [191]. However, the working principle was not based on detection of miRNA-DNA probe complexes as in previous works. Instead, the miRNA-20a was used as an input molecule for an enzymatic reaction, while the frequency of the pulses produced by the output sequence of the enzymatic reaction (polydT_{20}) was measured (Figure 2.23) [191]. For the enzymatic reaction, the miRNA 20a was hybridized with two partially complementary DNA sequences: DNA template and DNA primer, making a three-way junction structure. The enzymatic reaction started with Bst polymerase binding to the DNA primer and adding nucleotides to the DNA template. After the polymerase finished with adding nucleotides, the nicking enzyme Nt.Alw was employed to cut the newly added DNA sequence (poly dT_{20}). By cleaving the newly added strand, the polymerase reaction could start again. This enzymatic amplification cycle lasted for ~ one hour, followed by measurement of the resistive pulses produced by poly $dT_{20.}$ The output dT_{20} sequence was measured in asymmetrical 0.2 / 2 M KCl *cis/trans* conditions with αHL nanopore[191]. By using this approach, they reported a limit of detection of 1 fM [191].

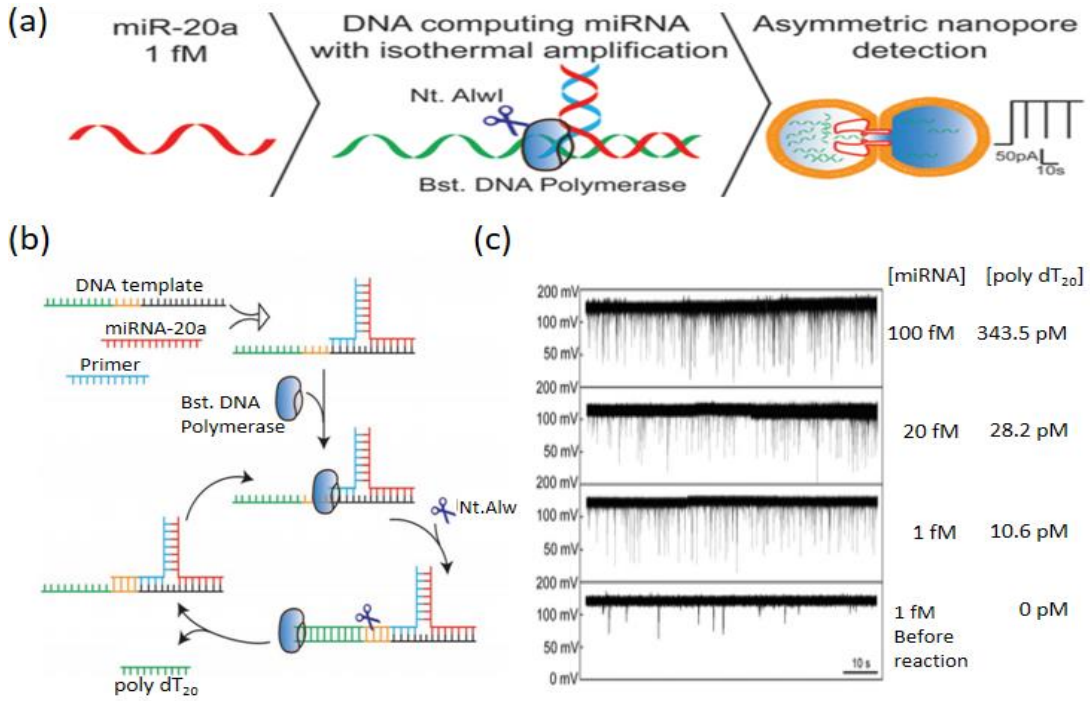

Figure 2.23. a) Schematic of miRNA-20a enzymatic amplification and measurement using nanopore under salt gradient conditions. b) Enzymatic reaction scheme of the enzymatic reaction. Three input polynucleotide molecules (miRNA20a, DNA template and DNA primer) hybridize making the three-way junction. Bst.DNA polymerase adds the poly dT_{20} nucleotide strand on DNA template, which is then cleaved by Nt.Alw nicking enzyme. c) The single-channel αHL trance in the presence of [poly dT_{20}] produced as an output of input [miRNA 20 a]. modified from [191].

2.10.6 MicroRNA detection with solid-state nanopores

The detection and quantification of miRNA 122a hybridized with RNA probe with a 3 nm wide silicon nitride nanopore were demonstrated by Wanunu *et al*. [190]. The isolation of specific miRNA from the sample was done by addition of magnetic beads functionalized with p19 protein that has the ability to bind specifically to short dsRNAs. They showed a linear dependence of the pulse events frequency with miRNA concentration over three orders of magnitude, from 100 pM to 100 nM [190]. Solid-state nanopores do not suffer from membrane instabilities caused with high voltage and can withstand voltages as high as 1 V. Wanunu *et al.* used voltage of 500 mV to improve the capture rate of miRNA122 with a 3nm nanopore in silicon nitride membrane and were able to detect quantities as low as 100 pM miRNA122 [190].

Another study on miRNA detection with ~7 nm wide silicon nitrate nanopores utilized the modification of DNA probe with biotin to detect lung cancer-related miRNA 155 in solution without isolation and enrichment [192]. Addition of monovalent streptavidin, able to bind to biotin in DNA probe, resulted in higher capture rate and better discrimination of duplex and single-stranded molecules. The limit of the quantification of miRNA 155 in 0.9 M NaCl at the voltage of 500 mV was 10 nM [192], what was similar to the limit of quantification with the

biological αHL nanopore in 1 M KCl solution at 100 mV previously reported in [13]. The capture rate of heteroduplex increased exponentially with the applied voltage (Figure 2.24 b).

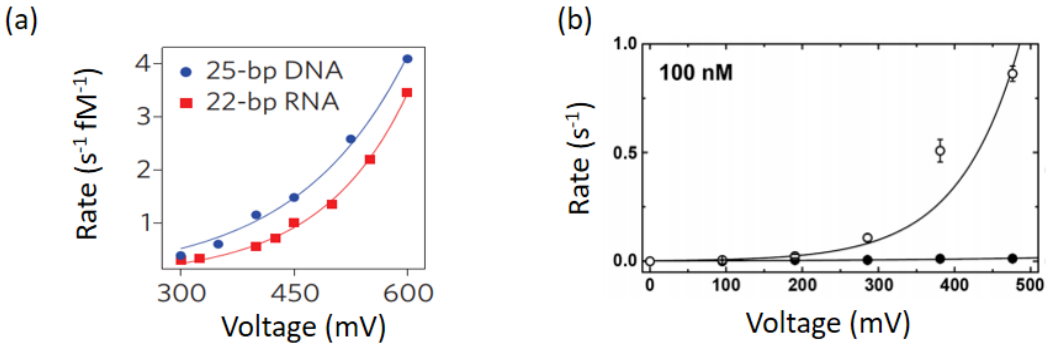

Figure 2.24. (a) The dependence of capture rate of DNA / RNA molecules on voltage for a voltage range from 300 – 600 mV. Taken from [190]. (b) The capture rate of 100 nM miRNA155:ssBio23:MS heteroduplex (white circle) and 100nM ssBio23:MS (black circles) for the voltage range of 0-500 mV. The lines present exponential fit to the data meaning that capture rate is voltage activated. Taken from [192].

The short summary of analytes, electrolyte solutions and applied voltage used in above-described experiments is given in Table 2.3.

Table 2.3. Experimental conditions used to detect miRNA target molecules with nanopores.

Experiment	***miRNA concentration***	***Electrolyte***	***Applied voltage***
Wang et al. [13]	0.1 pM-100 nM	0.5/3M KCl	180mV
Zhang *et al.* [17]	10 pM-100 nM	1M KCl	120 mV
Tian *et.al* [158]	50 pM-5 nM	1M KCl	180mV
Zhang *et al.* [191]	1 fM-100 fM	0.2/2 M KCl	100mV
Xi *et al.*[19]	50 pM-500 nM	0.5/3M KCl	100 mV
Wanunu et al. [190]	100 pM-100nM	1 M KCl	500 mV
Zahid *et al.* [192]	10 nM -150 nM	0.9 M NaCl	300-500 mV

2.11 Summary

Short non-coding microRNA molecules play an important role in post-transcription gene expression. It was shown that aberrant expression of miRNA is correlated with many diseases, including cancer. The fact that miRNAs are remarkably stable in biological fluids, which can be easily accessible, makes them potent disease biomarkers. Up to now, the golden standard for miRNA quantification in biological samples has been qRT-PCR. However, the short length and similar nucleotide composition of the targets complicate the primer design. Moreover, miRNA

precursors pre-miRNA and pri-miRNA can lead to an erroneous estimate of the actual miRNA concentration. The biosensor methods for miRNA detection and quantification are developing rapidly. However, the complexity of the design, difficult reproducibility and lack of multiplex assays are main drawbacks of the existing technologies.

Nanopore resistive pulse sensing (NRPS) is a novel technique that can be used for rapid, label-free and multiplex detection of miRNA molecules. Nanopores can be divided into solid-state and biological. Solid-state nanopores consist in nm orifices opened in different materials, while biological pores can be fabricated by inserting a protein-pore in a supported lipid bilayer membrane. The pores are placed in the interface between two chambers filled with electrolytes, and a voltage difference is applied between the chambers. The negatively charged DNA molecules can traverse through a pore in direction of the electric field. The interaction of a miRNA-DNA duplex with the αHL pore can be detected as a specific multilevel resistive pulse.

The concentration of miRNA molecules is simply related to the frequency of the current pulses through the pore. Most of the miRNA studies using NRPS were performed using the biological alpha hemolysin (αHL) nanopore. Because of its narrowest constriction of 1.4 nm, this pore is ideal for discriminating dsDNA from ssDNA molecules. The previous reports on miRNA detection and quantification with αHL pore demonstrated a broad range of detection (10 pM-500 nM) without any need for amplification or labelling of the targets [13, 17, 19].

The main challenge of this technology is the low capture rate of miRNAs, being their concentration extremely low in biological samples. As reported by Zhang *et al.* and Wanunu *et al.*, at least ~200 stochastically distributed events should be acquired to estimate the concentration of the target with > 90% accuracy [17, 190], thus collecting such a number of events with sub-pM concentrations of miRNAs becomes difficult. It was shown that pairing the target with a ssDNA probe, and extending the probe with capture overhangs improved the miRNA capture rate. The position at which the capture overhang is attached to the DNA probe has an influence on the capture rate since the αHL pore showed higher preferences for probes with dC_{30} overhang attached to its 3' end [13].

The most intuitive way to increase the capture rate of negatively charged miRNA-DNA duplexes is raising the voltage. Although all the studies showed a significant increase of the capture rate of miRNA-Probe with the voltage, the conventional voltage used to quantify miRNA-Probe resistive pulses was always in the range of ~100-120 mV. This is because the lipid bilayer is more stable at low voltages (<150 mV), and the dwell time of the miRNA-DNA duplex is exponentially reduced with the voltage. In addition, studies on miRNA detection with αHL nanopore used salt gradients conditions to increase the capture rate of miRNA-DNA duplex by the pore [13, 19]. However, none of these studies investigated the influence of the salt gradient on the miRNA-DNA duplex characteristics, nor the stability of the lipid bilayer and αHL pore under salt gradient

conditions. Although Wang *et al.* reported impressive limits of quantifications, as low as 0.1 pM, in a salt gradient of 0.2 / 3 M KCl (*cis/trans*) at 100 mV, the number of collected events and time of the recording were not shown [13].

In this project, the influence of various salt gradients on miRNA-DNA duplex – αHL interactions was investigated. Moreover, the influence of DNA probe design on the capture rate under symmetrical and asymmetrical salt conditions has been examined. The experimental laboratory setup used for single-channel recording in our lab will be described in the following chapter.

Chapter 3: Methodology

This Chapter details the setup and protocols used in all experiments. It opens up explaining the hardware used and how the devices are integrated together and function (3.1). Following, the fabrication of the electrodes is shown. A novel method to create microscopic Teflon apertures is presented in 3.2. The final assembly of the chambers and the protocol adopted to build a stable lipid bilayer is pictured in 3.3. Section 3.4 shows how to insert the protein pore into the biological membrane and 3.5 explains how the procedure has been optimized to lower the electrical and mechanical noise in the recordings. Preliminary results to test the setup using PEG single molecules and A,C,U homopolymers are presented in 3.6 and 3.7 respectively. 3.8 sums up the progress that was made in this part of the project, with the full optimization of the system.

3.1 Experimental setup

3.1.1 Amplifier and digitizer

The experimental setup in this work is shown in Figure 3.1. It consists of the commercial Axopatch-200B (Molecular Devices) patch clamp amplifier, 16-bit Digidata 1440A digitizer (Molecular Devices), vibration table and the Faraday cage (Warner instruments). Axopatch-200B has a recording bandwidth of 100 kHz and the Digidata 1440A digitizer has a maximum sampling rate of 250 kHz. The nanopore experiments were performed with voltage clamp mode where applied voltage was fixed by the digitizer and the current through the pore (required to maintain that voltage) was measured. Axopach 200 B can operate in resistive or capacitance feedback. In this work the current recordings were made with whole cell settings (β=1), which uses a 500 MΩ resistor. The Axopatch -200B converts the output analog current signal to output voltage analog signal, which is then fed to Digidata 1444 A digitizer.

The Digidata 1444 A converts the analog signal of the amplifier to the digital signal. It is also used to control the sourced voltage of the amplifier. The Digidata 1444A is a 16 bit digitizer with a dynamic input range of ±10 V that provides resolution of 0.305 mV/bin (20 V/2^{16}) and a dynamic output range of ±10 nA, with the resolution of 0.305 pA/bin. The resolution can be increased by setting the additional output gain (from 0.5 to 500) on the Axopatch 200 B amplifier. In this work, the nanopore recordings were done by setting an additional gain of 10, which decreases the dynamic input range of recording to ± 1 nA but increases the dynamic output resolution to 0.035 pA/bin [193].

Low-pass filters (LPF) are commonly used in electrophysiology measurements to remove unwanted signals and the noise from the data. Axopatch-200 B has a built-in four-pole low pass

Bessel filter, with five(1, 2, 5, 10 and 100 kHz) cut-off frequencies(-3dB frequency). The -3dB cut-off frequency is the frequency at which output voltage signal fells to $\sqrt{1/2}$ of the amplitude of the input signal [194]. Selection of the right f_c is important because over filtering the signal might lead to the loss of a valuable information [194]. Another important parameter to consider is the sampling rate. Since the continuous current through the nanopore is digitized and stored on a computer for further analysis, it is important to select the appropriate sampling rate. The Nyquist theorem states that the minimum sampling rate should be at least 2 times the f_c, but it is better to oversample and select samplings of 5 to 10 times the f_c [92, 194]. In this work, the DNA duplex translocations were recorded by setting the cut-off frequency to 10 kHz and the sampling rate to 50 kHz.

Axopatch-200B is controlled by Clampex 10.2 software (Molecular Devices), while the data analysis of the measurements has been carried out Clampfit 10.2 software (Molecular Devices). Clampex software can operate in five different acquisition modes. All the resistive pulses in this work were recorded with gap-free acquisition mode. In this mode, the current through the pore can be continuously measured and stored in a computer hard drive like a continuous current-time data file. As an average, having a sample rate of 50 kHz, it was generated a ~350 MB data file from an hour of recordings.

3.1.2 Anti-vibrational table and Faraday cage

Electrical nanopore recordings were conducted in the enclosure to isolate the experimental measurements from the external electrical noise. In this work, the bilayer chambers, the electrodes and the headstage were placed in a 25 x 22 x18 inch aluminium Faraday cage (Warner instruments). All metallic parts used in the experiments (posts, holders and vibrational table) were connected to a common brass socket inside the Faraday cage, which was grounded with the common ground point from the rear of the Axopatch-200B amplifier. Since the lipid bilayer matrix is a very fragile structure, experiments with the planar lipid bilayers are extremely sensitive to vibrations and they are prone to breaking due to mechanical stress. Vibrations can arise from various sources like people walking, talking or closing drawers. Therefore, the bilayer fluidic cell was mounted on a magnetic holder and placed onto a heavy pneumatic vibration isolation table inside the Faraday cage.

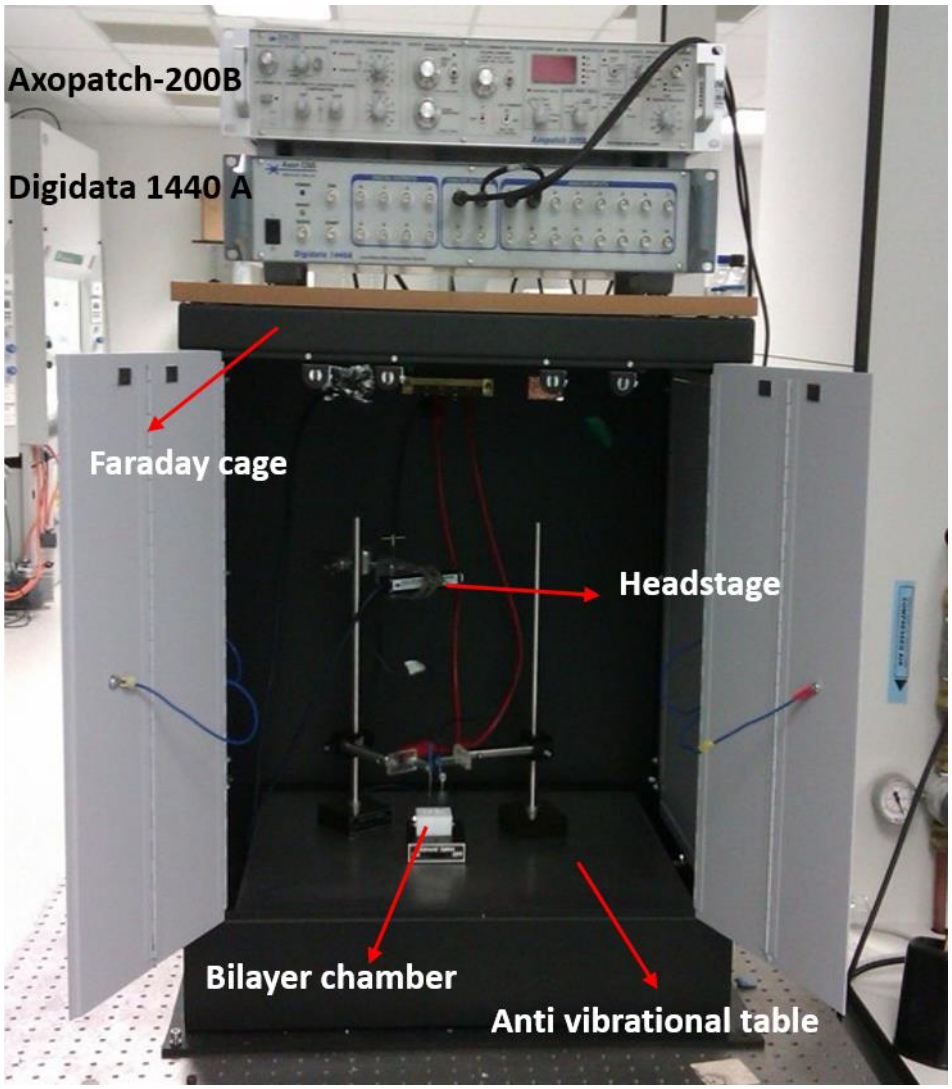

Figure 3.1. Experimental setup in our lab used for nanopore sensing experiments

3.1.3 Ag/AgCl electrodes

Electrodes can be described as transducers that convert an ionic current in a solution into an electron current in metal wires and vice versa. The gold standard for electrodes in electrophysiological measurements is the Ag/AgCl since they are chemically stable, reversible and have a low noise electrical performance (The Axon Guide). It must be stressed that these electrodes perform well only in solutions that contain Cl^- ions. For electrophysiology purposes, the Ag/AgCl electrodes are usually prepared either by immersing silver wires into bleach or by electroplating them in a solution containing Cl^- ions.

In this work, silver wires with a diameter of 0.8 mm were electroplated in 0.1 M HCl. Firstly, two equal silver wires were cut and rinsed with ethanol to remove surface contamination such are grease or dust. Silver wires were then connected to the positive pole of a 9 V battery and placed in the 0.1 M HCl solution along with a platinum wire, that was connected to the negative pole of the battery. The current through the wires was limited with a 47 kΩ resistor. It usually takes

around 2 minutes to get a uniform grey colour AgCl coating. If electroplating is too long, it can result in the creation of a darker AgCl coating that is fragile and brittle. On the contrary, when electroplating is too short there can still be some areas of the bare silver that are not coated with AgCl pellet.

When potential is applied to an electrodes pair in a solution containing Cl^- ions, the reversible chemical reaction occurring is:

$$Ag(s) + Cl^- \rightleftharpoons AgCl(s) + e^-$$

On the positive electrode (anode), an oxidative electrochemical reaction occurs where the Cl^- ions from solution react with Ag from the silver wire producing AgCl and an electron. The latter flows through the wire through an electrometer to the negative electrode (cathode), where a reverse reaction takes place (AgCl plus electron converts to Ag and Cl^- is released in solution). If the electrodes are immersed in chambers containing solutions with the different chloride concentrations, the potential difference between electrodes will arise and can be calculated from the Nernst equation:

eq 5

$$\Delta V = -\frac{RT}{F} ln \frac{[Cl]_{cis}}{[Cl]_{trans}}$$

where *R* is the universal a gas constant (8.314 J mol^{-1} K^{-1}), *T* is the temperature in Kelvin scale (+ 273.15 K), *F* is the Faraday constant (96485 C mol^{-1}) and [Cl] are activities of chloride ions in *cis* and *trans* compartment. The potential offset can be minimized by using an agar bridge between Ag/AgCl electrodes and the bath solutions. This keeps the concentration of Cl^- ions around the electrodes constant, which is important if an asymmetrical concentration of salt is used in the chambers.

In this work, an agar bridge made with 2% w/v agar in 3M KCl is used for all experiments. To prepare the gel, 200 mg of agar was added to 10 mL of 3 M KCl and put in the microwave for ~10 seconds to allow the agar to melt. The heated solution is rapidly extracted with a 10 mL syringe and transferred to 200 µL Gilson pipette tips, that are then stored in Eppendorf tubes containing 3 M KCl. Before the experiment, the chlorinated parts of the Ag/AgCl electrodes are immersed in the pipette tips containing the agar bridge. The rubber stopper was used to immobilise the electrode in the pipette tip, and to prevent drying of the salt bridge solution.

The Ag/AgCl electrodes are exhaustible, which means that AgCl coating is exhausting with the current flow, and might result in an exposure of the bare silver wire to the solution. This can lead to unpredictable potential offsets and current fluctuations. Therefore, electrodes should be cleaned

and re-chloridated frequently in order to avoid current fluctuations and unpredictable voltage offsets.

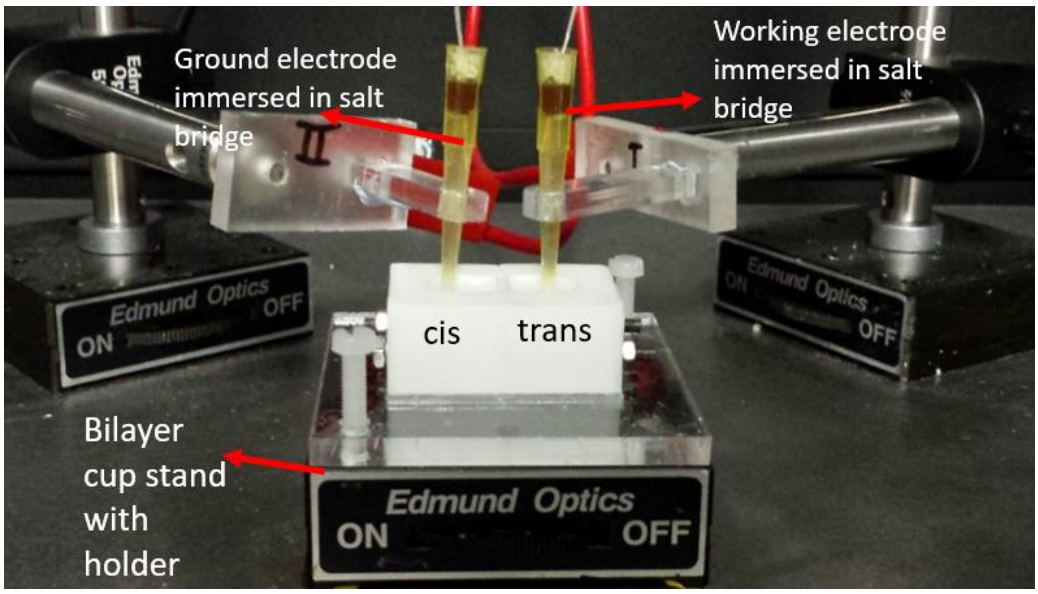

Figure 3.2. Bilayer chamber with two electrodes immersed in each cup. Silver chloride electrodes are inside 200 µl Gilson pipette tips filled with 2 % agar in 3 M KCl. Rubber stopper is used to fix the electrodes and to preserve the salt bridge.

3.2 Fabrication of apertures in Teflon

Formation of the bilayer is the crucial step for any experiment with biological nanopores, since the lipid membrane provides the environment for the incorporation of a biological pore. Ideally, bilayers should be stable over long periods of time, to provide more results from the experiments. Moreover, noise in electric recordings is largely affected by the size of the bilayer, hence bilayers with the smaller area are more desirable [195, 196]. Bilayer stability and area is mainly depended on the aperture over which bilayers are formed.

The plastic in which the aperture is situated is of great importance for bilayer stability and electronic noise. Teflon is a polymer that is widely used both for bilayer chamber fabrication and as a sheet in which the small aperture is punctured. It is resistant to a wide broad of solvents, it is mechanically robust, it can be clamped between chambers easily and has a low dielectric constant, which contributes to lower noise in recordings [195, 196]. Techniques that are used for fabricating apertures in Teflon include 'shaving' and hot needle techniques, or high voltage pulse to burn through the Teflon sheet [195]. Mayer *et al*. reported microfabrication of 2-800 µm diameter apertures in Teflon by using soft lithography casting [196].

Alternatively, apertures in polymer films might be machined by using laser ablation. The UV excimer laser ablation was used for fabrication of apertures with 4 – 105 µm diameter in 20 µm thick Poly(methyl methacrylate) (PMMA) [197, 198]. The CO_2 laser was used for fabrication of

~300 µm apertures in ethylene tetrafluoroethylene (ETFE) [199]. The ablation with a CO_2 lasers is of particular interest since CO_2 lasers are commonly used, simple to operate and powerful. The energy of infrared photons is transferred to thermal vibration of polymer molecules. As a result, the irradiated zone is heating at high rates, similarly to a strong heating shock, which leads to the breakdown of the polymeric material.

3.2.1 Air suspended Teflon apertures

For the fabrication of Teflon apertures, 30 W CO_2 (Epilog mini Helix USA) laser was available in the lab. The laser has a computer interface and it is simple to handle. It can operate in raster, vector or combined mode. Vector mode was selected for fabricating apertures since in this mode the laser is cutting through the material. Furthermore, it is possible to change the settings for speed, power and frequency, which enables several combinations of the laser settings. The power can be varied between 1 and 100 percent of the full value (30 W). Frequency is defined as pulses per inch (ppi) and can be selected between 10 and 5000. The 50 µm thick Teflon sheets were purchased from Goodfellow Cambridge Ltd (UK). The 50 µm thick Teflon sheet was cut into 1.5 cm wide and 7 cm long stripes which were mounted on a shallow PMMA base holder. However, when these air-suspended Teflon stripes were used for CO_2 laser ablation, the output apertures were severely irregular with lots of Teflon debris around the edges (Figure 3.3).

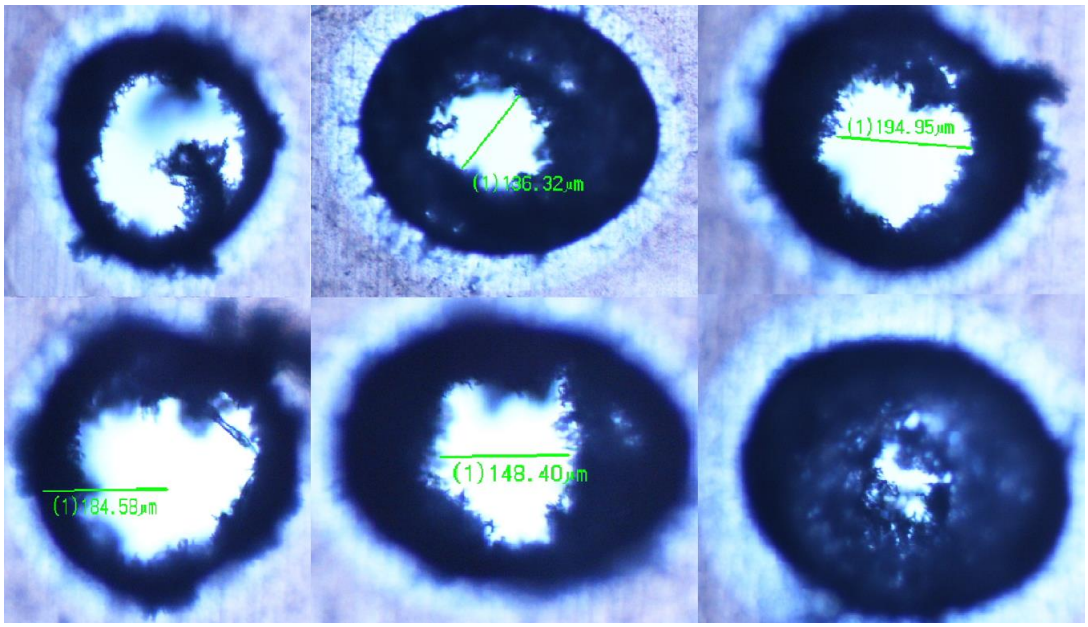

Figure 3.3. Air suspended Teflon apertures produced with laser cutter with the settings (P = 4, S = 5, F = 100)

It was hard to find a correlation between laser settings and size of the air suspended apertures. The power required to ablate the Teflon was found to be 4 % at the speed 5 and frequency of 100. However, the exact size of the obtained apertures was hard to determine since their shape was irregular due to the Teflon debris at the edges. The estimated size of the laser-ablated apertures in

the air- suspended Teflon apertures was ~150 µm. The bilayer formation in these apertures was hard to achieve. Moreover, the bilayers formed over those apertures were stable up to a maximum of one hour and prone to breaking.

3.2.2 Substrate suspended Teflon apertures

To overcome this problem, the Teflon sheet was clamped onto solvent resistant PMMA, which acts as a base and 1.9 cm wide scotch tape (3M, type 550) made from the acrylic adhesive and biaxially oriented polypropylene (BOPP). Apertures were designed in Corel Draw 16 software as black dots with a diameter of 40 µm. Each Teflon stripe was cut from the sheet with dimensions of 7.5 cm x 1.25 cm, which provides space for six designed apertures. The PMMA base had dimensions of 8 cm x 8 cm and, usually, three to four Teflon stripes could be adhered onto it (Figure 3.4).

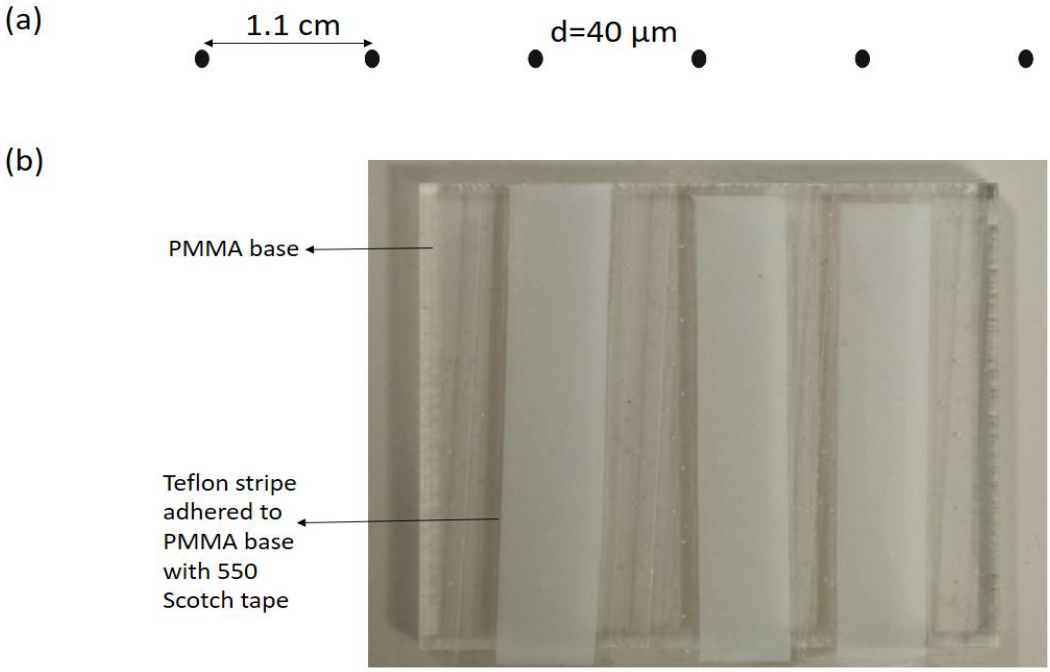

Figure 3.4. (a) The simple design of apertures for laser cutter. Every dot presents three overlapped dots of the same size. (b) Three 50µm Teflon stripes adhered to PMMA base with scotch tape type 550 (3M).

This means that with one laser run 18 to 24 apertures can be made. It is easy to set the laser to penetrate through Teflon with the higher power, but the outcome will most probably be large apertures (200-500 µm). Therefore, the focus was set on finding power settings that do not penetrate trough Teflon immediately, but rather on those that are not sufficient to penetration. Laser power setting was found to be 3 (3% of total power), lower compared to air-suspended Teflon sheet. The speed of the laser was set to 1, which is the slowest possible but that can be further reduced by designing overlapping dots (Figure 3.4). In this case, 3 dots of 40 µm diameter were drawn on top of each other. With this design, the laser delivers energy beam three times to

irradiated area. By keeping these two settings constant, the frequency is the only variable that has been changed in order to get apertures in Teflon. When the frequency was set between 2000 and 2300 ppi, nice and regular apertures were made with a high reproducibility. The obtained shape of these apertures was circular or elliptical, with smooth edges. This was a significant progress over the air suspended laser cut Teflon apertures. To test the reproducibility of the laser cut, ten Teflon stripes was clamped between PMMA and scotch tape and ablated with laser cutter 43 out of 60 apertures were formed successfully.

Good apertures were considered to have circular or elliptical shape. In 17 cases laser did not penetrate or the apertures were badly shaped (Figure 3.6 a). From this results, laser efficiency can be roughly estimated to be ~ 70% (Table 3.1). Good apertures were further processed with ImageJ software (Figure 3.5). In order to obtain the shape of the aperture, a circle was fitted with abSnake plugin in Image J software [200].

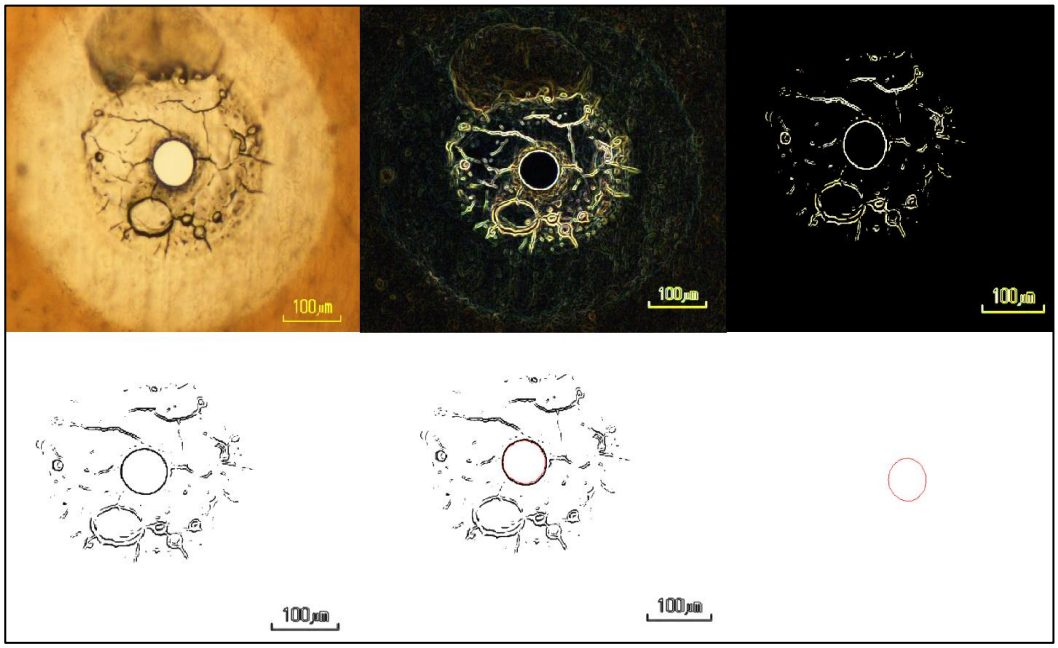

Figure 3.5. Aperture shape extraction steps with imageJ. The shape has been extracted by fitting circle inside aperture with abSnake plugin.

Table 3.1. Estimation of laser efficiency and aperture characteristics based on diameter and circularity.

Total number of apertures	Good	Bad/not formed	Laser efficiency	Average diameter(µm)	Average circularity
60	43	17	72%	88.62±20.20	0.87±0.03

With this method, it is hard to get apertures with reproducible size. The average diameter of 43 apertures produced with S=1; P=3 and F=2000 was found at 88.7 ± 20. 2 µm what is much lower compared to the 305 µm previously reported with Teflon [199]. In some cases, the apertures had only ~10-20 µm diameter (Figure 3.6).

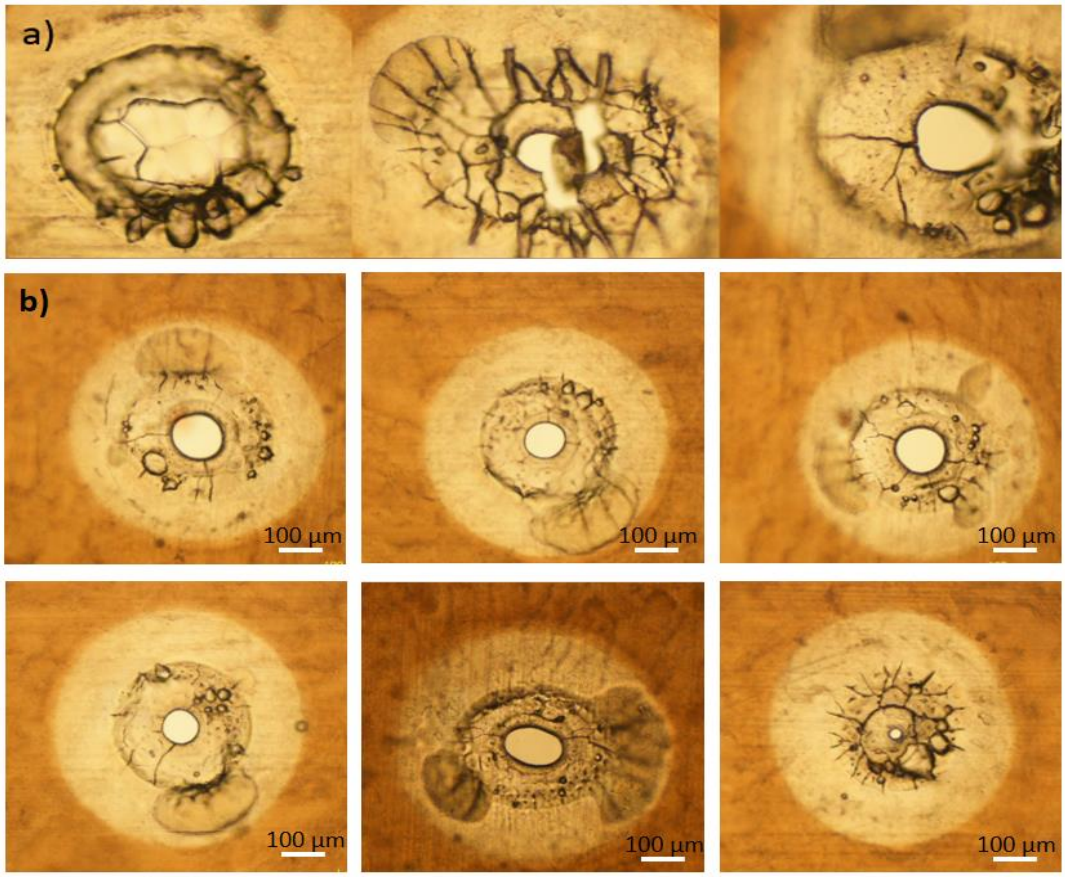

Figure 3.6. a) Cracked, irregular apertures produced with laser cutter. b) Good, circular apertures made by the Epilog mini Helix USA laser cutter.

The difference between air suspended and PMMA-Tape clamped Teflon apertures is easy to spot (Figure 3.3, Figure 3.6 b,). Clamped Teflon apertures have well-defined shapes and don't present Teflon fibres pointing out from the edges. Moreover, the cross-sectional cut of an aperture showed that Teflon is thinned in aperture vicinity, which leads to a triangular shape of the cross-section area.

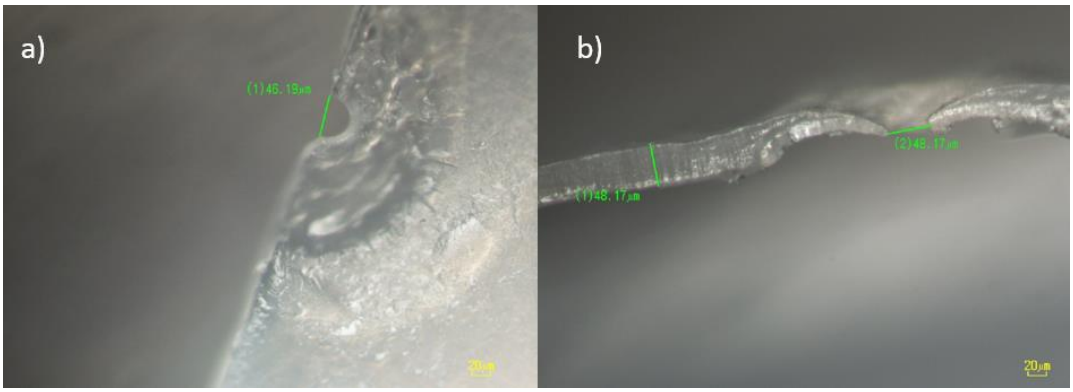

Figure 3.7. Cross section area of apertures made by Nikon Eclipse LV100.

The efficiency of the laser is highly affected by the focal distance of the laser beam. The focus is adjusted manually, which leads to variations between experiments. Furthermore, the laser cutter honeycomb might not be perfectly levelled hence the focal distance can vary for the different positions where the PMMA base is set in the laser cutter. Moreover, Teflon sheet needs to be clamped tightly to PMMA base, without any air bubbles between Teflon and Scotch tape 550, because the outcome will be badly shaped and irregular apertures. It must be noted that manufactured thickness variation of Teflon sheet is 20 %, which can be another reason for the variations in diameter.

By clamping the Teflon sheet between PMMA and tape, the debris fibres, characteristic for the air-suspended Teflon sheet, disappear. This is probably due to the raising of the temperature in the area, which is sufficient for melting these artefacts. It is difficult to give a precise recipe for the formation of these apertures since laser irradiation affects four different materials (BOPP, adhesive, Teflon, PMMA). First of all, with the above-mentioned settings, the laser does not penetrate through the Teflon film if it is not covered with tape. If no PMMA base is inserted, the apertures are not formed properly. Even the specific adhesive of the tape plays a very important role in the fabrication of apertures. For example, the scotch tape used in these experiments is 3M 550, with a total thickness of 50 µm which is comprised of 30 µm BOPP and 20 µm of adhesive. When another tape from the same manufacturer was used (type 508, comprised of 25µm BOPP and 15 µm of adhesive), laser efficiency and quality of apertures decreased significantly.

Overall, clamping Teflon stripe between PMMA base and tape gave encouraging results for the cheap and rapid fabrication of apertures. The whole process takes only about five minutes for 18~24 apertures. For example, a single Teflon sheet of 30 x 30 cm can give around 400 apertures when designed like in Figure 3.4, with a 70% efficiency. Another advantage of Teflon is its chemical resistance to strong solvents. This enables cleaning of apertures with chloroform, hexane acetone and isopropanol in order to remove contamination of materials such as Vaseline, lipids or proteins used in the experiments.

3.2.3 Bilayer fluidic chamber

In this work, custom-built Teflon chambers with a volume of ~ 1.25 mL were used (Figure 3.8 a,d). As previously discussed, Teflon is the usual material of choice for the electrophysiology bilayer experiments since it has excellent chemical resistance, high electrical resistivity and low dielectric constant which reduces the noise in the setup [196]. Before the experiment, all impurities like dust, solution, proteins or DNA had to be removed from the bilayer chambers. Hence, prior to experiment, chambers were rinsed with water, followed by thoroughly washing with organic solvents such as isopropanol, ethanol and methanol. The 50 µm Teflon septum containing an aperture (Figure 3.8 b) with diameter from 80- 120 µm was then clamped between two chambers so that the aperture was in the upper middle position of the contact area between the chambers.

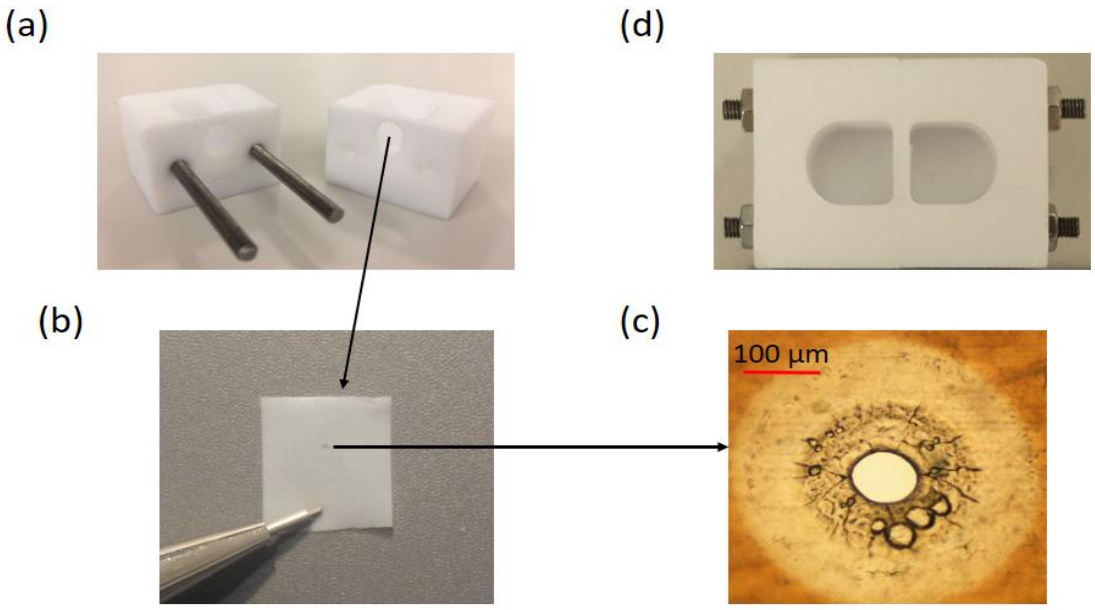

Figure 3.8. Two 1.25 mL Teflon bilayer chambers with 5 x 7 mm contact area. b) The Teflon septum containing laser drill aperture is placed in the contact area between two cells so the aperture is in the upper middle position. c) The microscope image of typical apertures with diameter ~80 µm d) Assembled bilayer chamber ready for the experiment

3.3 Bilayer formation and stability in novel apertures

The duration of a nanopore experiment with αHL is heavily depended on the bilayer stability, hence the formation of a stable lipid membrane is the essential step in nanopore experiments. In this work, the planar lipid bilayer membrane was formed by the folding method developed by Montal and Muller [201]. The advantage of this folding technique is that the formed bilayers can be made from different lipid composition [82, 202, 203]. The lipid used to form the membrane was diphytanoyl phosphatidylcholine (DPhPC) purchased from Avanti lipids (Alabaster USA).

This lipid is the most used for formation of suspended planar lipid bilayers since it has excellent bilayer forming ability and it is stable to oxidation [92]. The lipid solution was made by dissolving DPhPC in chloroform to the final concentration of 20 mg/mL.

The schematic of the folding method is presented in Figure 3.9. The Teflon aperture (Figure 3.8 b,c, Figure 3.9 a) was pre-treated with ~1µl of a solution containing 5 % hexadecane in hexane. Pre-treating the aperture is an important step since the oil, in this case hexadecane, creates an annulus around the aperture that serves as an interface between the hydrophobic Teflon aperture edge and the lipid bilayer [203]. Hexane was then gently dried with nitrogen blow for a couple of seconds. Care must be taken when drying the aperture with nitrogen blow because if it is excessively dried the oil annulus might be removed from the aperture and the formation of the bilayers becomes difficult. The Teflon film with the aperture was then clamped between the two chambers. Vaseline or silicone grease were used as a sealant between the two sides of the sheet and the two half chambers, in order to prevent electrolyte leakages. It was important not to exceed with the amount of sealant because it might come in contact with the aperture and permanently clog it. After assembling the bilayer chamber, both half chambers were filled with the desired electrolyte solution just below the aperture level. This was followed by adding about 5 µL of lipid solution in both chambers. It usually takes 5-10 minutes for chloroform to evaporate, which leaves two monolayers of lipids in each chamber. In order to form the bilayer across the Teflon aperture, monolayers are brought together by slowly raising electrolyte solution in both chambers above the aperture (Figure 3.9 b). The solvent annulus (hexadecane) spread over the walls of the aperture supports the lipid bilayer (Figure 3.9 c). It must be noted that the schematic of the folding method presented in Figure 3.9 is not drawn to scale, since the thickness of the Teflon septum (50 µm in this work) is several orders of magnitude thicker than the lipid bilayer (~5 nm). This also means that the amount of the annulus (hexadecane) that supports the lipid bilayer is much higher than presented in the Figure 3.9 c.

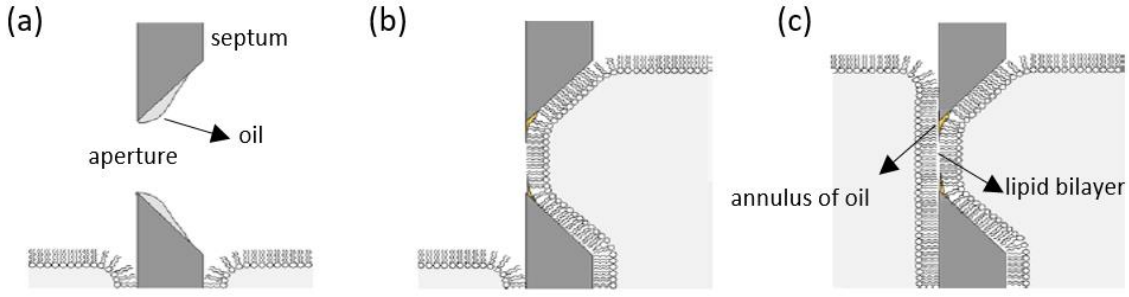

Figure 3.9. The schematic of the folding method for the bilayer formation. (a) The dry aperture is 'pre-treated' with the oil (hexadecane or squalene) which presents a supporting annulus for the bilayer formation. (b)(c) Two lipid monolayers are brought together by raising and lowering solution across the aperture. This scheme is not drawn to scale. Modified from [202].

The lipid bilayer is acting as a capacitor, so when a voltage triangular wave function is applied, the response is a square wave function (Figure 3.10 a). From its output, it is possible to determine

capacitance and quality of bilayers. The triangular function is set in a way that *dV/dt* =1, so the capacitance value can be read instantly from the current trace (equation 5).

eq 6

$$I = C \cdot \frac{dV}{dt}$$

Where *I* is the capacitive current amplitude and *dV/dt* is the voltage change. Figure 3.10 b shows the square current output as a response to the triangle voltage function. The presence of a slope in the square output could be linked to a resistance current flowing through the bilayer. These leaky bilayers need to be broken until a good, square wave output capacitance is obtained.

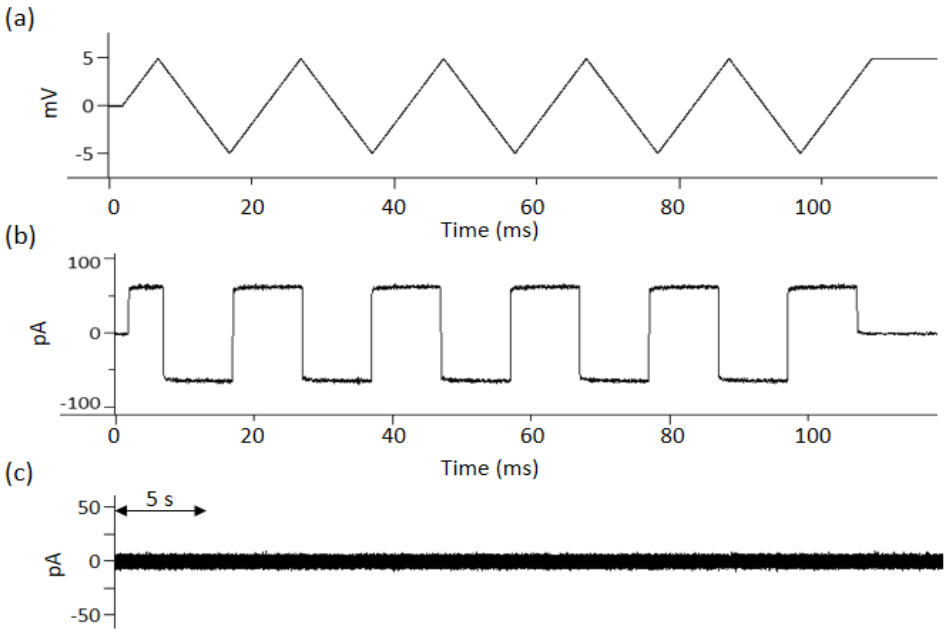

Figure 3.10. a) Voltage applied to the system as a triangular function with ΔV = 10 mV, Δt = 10 ms b) Square current output enables capacitance measurement c) The ideal bilayers when the constant voltage V = 120 mv was applied the current is ~0 pA. Recording solution 1 M KCl, 5 mM HEPES, pH = 7.4

The capacitance of the bilayer can be theoretically calculated from the equation:

eq 7

$$C = \frac{\varepsilon_0 \varepsilon A}{d}$$

Where ε_0 is the permittivity of vacuum, ε is the relative dielectric constant of lipids (~2.7), A is the area of the bilayer and *d* is the thickness of the lipid bilayer (around 5 nm). The capacitance estimation can be simplified by introducing a specific capacitance of lipid bilayers, which is around 0.9 μF/cm^2 [201] so the equation can be represented as:

eq 8

$$C = C_{spec} \, x \, A$$

The capacitance read from the square wave is the sum of the three capacitances. The first comes from electrodes and has a value of ~10 pF, the second comes from the Teflon sheet clamped between the chambers and has a value of nearly~ 10 pF that is similar to electrode capacitance and the third comes from the bilayer itself and it is proportional to the aperture size. The capacitance value of the lipid membrane can be estimated by using equation 8.

For example, the bilayer capacitance for apertures with a diameter of 100 µm is expected to be around 70 pF. If background capacitance of electronics and Teflon sheet is taken into account (~20 pF), the total capacitance obtained in experiment would be around 90 pF.

Three experiments with apertures of diameter 80, 100 and 115 µm were used to show that bilayers can be stable for more than one day. In order to determine the capacitance of bilayers, six apertures with different diameters were used (Table 3.2).

Table 3.2. Experimental and theoretical bilayer capacitance over various apertures.

Aperture size (µm)	**Total capacitance**	**Bilayer capacitance**	**Expected from eq. 7**
60	24	4	24
70	35	15	33
80	40	20	45
90	45	25	57
100	60	40	70
115	70	50	94

Formation of bilayers in 60-150 µm apertures was easily achieved, but when the apertures smaller than 50 µm were used for experiments it was complicated to remove the oil from the aperture and to consequently form the bilayer. The capacitance values of smaller apertures (50 µm) were close to ~20 pF, which is the same capacitance of the sum of the ones from the electronics and the clamped Teflon sheet. This might suggest that hexadecane is taking the majority of the aperture. Therefore, using a pre-treatment solution with a lower concentration of hexadecane might be more convenient for smaller apertures. Bilayers suspended in shaped Teflon apertures proved to have comparable stability as in shaped apertures in SU8 previously developed in our lab [204]. Moreover, the apertures in Teflon could be reused many times after experiment since Teflon allows cleaning with aggressive solvents such as chloroform to remove all the lipid/oil and Vaseline residues on the membranes.

3.4 Insertion of alpha hemolysin to the lipid bilayer

Alpha hemolysin (Sigma Aldrich) pore was dissolved in 150 mM KCl, 10 mM HEPES, pH=7.4 to the final concentration of 0.5 mg/mL and stored at -80 ^{0} C prior to experiments. The pore was added to the *cis* chamber after the DPhPC bilayers were formed. The final concentration of protein in the 1.1 mL chamber was 0.1-0.5 µg/mL. It is, ideally, desirable to have only one pore in the bilayer since the insertion of many pores might lead to leaky bilayers and complicate the data analysis. It usually takes 5 to 15 minutes for single pore insertion when 0.5 µg/mL of αHL is added in 1.1 mL 1 M KCl solution in *cis* chamber. Insertion of the pore in the bilayer was detected by applying a voltage of +120 mV (*trans* side positive) across the bilayer. As above mentioned, the bilayer membrane is an insulator and prevents the passage of ions which generate ionic current. However, when αHL inserts in the bilayer, the current suddenly jumps from 0 to 120 pA if 1 M KCl is used (Figure 3.11 a). After single pore insertion, the concentration of αHL was decreased by manual perfusion of the *cis* side solution containing αHL by the fresh recording solution. The current value is proportional to the total number of inserted pores. The pore remains active for long time with occasional, very infrequent and short, closing events (Figure 3.11 b,c).

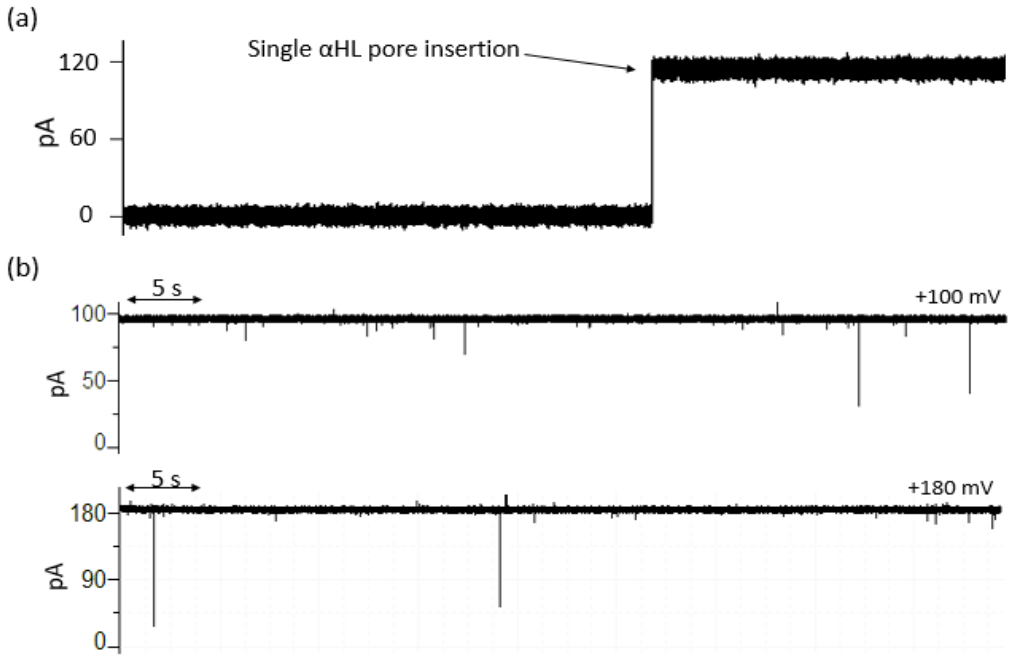

Figure 3.11. (a) Insertion of αHL protein in DPhPC bilayers at 120 mV in 1 M KCl solution. (b) The single αHL current traces in 1 M KCl at +100 and 180 mV

3.4.1 I-V relation of the αHL pore in 1 M KCl solution

The αHL ionic current was obtained for the range of voltages from -200 to +200 mV. The I-V plot was constructed by averaging currents from three independent recordings in 1 M KCl (Figure 3.12 c). The αHL pore has the ability to rectify ionic current in a way that I (+V) ≠ I (-V). Current values at the positive voltage were higher compared to the negative ones when αHL was inserted

in bilayer with its vestibule in *cis* side (Figure 3.12 a,b). The current asymmetry ratio (+V) / I (-V) was found at 1.6 and 1.4 for ±100 and ±120 mV respectively, which is consistent with previous work with αHL pore [155]. The αHL current rectification was subject of various theoretical and experimental works, where it was revealed that charged amino acids at the *trans* entrance of the pore are responsible for this feature [145, 153-155].

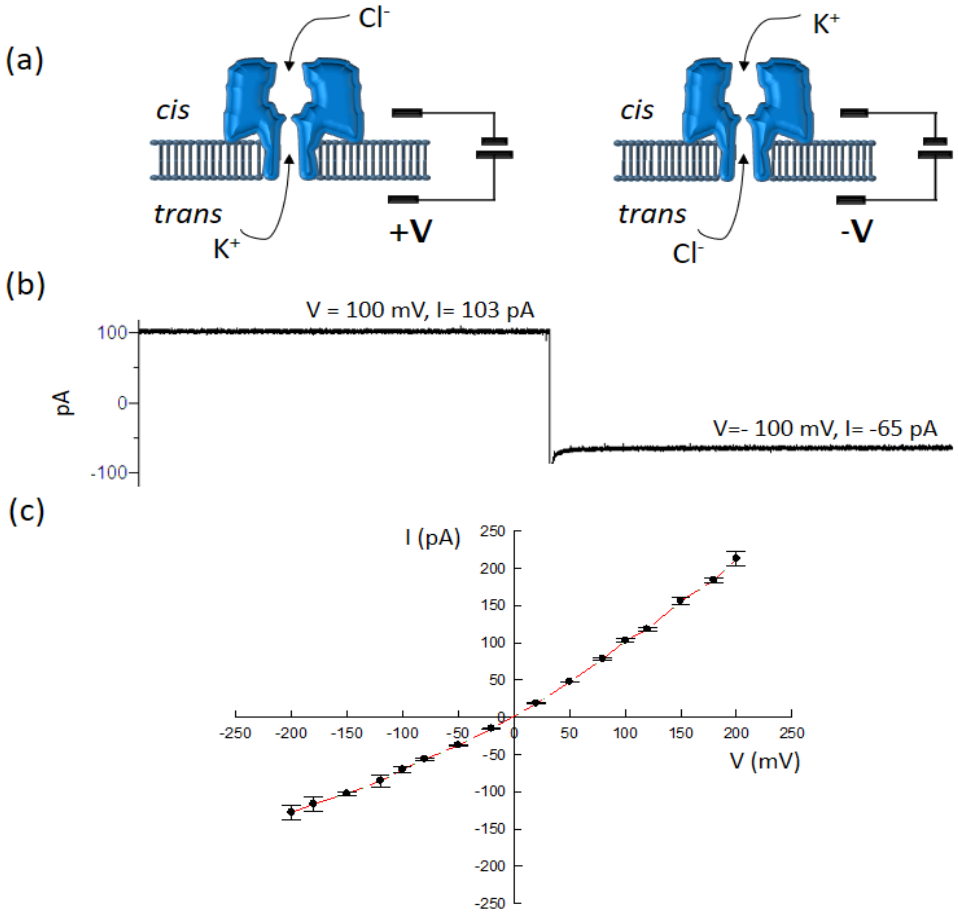

Figure 3.12. (a) Ionic current through αHL pore in KCl electrolyte. The current at positive voltage arises from the I (K^+) in *trans* to cis direction *trans* and I (Cl^-) in *cis* to *trans* compartment. (b) Current rectification of αHL channel I(+100 mV) ≠ I(-100 mV) (c) I-V plot for αHL in 1 M KCl, 10 mM Tris, 1mM EDTA, pH = 8. Current at positive voltage is higher than the absolute value of currents at negative voltage.

3.5 Noise in setup

The insulating lipid membrane is the core of the biological nanopore measurement system. The majority of biological nanopore research uses aperture-suspended lipid bilayer in which conductive biological pore is reconstituted. One of the main challenges in nanopore technologies and electrophysiology experiments is reducing the noise of the system, which would improve the resolution of the recordings. The disadvantage of using aperture suspended lipid bilayers is the electrical noise that arises mainly from the capacitance of planar lipid bilayer. There are three main sources of the current noise in planar lipid bilayers that can be characterized by the noise spectral density S^2 (A^2 Hz^{-1}) or the noise variance i (A^2) [195, 196]. The first source of noise

comes as a result of the interaction of headstage input voltage noise and the total input capacitance [195, 196]. Its spectral density (S_{VC}^2) and current variation (i_{vc}^2) are given by:

eq 9

$$S_{VC}^2 = 4e_n^2\,\pi^2 C_t^2 f^2$$

eq 10

$$i_{vc}^2 = e_n^2 \pi^2 C_t^2 B^3$$

Where e_n is the root mean square noise voltage in the headstage input, C_t is the total capacitance (sum of the capacitance that comes from the electrodes, capacitance of the clamped septum material and the membrane capacitance C_m). Finally, B presents the bandwidth of the recording.

Another source of current noise arises when the thermal voltage noise in access resistance is clamped across the membrane capacitance (C_m) [195, 196]. Its spectral density (S_{rc}^2) and noise variance (i_{rc}^2) are given by:

eq 11

$$S_{rc}^2 = 4kT\,\frac{4\pi^2 f^2 R_a^2 C_m^2}{R_a(1 + 4\pi^2 f^2 R_a^2 C_m^2)}$$

eq 12

$$i_{rc}^2 = \frac{4kt}{R_a}\left(B - \frac{\arctan(2\pi R_a C_m B)}{(2\pi R_a C_m)}\right)$$

Where k is the Boltzmann constant, T is the absolute temperature on the Kelvin scale (K), R_a is the access resistance and the B is the bandwidth of the recording (Hz).

Another important contributor to current noise in the bilayer measurements comes from the dielectric noise as a result of the thermal fluctuations in lossy dielectric materials with a capacitance C_t. Therefore it is dependent on the type of material in which the aperture is punctured. Its spectral density (S_d^2) and noise variation (i_d^2) are given by:

eq 13

$$S_d^2 = 8kt\pi D C_t f$$

eq 14

$$i_d^2 = 4kT\pi D C_t B^2$$

Where *k* is the Boltzmann constant, *T* is the temperature on the Kelvin scale and the *D* is the dielectric constant of septum material.

It can be seen that the three noise sources characterised in equations 9-14 strongly depend on the bandwidth of the recordings and the membrane capacitance (C_m) that obviously increases with the size of the aperture in which lipids are suspended.

Other sources of noise in planar lipid bilayer such are shot noise, Johnson noise and 1/f noise do not contribute to overall noise as much as the three noise sources characterised by equations 9-14 [196]. In their work Mayer *et al*. grouped these noise sources into an excess noise (i_e) [196]. The most noise sources in electrophysiology measurements (such is nanopore sensing) are uncorrelated meaning that the total background noise can be obtained by the root mean square (RMS) fashion.

eq 15

$$i_{tot} = \sqrt{i_{vc}^2 + i_{rc}^2 + i_d^2 + i_e^2}$$

The RMS current noise is the deviation of current from its mean value and can be obtained experimentally by the current trace analysis in Clampfit software.

In this work, RMS noise is compared for different bandwidths (1 – 10 kHz) for an 80 µm aperture, that was usually used for experiments.

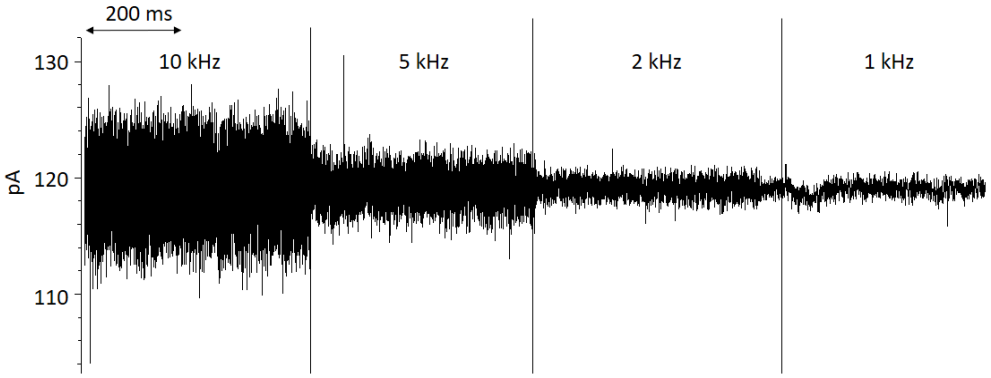

Figure 3.13. Current trace of single αHL in DPhPC bilayer at 120 mV at various filter values.

Table 3.3 shows how that noise is gradually increasing while adding more items to the system. Noise is increasing with the bandwidth, so at 10 kHz it is about four times larger than at 1 kHz in case of αHL pore in bilayers.

The RMS noise obtained in 1 M KCl at 120 mV when one αHL pore was presented in the bilayer at 10 kHz bandwidth was 2.2 pA, which can be considered as a substantial noise for the single channel recordings. Fortunately, the conductance of αHL pore in symmetrical 1 m KCl and is ~1

nS (~100pA at 100 mV) hence the noise level of 2.2 pA does not hinder the channel conductance. Moreover, the analytes studied in this work (RNA-DNA and DNA-DNA duplexes) were shown to induce the resistive with a residual amplitude of I/I_0 of ~ 0.1 (for example current drops from 100 pA to 10 pA when duplex enters the pore and starts to unzip) [13]. Therefore, the interaction of the duplexes with αHL pore is not expected to be obscured by the noise in the measurement system used for this work.

Table 3.3. Noise values at different bandwidths

RMS noise (pA)			
Bandwidth (kHz)	**Headstage only**	**Bilayer**	**αHL in bilayer**
1	0.195 ± 0.015	0.22 ± 0.01	0.51 ± 0.07
2	0.28 ± 0.014	0.34 ± 0.011	0.67 ± 0.03
5	0.49 ± 0.01	0.75 ± 0.015	1.18 ± 0.03
10	0.86 ± 0.02	1.78 ± 0.03	2.22 ±0.04

3.6 Single molecule spectrometry

An experiment similar to those of Robertson and Baaken was performed in order to test the capacity of the setup to discriminate between small current changes produced by the polyethylene glycol (PEG) polymers [169, 170]. The DPhPC bilayers were formed as described in section 3.3. The electrolyte solution was 4 M KCl, 10mM HEPES, pH=7.4. The polydisperse PEG 1000 (Fluka) was used in the experiment. Prior to the experiment PEG 1000 was dissolved in 4 M KCl,10 mM HEPES, pH=7.4 to a final concentration of 10 mg/mL. The αHL pore was added in the cis chamber in the vicinity of the bilayer with a final concentration of 0.5 µg/mL. After αHL insertion, the PEG 1000 was presented to the *trans* side of the bilayers, with a final concentration of 0.5 mg/mL. The applied voltage was 30 mV (*trans* side positive). A representative αHL current trace in presence of 0.5 mg/mL of PEG 1000 is shown in Figure 3.14

Figure 3.14. Singe channel current trace in the presence of 0.5 mg/mL PEG 1000 in 4 M KCl solution at +30 mV.

Events were processed by Clampfit 10.2 software using a threshold method, with respect to their dwell time and current amplitude. Events shorter than 0.5 ms were excluded and 7155 events were detected in the one minute of current trace. Baseline (I_0) current was obtained with the Gaussian fit of the open pore current segment. The ratio I/I_0 was calculated for each event in order to compare the results with the previous works of Baaken and Robertson, where peaks for 28 and 29 PEG monomers were found at 0.26 and 0.25 I/I_0 respectively [169, 170]. This implies that the two PEGs are separated by 0.01 I/I_0 value. From Figure 3.15a it is clear that the resolution between polymers in PEG 1000 is not as high as for the PEG 1500 polydisperse powder used in [169, 170]. The resolution was improved when the cut off filter was set to 1 ms, and PEG blockages shorter than 1 ms were excluded (Figure 3.15 b). The distributions of PEG 1000 events with 0.5 ms and 1 ms cut off filter were fitted with Gaussian function. The peak of I/I_0 of the 0.5 ms PEG 1000 distribution was found at 0.34 while the peak of 1 ms cut –off distribution was found at 0.31. When compared to results of Bakeen and Robertson those peaks would correspond to PEG of 22 r.u and PEG of 24 r.u, with molecular weights of 986 and 1074 g/mol.

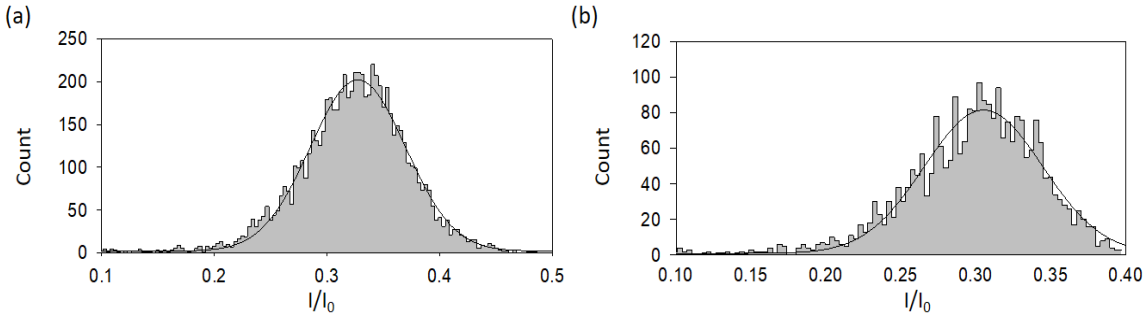

Figure 3.15. Amplitude distribution of 0.5 mg/mL PEG 1000 in 4 M KCl solution at +30 mV for (a) 0.5 ms cut-off time and (b) 1 ms cut-off.

This result implies that by increasing the cut off time, the I/I_0 value shifts to bigger PEG polymers. Therefore, to detect polymers with higher molecular weight, the cut-off time needs to be longer. For example, when the cut-off filter was increased to 2 ms, only 725 events were detected but the resolution between neighbouring peaks increased significantly (Figure 3.16).

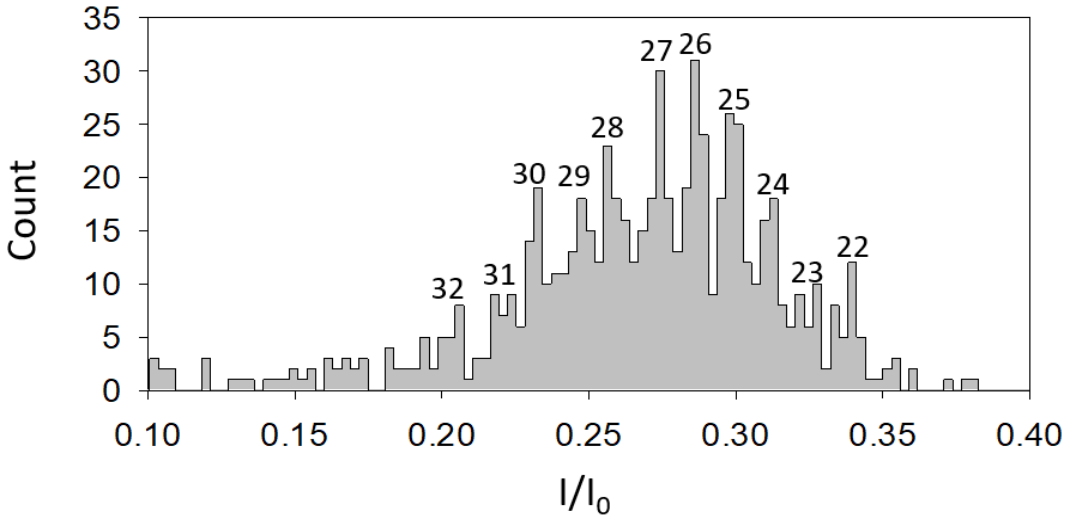

Figure 3.16. I/I_0 distribution of 0.5 mg/mL PEG 1000 event amplitudes in 4 M KCl at +30 mV PEG for a 2 ms cut off time.

It can be seen that the peak for 29 monomeric PEG is almost on 0.25, which is consisted with results shown in [169]. Neighbouring peaks can be used to evaluate other PEGs in solution. This encouraging result shows that the lab equipment can be used for detecting small current changes produced by PEG polymers. However, PEG 1000 might not be convenient for this experiment since there were too many short events that can obscure the resolution of the experiment. The previously reported resolution spectra of PEG molecules with wild type αHL pore was from 24-48 repeating units [169, 170]. For the PEG 1000 used in this work, only small fraction of polymers with the desired number of repeating units were presented in the sample. The average molecular weight of PEG 1000 corresponds to PEGs with 23 repeating units, that is just below the resolution with αHL pore. When events shorter than 2 ms were excluded, resolution improved significantly and PEG monomers could be separated clearly, even if the number of events was reduced.

3.7 Discrimination of RNA homopolymers with αHL pore

Unlike PEG molecules, which are neutral polymers, DNA/RNA molecules are negatively charged and can be electrophoretically driven through the nanopore. In order to show that the laboratory set up is able to discriminate between various RNA homopolymers, POLY A, C and U were purchased from Sigma Aldrich (UK). The homopolymers were dissolved in 10 mM Tris, 1mM EDTA, pH=8 buffer solution to the final concentration of 2 mg/mL. The DPhPC bilayers were formed by folding technique as described in section 3.3. The bilayer chambers were filled with 1 M KCl, 10 mM Tris, 1 mM EDTA, pH=8. After bilayer formation, αHL protein was added in the grounded *cis* chamber (final concentration 0.1-0.5 µg/mL). The homopolymers poly A, poly C and poly U were added to the *cis* chamber to a final concentration of 100 µg/mL. The transmembrane current was set to 120 mV (*trans* side positive).

3.7.1 Voltage-dependent poly A interactions with αHL pore

The transmembrane voltage plays an important role in the interaction between negatively charged DNA/RNA macromolecules with the pore. To show the voltage dependence on RNA-αHL interactions, negatively charged poly A was dispersed in the *cis* chamber after single αHL inserted in the bilayer. The RNA strand was pulled with electrophoretic force by applying the positive voltage from the *trans* side of bilayer. Interaction of poly A with αHL pore was strongly depended on voltage. At 60 mV, only short interactions without poly A translocations were observed (Figure 3.17). The number of short interactions of poly A with αHL increased at 80 mV, but few translocations could be highlighted. At higher voltages (120 and 140 mV) the number of interactions increased drastically (Figure 3.17)

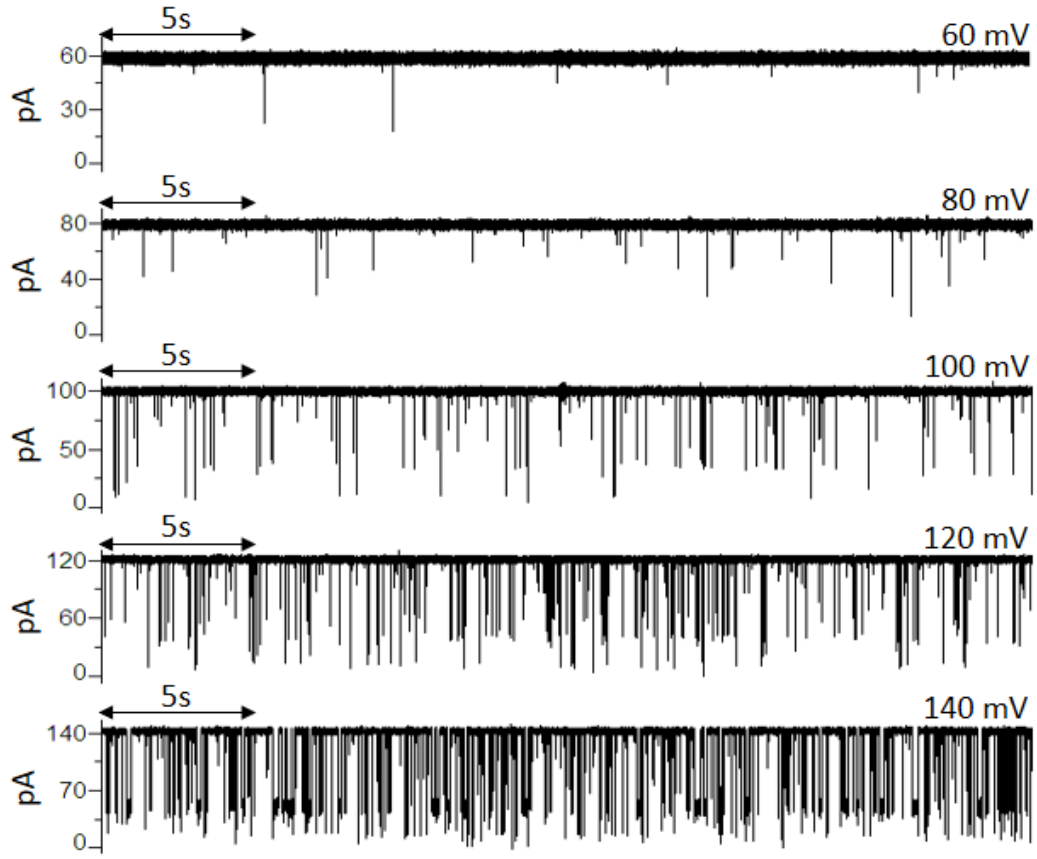

Figure 3.17. Single αHL channel traces in presence of 100 µg/mL of poly A at various voltages. The recording electrolyte was 1 M KCl, 10 mM Tris, 1 mM EDTA, pH = 8.

3.7.2 Poly A blockage events

The poly A was shown to produce two specific blockages upon interacting with αHL pore. The first was associated with longer vestibule blockages with the I/I_0 =0.43 [127]. The second type of blockage was associated with poly A translocation through the pore and had I/I_0 = 0.17 [127]. The most interesting poly A blockages consisted of both type I and type II blockages, where poly A was suspected to first partially block the αHL pore and then finally translocate through the β barrel

of the αHL channel. In this work, the blockages produced with poly A were in agreement with the previous work. The representative single-channel αHL current trace in presence of 100 µg/mL poly A at 120 mV is shown in Figure 3.18 a.

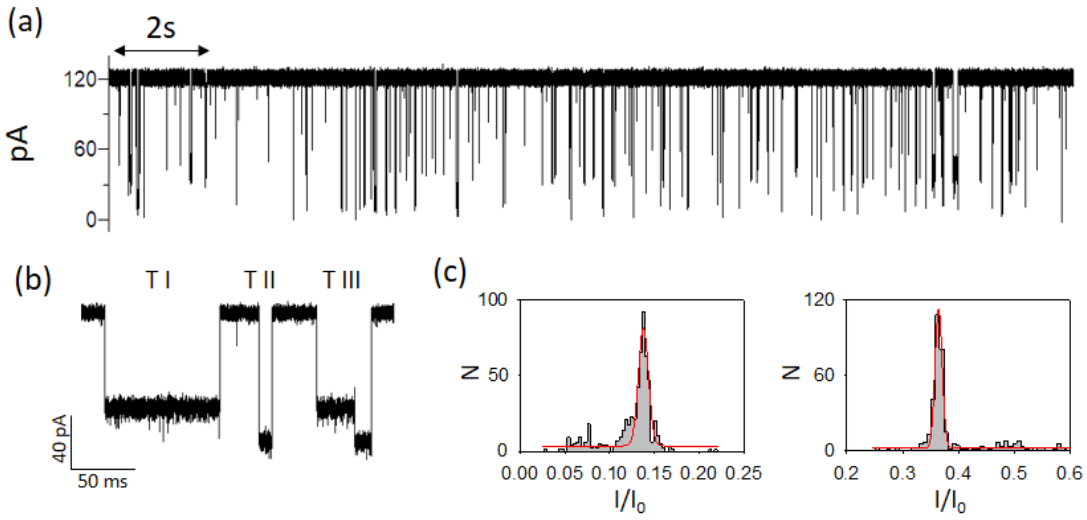

Figure 3.18. (a) Representative αHL current trace in presence of 100 µm/mL poly A. Recording solution was 1 M KCl, 10 mM Tris , 1 mM EDTA, pH = 8.(b) The three types of blockages (T I-III) produced by poly A. T I only partially blocks αHL pore, T II presents translocation of poly A through αHL pore. T III consists of type I and type II blocks where poly A extends and translocates through the pore (c). The histogram of type II blockage level (left) and type I blockage level (right). The values of I/I_0 for type I and type were found at 0.36 and 0.15 respectively. The red line presents Gaussian fit to the data.

Two well-defined blocking levels could be separated from the histogram data. The residual amplitudes for type I and type II were found at 0.36 and 0.15, that is in close agreement with 0.43 and 0.17 observed in Akeson *et al.*[127]. The average duration of type II blocking events that are associated to the poly A translocation through αHL pore was calculated from 559 blockage events with the mean value of 5.4 ± 0.05 ms.

3.7.3 Poly C blockage events

In this experiment, the poly C homopolymers were dispersed in the grounded bilayer *cis* chamber to the final concentration of 100 µg/mL. The recording solution was symmetrical 1M KCl with 10 mM Tris, 1 mM EDTA. The pore current was recorded at +120 mV (*trans* side positive).

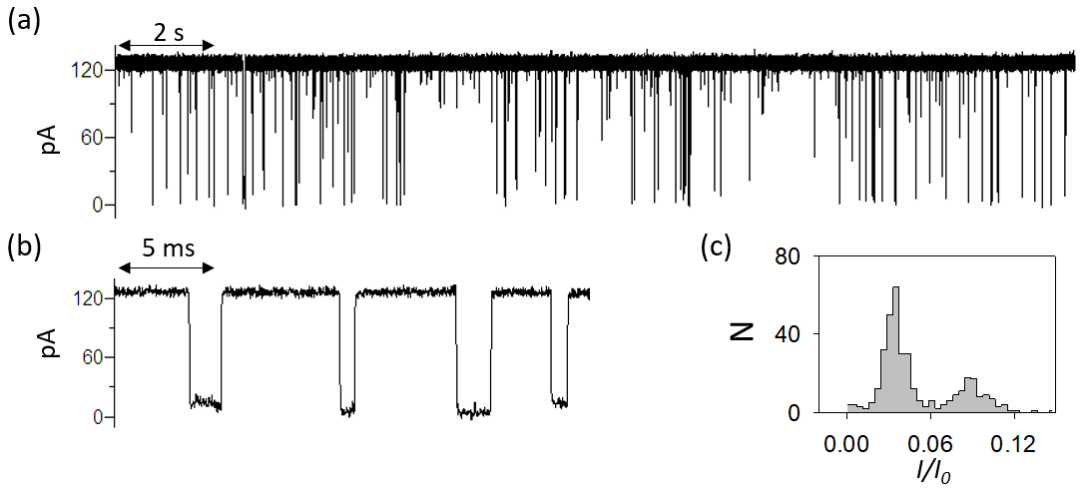

Figure 3.19. A) Single-channel current trace in presence of 100 µg/mL poly C in 1 M KCl, 10 mM Tris, 1 mM EDTA, pH = 8. The pore current was recorded at +120 mV (*cis* side grounded). (b) The αHL resistive pulses produced by poly C homopolymers. c) The amplitude histogram of poly C resistive pulses. The bimodal residual amplitude distribution was observed where the deeper blockage was found at I/I_0 = 0.035, while shallower blockage was found at I/I_0 = 0.09.

From the histogram of poly C amplitude events there are two well distinguished I/I_0 current block levels observed. The deeper I/I_0 was found at 0.035, while shallower was found at 0.09 I/I_0. Moreover, the number of events under deeper amplitude was ~3 times higher compared to a number of events under shallower amplitude. The bimodal amplitude of poly C analyte was in agreement with results from Akeson *et al.*, where the observed levels were 0.05 and 0.09 [127]. The bimodal amplitude of the poly C block originates from the entering of the homopolymers either from 3' or 5' end in the αHL channel [205]. The poly C blockages are lacking the partial block level of αHL pore observed for poly A homopolymers. The reason for this might be related to the diameter of poly C, estimated to ~1.3 nm, smaller than the 1.4 nm of αHL constriction. Therefore, the coil doesn't need to unwind in order to pass through the pore, unlike 2.2 nm poly A coil [127]. Mean dwell time for poly C was calculated from 383 translocation events and was found to be 1.1 ms that is about 3 times shorter than for poly A translocation.

3.7.4 Poly U blockage events

Finally, the last experiment with homopolymers was done with poly U. The concentration of poly U was 100 µg/mL. The recording solution was symmetrical 1 M KCl,10 mM Tris, 1 mM EDTA, pH=8.

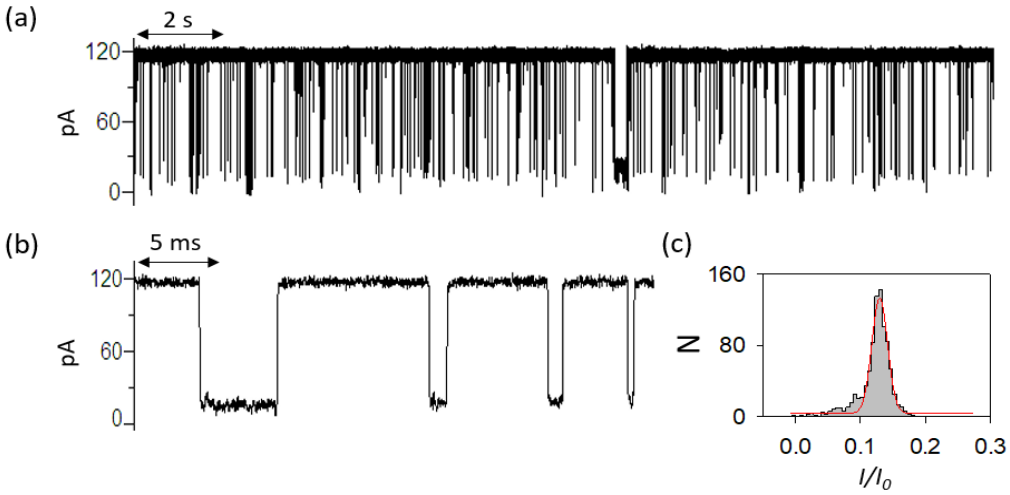

Figure 3.20. (a) Single-channel current trace recorded in 1 M KCl, 10 mM Tris, 1 mM EDTA, pH=8 at +120 mV in the presence of 100 µg/mL Poly U. (b) The representative poly U current blockages. (c) The amplitude histogram of poly U blockages. The mean I/I_0 value was found at 0.12. The red line presents the Gaussian fit to data.

The current block level of the poly U block was found at I/I_0 = 0.12. This value is similar to type II amplitude of block found for poly A, which is again in agreement with previous observations, where the current block level of poly U block was found at ~0.15 I/I_0 [126, 127]. Because of the similar block amplitude, these two polymers would be hardly distinguished if their mixture was present in the same sample. However, mean translocation time calculated from 830 poly U transitions was 1.2 ms, which is shorter than poly A and slightly longer than poly C blocking events.

3.8 Summary

This chapter described the electrophysiological instrumentation used for the nanopore recordings in our lab. The newly fabricated Teflon apertures proved to support the lipid bilayer for hours in 1 M KCl solution, which is a conventional electrolyte for nanopore experiments. The αHL used in experiments showed very infrequent short closing and opening activities without the presence of the analytes in solution. The experiment with PEG 1000 demonstrated that our set up can separate between PEGs that differ in only one repeating unit or 44 g/mol based on their current amplitude. This experiment also confirmed that αHL and bilayers are stable in high salt (4 M KCl) conditions, which is important for later experiments, having salt gradients across the αHL pore.

Furthermore, the laboratory equipment was tested in experiments with single-stranded poly A, poly C and poly U homopolymers (described in section 3.7). It was possible to reproduce the results published in previous works where the resistive pulses of the individual homopolymers were distinguished based on their specific current signatures and their dwell times. For the poly C RNA homopolymers, it was possible to distinguish between 5' and 3' entries of the poly C inside the αHL channel.

In this work, the target analytes for the αHL nanopore detection were miRNA-DNA duplexes. As previously reported in the literature, these molecules are suspected to produce longer αHL current blockages (0.2 s – 1s) with a residual amplitude of I/I_0 = 0.1 (considering applied voltage of ~100 mV and 1 M KCl electrolyte as experimental conditions) [13, 16]. Being the bilayers formed in the novel laser-cut Teflon apertures stable for several hours, they were suitable for the nanopore recordings and duplex detection. The RMS current noise of ~2 pA (at 10 kHz bandwidth) is not expected to influence the detection of duplex resistive pulses, since the αHL current drops to 10 % of the initial open pore value when the duplex is captured by the nanopore. Considering that the open pore current is ~100 pA (at 100 mV in 1 M KCl), then the current decreases for 90 pA upon duplex translocation through the αHL pore. Such value is 45 times higher than the RMS noise observed in the experimental nanopore electrical recording equipment used in this work. These observations suggest that the experimental set up is suitable for the detection and analysis of miRNA-DNA duplexes.

The next chapter will explore and discuss the nanopore sensing of DNA/DNA and RNA/DNA duplexes comprised of miDNA155, miRNA155 and miDNA21 sequences hybridized with their complementary probes in symmetrical 1 M KCl solution. The laser-ablated Teflon apertures will be used in all experiments for bilayer formation. The nanopore currents will be recorded at 50 kHz sampling rate and filtered with 10 kHz low pass Bessel filter.

Chapter 4: Duplex nanopore sensing in symmetrical electrolyte

In this chapter, detection of two cancer-related miRNAs was performed under symmetrical electrolyte conditions. miRNA detection with αHL nanopore is based on hybridization with the corresponding DNA probe. It was shown that miRNA-DNA probes produced a significantly longer resistive pulse upon interaction with an αHL pore compared to single-stranded miRNA or DNA probes alone. Moreover, the current resistive pulse was found to have a specific multilevel signature, which is more suitable for the discrimination from other nanopore current blocks. The majority of the existing research on miRNA sensing with nanopores was performed under symmetrical 1 M KCl conditions at voltages in the range of 100-180 mV. This chapter describes the detection and quantification of cancer-related miRNAs and their miDNA counterparts in symmetrical electrolytes, especially using symmetrical 1 M KCl solution. The dependence of dwell time and capture rate of miDNA155-P155, miDNA21-P21 and miRNA155-P155 on voltage will be discussed as well. Following this, it will be shown how the design of the DNA probe extension influences the current block and the capture rate of miRNA155. The chapter will also compare the difference between miRNA-P155 and miDNA155-P155 duplexes. The influence of electrolyte composition on miDNA155-P155 resistive pulses will be further investigated.

4.1 Preparation of DNA and miRNA oligonucleotides for nanopore experiments

The miRNA sequences with their corresponding DNA probes were purchased from Sigma Aldrich (Table 4.1, Figure 4.1). For the practical reasons, the majority of experiments were performed with miDNA 155 and miDNA 21 (DNA equivalents of miRNA155 and miRNA21) since the DNA is more stable than RNA molecule. The oligonucleotides were obtained PAGE purified in dried form. The stock solutions were made by re-suspending oligonucleotides in TE buffer (10 mM Tris, 1mM EDTA, pH=8, Sigma Aldrich) to a final concentration of 100 µM. For the hybridization miDNA, miRNA and their corresponding probes were mixed so the concentration of the DNA probes was two times higher compared to miDNA/miRNA concentrations. This was to ensure that most of the miRNA sequences would bind to their complementary DNA probe. For example, 8 µL of 100 µM P155 was mixed with 4 µl of 100 µm miDNA155 and 188 µL of hybridization buffer (50 mM KCl, 10 mM Tris, 1 mM EDTA, pH=8). The solution was gently mixed for ~5 s and heated at 90° C for 5 minutes. After that, the heater

was turned off and the oligo mixture was left to cool down to room temperature, a process that took an average around half an hour. After hybridization, the DNA duplex with a final concentration of 2 μM was stored in a fridge at +4 °C. The same procedure was carried out in the control experiments, where only single-stranded oligonucleotides were used individually.

Table 4.1. Oligonucleotide sequences used in the work

DNA/RNA molecule	Sequence
miRNA 155	5'-UUAAUGCUAAUCGUGAUAGGGG-3'
miDNA 155	5'-TTAATGCTAATCGTGATAGGGG-3'
miRNA 21	5'-UAGCUUAUCAGACUGAUGUUGA-3'
miDNA 21	5'-TAGCTTATCAGACTGATGTTGA-3'
P155	5'-$(C)_{30}$ CCCCTATCACGATTAGCATTAA-$(C)_{30}$-3'
$(dC)_{30}$-5'-P155	5'-$(C)_{30}$CCCCTATCACGATTAGCATTAA-3'
P155-3'$(dC)_{30}$	5'-CCCCTATCACGATTAGCATTAA-$(C)_{30}$-3'
P21	5'-$(C)_{30}$ TCAACATCAGTCTGATAA GCTA-$(C)_{30}$-3'

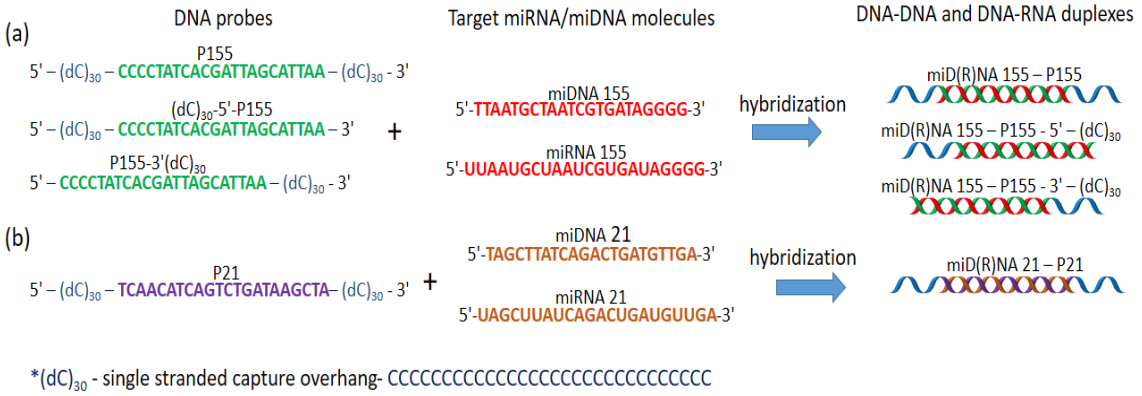

Figure 4.1. The schematic of DNA probes and their target miRNA/miDNA molecules used in this work. (a) DNA probes: P155, dC_{30}-5'-P155 and P155-3'-$(dC)_{30}$ were used to hybridize with their complementary miRNA155/miDNA155 targets (red). Complementary sequence of the DNA 155 probes is coloured in green, while the single-stranded dC_{30} overhang is presented in blue colour. These probes differ by the position of $(dC)_{30}$ capture overhang. P155 has the dC_{30} overhang attached to the both 5' and 3' ends. On the contrary, capture overhang $(dC)_{30}$ was attached to 5'-end of the probe dC_{30}-5'-P155 and to 3'-end of the DNA probe P155-3'-(dC). (b) The sequence of the probe P21 (complementary strand to miDNA21 is coloured in purple) used to hybridise with the target miRNA21 and miDNA21 (orange). The dC_{30} capture overhang was attached to the complementary miRNA sequence at the both 5' and 3' side.

4.2 Nanopore sensing of single-stranded oligonucleotides

For the nanopore sensing of nucleotides, DPhPC bilayers were formed over the Teflon aperture by folding method, as previously described (section 3.3). The recording solution was 1 M KCl, 10 mM Tris, 1 mM EDTA, pH=8. In order to show that the hybridization of miDNA with the corresponding probe is crucial for miRNA detection with the nanopore, experiments with only single-stranded miDNA155 and P155 individually were performed. After formation of the bilayer and αHL reconstitution in the membrane, single-stranded miDNA155 and P155 were dispersed

in the grounded *cis* chamber to a final concentration of 100 nM. The applied voltage was +120 mV (*trans* side positive). Representative current traces are shown in Figure 4.2.

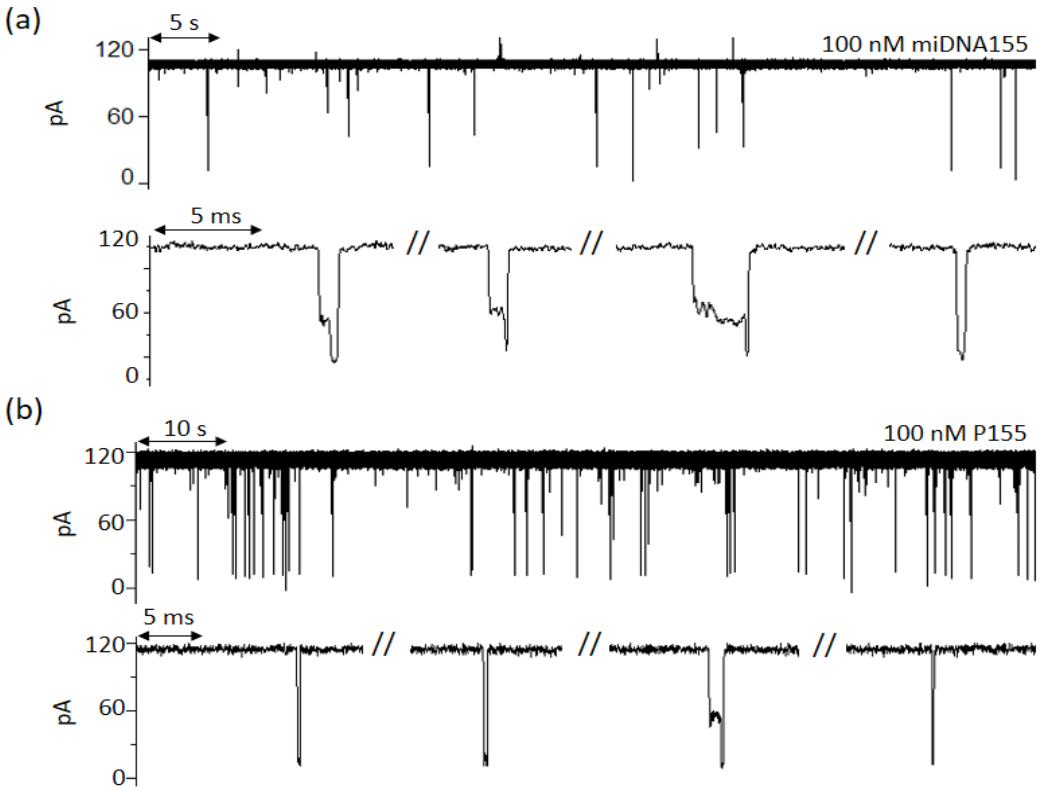

Figure 4.2 (a) Singe αHL current trace at 120 mV in 1 M KCl in the presence of 100 nM miDNA155. The bottom trace shows characteristic short resistive pulses produced the with the single-stranded miDNA155 sequence. (b) Single αHL current trace in the presence of 100 nM P155 recorded at +120 mV in 1 M KCl. The bottom trace shows zoomed in resistive pulses characteristic for P155 at +120 mV.

As expected, the single-stranded miDNA155 and P155 sequences produced resistive pulses with a mean duration of 119 ± 24 μs and residual current amplitude of I/I_0 = 0.105 (Figure 4.3). The duration of shorter miDNA155 was not determined since the number of events was too low to obtain dwell time histogram.

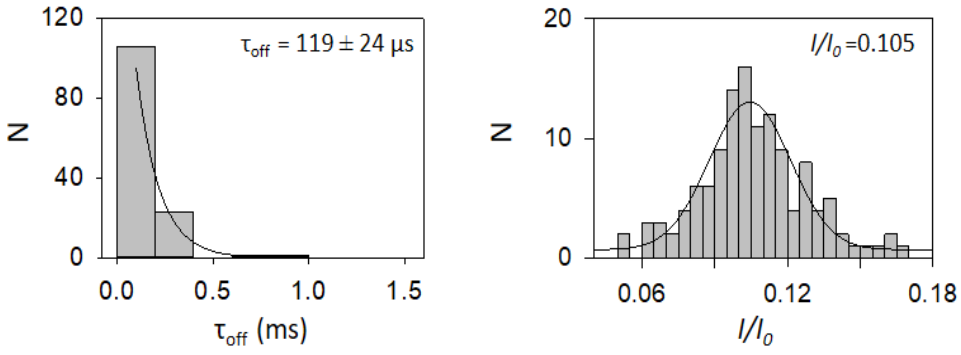

Figure 4.3. Duration and current amplitude of 100 nM P155 in 1 M KCl at 120 mV. The solid lines present exponential fit to dwell time data and Gaussian fit for current amplitude.

4.3 Nanopore sensing of miDNA155-P155 duplex

In order to compare the resistive pulses of miDNA155 and P155 with the resistive pulse produced by miRNA155-P155 duplex, two oligonucleotide sequences miRNA155 and P155 were hybridised as described in 4.1. After bilayer formation and the reconstitution of αHL pore, the miDNA155-P155 duplex was added in the grounded *cis* chamber to a final concentration of 100 nM. The single-channel currents were recorded at holding potentials from 60 - 180 mV Figure 4.4.

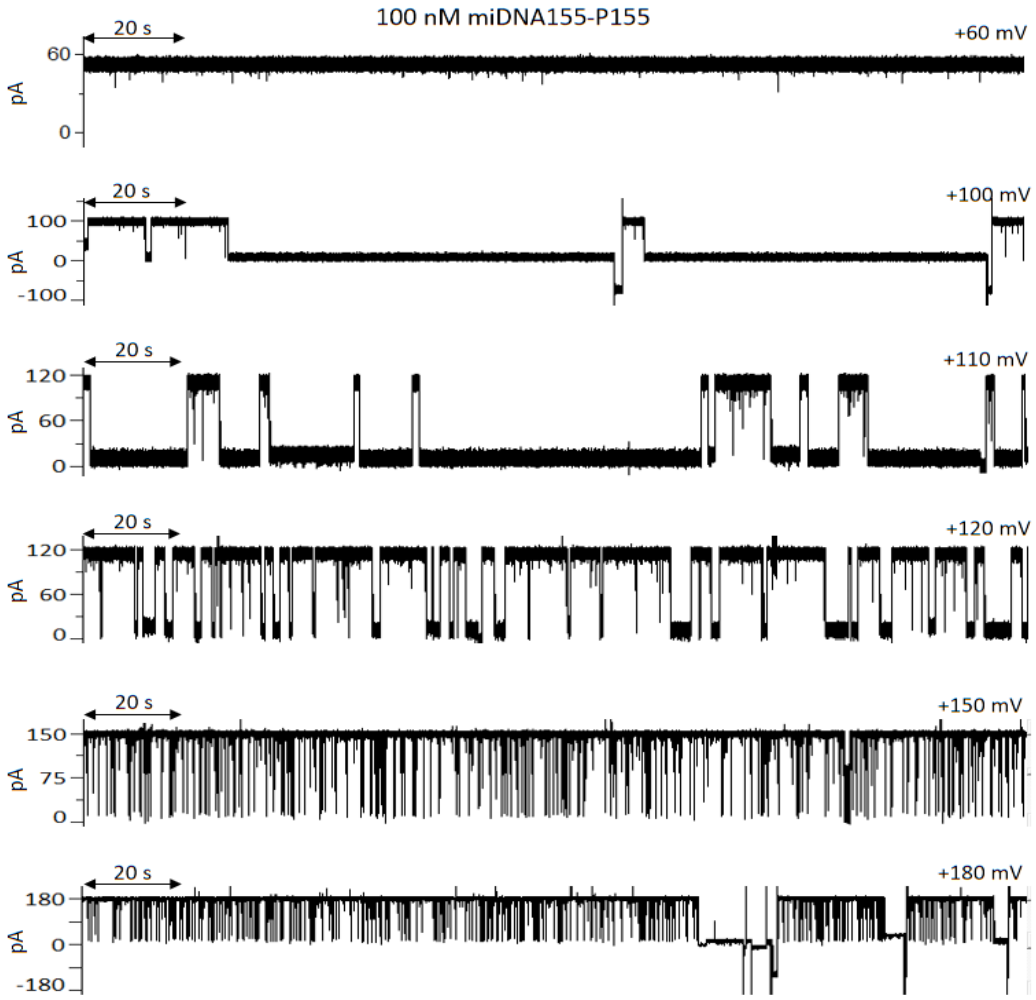

Figure 4.4. Representative single αHL current trace in the presence of 100 nM miDNA155-P155 at different voltages. The number of resistive pulses produced by miDNA155-P155 increased with the voltage. At +60 mV no translocations were observed, meaning that this voltage was not strong enough to pull and unzip the miDNA155-P155 duplex through the pore. At +100 mV the resistive pulses of miDNA155-P155 were too long, and the voltage was reversed to -100 mV to eject the duplex from the pore. At +180 mV nonspecific pore closures were observed, and could be removed by reversing voltage.

As shown in Figure 4.4, the capture of the miDNA155-P155 duplex was heavily dependent on the applied voltage. At 60 mV the pore current was permanently open and resembled the current trace without any presence of an analyte in solution. The minimal voltage required to capture and unzip the duplex was found to be ~ +100 mV, but in those conditions, once miDNA155-P155 was

captured, it unzipped really slowly (>20 s). With further increase of voltage to 120 mV, the duplex started to unzip readily. The number of miDNA155-P155 interactions with the αHL pore increased significantly at higher voltages (150 and 180 mV).

4.3.1 αHL clogging in the presence of the miDNA155-P155 duplex

Once inserted in the lipid bilayer, the αHL pore showed no gating or closed states in symmetrical 1 M KCl conditions at 120 mV. However, upon addition of DNA duplexes in solution, prolonged pore clogging was observed. The pore clogging was more frequent at higher voltages (Figure 4.5) and some of them could be attributed to DNA or RNA molecules stuck in the pore [133, 206]. Hence, the voltage was briefly reversed to a negative value and then set back to the positive value in order to eject the DNA molecule from the αHL pore.

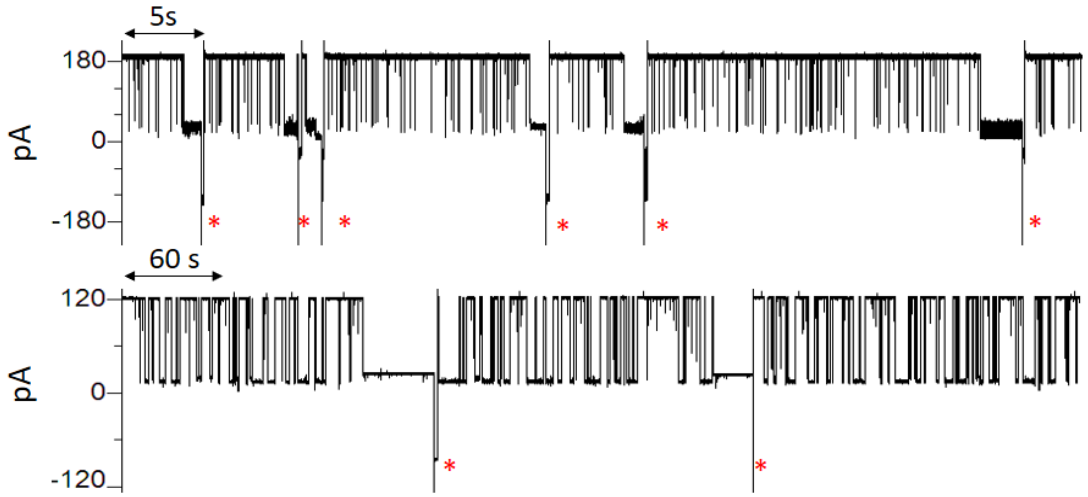

Figure 4.5. Representative current traces for 100 nM miDNA155-P155 duplex in symmetrical 1 M KCl at +180 mV (top trace) and at +120 mV (bottom trace). The red asterisks mark the instants where negative potentials of -180 mV and -120 mV were applied to re-open the pore after a long period of clogging.

These nonspecific pore closures prolong the current recording and complicate the traces analysis with software such as Clampfit 10.2.

4.3.2 Resistive pulse fingerprint of DNA duplex

When compared to single-stranded blocking events of 100 nM miDNA155 and 100 nM P155, their duplex produced significantly longer resistive pulses compared to single-stranded miDNA155 or single-stranded P155 probe in 1 M KCl at 120 mV Figure 4.6

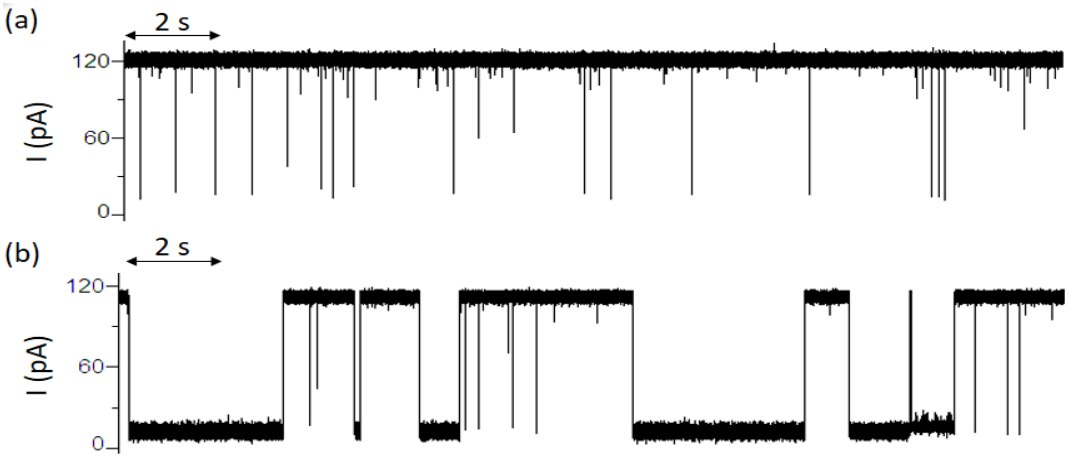

Figure 4.6. The representative single αHL current trace at 120 mv in symmetrical 1 M KCl in the presence of (a) 100 nM P155 and (b) 100 nM miDNA 155-DNA 155 probe duplex.

Previous studies revealed that dsDNA duplex produced not only longer and deeper resistive pulses through the pore but also created specific multilevel current blocks or electric fingerprints upon interaction with αHL pore [13, 16, 17]. Firstly, upon translocation through the nanopore, the DNA duplex produces a characteristic block signature that can be easily distinguished from single-stranded DNA sequence and from other blockages types. Figure 4.7 shows few representative resistive pulse signatures. Level-0 is the open pore current, level-1 with I/I_0 ~0.1 represents capture and unzipping of the DNA duplex. It is followed by level-2, that corresponds to miDNA155 in the vestibule of αHL channel, and has a residual current of I/I_0 = 0.42. Finally, level-3 stands for the translocation of miDNA155 thorough the αHL pore and it is associated with the shortest duration and a residual current of I/I_0 = 0.1. However, not all of the resistive pulses ended with this characteristic multilevel signature. Sometimes, miDNA escapes from the αHL pore immediately after unzipping, so level-2 and 3 cannot be observed. Resistive pulses that consist of level 1 and 2 only correlate to events in which miRNA does not translocate through the pore once unzipped from the DNA probe.

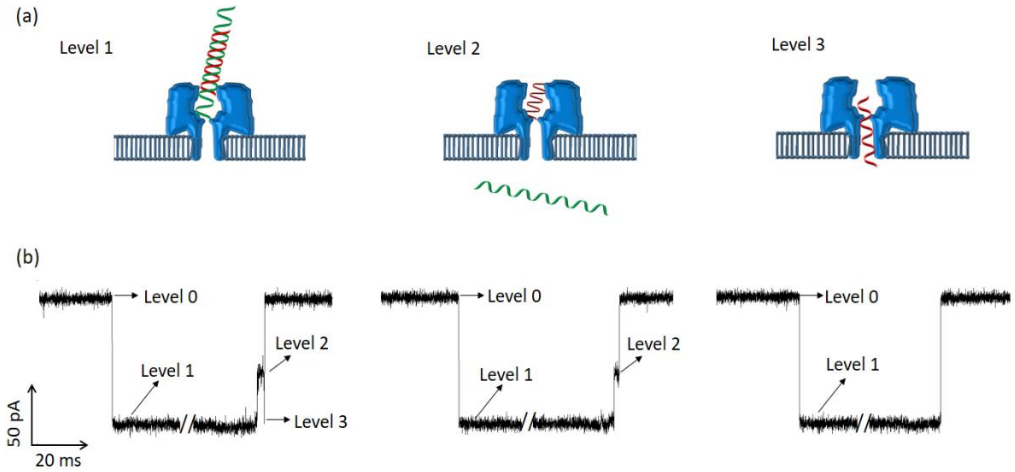

Figure 4.7. Scheme of the multilevel miDNA-DNA probe duplex with αHL pore as proposed by Wang *et al.*[13]. (b) Three types of miDNA155-P155 resistive pulses. The level 0 represents open pore current. The signature event starts with level 1 that is related to the unzipping of miDNA from the DNA probe and has a residual current amplitude of I/I_0=0.1. Level 2 portrays the miDNA155 occupying the vestibule of the pore, with residual current amplitude I/I_0=0.42. Level 3 symbolizes miDNA155 translocation through αHL nanopore. The resistive pulse reported in the middle is missing level 3, which indicates that miDNA escaped from the pore vestibule and returned to the *cis* side. The resistive pulse on the right instead is lacking both level 2 and 3, indicating that the miDNA molecule escaped from αHL pore immediately after being unzipped from the DNA probe.

The signature consisting of all three levels simplifies the identification of miRNA since in real biological samples various molecules can have similar dwell time durations and amplitudes.

4.4 DNA duplex resistive pulse detection and analysis

The blockage events are recognized using Clampfit 10.2 software by setting a baseline (the open pore current I_0) and a threshold level, that the current needs to cross in order to be accepted as an occurrence (Figure 4.8). Abnormally long or short events can be eliminated by setting minimal and maximal duration limits to the automatic detection.

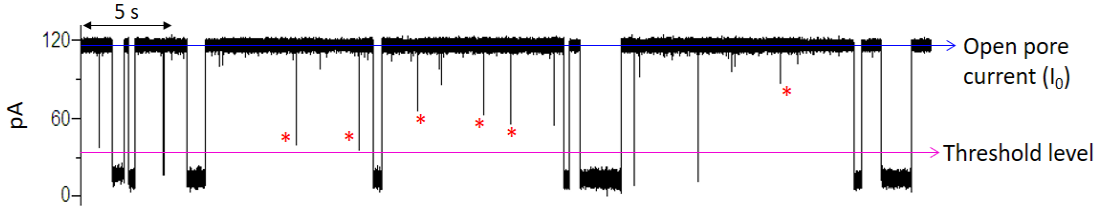

Figure 4.8. The αHL single-channel current in presence of 100 nM miDNA155-P155 duplex. The blue arrow represents the open pore current, while the purple arrow depicts the threshold level set to detect events. The red asterisks mark the pulses that probably correlate to short collisions of the DNA with the pore mouth or to ssP155 translocations.

Since the duration of single-stranded sequences at 120 mV did not exceed 1 ms, the lower cut-off value was set to 1 ms. Hence, events shorter than 1 ms were excluded from the analysis. After the event detection with Clampfit 10.2 software, a results table including data sets for dwell time,

interevent interval and current amplitude of the blocks could be retrieved and analysed. The analysis of the data set parameters is described in next section.

4.4.1 Histogram fitting of dwell time and interevent interval distributions

Data analysis for nanopore resistive pulse sensing is similar to the one for single-channel recording. Opening and closing times are displayed as histograms, having on the ordinate the number of events that fall into each specific range of time (bin) specified on the x-axis. Both dwell time and interevent intervals follow an exponential distribution, and the time constant can be obtained by fitting an exponential probability function to the data [207]. The accuracy of the mean time obtained by fitting will be higher if sufficient data points are used to construct the histogram [208]. The graphs can be obtained in Clampfit software by using linear or logarithmic bin sizes. In conventional histograms, bins are equally separated by a manually-specified value, whereas in logarithmic charts, the histogram bin size is not the same for neighbouring bins [209]. This is convenient in representing wide ranges of values, such are dwell and interevent time data obtained with nanopore sensing.

In order to show how the obtained time constants for dwell and interevent times can vary with the histogram presentation and bins size selection, a set of 361 resistive pulses obtained with 1 M KCl was used to optimize the histogram-fitting procedure. The data of dwell and interevent events were either presented as a linear binned histogram and fitted with exponential probability function, or as a logarithmic binned histogram and fitted with log-transformed exponential probability function. Both of the fitting functions are available in the Clampfit 10.2 software (Molecular Devices).

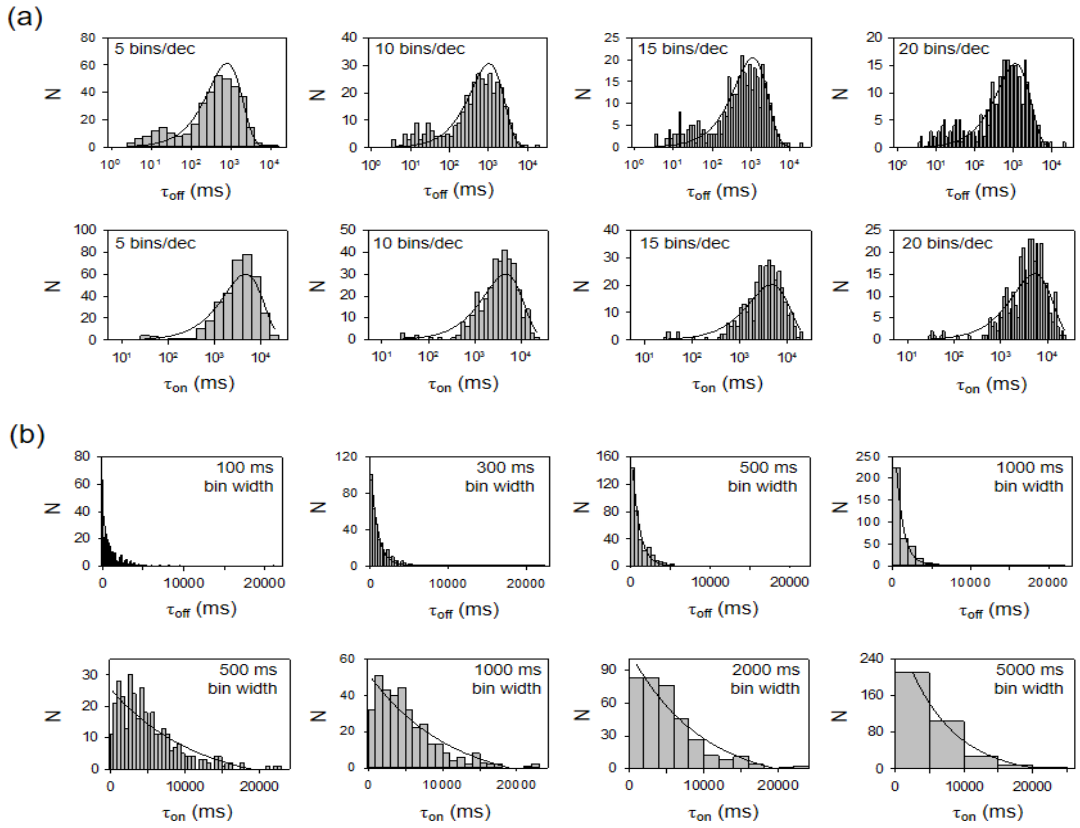

Figure 4.9. 361 dwell time and 357 interevent time events obtained with 100 nM miDNA155-P155 duplex at 120 mV presented as: (a) logarithmic histograms and (b) linear binned histograms with various bin sizes.

The results of the time constants obtained with exponential probability and exponential log probability functions are shown in Table 4.2.

Table 4.2. Comparison of mean interevent and dwell times obtained with fitting log-binned histograms (exponential log probability function) and linear-binned histograms (exponential probability function)

Exponential log probability			**Exponential linear probability**			
Bins per decade	**τ_{on} ± S.E. (ms)**	**τ_{off} ± S.E. (ms)**	**Bin width (ms)**	**τ_{on} ± S.E. (ms)**	**Bin width (ms)**	**τ_{off} ± S.E. (ms)**
5	4669 ± 1050	807± 124	500	11420 ± 3666	100	718 ± 45
10	4671 ± 865	1030 ± 128	1000	11038 ± 3679	300	878 ± 26
15	4748 ± 812	1155 ± 151	2000	9614 ± 2881	500	912 ±32
20	5297 ± 934	1156 ± 141	5000	6920 ± 978	1000	930 ± 51

Mean values were less dependent on the bin size when logarithmic histograms were used instead of linear histograms. Hence, logarithmic histograms were used for the analysis of the dwell and interevent times. The fit function in Clampfit 10.2 software also provides the mean value S.E.

(standard error), which tell us how accurate the estimation of the mean value is. The selected bin size of log-binned histograms was set to 10 bins/decade. Values for dwell and interevent times from multiple experiments were calculated by averaging mean values from the individual experiments, as presented in Table 4.3.

Table 4.3. The dwell and interevent mean times obtained from three different experiments and the capture frequency (f=1/τ_{on}) with αHL in 1 M KCl in the presence of 100 nM DNA 155-P155 at 120 mV.

N	τ_{on} ± S.E. (ms)	τ_{on} ± S.D. (ms)	f_{on} (s^{-1})	f_{on} (s^{-1})	τ_{off} ± S.E. (ms)	τ_{off} ± S.D. (ms)
1	4671 ± 865		0.21		1030 ± 128	
2	4226 ± 591	5167 ± 1264	0.24	0.2 ± 0.044	1044 ± 160	1043 ± 13
3	6603 ± 823		0.15		1056 ± 47	

4.4.2 Influence of number of events on time constant calculation

The previous section showed the influence of histogram and fitting functions on the determination of dwell time and interevent time constants. Since both parameters follow an exponential distribution, the histogram fitting should be done on larger sets of data to obtain more accurate time constants. Fitting the histograms constructed from a low number of events can lead to large errors in dwell time and interevent time estimation. The latter is more important since it is used to calculate the capture frequency associated with the concentration of miRNA. As proposed by Zhang *et al.* in the work on αHL detection of miRNA, about ~200 events are required to secure ~5 % relative error, while 70 events are enough to have a 10 % error [17]. Similarly, Wanunu *et al.* in their work on miRNA detection with SiN nanopore considered that about 250 events would be sufficient to determine the concentration of miRNA with 93 % certainty [17, 190].

In order to determine the influence of the number of events on the accuracy, data sets of 20,50,70,100,150 and 200 events were randomly selected 10 times from 357 interevent events. The associated interevent interval was obtained from histogram fit in Clampfit software 10.2 and the relative error was calculated by using the mean time constant of all 357 events. The procedure can be summarized as follows:

1. Presentation of all events (357) as a logarithmic histogram
2. Fitting with log transformed function
3. Randomization of the events list in Excel and selection of N data points for ten times
4. Fitting of every data set in Clampfit software and extraction of the mean value
5. Calculation the relative error as

$$\sigma = \left|\frac{(\tau_i - \tau)}{\tau}\right|$$

Where τ_i represents the mean value obtained from the randomly selected set of data and t is the mean value obtained with the total number of events. The fitted interevent mean time from the complete set was found to be 4671 ms.

Table 4.4. Mean interevent interval values obtained with various data set size randomly selected from all data points.

N	1	2	3	4	5	6	7	8	9	10	Error
20	3568	5129	7308	5208	6005	4955	2511	7370	5405	3162	**29%**
50	2512	4425	5150	5016	4576	5401	5745	5248	5487	5355	**15%**
70	5232	3857	4829	4347	4871	4818	5456	4946	4999	4829	**8%**
100	5667	4702	4206	4541	4202	5706	5116	4386	5670	5091	**11%**
150	5194	5276	4700	4687	4683	5032	4984	5177	5072	4461	**6%**
200	5436	4619	4743	4724	4918	5009	4677	4926	4527	4615	**4%**
357	4671 ms										

It can be seen that 20 events would yield to results that on average deviate about 30 % from the value obtained with the full data set. The error of the dwell time is decreasing with the number of events. The set of 200 randomly selected events would secure an error that is in average 4 % around the mean value. Around 70 -100 stochastically distributed events are required to have a 10 % error that is in agreement with Zhang *et al*. [17]. This means that the collection of about 70 events in a 100 nM miDNA155-P155 sample at 120 mV, the nanopore experiment should last at least 6.65 min, while the collection of the 200 pulses required for securing a 4 % error would require ~20 min of uninterrupted recording.

4.5 Voltage influence on DNA duplex capture frequency and dwell time

As previously shown, to statistically determine the interevent interval 70-100 stochastically distributed events are required to lower the error to 10 %, and 200 to restrict it to ~5 %. The capture frequency for DNA increased with voltage, that is favourable for nanopore detection of miRNA since increasing capture rate means decreasing the total time required to collect a sufficient number of events for analysis. Previous nanopore studies on miRNA-DNA probe showed linear dependence of capture rate on concentration [13, 17]. To determine the influence of voltage on dwell and interevent time on DNA duplex, the concentration of miDNA155 –P155 duplex was kept constant at 100 nM and the resistive pulses were collected at three different voltages: 120, 150 and 180 mV respectively (Figure 4.10). Dwell time for the miDNA155-P155 duplex at 120 mV was found at 1030 ms and it decreased non linearly to 10.67 ms and 2.4 ms at 150 and 180 mV.

Capture frequency was calculated as $f_{on} = 1/\tau_{on}$ (events s^{-1}), where τ_{on} is the mean interevent time obtained from an exponential fit of log-binned data histogram. At 120 mV in symmetrical 1 M KCl the capture rate of 100 nM miDNA155-P155 duplex was found at 0.2 ± 0.04 s^{-1} and increased to 0.9 ± 0.18 and 1.76 ± 0.04 at 150 and 180 mV respectively. The frequency – voltage plot in Figure 4.11 revealed a linear increase in capture rate with applied voltage, in accordance with what was also observed by Wang *et al.* for miDNA155- P155-3'$(dC)_{30}$ [16].

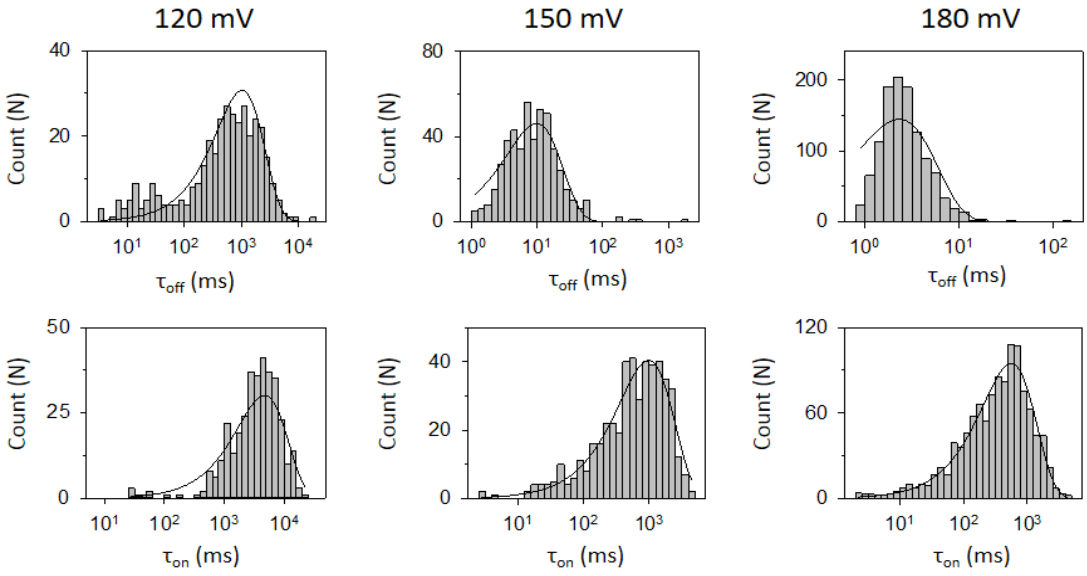

Figure 4.10. Dwell time and interevent time histograms for 100 nM miDNA155-P155 duplex at three different voltages. Solid lines represent the fit with exponential logarithmic probability function in Clampfit 10.2 software.

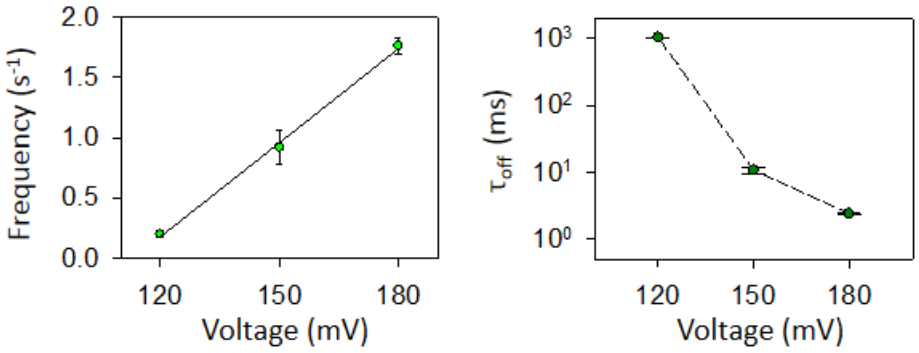

Figure 4.11. The miDNA155-P155 events increase linearly in the potential range from 120 -180 mV (left panel). The level 1 duration reduces significantly with applied voltage (right panel).

4.6 Amplitude and dwell time characterization in symmetrical 1 M KCl conditions

Amplitude of resistive pulses produced by 100 nM miDNA155-P155 was analysed at three different voltages: 120,150 and 180 mV respectively. At 120 mV, the level 1 stage had bimodal I/I_0 residual current amplitude distribution, one deeper at 0.1 I/I_0, and one shallower at 0.12 I/I_0, unlike the single amplitude level 1 reported in Wang *et al*. where the residual amplitude of level 1 was 0.1 I/I_0 [13]. The I/I_0 values of level 2 and level 3 were found at 0.42 and 0.1 I/I_0 which is in agreement with the previous work [13].

The mean duration of level 1 for the miDNA155-P155 duplex at 120 mV was found at 1030 ms, that was more than thousand times longer compared to 0.77 ms long level 2 and 6.5 thousand times longer than level 3 duration which was 0.16 ms (Figure 4.12 and Table 4.5). Hence, the duration of level -1 can be taken with good approximation as a duration of the whole resistive pulse.

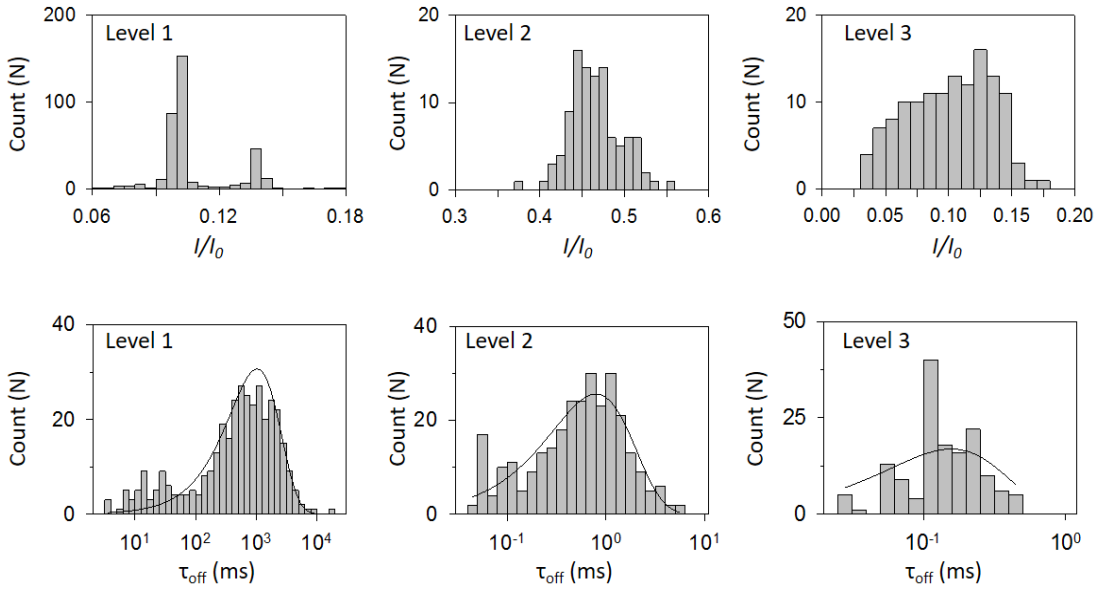

Figure 4.12. Current amplitude and duration histograms for three different block levels produced by the 100 nM miDNA155-P155 duplex at 120 mV.

Table 4.5. Amplitude and dwell time duration of 100 nM miDNA155-P155 duplex resistive pulse signature in 1 M KCl, 10 mM Tris, 1mM EDTA, pH=8 solution at three different voltages. Results in the table are obtained in the single experiment. The duration is reported as a mean ± S.E.

Voltage (mV)	**120**			**150**			**180**		
Level	***1***	***2***	***3***	***1***	***2***	***3***	***1***	***2***	***3***
Residual amplitude (I/I_0)	0.1 0.14	0.42	0.1	0.12 0.14	0.44	0.13	0.15 0.19	0.39	0.14
Duration (ms)	1030±128	0.77±0.2	0.16±0.1	10.6±1.5	0.9±0.3	0.11±0.05	2.4±0.8	0.98±0.13	0.1±0.05

The dwell time of level- 1 was the most affected by voltage; in this level, a sharp and nonlinear decrease was observed. Level- 2 and level- 3 were less dependent on voltage increase. It is interesting that level 2, that represents miDNA occluding the vestibule of αHL channel, is slightly increasing with voltage. At 180 mV, level-1 is about two times longer compared to level 2. The short duration of level- 1 at 180 mV also makes the detection and quantification of miDNA hard, since the duration of 2.4 ms is close to the 1 ms exclusion criterion used to eliminate the single-stranded polynucleotide interactions with the pore and any other short unspecified nucleotide-pore interactions.

4.7 Analysis of level 1 miDNA155-P155 amplitude under symmetrical 1 M KCl conditions

The miDNA155-P155 level–1 events were found to cluster around two distinct residual I/I_0 current amplitudes. Since the miDNA155-P155 duplex can enter and unzip into the αHL channel with two possible orientations (5'-first or 3'-first), the bimodal peak was considered to originate from the entrance of the P155 probe from either 5' end or 3' end first inside the αHL pore. The shallower amplitude was speculated to come from the entrance of P155 with its dC_{30} overhang from 5' end, while the deeper amplitude was attributed to the entry of dC_{30} overhang from 3'-end of the P155. This amplitude assignment was based on previous work on miRNA155-P155 detection by Wang *et. al*, where it was observed a 20 times higher capture rate of the duplex with the probe extended with dC_{30} from the 3' end compared to the capture rate of duplex with the probe extended with dC_{30} from the 5' end [13]. From the current amplitude histogram of the resistive pulses collected in this work, the number of events under deeper amplitude was found ~3 times higher than the number of events under shallower amplitude; therefore we assessed that the larger population of events, clustered around the deeper amplitude block, might represent the 3'-entries of the duplex.

The bimodal amplitude block was also observed with dA_{50} and rC_{50} homopolymers, and even in this cases, it was assigned to the orientation from which the probes entered the pore (5' or the 3') [132, 134, 210]. These works revealed that the deeper amplitude comes from a 3'-first entry, while the shallower amplitude comes from 5'-first entry. The number of rC_{50} events assigned to 3'-entry was 2 times higher than 5' first [205]. Moreover the duration for dA_{50} translocations associated with 3' first was 2 times shorter compared to 5' –end first translocations. The higher capture rate and shorter dwell time of 3'- first translocation were attributed to a geometrical effect since the nucleotide bases were founded to be tilted towards 5' end with respect to the phosphate backbone upon translocation through the αHL channel pore [132, 134]. Hence when the polymer is translocating with the forward 5' directions, the bases are tilted in a way which gives an additional mechanical friction compared to translocation of the polymer with the forward 3' direction [134].

Based on these observations, the bimodal amplitude of level-1 was analysed for three different experiments with the miDNA155-P155 probe. The amplitude, duration and number of events assigned to 5' and 3' entries is given in (Figure 4.13 and Table 4.6). Consecutive experiments with miRNA155 and P155 probe modified with single capture dC_{30} overhangs either on 5' or 3' will confirm that this assignment was correct.

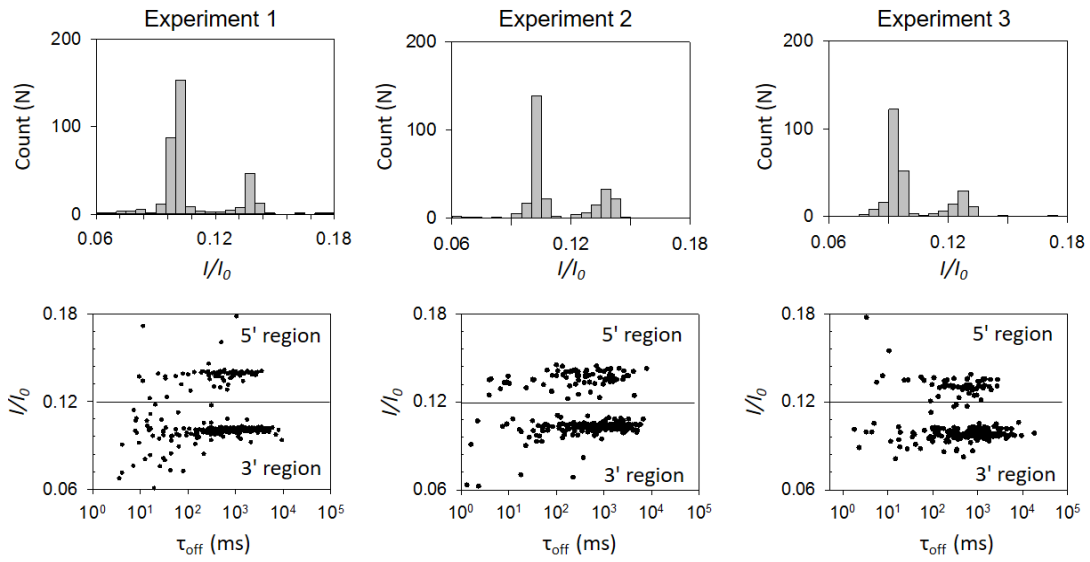

Figure 4.13. Level 1 current block level and dwell time durations for 100 nM miDNA155-P155 duplex in symmetrical 1 M KCl (*cis/trans*) at 120 mV collected in three independent experiments. The solid black line at ~ I/I_0=0.12 separates deeper 3' entry of DNA duplex and shallower 5' entry of miDNA155-P155 duplex. In all experiments, the number of 3' was larger compared to 5' entries.

Table 4.6. Analysis of three individual experiments with 100 nM miDNA155-P155 duplex in symmetrical 1 M KCl at 120 mV, with the assignment of 5' and 3' entry events.

N	Open-pore current (pA)	I / I_0		Number of events			τ_{off} (ms)	
		3' entry	5' entry	Total	3' entry	5' entry	3' entry	5' entry
1	115.5	0.101	0.138	361	278 (78.8%)	75 (21.2%)	1085 ± 144	670 ± 216
2	117	0.103	0.138	285	191 (70.2%)	81 (29.8%)	1149 ± 150	725 ± 255
3	123	0.089	0.124	280	204 (76.4%)	63 (23.6%)	1151 ± 225	602 ± 149
All	**118.5 ± 4**	**0.098 ± 7.8 %**	**0.132 ± 6.1%**		**75.1%**	**24.9%**	**1128 ± 38**	**665 ± 62**

When all resistive pulses were taken into account, 75.1% of the events were assigned to the 3'-first entry while 24.9 % were assigned to 5'- first entry. This result is in agreement with the work of Butler *et al.* on the rC_{50} translocation through αHL pore, which revealed 64% of events with 3'-entry having a deeper block amplitude, whereas the 36 % of shallower block events were associated with 5'-entry of rC_{50} [205]. The reason for the lower capture rate of 5' leading cytosine overhang might be the result of the geometrical structure of the cytosine strand, as the cytosine bases are tilted towards 5' end with the respect to the phosphate backbone [132-134, 210].

The duration of level-1 events of miDNA155-P155 duplex associated with 3'-first entry was almost 2 times longer compared to 5'-first entry. This is different from the observations with dA_{50}, where dwell time associated with 5'-entry was two times longer compared to the 3'-entry translocation time [132, 134].

At higher voltages, the number of 5'-assigned events increased with respect to the 3'-assigned events. Figure 4.14 shows I/I_0 and τ_{off} distributions of level-1 amplitudes at +150 and +180 mV. The number of events associated with 5' first increased from 25 % at 120 mV to 47.9 % at 180 mV, which implies that the stronger electrophoretic force reduces the orientation-depended DNA capture.

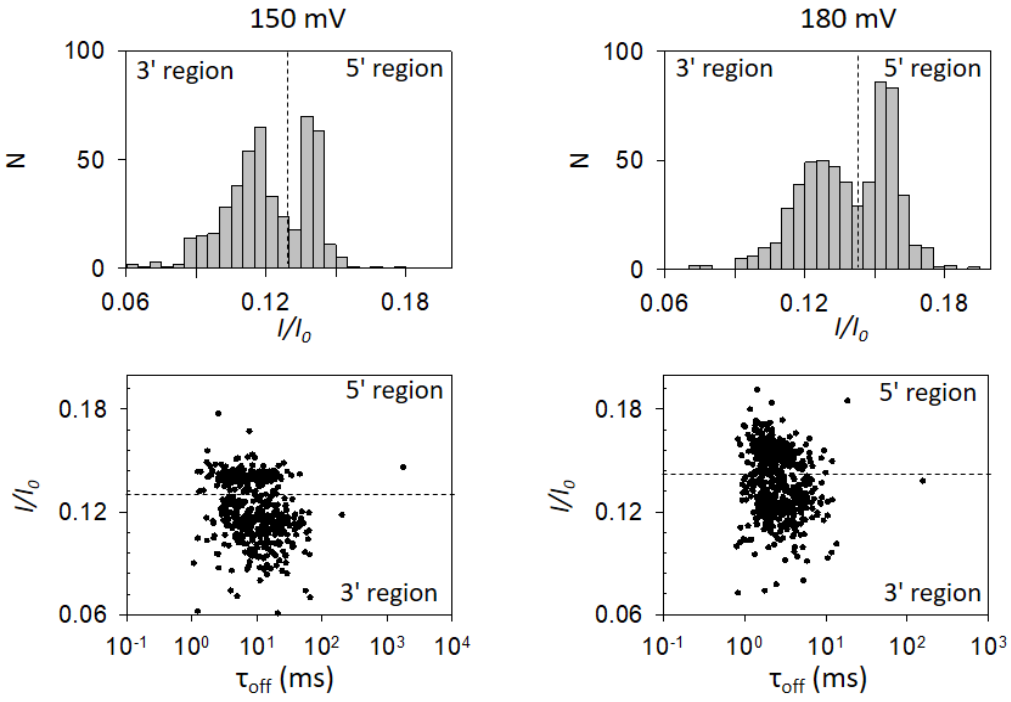

Figure 4.14. The distribution of level -1 I/I_0 and τ_{off} values for 100 nM miDNA155-P155 duplex at 150 and 180 mV. The dashed line presents the border between events assigned to 5' and 3'-first entries.

4.8 Sensitivity of miDNA155 detection with nanopore in symmetrical 1 M KCl solution

The concentration of miRNA in the sample can be obtained by measuring the capture frequency of miRNA-DNA probe since the concentration of miRNA was found linearly dependent on the capture rate (f_{on}). The interevent time can be obtained as a time constant from the fitted histogram, containing interevent data points or simply dividing the number of pulses with the total recording time. In this work, the capture frequency for 100 nM miDNA 155-P155 at 120 mV in 1 M KCl

was found at 0.2 ± 0.04 s^{-1} while the dwell time was found at 1.043 ± 0.012 s. In order to investigate the relationship between the capture frequency and the concentration of the miDNA 155-P155 duplex, the capture frequency was measured for 50 nM and 10 nM miDNA155-P155 concentrations. The number of events for lower concentrations of the miDNA155-P155 duplex was low, therefore multiple αHL pores were inserted in the bilayer used to detect the duplex in solution. The frequencies of 50 nM and 10 nM were obtained by dividing the number of pulses by the total recording time and the number of pores. With this approach, the capture rate was determined with 10, 50 and 100 nM in 1 M KCl solution at 120 mV (Figure 4.15 b).

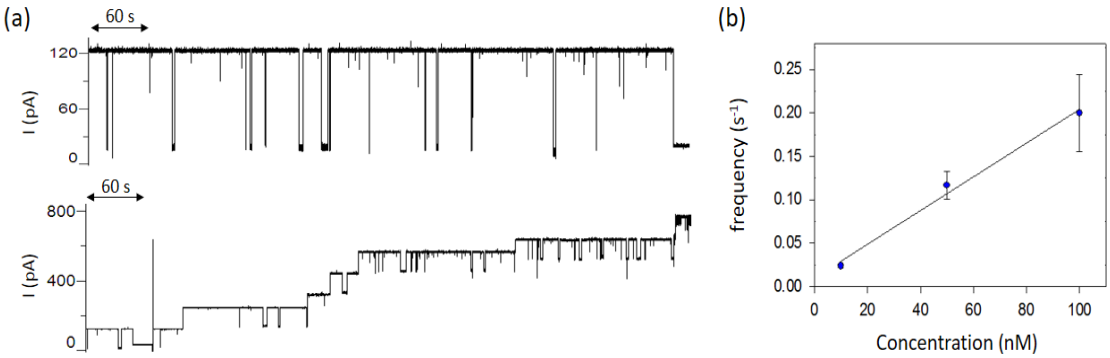

Figure 4.15. (a) Representative current trace through αHL pore in the presence of 10 nM miDNA 155-P155 duplex. Bottom panel current trace of multiple αHL pores in the presence of 10 nM miDNA155-P155 duplex at 120 mV. (b) Dependence of frequency of resistive pulses on miDNA 155-P155 duplex concentration. The line shows linear fit (y=ax) with R^2= 0.9852.

The capture rates for 50 nM and 10 nM DNA duplex were 0.117 ± 0.02 s^{-1} and 0.024 ± 0.002 s^{-1} respectively. The capture rate was found to be linear with the concentration of DNA duplex. The resistive pulse of miDNA155-P155 for the 10 nM concentration was occurring every 42 seconds, therefore the frequencies of lower concentrations were not measured. The expected frequency for 1 nM concentration from the linear fit is 0.0021 s^{-1}, that means one resistive pulse every ~500 s. Collection of around 100 events for 1 nM concentration at 120 mV in 1 M KCl would last at least 35 hours with one αHL nanopore, which is obviously too long.

Increasing the voltage can help to increase the capture frequency of DNA duplexes, but at the same time, it reduces the bilayer lifetime and exponentially decreases the dwell time. In this work, the occurring pore closures with high voltage were observed, which demanded frequent applications of the voltage reversal. The detection of events was made with Clampfit software, that is common for analysis of electrophysiological recordings. However, the detection of duplex events in a current recording having a changing baseline when the voltage reversal was applied made the detection of events difficult and resulted in frequent software crashing.

An alternative approach might be taken by employing multiple αHL pores to detect duplex at low voltages. The main challenge for this approach is to keep the number of pores constant for long periods of time. After insertion of one pore, the solution in the *cis* side was perfused with fresh

electrolyte solution in order to reduce further αHL insertions. For the experiment with numerous pores, the solution was not perfused, hence the concentration of αHL in *cis* chamber was 5 µg/ml. This can lead to numerous pore insertions, and it can be challenging to determine the exact number of the pores. The dynamic range of recordings is determined by the gain of the amplifier, which was set to 10. This setting enabled recordings in the ± 1 nA range, that is enough to monitor a current of ~8 αHL pores in 1 M KCl at 120 mV (8*120pA). Nevertheless, when it becomes too complex to determine the number of pores, the bilayers should be disrupted and reformed again.

During bilayer reformation, some pores might insert from the opposite side, with their cap openings facing the working electrode. In order to test how the insertion of αHL influences the miDNA155-P155 detection the αHL pore was added to the *trans* chamber, while miDNA155-P155 duplex was dispersed in the *cis* chamber to a concentration of 100 nM. Since the αHL was now inserted in the bilayer from the other side, the current at 120 mV (*trans* side positive) was ~82 pA while at -120 it was ~ -114 pA. Figure 4.16 shows the representative current traces of αHL channel in 1 M KCl at 120 and 150 mV.

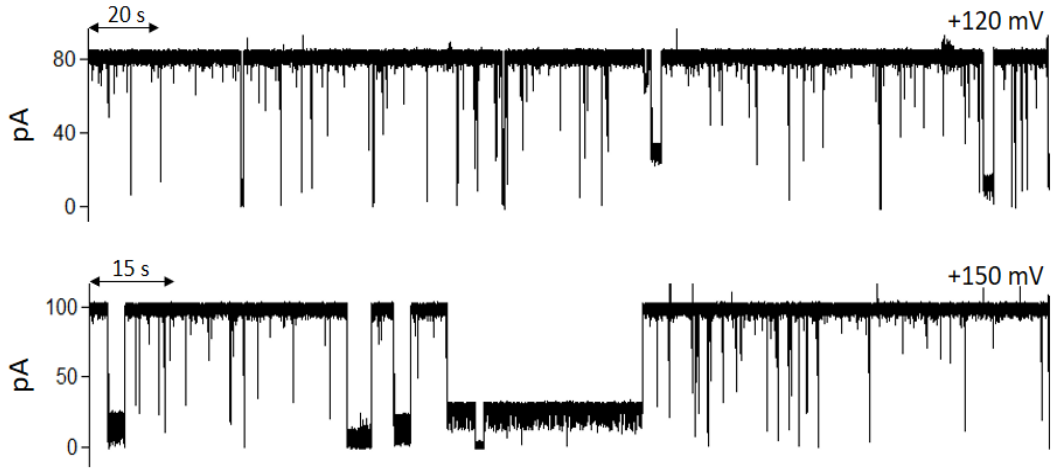

Figure 4.16. Single-channel αHL traces inserted from *trans* side of the bilayer in 1 M KCl at 120 and 150 mV in the presence of 100 nM miDNA155-P155 duplex.

The miDNA155-P155 blockages were observed for both 120 and 150 mV but, compared to experiments with the conventionally-oriented αHL, the resistive pulses did not have the multilevel signature characteristic for duplex unzipping. The frequency of blocks for the stem – cap direction at 120 mV was found 0.05 s^{-1} that was 4 times lower compared to cap – stem capture frequency. The lower capture rate of the duplex by the stem might be the result of geometrical and electrostatic contributions. The stem opening of αHL channel is about 2.2 nm wide, which is narrower than the 2.6 nm wide cap diameter. Moreover, the negatively charged stem entrance of αHL pore can act repulsively on the DNA molecules. Henrickson *et al.* and Muzard *et al.* reported ~8 times lower capture frequencies of poly C and DNA hairpin molecules from the stem-cap direction compared to cap-stem direction [134, 145]. Short current spikes might represent the short collisions of the DNA duplex with the *trans* entrance of the pore, or translocations of single-

stranded P155 since this molecule is in excess for the experiments. The insertion of the αHL in opposite direction would thus be problematic in the presence of multiple αHL pores in the bilayer since the estimation of the total number of pores would be difficult. For example, it would be easy to distinguish one properly oriented αHL and the second one in the opposite direction for their current output at +120 mV would be around 200-pA current (120 pA from conventionally oriented and 80 pA from the different side). However, when numerous pores are inserted, in presence of duplex molecules that are able to produce long current blockages and nonspecific pore clogging, the exact determination of pores and their orientation gets complicated and impairs the quantification of DNA.

4.8.1 miDNA21-P21 experiments

In order to test the sequence dependence on the duplex detection, another sequence- miDNA21 was mixed with its complementary P21 probe. The P21 probe was extended with poly dC_{30} overhangs from both 5' and 3' end just like P155. After formation of the DPhPC and αHL reconstitution in the membrane miDNA21-P21 duplex was dispersed in the grounded *cis* chamber to a final concentration of 100 nM. The dwell time of miDNA21-P21 duplex was found at 1763 ± 264 ms at 120 mV that decreased to 16.4 ± 3.8 ms and 4.3 ± 1.4 ms at 150 and 180 mV respectively (Figure 4.17 d). The bimodal I/I_0 distribution of level-1 was again observed as well for miDNA155-P155duplex. The deeper 3'-entries had a block amplitude of 0.11 I/I_0, while shallower 5'- entries had residual amplitude 0.16 I/I_0 .

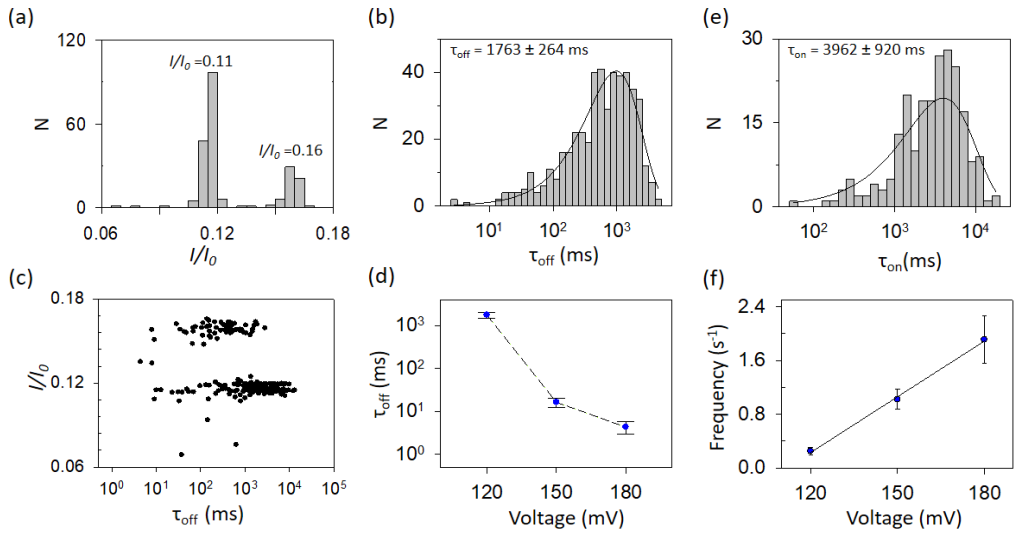

Figure 4.17. (a) The histogram of level-1 amplitude shows that the deeper block occurs more frequently than the shallower block as demonstrated with miDNA155-P155 duplex. (b) Logarithmic probability histograms for the time constructed with of 224 resistive pulses obtained in the single experiment (100 nM miDNA21-P21 duplex in 1 M KCl at 120 mV). (c) Distribution of level -1 I/I_0 and τ_{off} values for 100 nM miDNA21-P21 duplex in 1 M KCl at 120 mV. The events under deeper block were longer compared to the duration of the event under the shallower block. (d) Dependence of miDNA21-P21 level-1 duration on voltage (e) Histogram of ton distribution fitted with logarithmic probability function (f) Capture frequency increases linearly with the voltage range between +120 and +180 mV

The capture frequency of 100 nM miDNA21-P21 increased linearly with the voltage (Figure 4.17 f). The capture rate for 100 nM miDNA21-P21 duplex at +120 mV was found at 0.25 ± 0.06 s^{-1} what is similar to 0.20 s^{-1} obtained with the 100 nM miDNA155-155 duplex. The frequency was increased to 1.02 ± 0.15 s^{-1} at 150 mV and 1.91 ± 0.35 s^{-1} at 180 mV. The observed frequencies were similar for both miDNA21-P21 and miDNA155-P155. This was expected since the DNA probes were modified with the same capture overhangs.

4.9 Selectivity test in symmetrical 1 M KCl solution

Detection of miRNA with NRPS technique relies on hybridization of miRNA with a complementary DNA probe creating duplex that is able to produce a characteristic multilevel resistive pulse upon interacting with αHL nanopore. Based on a dwell time, that is almost 10^4 times longer for duplex compared to ssDNA translocation it is easy to distinguish resistive pulses produced by target miRNA –DNA probe duplex from short transient pulses produced by ssDNA or RNA species. Ideally, the probe will fully hybridize only with complementary miRNA in the sample while not interacting with other miRNA sequences in the sample. Previous works demonstrated significant reduction of dwell time with introducing mismatches in DNA probe-miRNA duplex [13, 19].

For the selectivity assay, 100 nM of miDNA155 was mixed together with 100 nM non-complementary P21 probe. The DNA molecules were dispersed in grounded *cis* chamber and voltage was applied so the *trans* side was at +120 mV compared to *cis* side (Figure 4.18)

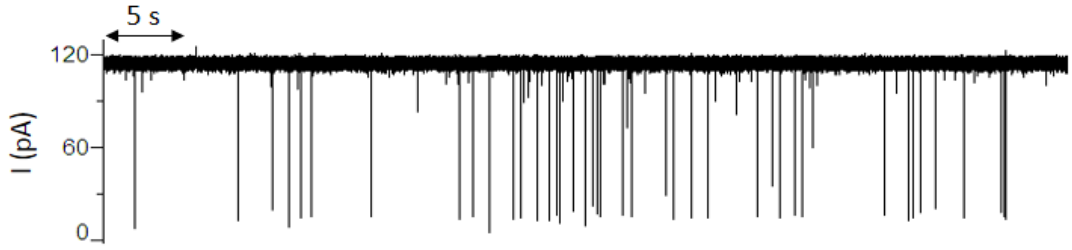

Figure 4.18. Representative αHL current trace in the presence of 100 nM miDNA155 and 100 nM P21 at 120 mV in symmetrical 1 M KCl, 10 mM Tris, 1mM EDTA, pH=8 at 120 mV.

Unlike for fully hybridised miDNA155-P155 or miDNA21-P21 duplexes, no specific current signatures were recorded for the mixture of miDNA155 and P21 sequences, which means that miDNA155 and P21 do not hybridise, thus they are not able to produce characteristic DNA duplex signature upon interaction with the αHL nanopore.

4.10 miRNA155 sensing with the nanopore

The previous experiments in this work were carried on DNA analogue of miRNA155 and miRNA21 because the DNAs are more stable compared to RNA sequence. Wang *et al*. used DNA counterpart of miRNA155 as a model to study miRNA-DNA duplex capture by the αHL nanopore [16]. The miDNA155-P155 had same multilevel block as previously observed for miRNA155-P155 duplex [13, 16]. In this work, the multilevel signature of miDNA155-P155 was observed with the block levels in agreement with those previously observed. Moreover, the capture rate of miDNA155-P155 was similar to that observed by Wang *et al*.[16], which suggest that capture rate is depending more on the probe dC_{30} overhang extensions rather than on target molecule (miRNA or miDNA).

However, in the recent work by Perera. *et al.* the attention was brought on differences between unzipping the DNA-DNA duplex and RNA-DNA duplexes through the αHL nanopore [211]. Comparison between RNA-DNA duplex and DNA-DNA duplex translocation through αHL nanopore showed that RNA-DNA duplex unzipped about 15 times faster compared to DNA-DNA duplex [211].

In order to investigate the difference between DNA duplex and RNA/DNA hybrid, experiments with miRNA 155 and P155 was performed. An additional control experiment with the only miRNA155 will be carried to compare the differences between single-stranded and double-stranded resistive pulses.

4.10.1 Nanopore sensing of single-stranded miRNA155

Based on previous experiments with single-stranded sequences used in this work, the single-stranded miRNA155 was expected to produce short-lived current resistive pulses similar to P155 and miDNA155. After bilayer formation and αHL channel insertion, the miRNA155 was dispersed in the *cis* chamber and pulled through the pore by applying a positive voltage bias from the *trans* side. The voltages used in the experiment were 120 and 180 mV (Figure 4.19).

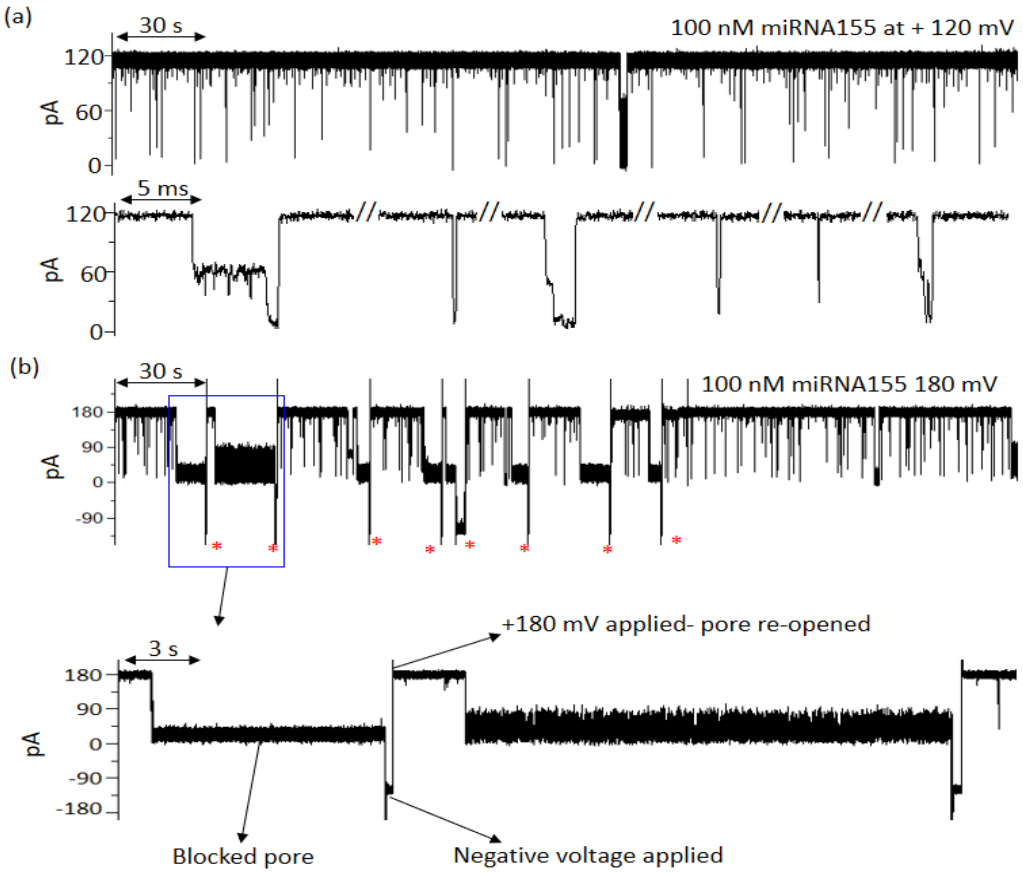

Figure 4.19. a) The representative single-channel traces recorded at +120 mV in the presence of 100 nM miRNA155. The lower panel shows the short blockages produced by single-stranded miRNA155. b) The representative single-channel current trace recorded at +180 mV. The high voltage induces long-lasting pore closures that might originate from miRNA155 stuck inside pore channel. Voltage reversal was applied frequently to reopen the αHL pore (lower panel).

For 100 nM miRNA155 at 120 mV, only 32 pulses were detected over 5 min recording. The average duration of miRNA155 block was found at 329 μs (Figure 4.20), similar to single-stranded P155.

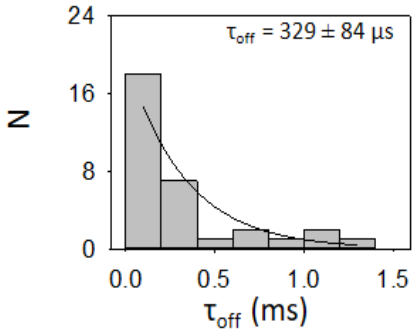

Figure 4.20. The histogram of dwell time durations of miRNA155 in 1 MKCL at 120 mV. The solid line represents the exponential fit to the data.

4.10.2 Detecting the miRNA155-P155 duplex with the nanopore

The miRNA-P155 duplex was prepared as described in section 4.2. After the bilayer formation and insertion of the αHL pore, the miRNA155-P155 duplex was dispersed in the grounded *cis* chamber to a final concentration of 100 nM. The positive voltage was applied from *trans* side of the membrane to pull miRNA155-P155 duplex toward the pore. At low voltages (<70 mV) there were no translocations of miRNA155-P155 duplex observed (Figure 4.21). At +80 mV the first translocations were observed. The duplex starts to unzip readily at +100 mV, a lower voltage compared to the one observed for miDNA-P155 unzipping (110 mV).

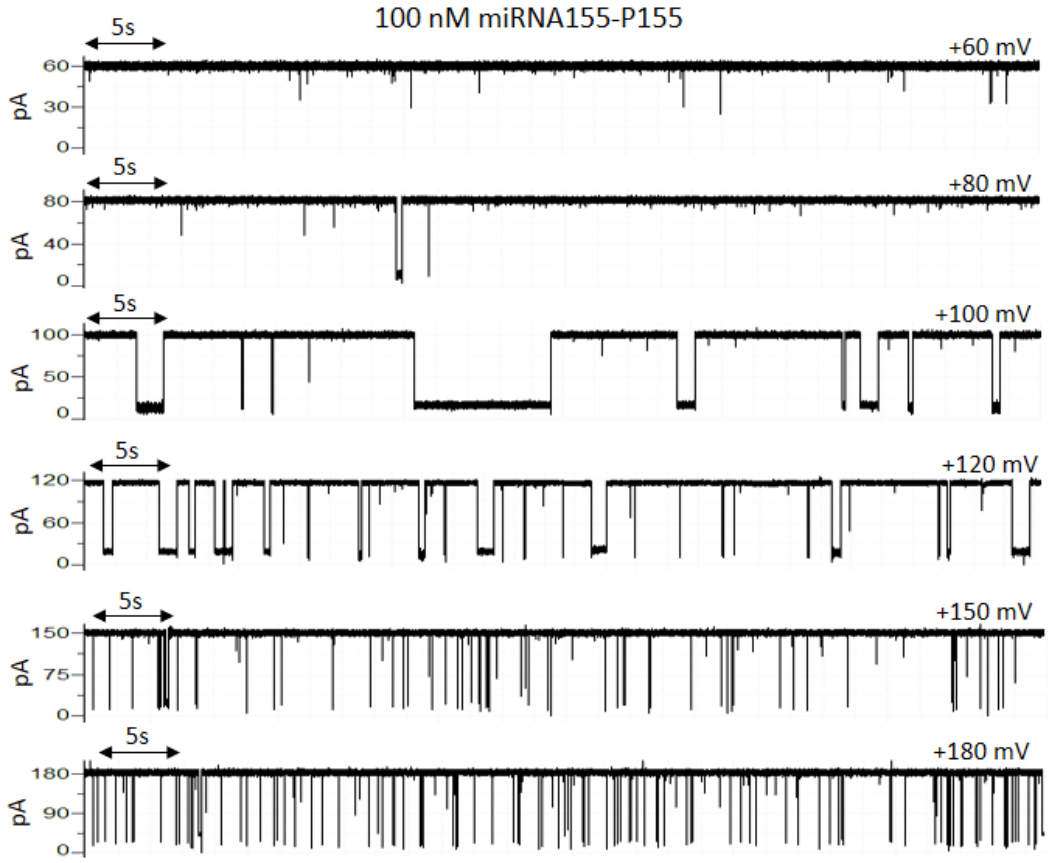

Figure 4.21. Representative single-channel αHL current traces in DPhPC bilayers at +60 to +180 mV. The recording solution was 1 M KCl, 10 mM Tris, 1mM EDTA, pH=8.

The number of interactions of the miRNA155-P155 duplex with the αHL pore obviously increased with the voltage (Figure 4.21). However, at high voltages, the nonspecific pore blockings were observed frequently just like in the case of miDNA155-P155 duplex. Therefore, voltage reversal was frequently applied to eject the DNA or RNA molecules to reopen the αHL pore. However, in some cases pore was permanently blocked (>1 min) even when a voltage reversal was applied (Figure 4.22).

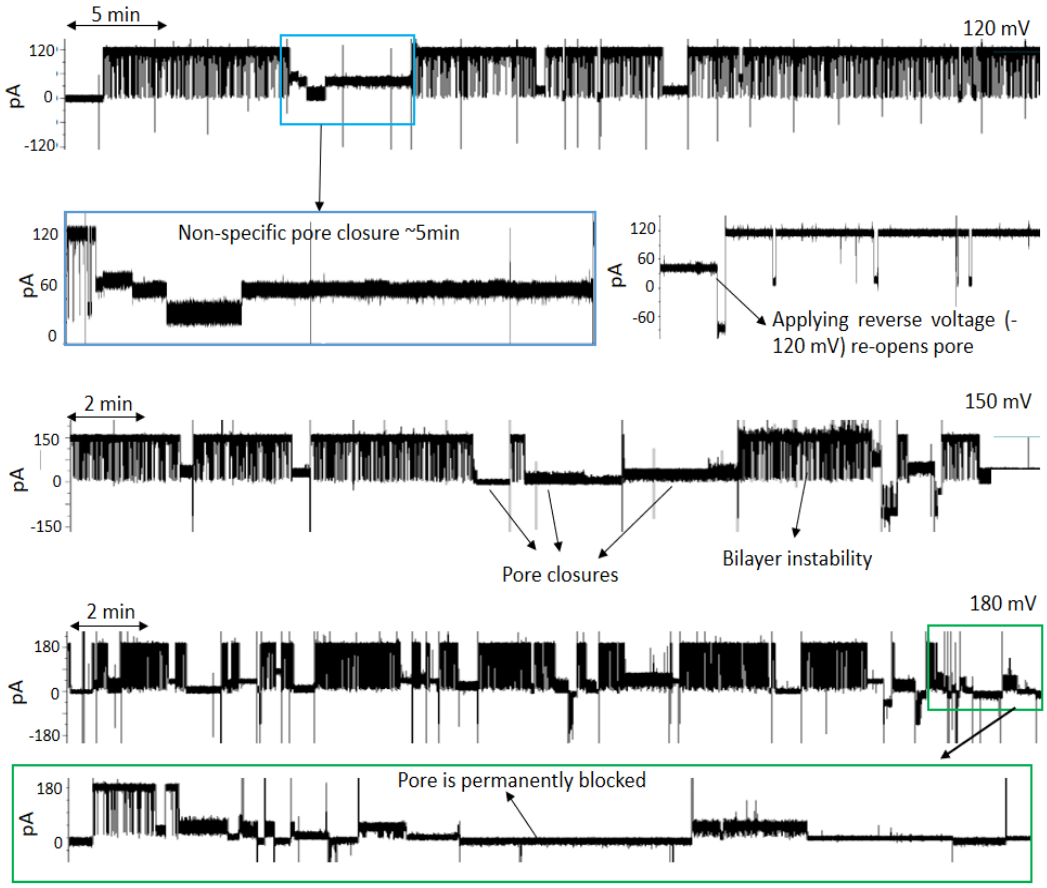

Figure 4.22. a) The single-channel αHL in the presence of 100 nM miRNA155-P155 probe at 120 mV. The long~5min non-specific pore closures were observed occasionally. Pore current can be restored by applying a negative voltage -120 mV that ejects stuck DNA/miRNA molecule from the pore. The pore closures and bilayer instabilities at +150 mV and +180 mV are more frequent and voltage reversal needs to be applied more frequently.

The analysis of 100 nM miRNA155-P155 resistive pulse parameters in 1 M KCl at various voltages is shown in Figure 4.23 and Figure 4.24.

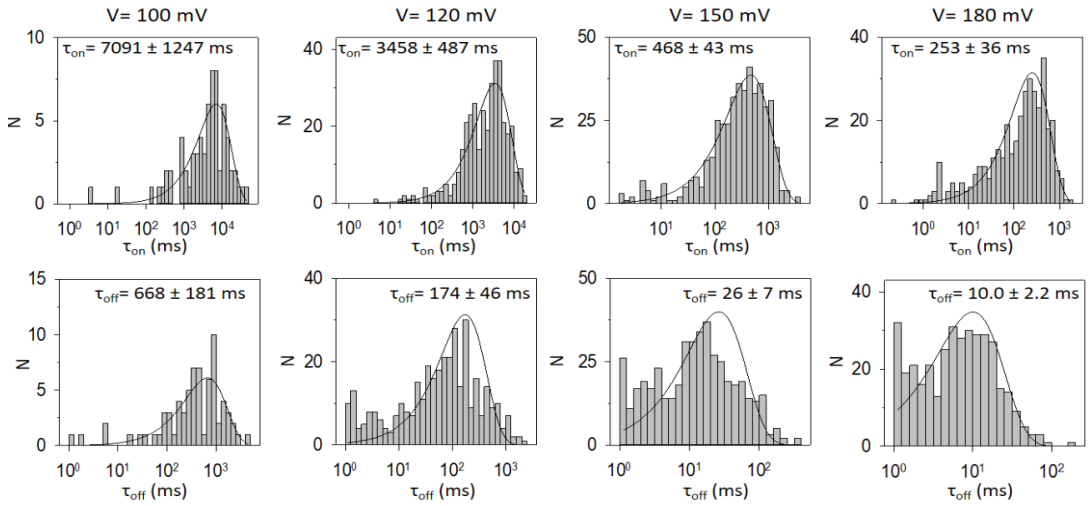

Figure 4.23. Interevent and dwell time distributions of 100 nM miRNA155-P155 duplex at 100,120,150 and 180 mV. The solid line presents the fits with exponential logarithmic probability function. The values for τ_{off} and τ_{on} and their S.E. are obtained from single nanopore experiment.

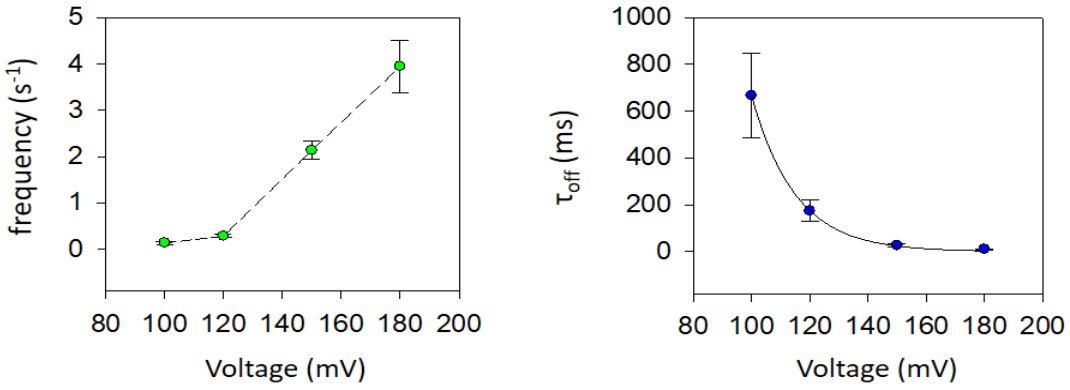

Figure 4.24 Event frequency (left panel) and event dwell time (right panel) dependence on voltage. The frequency of events increases linearly in 120 mV to 180 mV voltage region. The dwell time of miRNA155-P155 duplex exponentially decreases with the voltage. The solid line presents exponential fit to the dwell time data points. The values were obtained with single αHL experiment; the error bars represent S.E.

At 100 mV the capture frequency of 100 nM miRNA155-P155 was 0.14 s^{-1}, meaning one resistive pulse event every ~7 seconds. At 120 mV the capture frequency of miRNA155-P155 duplex was found at 0.29 s^{-1}, slightly higher than with the miDNA155-P155 duplex (0.2 s^{-1}). At higher voltages (+150 and +180 mV) the capture frequency increased but, as before mentioned, pore closures were more frequent and the reversal potential needed to be applied in order to re-open the pore from channel clogging. The dwell time decreased exponentially from 668 ± 181 ms at 100 mV to 10 ± 2.2 ms at 180 mV.

4.10.3 Characteristic signatures of miRNA155-P155 duplex

The miRNA155-P155 signatures were collected at various voltages. Similarly to previous studies and to the miDNA155-P155 experiments, the multilevel resistive pulse signature was observed for all voltages. Figure 4.25 shows the resistive pulses of miRNA155-P155 at 120 and 180 mV in 1 M KCl solution.

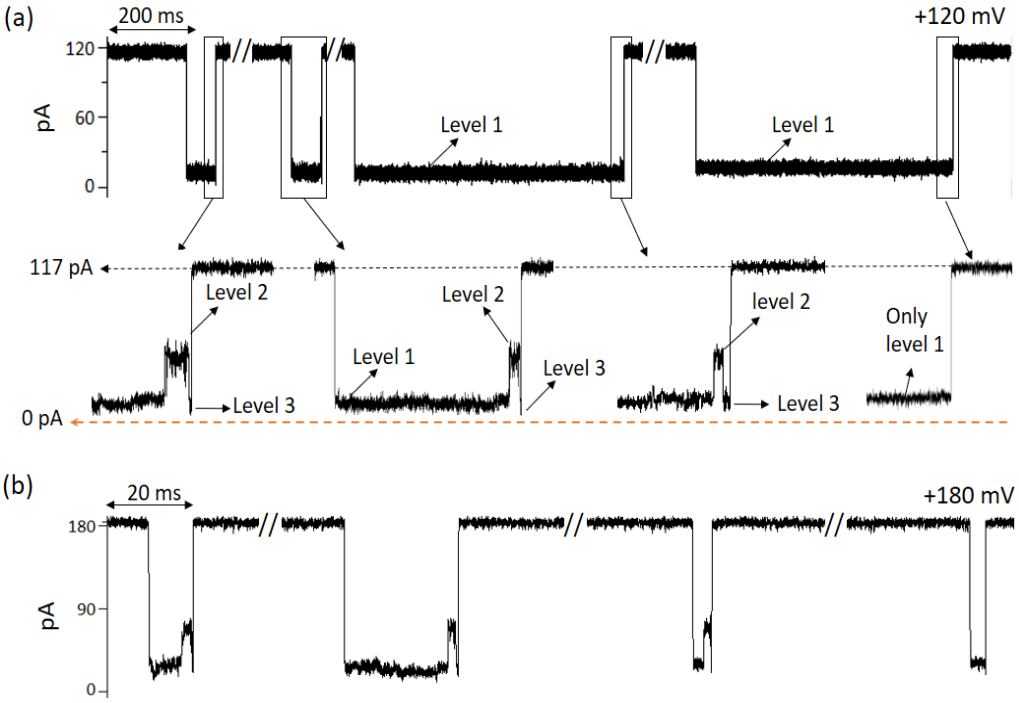

Figure 4.25. (a) Characteristic resistive pulses produced with 100 nM miR155-P155 duplex through the αHL pore at 120 mV in 1 M KCl. The lower panel shows characteristic multilevel current signature produced by miRNA155-P155 duplex. The longest level-1 had a duration of 170 ms, level-2 had an amplitude of 0.43 and lasted 840 µs while level-3 produced the deepest 0.1 amplitude and shortest duration of 550 µs. b) The characteristic miRNA155- P155 duplex signatures at +180 mV. The duration of level 1 was found at 10.0 ms, significantly shorter than duration of level 1 at 120 mV

The analysis of resistive pulses of 100 nM miRNA155-P155 probe at 120 mV and 180 mV is shown in Figure 4.26 and Figure 4.27.

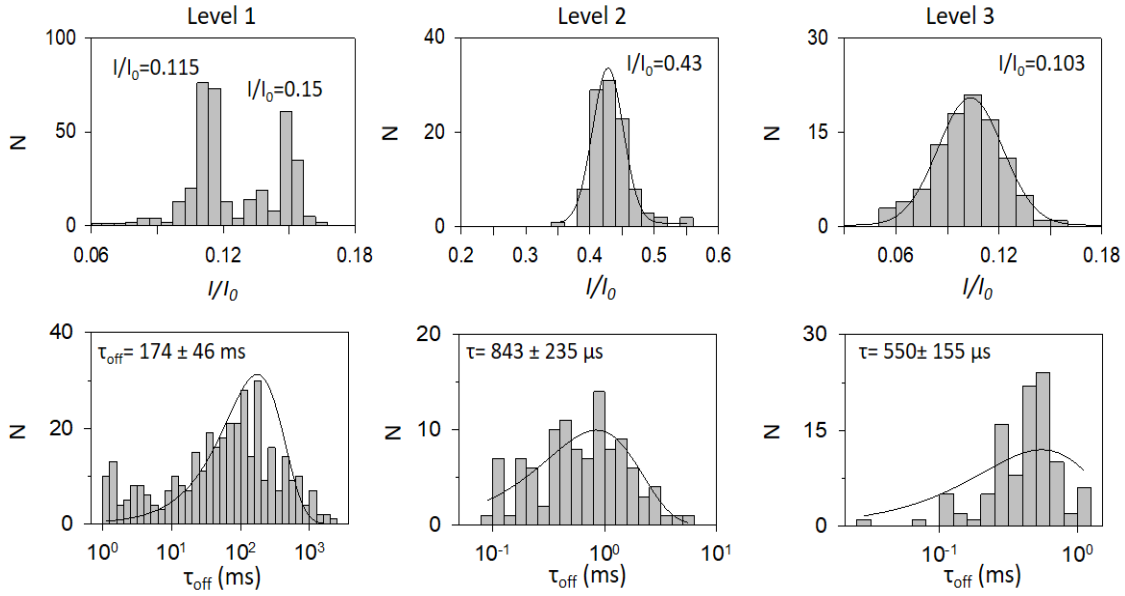

Figure 4.26. The level current amplitudes and their corresponding dwell times for the 100 nM miRNA155-P155 duplex at 120 mV in 1 M KCl, pH=8. The results were obtained from a single experiment. The solid line shows the fit with the exponential log function. The values are given as a mean ±S.E.

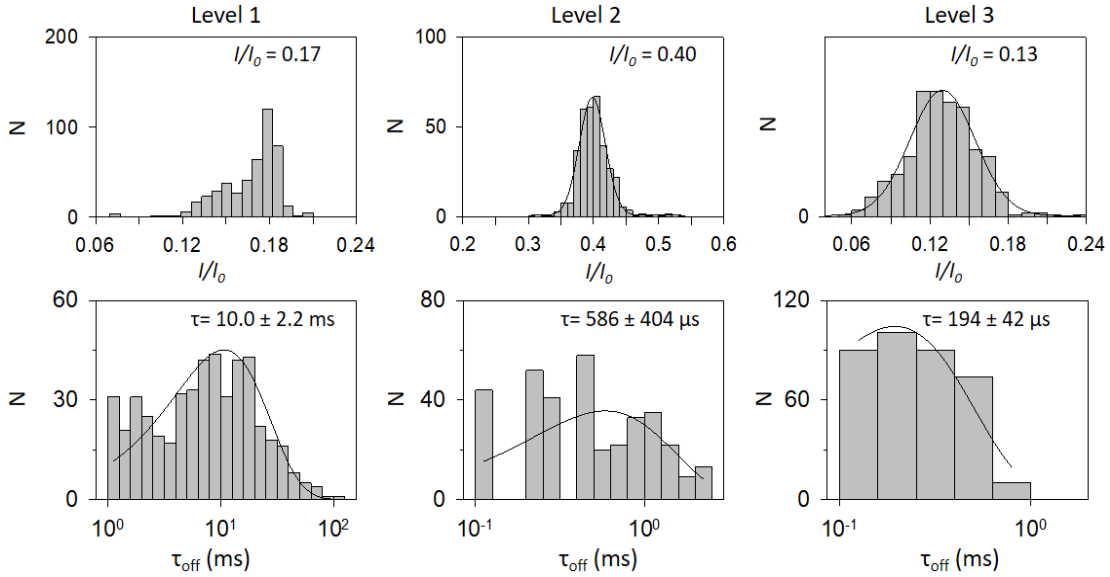

Figure 4.27. Current level amplitudes and their corresponding dwell times for the 100 nM miRNA155-P155 duplex in 1 M KCl at 180 mV. Results were obtained within a single experiment. The solid line represents the fit with the exponential log function. Influence of DNA probe design on amplitude and capture frequency of miRNA. Values are shown as mean ±S.E.

The bimodal amplitude of level-1 was observed again for miRNA155-P155, just like for the previous two duplexes: miDNA155-P155 and miDNA21-P21. At 180 mV the amplitude distribution was more dispersed compared to the one at 120 mV. The amplitudes of level-2 and level-3 were similar to those previously observed for miDNA155-P155 in this work (see Table 4.5).

4.11 Influence of dC_{30} overhang position on capture rate and level-1 amplitude

Previous experiments demonstrated that the distribution of I/I_0 level-1 obtained with double overhang P155 has bimodal I/I_0 level-1 amplitude for all investigated duplexes: miDNA155-P155, miDNA21-P21 and miRNA155-P155. The bimodal I/I_0 residual amplitude distribution was observed at all voltages and it was speculated to be the result of the probe entering either from its 5' or 3' end in the αHL channel.

In order to understand the probe modification influence on the capture frequency and I/I_0 residual amplitude of the level-1, two additional probes with the single dC_{30} overhangs: P155-5'-(dC_{30}) and P155-3'-(dC_{30}) were used for miRNA155 detection (Figure 4.1). The experiments with different probes were performed by Mrs Shengmiao Zhou.

4.11.1 Experiments with miRNA155-P155-5'-(dC_{30}) duplex

The resistive pulses for 100 nM concentration miRNA155-P155-5'-$(dC)_{30}$ duplex were recorded at two voltages of +120 mV and 180mV.

Figure 4.28. (a) The miRNA155-P155-5'-$(dC)_{30}$ duplex The representative single-channel traces recorded at 120 mV (top trace) and 180 mV (bottom trace) in the presence of 100 nM miRNA155-P155- 5'-dC_{30}.

As expected, nonspecific pore blockages were more pronounced at higher (+180 mV) voltage than at lower (+120 mV) voltage Figure 4.28. The statistical analysis of current blockages produced by 100 nM miRNA155-P155-5'-$(dC)_{30}$ duplex at +120 mV and +180 mV is shown in Figure 4.29 and Figure 4.30

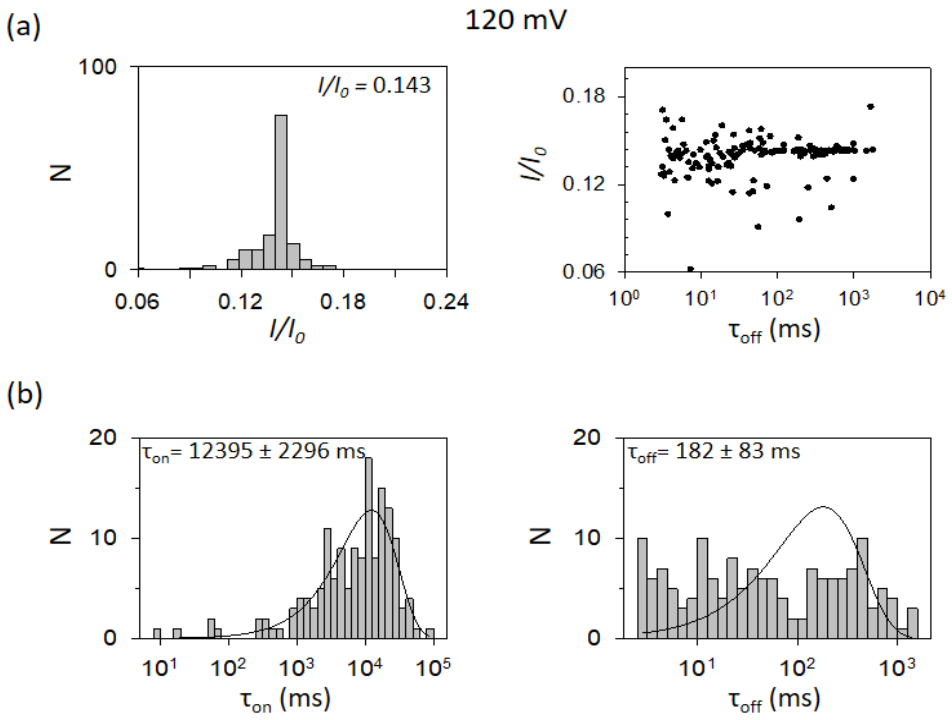

Figure 4.29. (a) Histogram of I/I_0 level -1 distribution (left panel). Distribution of level-1 I/I_0 and τ_{off} values for 100 nM miRNA155-P155-5'-$(dC)_{30}$ in 1 M KCl at 120 mV(right panel). (b) Interevent time and dwell time probability distributions of 100 nM miRNA155-P155-5'-$(dC)_{30}$ in 1 M KCl at +120 mV.(Data recorded by Mrs Shengmiao Zhou)

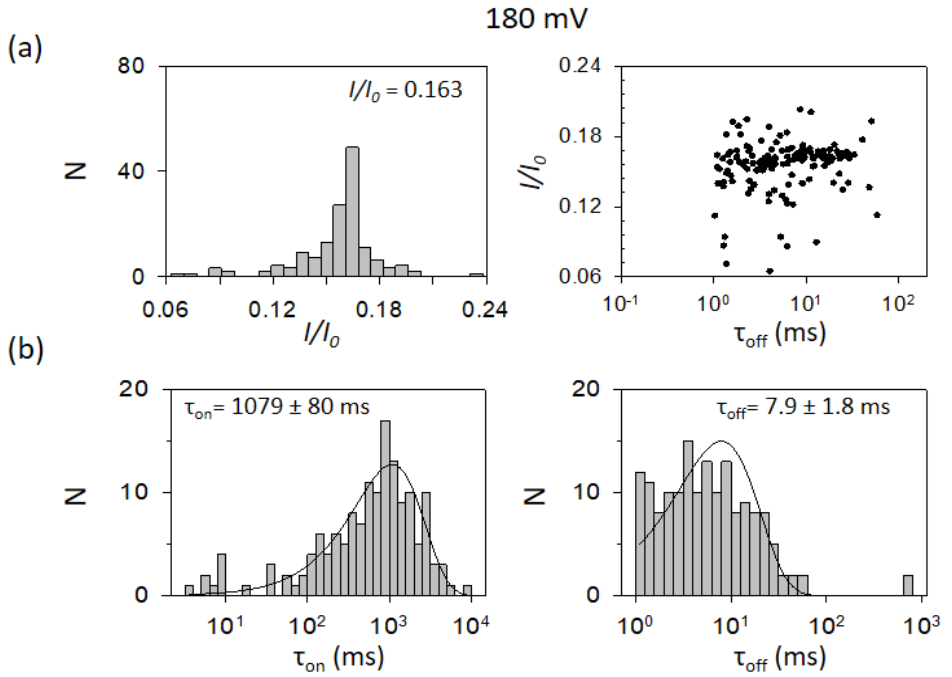

Figure 4.30. (a) Histogram of I/I_0 level -1 distribution (left panel). Distribution of level-1 I/I_0 and τ_{off} values for 100 nM miRNA155-P155-5'-$(dC)_{30}$ in 1 M KCl at 180 mV(right panel). (b) Interevent time and dwell time probability distributions of 100 nM miRNA155-P155-5'-$(dC)_{30}$ in 1 M KCl at +180 mV. (Data recorded by Mrs Shengmiao Zhou)

As shown in Figure 4.29 and Figure 4.30 the miRNA155-P155-5'-$(dC)_{30}$ duplex produced a single block level-1 of 0.145 I/I_0 at 120 mV and 0.163 I/I_0 at 180 mV. The capture frequency for the miRNA155-P155-5'-$(dC)_{30}$ duplex were 0.08 s^{-1} and 0.93 s^{-1} at 120 mV and 180 mV respectively. The dwell times of the miRNA155-P155-5'-$(dC)_{30}$ were 182 ± 83 ms and 7.9 ± 1,8 ms at 120 and 180 mV respectively.

4.11.2 Experiments with miRNA155-P155-3'-(dC_{30}) duplex

The same experiment was carried out with the miRNA155-P155-3'-$(dC)_{30}$ duplex, where 100 nM of the duplex was dispersed in the *cis* side of the pore and the transmembrane voltage was applied so that *trans* side was positive to the *cis* side. The current traces of the 100 nM miRNA155-P155-3'-$(dC)_{30}$ duplex were recorded at +120 and +180 mV Figure 4.31.

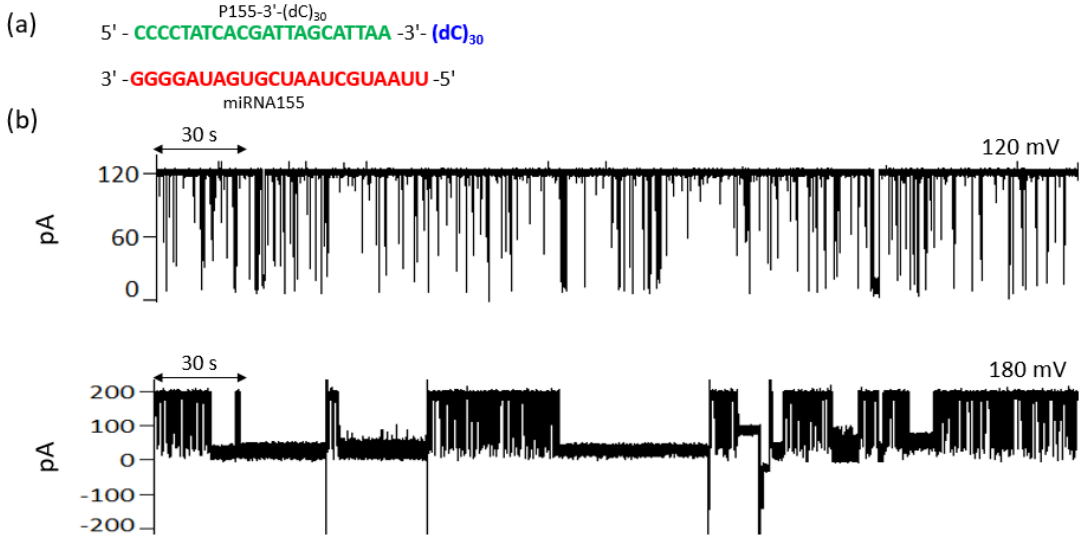

Figure 4.31. (a) The miRNA155-P155-3'-$(dC)_{30}$ duplex. (b) The representative single-channel current traces in 1 M KCl recorded at 120 mV (upper panel) and 180 mV (lower panel) in the presence of 100 nM miRNA155-P155-3 duplex. (Recorded by Mrs Shengmiao Zhou)

The analysis of the miRNA155-P155-3' resistive pulses in 1 M KCl at 120 and 180 mV is shown in Figure 4.32 and Figure 4.33.

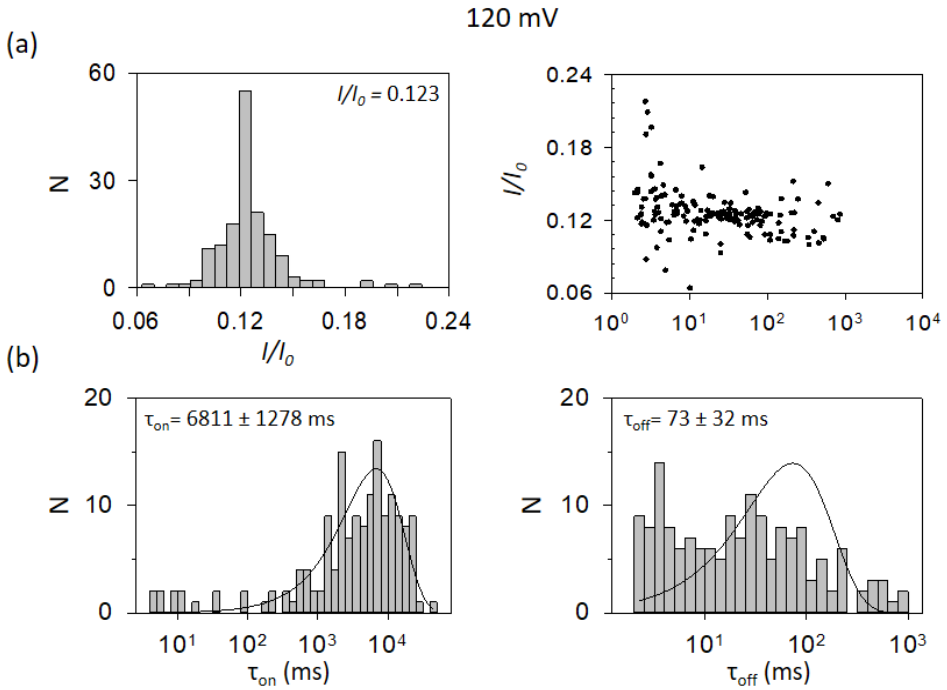

Figure 4.32. (a) Histogram of I/I_0 level -1 distribution (left panel). Distribution of level-1 I/I_0 and τ_{off} values for the 100 nM miRNA155-P155-3'-$(dC)_{30}$ in 1 M KCl at 120 mV (right panel). (b) Interevent time and dwell time probability distributions of 100 nM miRNA155-P155-3 in 1 M KCl at +120 mV. (Data recorded by Mrs Shengmiao Zhou)

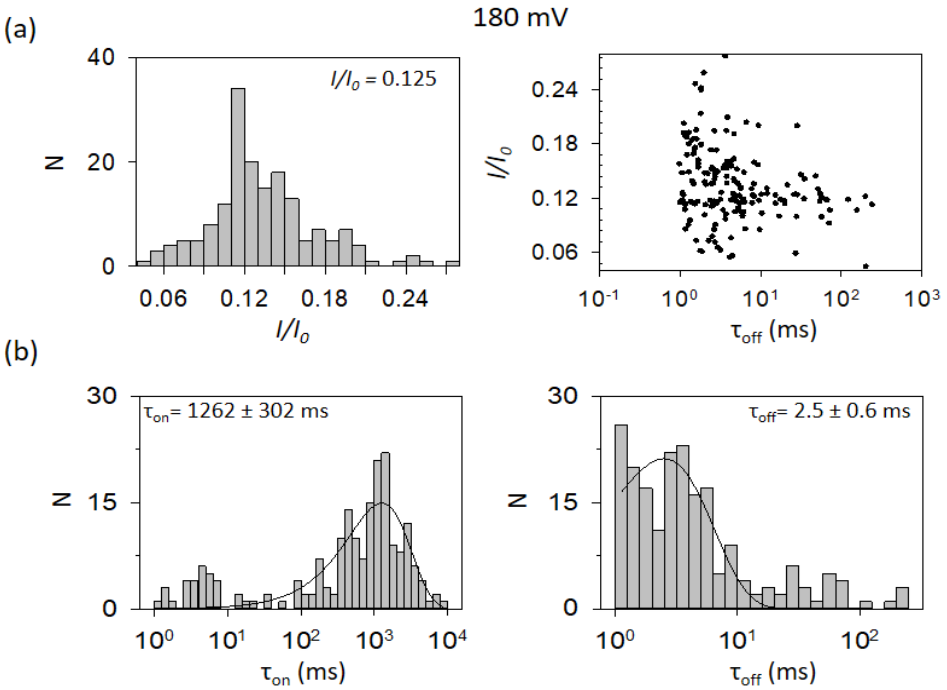

Figure 4.33. (a) Histogram of I/I_0 level -1 distribution (left panel). Distribution of level-1 I/I_0 and τ_{off} values for 100 nM miRNA155-P155-3'-$(dC)_{30}$ in 1 M KCl at 180 mV (right panel). (b) Interevent time and dwell time probability distributions of 100 nM miRNA155-P155-3 in 1 M KCl at +180 mV. (Data recorded by Mrs Shengmiao Zhou).

The miRNA155-P155-3'-$(dC)_{30}$ duplex had a single block level-1 I/I_0 = 0.123 I/I_0 at 120 mV and I/I_0 = 0.163 at 180 mV. The capture frequencies for the miRNA155-P155-3'-$(dC)_{30}$ duplex were 0.15 s^{-1} for 120 mV and 0.79 s^{-1} for 180 mV. The durations of the miRNA155-P155-3'-$(dC)_{30}$ dwell times were 73 ± 32 ms and 2.5 ± 0.6 ms for 120 mV and 180 mV respectively.

4.11.3 Assignment of miRNA155-P155 duplex side entry into the αHL

After demonstrating that current amplitude levels are dependent on the side at which duplex was entering the pore, it was possible to assign and analyse the number and duration of the 5' and 3'-entries of the miRNA155-P155 duplex with double dC_{30} overhang. The analysis of three independent experiments with 100 nM miRNA155-P155 in 1 M KCl at 120 mV is shown in Figure 4.34 and Table 4.7.

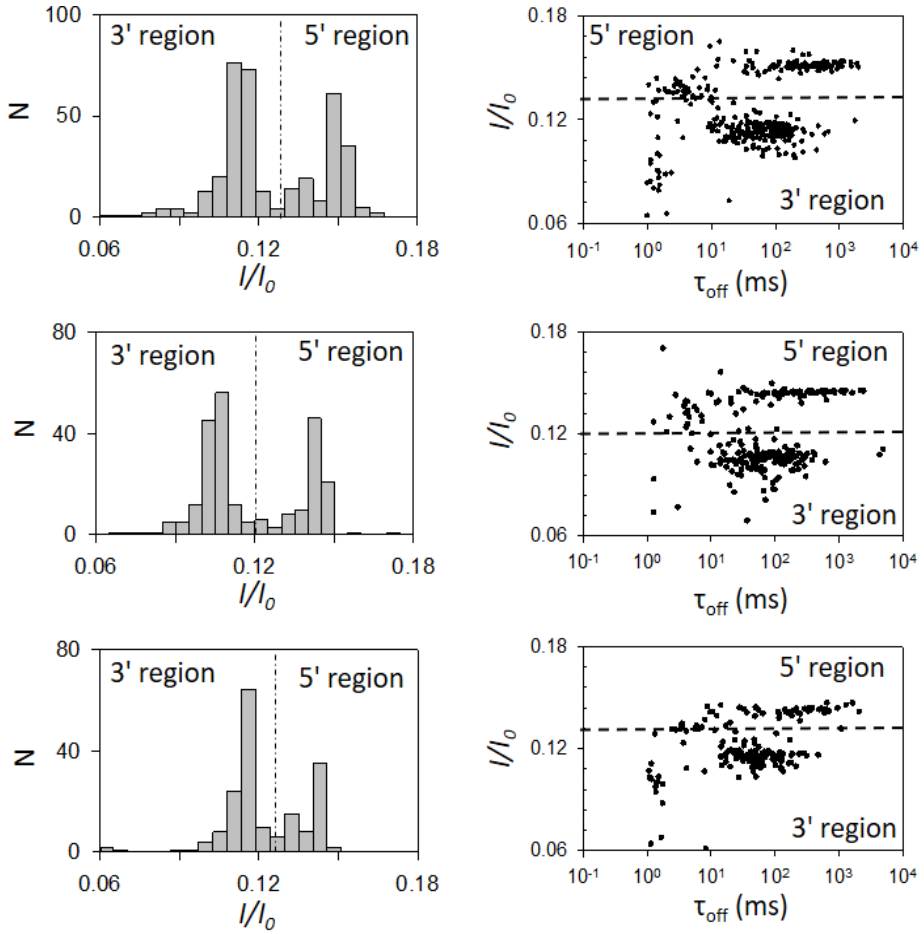

Figure 4.34. Distribution of level-1 I/I_0 and dwell time (τ_{off}) values for three independent experiments with 100 nM miRNA155-P155 probe at +120 mV. Dashed lines present the border between 5'- entry and 3'- entries of the duplex in the channel.

Table 4.7. Analysis of three independent experiments with 100 nM miRNA155-P155 duplex with assigned of side entry into αHL pore.

N	I / I_0		Number of events			τ_{off} (ms)	
	3' entry	5' entry	Total	3' entry	5' entry	3' entry	5' entry
1	0.106	0.144	244	152 (62.3%)	92 (37.7%)	76.0± 13.0	259.1 ± 90.2
2	0.116	0.141	182	132 (72.5%)	50 (27.5%)	64.4 ± 17.7	297.5 ± 99.9
3	0.113	0.150	367	232 (63.2%)	135 (36.8%)	85.0 ± 17.2	330.5 ± 97.4
All	**0.112 ± 4.5%**	**0.145 ± 3.2%**		**66%**	**34%**	**76.1 ± 8.8**	**295.7 ± 35.7**

The number of events under deeper I/I_0 level assigned to 3'-entry was ~2-fold higher compared to the number of events under the shallower, 5'- entry assigned levels (Table 4.7). Interestingly the duration events assigned to the 5'-entry was almost 4-fold longer than the duration of events assigned to 3'-entry (Table 4.7). This observation was in contrast with miDNA155-P155 duplex, where events assigned to 5' entry were 2-fold shorter than events assigned to 3'-entry (Table 4.6), which demonstrates the ability of nanopore to distinguish between two different duplex structures.

In order to compare the assignment of the duplex side entries with respect to the voltage, the distribution of amplitudes for level-1 and dwell times were shown for lower (100 mV) and higher (180 mV) in Figure 4.35. Interestingly, the distribution of events for 100 nM miRNA155-P155 at 100 mV almost entirely fell under the deeper block level assigned to 3'- first entry. At 180 mV, the majority of events seemed to fall under the shallower block assigned to 5'-entry.

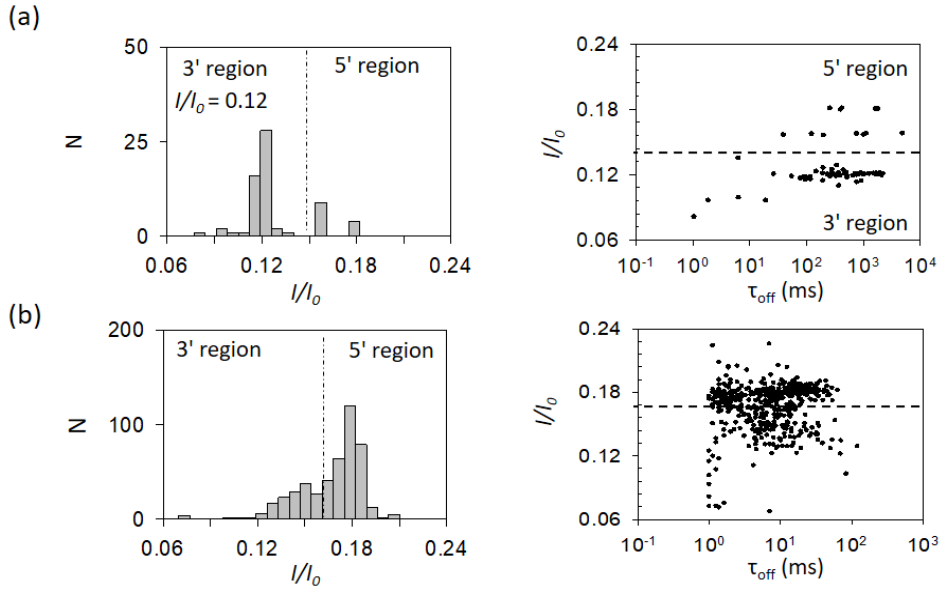

Figure 4.35 Distribution of level-1 amplitude and τ_{off} values of 100 nM miRNA155-P155 at a) 120 mV and b) 180 mV. The dashed line presents border between 5' and 3'-entries.

4.11.4 Comparison of the resistive pulse parameters of duplexes with various DNA probe modification

The final comparison of resistive pulses parameters for the three duplexes with various dC_{30} overhang positions at two voltages of 120 and 180 mV is shown in Table 4.8.

Table 4.8. Dwell time and interevent time comparison of the duplexes with a different dC_{30} DNA probe modification. All values are obtained in a single experiment and reported as a mean ± S.E except the values for dwell time and capture frequency of the 100 nM miRNA155-P155 at 120 mV (marked with *) which are obtained from three different experiments and shown as a mean ± SD.

Duplex	**120 mV**		**180 mV**	
	τ_{off} ± S.E. (ms)	**f_{on} (s^{-1})**	**τ_{off} ± S.E. (ms)**	**f_{on} (s^{-1})**
miRNA155-P155-5'-(dC_{30})	182 ± 83	0.08 ± 0.02	7.9 ± 1.8	0.93 ± 0.07
miRNA155-P155-3'-(dC_{30})	73 ± 32	0.15 ± 0.03	2.5 ± 0.6	0.80 ± 0.19
miRNA155-P155	149 ± 22*	0.301 ± 0.04*	10.0 ± 2.2	3.95 ± 0.60

As shown in Table 4.8 the highest capture rate was obtained when P155 with double dC_{30} was used for miRNA155 detection for at both 120 and 180 mV. The capture frequency of miRNA155-P155 duplex was 2 times higher than for miRNA155- P155-3'-(dC_{30}) and four times higher than for miRNA155-P155-5'-(dC_{30}) duplex in 1 M KCl at 120 mV.

4.12 miRNA155 quantification in symmetrical 1 M KCl

The experiments with miRNA155-P155 duplex revealed lower voltage necessary to unzip RNA-DNA duplex compared to miDNA155-P155 duplex. At high voltages, the αHL pore closures and bilayer instabilities were frequently observed. As those complicate the event analysis and increase the time of the recording, the 120 mV was selected as a voltage for miRNA155-P155 quantification with αHL nanopore.

The probe P155 with double dC_{30} overhang had the highest capture frequency (0.31 ± 0.04 s^{-1}) when compared to probes with single dC_{30} overhangs on either 5'-end (0.08 s^{-1}) or 3'-end (0.15 s^{-1}). Therefore, P155 with double dC_{30} overhang was used for miRNA155 detection.

Concentrations of the miRNA155-P155 duplex were 10, 50 and 100 nM. The capture frequencies of 10 nM and 50 nM concentrations were obtained by counting the number of events and dividing by the total open pore time just like for the miDNA155-P155 duplex. The values for capture

frequencies were 0.034 ± 0.01s^{-1}, 0.165 ± 0.011 s^{-1} and 0.301 ± 0.04 s^{-1} for 10, 50 and 100 nM respectively.

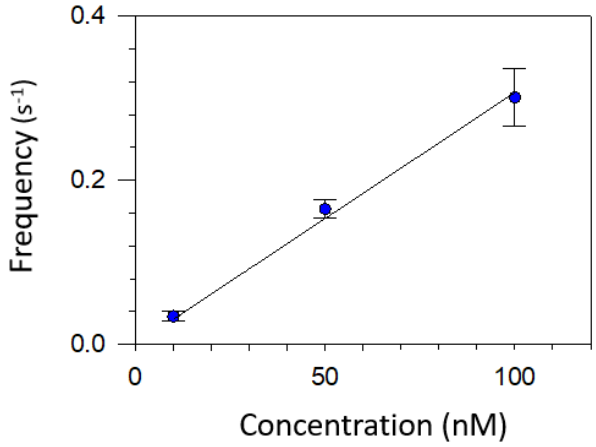

Figure 4.36. Event frequency as a function of miRNA155-P155 concentration in 1 M KCl at +120 mV. The line represents linear fit (y= ax, a=0.0031) with R^2= 0.995. The experiments with 10 and 100 nM were repeated 3 times while 50 nM was repeated twice.

The event frequency was linearly dependent on concentrations in the range of 10-100 nM. For the lowest concentration of 10 nM the total number of collected pulses in three experiments was 218 in 101 min recording time, that means ~2 pulse per minute. That is in good agreement with capture frequency of 10 nM miRNA155-P155 obtained by Wang *et al.* in 1 M KCl at 100 mV [13]. Moreover, the same group reported a similar capture frequency (0.027s^{-1}) for the miRNA155-P155 duplex in the biological samples extracted from lung cancer patients, suggesting that 10 nM is the pathophysiological concentration [13].

The frequency of the lower concentration can be estimated from the reported fit function. For example, 1 nM concentration of miRNA-P155 duplex would result in one pulse every ~300 s, hence collecting at least 20 events the total recording time should be 1.5 hours.

4.13 Comparison of miRNA155-P155 duplex resistive pulse parameters with miDNA155-P155 duplex

As previously said, the preliminary tests and calibration of the setup were done with a more stable DNA analogue of miRNA155. However, in a recent work Perrera *et al.* observed that 23 bp RNA-DNA duplex unzipped ~15 times faster than 23 bp DNA-DNA duplex in αHL nanopore [211]. The DNA probe complementary to RNA and DNA sequences were modified with 10 and 24 nt long dC overhangs [211]. The possible explanation why the duration of the DNA-DNA unzipping is longer than the DNA-RNA duplex unzipping was proposed to originate from differences in the structure between these two complexes [211]. The DNA-DNA duplex has 2 nm wide, B-form structure, whereas DNA-RNA duplex has the 2.4 nm wide A-form structure [212]. In addition,

the RNA-DNA duplexes were found to have higher melting temperature compared to DNA-DNA duplexes, implying higher stability of DNA-RNA duplex. Hence, a longer dwell time was expected for RNA-DNA duplexes. On the contrary, it was observed that DNA-DNA duplex unzipped 15 times slower compared to RNA-DNA duplex. It was proposed that the longer dwell time of DNA-DNA duplex is related to the ability of the 2 nm wide B-form structure to enter in the vestibule of αHL channel, where it unzips in a strictly confining environment, while the 2.4 nm wide A-form RNA-DNA duplex cannot enter the vestibule of αHL channel and unzips outside the channel [211].

In this work, the dwell time of miDNA155-P155 duplex at 100 mV was too long to be determined (>20 s), while the dwell time of miRNA155-P155 duplex was found at 668 ms. At 120 mV the τ_{off} duration of the miDNA155-P155 duplex was seven times longer compared to miRNA155-P155 duplex (1043 ms vs 149 ms) with a similar capture rate (0.20 s^{-1} vs 0.301 s^{-1}). However, when the voltage was further increased to 150 and 180 mV miRNA-P155 duplex had 2.5 and 4.5 times longer dwell times compared to miDNA155-P155 duplex. Comparison of resistive pulse parameters of miDNA155-P155 and miRNA155-P155 duplexes is given in Table 4.9.

Table 4.9. Comparison of dwell time and capture frequency values between 100 nM miDNA155-P155 and 100 nM miRNA155-P155 duplexes at 100, 120,150 and 180 mV in 1 M KCl. The results are obtained from a single experiment are presented as a mean ± S.E, except for the data at120 mV where the values are obtained from three individual experiments and presented as a mean ± SD

Voltage (mV)	**100**		**120***		**150**		**180**	
	τ_{off}(ms)	f_{on}(s^{-1})	τ_{off}(ms)	f_{on}(ms)	τ_{on}(ms)	f_{on}(s^{-1})	τ_{off}(ms)	f_{on}(s^{-1})
miDNA155-P155	>10 s	N.D	1043 ± 13	0.20 ± 0.04	10.6±1.5	1.1	2.4±0.8	1.80±0.14
miRNA155-P155	668±181	0.14 ±0.02	149 ± 22	0.31 ± 0.04	26 ± 7	2.1 ±0.2	10.0±2.2	3.95±0.60

Both miRNA155-P155 and miDNA155-P155 produced specific multi-level signatures upon interaction with the αHL nanopore. The bimodal level-1 I/I_0 distribution was found for both duplexes, meaning that the pore it capable to discriminate between 5' end and 3'-end capture in both cases. It is interesting that events belonging to the deeper level (assigned to 3'-end capture) had longer dwell time compared to 5'-end capture in miDNA155-P155 case, while the opposite was observed for miRNA155-P155 duplex, where the events assigned to 5' end entry had almost four times longer dwell time compared to events associated with 3'- end capture. For both miDNA155-P155 and miRNA155-P155 duplexes, the number of events assigned to 5'- entry was lower compared to a number of events assigned to 3'- entry at low voltages. At 100 mV almost

all events were associated with 3'-entries for miRNA155-P155. The capture rate at the preferred voltage (V=120 mV) was similar for miDNA155-P155 and miRNA155-P155 duplexes and increased linearly with voltage in the 120 -180 mV region for both duplexes. At higher voltages, non-specific pore clogging was observed more frequently for both miRNA155 and miDNA155-P155 duplexes. The dwell time decreased nonlinearly for both cases, which is unfavourable for the sensitivity of the technique. For example, the dwell time of miDNA155-P155 duplex at 180 mV was 2.4 ms, close to the 1 ms cut off set to eliminate unspecific short pore blockages.

4.14 Modulation of miDNA155-P155 duplex resistive pulse properties with various electrolytes

The common electrolytes used in nanopore experiments with DNA are 1 M KCl and 1 M NaCl. However, it was shown that the dwell time of DNA upon translocation through both solid-state and biological pores can be modulated with various electrolytes *i.e.* the dwell time was prolonged when KCl was substituted with LiCl because of cation-specific stabilization of the DNA duplex [213]. The longer dwell time is desirable because it increases the resolution of the nanopore technique [213, 214].

To gain insight on the influence of electrolyte species on resistive pulse parameters of the miDNA155-P155 duplex, the experiments were performed in the symmetrical 1 M KCl, NaCl, LiCl, CsCl and NH_4Cl solutions containing 10 mM Tris, 1 mM EDTA, pH=8.

4.14.1 Dwell time and capture frequency modulation of miDNA155-P155 duplex in different electrolytes

The αHL pore did not show any gating or closing periods depending on the electrolyte species. The dwell time of miDNA155-P155 duplex was found at ~ 1 s for all electrolytes, with the exception of LiCl where the dwell times at 120 mV were too long to get a sufficient amount of events, so the capture frequency was also not determined at 120 mV in the case of 1 M LiCl. At 180 mV the dwell time of miDNA155-P155 duplex was found in the range from 2 to 5 ms for all electrolytes, except for LiCl, where the dwell time was 41 ms (Table 4.10). Similarly, the capture rate increased linearly in the voltage range from 120 to 180 mV for all electrolytes, except for LiCl where the exponential increase was observed. Capture frequency was not determined for 1 M LiCl at the 120 mV because resistive pulses of miDNA155-P155 were too long to collect a sufficient amount for statistical analysis. However, with the increase of voltage, the capture rate of 100 nM miDNA155-P155 was found almost 2- fold higher at 180 mV in 1 M LiCl compared to 1 M KCl solution.

Table 4.10. Dwell time, interevent time and capture frequency of 100 nM miDNA155-P155 duplex in various symmetrical 1 M electrolytes at 120, 150 and 180 mV. The values are obtained from single experiments and presented as a mean ± S.E

	Voltage (mV)					
	120		**150**		**180**	
1 M [XCl]	**τ_{off} (ms)**	***f* (s^{-1})**	**τ_{off} (ms)**	***f* (s^{-1})**	**τ_{off} (ms)**	***f* (s^{-1})**
KCl	1030 ± 128	0.21 ± 0.04	10.60 ± 1	1.10 ± 0.12	2.4 ± 0.1	1.80 ± 0.14
NaCl	1211 ± 131	0.27± 0.04	18.3 ± 5.6	1.14 ± 0.19	5.1 ± 1.8	1.94 ± 0.33
CsCl	907 ± 114	0.30 ± 0.07	10.22 ± 1.4	1.01±0.13	1.5 ± 0.02	1.60 ± 0.20
NH_4Cl	1120 ± 173	0.49 ± 0.08	11.8 ± 2.1	1.73 ± 0.21	3.47 ± 1.2	2.85 ± 0.25
Li Cl	> 20,000	–	564 ± 186	1.36 ± 0.19	41 ± 12.4	3.29 ± 0.82

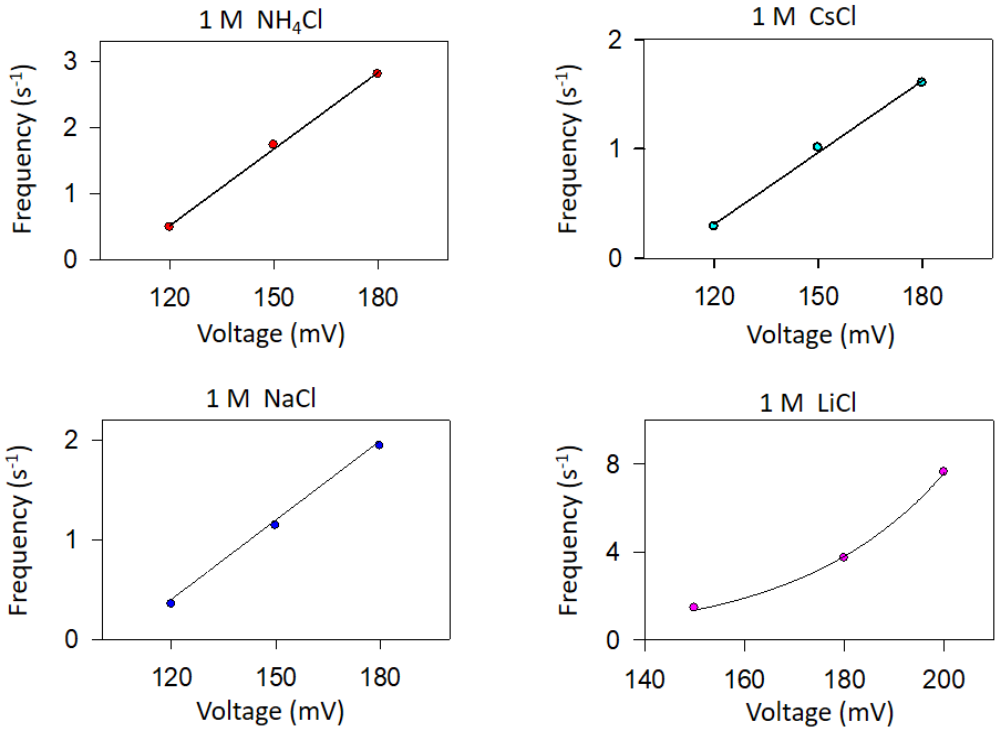

Figure 4.37. Influence of voltage on capture frequency of the 100 nM miDNA155-P155 duplex in various electrolyte species.

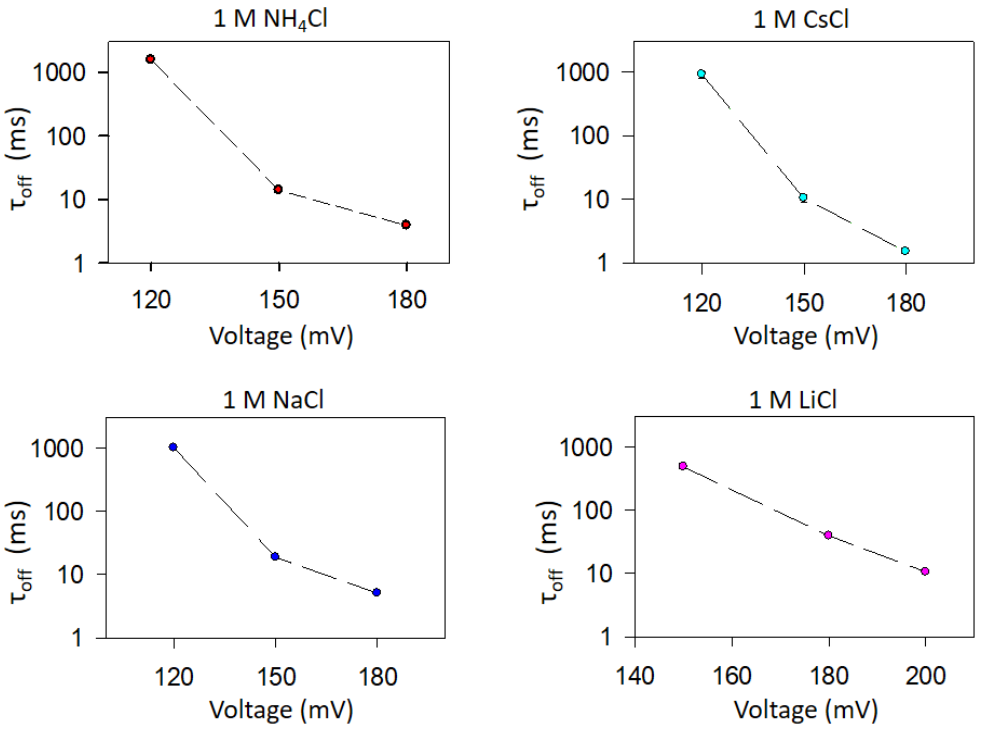

Figure 4.38. Influence of voltage on dwell time of the 100 nM miDNA155-P155 duplex in various electrolyte species.

The reason why the capture rate and the dwell time is higher in LiCl compared to other salts might derive from the electrostatic interactions between miDNA155-P155 duplex and αHL pore. As previously mentioned, the *trans* entrance of αHL beta barrel is negatively charged -7e which is believed to contribute to electrostatic repulsion between negatively charged polymers and the pore [153]. The overall negative charge of the *trans* side was found to be an important contributor to translocation properties of negatively charged polymers through the αHL pore [145, 152, 165, 166]. In the work of Bhattacharya *et al.* it was shown that lithium ions had the highest affinity to bind to negatively charged amino acids (D127 and D128) at the entrance of αHL nanopores [155]. As a result, current asymmetry factor I(+V) / I(-V) of the αHL nanopore at 120 mV was found at 1.1. This is a similar value of current asymmetry factor of 1.06 to the one obtained by Wong and Muthukumar, who lowered the pH in *trans* side to pH=4 in order to protonate D127 and D128. They observed 2- fold increase in capture rate of NaPSS (MW=57.5 kg/mol) with αHL pore when pH in *trans* side was lowered from 7.4 to 4 [152].

Hence, the influence of lithium ions might have the similar effect on capture rate and current asymmetry of αHL pore just like pH on *trans* side of the channel. The strong binding of Li^+ ions to negatively charged D127 and D128 would result in a decreased electrostatic repulsion between negatively charged DNA and negatively charged *trans* entrance of the αHL pore. The current asymmetry factors measured in this work were obtained by dividing the αHL pore current at +120 mV with the absolute value of the pore current at -120 mV. The observed values are given in the Table 4.11 and are in good agreement with values obtained by Bhattacharya *et al.* [155]. The

lowest current asymmetry factor was observed in 1 M LiCl at 1.14 that increased to ~1.4 for NH_4Cl, 1 M CsCl and 1 M KCl.

Table 4.11. The αHL I (+V) / I (-V) ratio for the symmetric 1 M XCl *cis/trans* conditions measured for ±120 mV.

Electrolyte	**I (+V) / I (-V)** **For a voltage of ± 120 mV**
1 M LiCl / 1M LiCl	1.14 ± 0.02
1 M NaCl / 1M NaCl	1.29 ± 0.03
1 M NH_4Cl / 1M NH_4Cl	1.35 ± 0.05
1 M CsCl / 1M CsCl	1.38 ± 0.02
1M KCl / 1 M KCl	1.40 ± 0.02

4.14.2 Amplitude analysis of miDNA155-P155 duplex in various electrolytes

The amplitude of the level-1, which presents the unzipping of the miDNA155-P155 was analysed in various salt species Figure 4.39. The bimodal I/I_0 level-1 amplitude was found for all electrolyte solutions. The number of events under deeper amplitude peak that was associated with the entry of the duplex from 3' first entry was higher compared to shallower 5' entry for all solutions at 120 mV. The best separation of bimodal peak amplitude was obtained in 1 M NH_4Cl where the difference between two peaks was 6.3 pA, while the lowest separation of the two peaks was observed for 1 M NaCl and was found at 2.95 pA.

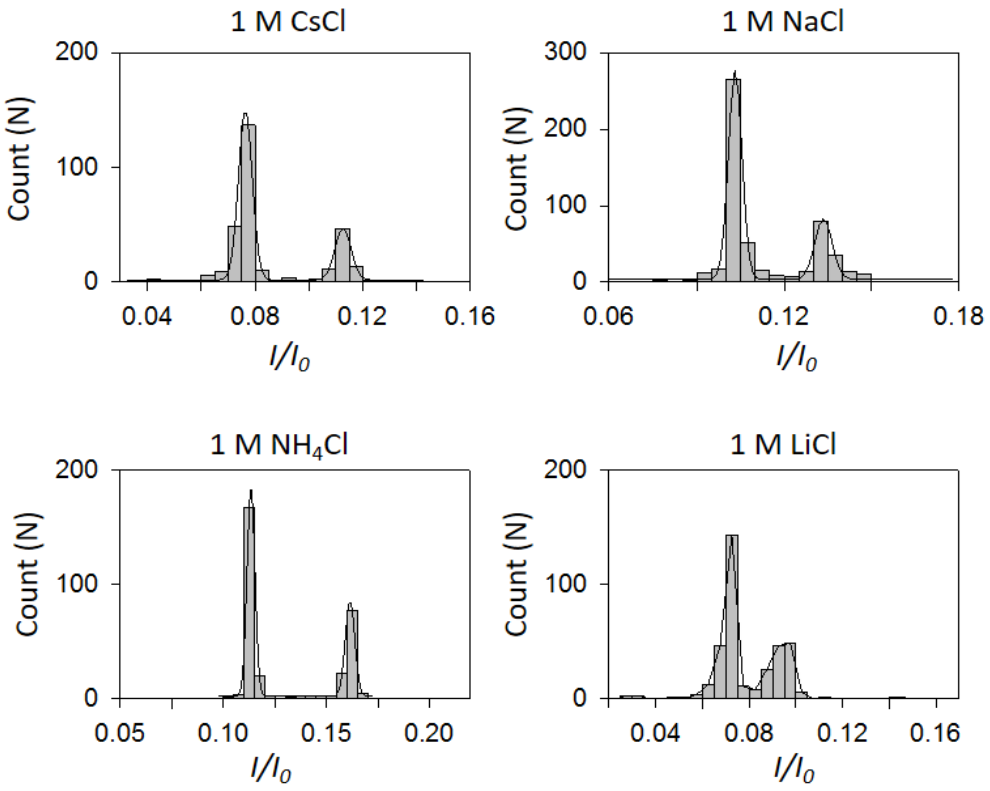

Figure 4.39. Level 1 amplitude histogram for 100 nM DNA155-P155 duplex in various electrolytes. The voltage was 120 mV for all salts except for 1 M LiCl where the voltage was set to +150 mV.

4.15 Summary

This chapter describes the detection of target miRNA/miDNA duplexes with the αHL nanopore in conventional 1 M KCl solution. The experiments with miRNA155, miDNA21 and miRNA155 with their corresponding probes confirmed previous studies, showing that the resistive pulses of the duplexes can be easily separated from the resistive pulses of single-stranded molecules based on the duplex pulse duration and its specific current block signature. The characteristic multilevel duplex signature was observed only when DNA probes were mixed with their complementary miRNA sequences. For example, mixing the noncomplementary P155 with miDNA21 did not produce a specific multilevel current signature upon interaction with the αHL nanopore (see section 4.9).

The concentration of miRNA can be simply obtained by counting the number of characteristic duplex signatures during the duration of the experiment. The present work confirmed the linear relationship between duplex concentration and duplex capture frequency on concentrations spanning one order of magnitude (10 nM -100 nM). The reason for this narrow quantification range is the low capture frequency of the miRNA-DNA duplex. For example, the capture frequencies of 100 nM and 10 nM miRNA155-P155 duplexes were (0.3 s^{-1}) and 0.034 s^{-1}

respectively, which means only one duplex capture event every 30 seconds for the 10 nM of the duplex. In a real physiological sample, such are plasma or serum, the expected amount of individual miRNA (extracted from 1 mL of plasma) would be in the 0.1 – 1 amol range [7, 215]. Such amount, once resuspended in the 1mL chamber used in this work, would yield to concentrations five orders of magnitude lower than the 10 nM limit of quantification achieved with the present setup. Hence, a significant increase in the duplex capture frequency was necessary in order to improve the sensitivity of the nanopore biosensor. The capture frequency can be increased in several ways such as: increasing the transmembrane voltage, modification of DNA probe, pore bioengineering and introducing the salt gradient across the pore.

In section 4.1 the influence of voltage on duplex capture frequency was examined. The capture frequency can be increased with voltage but it comes at the expense of the reduced dwell time of the duplex which can influence the specificity of technique. For example, it can be complicated to distinguish between short duplex resistive pulses and non-specific pore blockages with similar amplitude. Moreover, the αHL pore was frequently being blocked when voltage >150 mV were used which complicates the analysis of the current traces. Hence, in this work, the quantification of miRNA155-P155 was performed at holding potential at 120 mV.

Furthermore, the influence of the DNA probe was discussed. The core of the DNA probe is the complementary sequence of its target miRNA molecule that ensures selective hybridization in the solution. In order to ease the capture of the DNA-miRNA duplex, the DNA probe was modified with single-stranded dC_{30} capture overhang. The dC_{30} overhang can be attached only at one end of the probe (the probe is elongated by dC_{30} from either the 5' or the 3' - end) or it can be attached on both ends of the probe. When DNA probes with single capture overhangs were used for miRNA155 detection in 1 M KCl at 120 mV, their capture rates were significantly lower compared to P155 probes with double dC_{30} overhangs (see section 4.11). The capture frequency of the probe with dC_{30} overhang attached to 5' was four times lower compared to the capture rate of the probe P155, while probes with dC_{30} overhang attached to 3' end had two times lower capture rates than P155. Therefore, the double overhang is desirable to achieve higher capture frequencies and a higher sensitivity of the technique.

Although the ability of αHL to discriminate at which side homopolymers enter the pore based on the different current level blockages for 5' or 3'-end, this has never been shown previously with miRNA-DNA probe duplex detection. In this work, the ability of αHL to detect duplex translocation either from 5' or 3' - ends was presented by comparing the blockage current levels of the probes with single capture overhangs either at 5' and 3' prime with residual current amplitude produced by the probe with double dC_{30} overhangs (section 4.7 and 4.11.3). It was observed that 3'-first blockage event produced deeper blockages compared to 5'-first blockage events. This could be used for potential multiplex detection of miRNA in solution.

In order to increase the capture frequency of DNA with the silicon nitride nanopore Wanunu *et al.* proposed transmembrane salt gradient mechanism [151]. The salt gradient approach was later used by Li Qun Gu group to improve the capture frequency of the miRNA with the αHL nanopore [13]. However, the influence of salt gradient on the key duplex translocation parameters was not comprehensively studied. Therefore, the next chapter will explore the influence of salt gradient conditions on the duplex dwell time, residual amplitude and the capture frequency of the duplex.

Chapter 5: Effect of *cis/trans* salt gradient on DNA duplex translocation properties

Previous studies have shown that the transmembrane salt gradient increased the capture rate of dsDNA molecules with the solid-state nanopore. Moreover, the salt gradient was shown to increase the capture rate of negatively charged NaPSS [165, 166] and miRNA-DNA duplexes [13, 19] with the αHL nanopore. However, the key parameters such are capture frequency, dwell time and the amplitude of the miRNA-DNA probe duplexes under the salt gradient conditions with the αHL nanopore were not analysed in the previous literature. This chapter describes the effect of salt gradient on miRNA-DNA duplex resistive pulse parameters. In the first section, the duplex capture rate and dwell times will be measured under various of salt gradients. The optimization of the salt gradient was carried in the presence of 100 nM miDNA155-P155 duplex. The aim of the experiments was to find the conditions at which the capture rate of the duplex is maximized but without excessive loss of sensitivity of technique via decreasing dwell time, which was observed for higher voltages in the previous chapter. In section 5.2, the probe design was evaluated in the salt gradient conditions. After establishing the optimized conditions, the experiments with lower miDNA155-P155 duplex concentrations were performed to investigate the sensitivity of the technique in section 5.3. Subsequently, the optimized assay parameters were applied on miRNA155-P155 duplex and miRNA21-P21 duplex. Finally, the influence of different electrolyte species on the miDNA155-P155 duplex resistive pulse parameters was investigated in section 5.6.

5.1 Optimization of the salt gradient across the αHL pore for miRNA sensing

In this section, we have investigated the miDNA155-P155 duplex interactions with αHL nanopore under various KCl *cis/trans* gradients. The first set of experiments were performed by keeping the $[KCl]_{cis}$ constant at 1 M KCl while varying the $[KCl]_{trans}$ from 1 to 4 M KCl. The second set of experiments were conducted by keeping the $[KCl]_{trans}$ constant at 4 M while varying the $[KCl]_{cis}$ from 2 to 0.1 M. Concentration of the miDNA155-P155 duplex was 100 nM and the voltage was set at 120 mV (*trans* side positive).

5.1.1 Influence of KCl concentration in *trans* side on duplex capture frequency and dwell time

The influence of *trans* side KCl concentration on the miDNA155-P155 resistive pulse parameters was investigated by varying $[KCl]_{trans}$ from 1 to 4 M while keeping $[KCl]_{cis}$ constant at 1 M. Concentration of the miDNA155-P155 duplex was 100 nM and the voltage was set at 120 mV (*trans* side positive). The single-channel current traces under various salt gradients in the presence of 100 nM miDNA155-P155 duplex is shown in Figure 5.1.

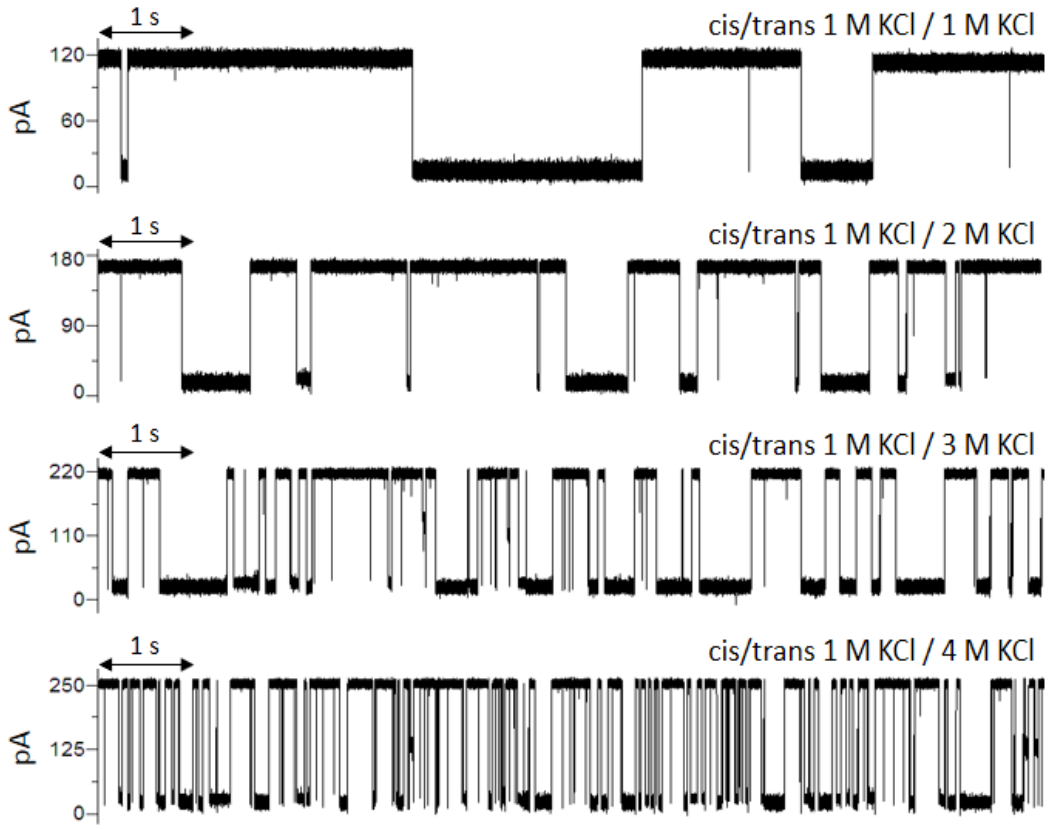

Figure 5.1. Representative current traces in the presence of 100 nM miDNA155-P155 duplex at 120 mV at various (*cis/trans*) salt gradients.

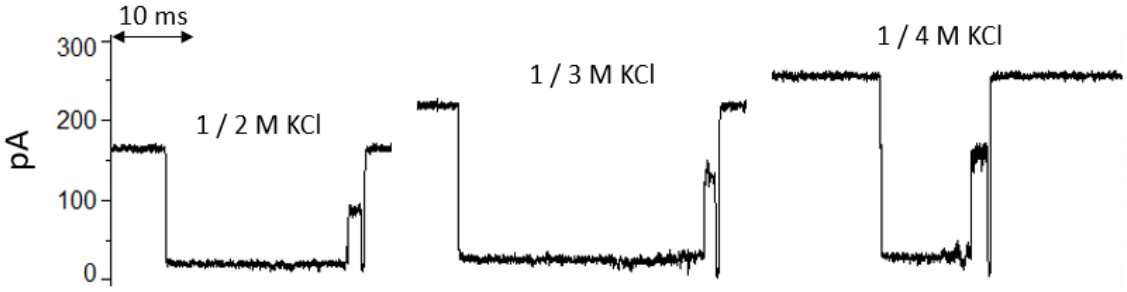

Figure 5.2. Resistive pulses of the miDNA155-P155 in salt gradient conditions at 120 mV. *Cis* side solution was constant 1 M KCl while the concentration of KCl in *trans* varied from 2 to 4 M KCl. The multilevel (level -1 to level -3) block signature was observed just like in the symmetrical 1 M KCl.

The specific multilevel restive pulses produced with the miDNA155-P155 duplex were observed for all investigated salt gradients. Pore current along with dwell times, interevent times and event frequencies obtained in various salt gradients are shown in Table 5.1. The time constants representing mean dwell time and interevent interval were obtained by fitting the events histograms with an exponential log probability function as described in Section 4.4.1.

Table 5.1. Dwell time and interevent time along with the frequency of the 100 nM miDNA155-P155 duplex in (*cis/trans*) KCl gradients at the 120 mV. The data are presented as a mean ± S.D for three different experiments.

$[KCl]_{cis}$ / $[KCl]_{trans}$	**Pore current at 120 mV** (pA)	**τ_{off} (ms)**	**τ_{on} (ms)**	***f*** **(s^{-1})**
1/1	118 ± 4	1040 ± 12	5167 ± 1264	0.20 ± 0.04
1/2	172 ± 12	276 ± 57	973 ± 231	1.05 ± 0.25
1/3	219 ± 2	108 ± 27	354 ± 36	2.84 ± 0.28
1/4	254 ± 3	67 ± 3	190 ± 28	5.33 ± 0.85

As shown in Table 5.1, the capture frequency increased with the concentration of KCl in *trans* side. Capture frequency increased exponentially from 0.2 ± 0.04 s^{-1} in symmetrical 1 M KCl to 5.33 ± 0.85 s^{-1} in 1/ 4 M (*cis/trans)* KCl which is a significant ~ 30-fold enhancement (Figure 5.3). On the other hand, the dwell time decreased exponentially from 1042 ± 13 ms in symmetrical 1 M KCl (*cis/trans*) conditions to 67 ± 3 ms in 1 / 4 M KCl gradient.

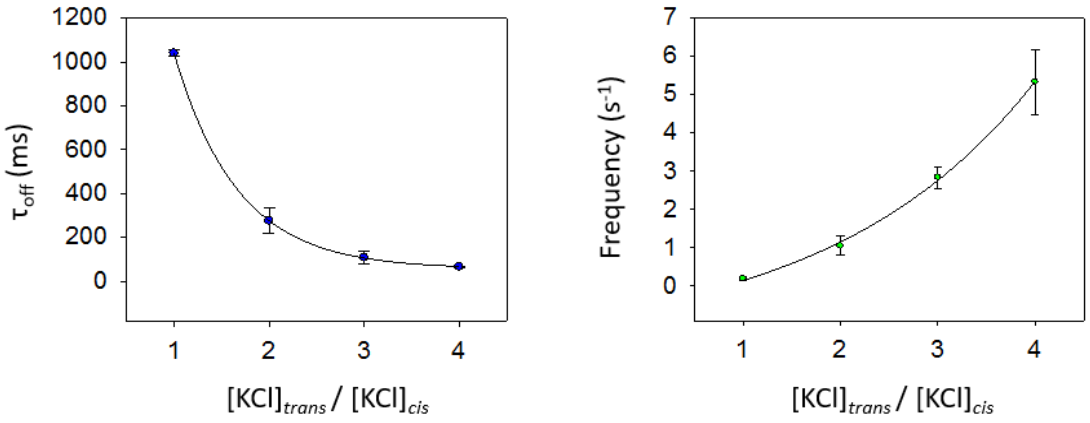

Figure 5.3. Dwell time and capture frequency of the 100 nM miDNA155-P155 under various KCl gradients with 1 M KCl concentration in the *cis* compartment and 1-4 M KCl concentration in *trans* compartment. The solid lines present exponential fit to the data points.

The increased capture frequency in the salt gradient conditions is attributed to a locally enhanced electrical field near the *cis* pore entrance [151, 159, 216]. The locally enhanced electrical field is generated by the accumulation of cations near the *cis* entrance in order to meet the requirement for continuous current flow along the pore axis [151, 159, 216]. Therefore, the negatively charged molecule, such is miDNA155-P155 duplex, experience stronger electrophoretic force leading to

increased capture frequency and shorter dwell time. However, Wanunu *et al.* on their work with the SiN nanopore showed that dwell time of dsDNA increased with the magnitude of the salt gradient [151]. The SiN nanopore has a negatively charged surface that contributes to the substantial EOF in the opposite direction of DNA translocation through the SiN pore [151, 159, 217]. Moreover, in the salt gradient conditions where $[KCl]_{trans} > [KCl]_{cis}$ the EOF has further enhanced inside SiN nanopore in the *trans-cis* direction, opposite of the DNA motion through the pore [151, 161, 218]. On the contrary, the αHL pore has heterogeneous charge distributions and it was demonstrated that EOF has a minor influence on the charged polymer translocation [165, 166, 219]. Jeon and Muthukumar showed, in their study on the capture of poly(styrenesulphonate) (NaPSS) by the αHL, that the capture frequency increased almost 20 times in 0.2 / 2 M KCl gradient compared to the symmetrical 1 M KCl [165]. In their other study, the dwell time of 35k NaPSS decreased from 1.6 ms in 1 / 1 M KCl to 1 ms in 0.5 / 1 M KCl *cis/trans* at 140 mV [166].

In our previous experiments with the miDNA155-P155 duplex in symmetrical 1 M KCl, we observed the increase of the 5'- entries of the duplex with the voltage with the respect to 3'-entries (Section 4.7 and Section 4.11). This indicates that, with higher electrophoretic force, subtle geometrical restrains for the 5' - 3' direction capture becomes less important. Figure 5.4 shows the level-1 amplitude of the miDNA155-P155 duplex in the salt gradient conditions at 120 mV. The percentage of 5'- assigned events increased from 25% in symmetrical 1 M KCl to 40 % in 1 / 2 M KCl and further to 43% in 1 / 4 M KCl. These ratios are similar to those obtained in 1 M KCl at the higher voltage (180 mV) where the number of events associated with 5' and 3'-entries was almost the same (see section 4.7). This observation confirms that enhanced electrophoretic force is acting on the DNA duplex in the salt gradient.

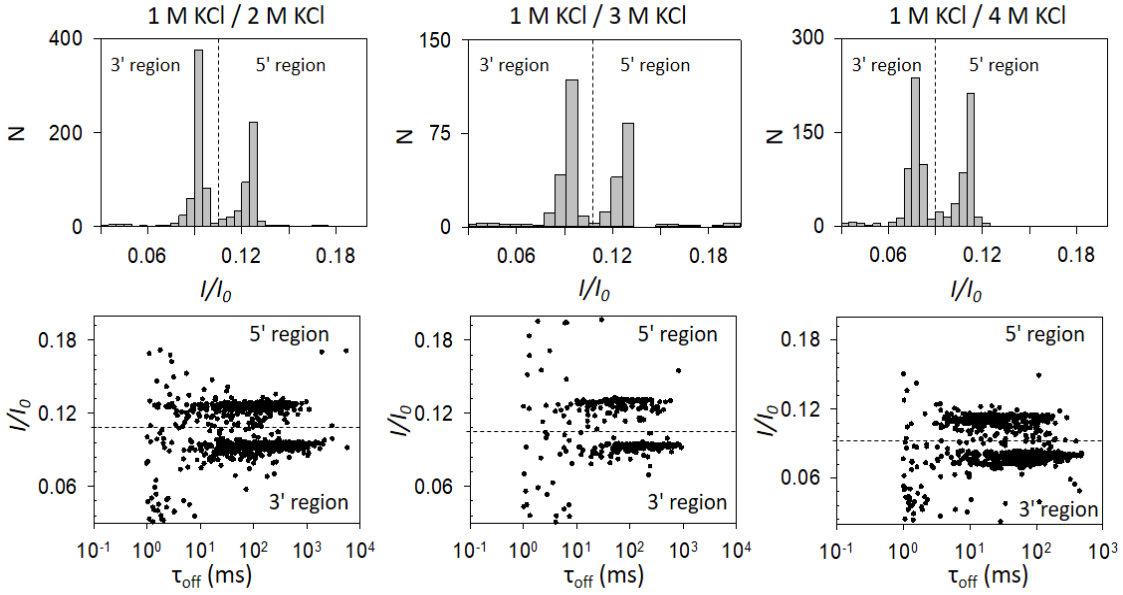

Figure 5.4. Distribution of level-1 I/I_0 and τ_{off} values for the 100 nM miDNA155-P155 duplex at 120 mV in three different salt gradients. The dashed lines present visually inspected boundary between events with shallower amplitude assigned to 5' entry and events with deeper amplitude associated with 3'entry.

Furthermore, electrostatic DNA- pore interactions in the salt gradient conditions might be altered. We have shown that in 1 M LiCl the capture frequency of miDNA155-P155 duplex is higher at 180 mV than in 1 M KCl at the same voltage. The current asymmetry ratio in 1 M LiCl was the lowest compared to other electrolytes which was attributed to the capability of Li^+ ions to bind to negatively charged amino acids (D127 and D128) at *trans* entrance of αHL pore that are main contributors to the αHL current asymmetry [155]. These amino acids act repulsively on negatively charged DNA molecule. The maximal distance at which electrostatic effect of a charged particle persists in the electrolyte solution is determined by the Debye length. In 1 M KCl, the Debye length has a value of ~ 0.3 nm which means that electrostatic repulsion might have a considerable effect on the translocation of a negatively charged molecule through the 2 nm wide pore [152]. Wong and Muthukumar showed that protonation of D127 and D128 by lowering the pH in the *trans* compartment to 4.5 resulted in decreased pore current asymmetry ratio (I/I_0 = 1.06) and increased capture frequency of the negatively charged NaPSS [152]. Reason being the decreased electrostatic repulsion between the αHL beta barrel and negatively charged NaPSS. The values of current asymmetries in various $[KCl]_{cis}$ / $[KCl]_{trans}$ gradients that are used in this work and the Debye length for $[KCl]_{trans}$ are shown in Table 5.2

Table 5.2. Current asymmetry ratios of αHL pore under various salt gradients and Debye length value for the $[KCl]_{trans}$. The I (+V) / |I (-V)| ratio was obtained by dividing the current value at +120 mV with the absolute current value measured at -120 mV.

KCl salt concentration [*cis*] / [*trans*]	**I (+V) / | I (-V)| For a voltage of ± 120 mV**	**Debye length (nm)**
1 / 1	1.40 ± 0.02	0.30
1 / 2	1.32 ± 0.05	0.21
1 / 3	1.21 ± 0.02	0.18
1 / 4	1.18 ± 0.01	0.15

The pore current asymmetry ratio reduced from 1.40 in symmetrical 1 M KCl to 1.18 in 1 / 4 M KCl indicating stronger shielding of the pore charges at the *trans* entrance Therefore, the high salt concentration in the *trans* compartment might affect the electrostatic interactions between the duplex and the αHL pore. However, in their work with NaPSS, Jong and Muthukumar did not observe significant changes in the dwell time when the concentration of KCl in the *trans* compartment was changed from 0.5 to 1.5 M, while the concentration of KCl in the *cis* compartment was 1 M [166]. The reason for this might be that the gradients they used were not as steep as those adopted in this work. Although the capture frequency of the miDNA155-P155 duplex increased in salt gradient the unspecific pore blockages in salt gradient conditions at 120 mV were observed more frequently than in symmetrical 1 M KCl at the same voltage (Figure 5.5).

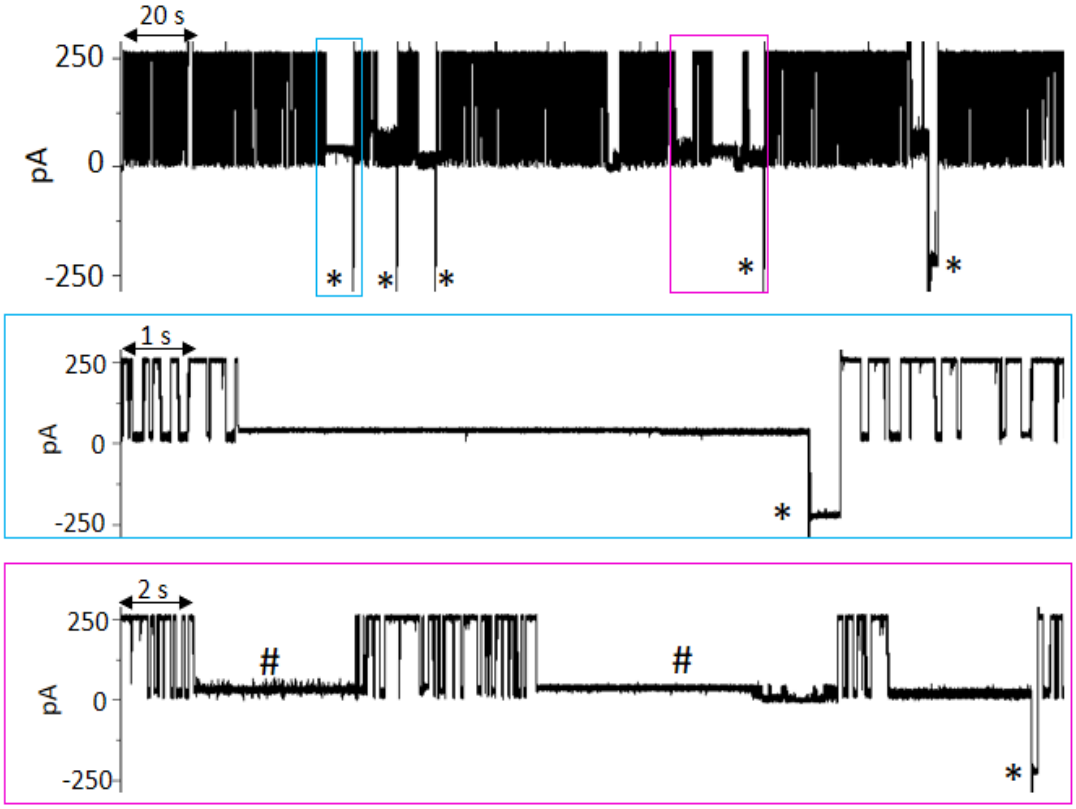

Figure 5.5. Single- channel current trace recorded at +120 mV in 1 M / 4 M KCl (*cis/trans*) gradient in the presence of 100 nM miDNA155-P155 duplex. The traces in blue and magenta boxes show zoomed-in unspecific pore blockages. Certain pore blockages are long and voltage reversal needed to be applied to reopen the pore (black asterisks). In some cases, pore current can restore itself without applying reversal voltage (black hashtags).

Although the pore blockages were observed more frequently, capture frequency of the miDNA155-P155 duplex was significantly higher than in symmetrical 1 M KCl at 120 mV, which considerably reduces the recording time for collection of sufficient events for statistical analysis. In order to relate the concentration of miRNA-DNA duplex to event frequency ~200 events are required to restrict the error to 5%. For example, it takes only ~ 51 seconds (200*0.190 s + 200 *0.067 s) to collect 200 resistive pulses produced by the 100 nM miDNA155-P155 duplex in 1 / 4 M KCl at 120 mV compared to the duration of 20 minutes in symmetrical 1 M KCl at 120 mV.

5.1.2 Influence of KCl concentration in *cis* side on duplex capture frequency and translocation time

The capture frequency increased exponentially while increasing the salt concentration in the *trans* compartment and keeping the KCl concentration at 1 M in the *cis* compartment (Figure 5.3). As expected, the highest capture frequency was found in the 4-fold gradient (1 / 4 M KCl), with an increase of 27 times compared to symmetrical 1 M KCl conditions. Considering that 4 M KCl is near the solubility limit of KCl at room temperature (~4.5 M), the effect of the salt gradient was subsequently investigated by maintaining the concentration in *trans* chamber at 4 M KCl while

varying the $[KCl]_{cis}$ from 2 M KCl to 0.1 M KCl. The pore current was recorded with an applied potential of 120 mV in the presence of 100 nM miDNA155-P155 duplex. Some representative αHL current traces under these conditions are shown in Figure 5.6

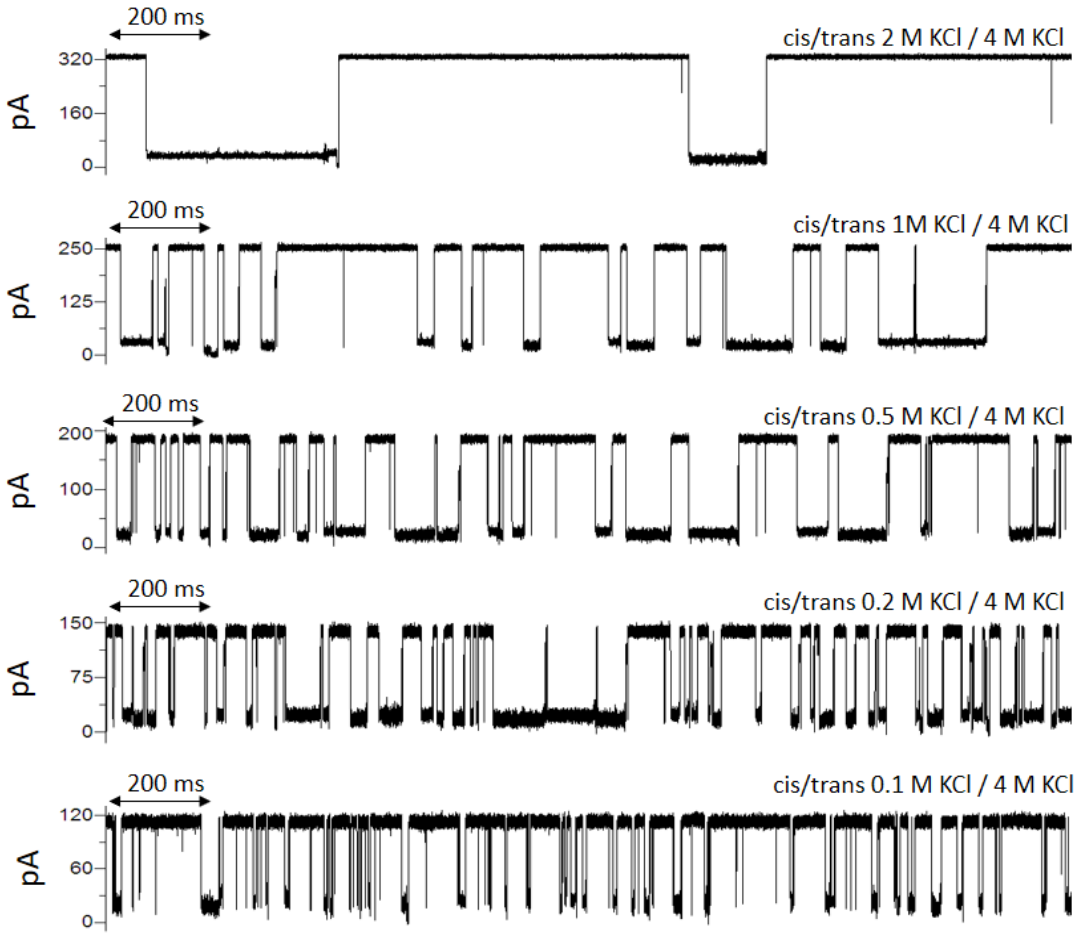

Figure 5.6. Representative αHL current traces, recorded at +120 mV, in the presence of 100 nM miDNA155-P155 duplex in *cis* compartment for various KCl salt (*cis/trans*) gradients.

By lowering the concentration in the *cis* compartment, the magnitude of the salt gradient increased which resulted in an increased capture frequency and a reduced dwell time. This is in agreement with the work on negatively charged NaPSS published by Muthukumar group [166]. As proposed, the degree of counterion absorption of the negatively charged polymer decreased by the lowering the salt concentration in the donor *cis* compartment [166]. This resulted in a stronger electrophoretic force acting on the negatively charged polymer leading to decreased dwell time and increased capture frequency of the negatively charged polymer [166]. The values of the dwell and interevent time along with the pore current and capture frequency are shown in Table 5.3

Table 5.3. Dwell time, and interevent time along with the frequency of 100 nM miDNA155-P155 duplex for (*cis/trans*) KCl gradients at the 120 mV and the pH=8.

$[KCl]_{cis}/[KCl]_{trans}$	I_0 at 120 mV (pA)	τ_{off} (ms)	τ_{on} (ms)	f (s^{-1})
2/4	323 ± 4	415± 10	1245 ± 157	0.81 ± 0.1
1/4	254 ± 3	66.7 ± 3.4	190 ± 28	5.33 ± 0.85
0.5/4	191 ± 6	33.5 ± 9	80.52 ± 7	12.5 ± 1
0.2/4	147 ± 7	15.36 ± 5.7	37.97 ± 7.8	26.90 ± 5.53
0.1/4	125 ± 12	5.34 ± 0.9	26.8 ± 5.3	38.20 ± 8.12

The capture rate increased exponentially from 0.81 ± 0.1 s^{-1} in 2 / 4 M KCl to 38.2 ± 8.1 s^{-1} for 0.1 / 4 KCl, while dwell time decreased from 415 ± 10 ms in 2 / 4 M KCl to only 5.44 ± 0.5 in 0.1 / 4 M KCl gradient. When compared to symmetrical 1 M KCl solution, the 40-fold gradient (0.1/ 4 M KCl) capture rate increased almost 200 times at 120 mV.

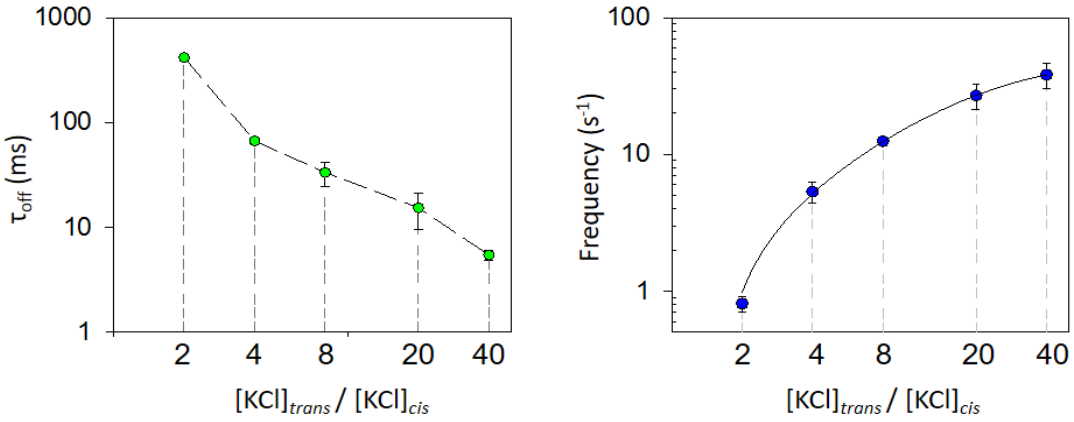

Figure 5.7. Dwell time and capture rate of 100 nM miDNA155-P155 duplex in different KCl salt gradients at +120 mV. The concentration of KCl in *trans* side is set to 4 M KCl, while the concentration of KCl in *cis* compartment varied from 0.1 M to 2 M.

Although the capture rate was vastly improved in high salt gradients compared to symmetrical 1 M KCl conditions, the high gradients (0.1 / 4 M KCl and 0.2 / 4 M KCl) destabilized the lipid bilayer and pore clogging was a more frequent event (Figure 5.8). Nonspecific αHL pore closures in low KCl concentrations (200 mM) have been previously reported and are believed to originate from the different electrostatic interactions between the charged amino acid pairs inside the pore [220]. The pore current under high salt gradient conditions could be monitored for a maximum of a couple of minutes before the bilayer was disrupted or a permanent pore closure occurred.

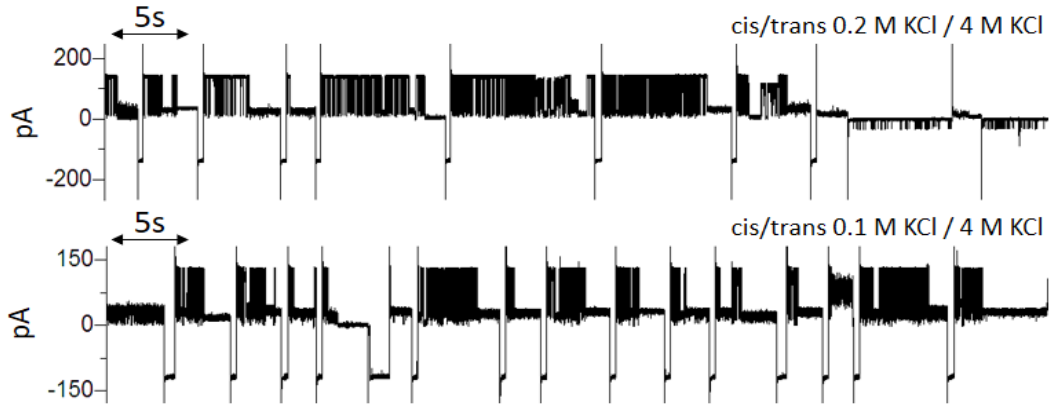

Figure 5.8. Representative 1 min trace of a single αHL pore in the presence of 100 nM miDNA155-P155 duplex in 20-fold and 40 –fold KCl gradient at 120 mV. The pore clogged frequently and the reversal voltage was applied frequently in order to reopen the αHL pore.

In this work, the 8 – fold gradient (0.5 / 4 M KCl) was selected as a good compromise for the miRNA detection. The analysis of resistive pulses of the 100 nM miDNA155-P155 in 8- fold gradient at 120 mV is shown in Table 5.4. Pore closures were observed more frequently compared to 1 M KCl conditions, but it was still possible to monitor the pore current for ~ 20 minutes. The longest pore activity that has been observed under 0.5 / 4 M KCl conditions was 45 min. The capture rate of 100 nM miDNA155-P155 duplex in 0.5 / 4 M KCl gradient was found to be 12.5 s^{-1}, 60-fold higher compared to symmetrical 1 M KCl solution and 2 times higher compared to the capture rate in the presence of a 1 / 4 M KCl gradient. The average dwell time of miDNA155-P155 in 0.5 / 4 M KCl salt gradient at +120 mV was found to be 33.5 ± 9 ms, showing a 30-fold decrease compared to the symmetrical 1 M KCl. Hence, for a collection of 200 resistive pulses of 100 nM miDNA155-P155 at 120 mV the required time of recording would be 23 s (200 * 0.0805s+ 200 * 0.0335 s).

Table 5.4. Analysis of 100 nM miDNA155-P155 resistive pulses in 0.5 / 4 M KCl at 120 mV from five independent experiments.

N	Open-pore current (pA)	Total number of events	Recording duration (s)	All-trace frequency (s^{-1})	τ_{on} ± S.E. (ms)	$1/\tau_{on}$ frequency (s^{-1})	τ_{off} ± S.E. (ms)
1	188.6	456	50.6	9.01	92 ± 12.3	10.87	25.2 ± 4.3
2	194.0	460	34	13.53	81.4 ± 11.0	12.29	23.8 ± 2.6
3	186.5	1411	118	11.95	76.8 ± 13.2	13.02	34.0 ± 2.4
4	185.0	1367	120	11.39	78.6 ± 16.6	12.72	43.2 ± 4.6
5	199.0	911	70	13.01	73.81 ± 15.1	13.55	41.5 ± 4.5
All	**191±5.6**	-	-	**11.76 ± 1.74**	**80.52 ± 6.98**	**12.49 ± 1.02**	**33.5 ± 9.0**

5.1.3 Voltage influence on capture frequency and dwell time under salt gradient

The influence of voltage on the capture frequency and dwell time of 100 nM miDNA155-P155 DNA duplex was determined for various salt gradients across the nanopore. The dwell time, interevent time and capture frequency were obtained in various gradients at 120 , 150 and 180 mV (Table 5.5).

Table 5.5. The dwell time and capture frequency for 100 nM miDNA155-P155 duplex in various *cis/trans* salt KCl conditions at the voltages of 120, 150 and 180 mV. The preferred salt gradient (0.5/4 M KCl) is highlighted in grey.

	Voltage (mV)					
Gradient $[KCl]_{cis}$ / $[KCl]_{trans}$	**120**		**150**		**180**	
	τ_{off} **(ms)**	f (s^{-1})	τ_{off} **(ms)**	f (s^{-1})	τ_{off} **(ms)**	f (s^{-1})
1 / 4	66.7 ± 3.4	5.33 ± 0.85	5.1 ± 0.2	14.7 ± 3	2.5 ± 0.2	22.6 ± 5.6
0.5 / 4	33.50 ± 9.0	12.5 ± 1	3.6 ± 0.61	35 ± 5	1.78 ± 0.21	65.7 ± 4.6
0.5 / 3	47.3 ± 2.6	6.71 ± 0.41	3.76 ± 1	17.4 ± 1.9	1.51±0.16	29.4 ± 4.5
0.2 / 4	15.36 ± 5.7	26.90± 5.53	2.4 ± 0.17	67.1 ± 17.0	1.2 ± 0.3	98.4 ± 12.9
0.1 / 4	5.34 ± 0.9	38.30 ±8.12	2.0 ± 0.95	68.7± 10.3	1.3 ± 0.83	116 ± 19.8

The 0.5 / 3 M KCl gradient was additionally investigated since this gradient was used in previous works [19]. However, the capture frequency of 100 nM miDNA155-P155 duplex under 0.5 / 3 M KCl at 120 mV was two times lower compared to 0.5 / 4 M KCl gradient used in this work. The capture rate increased with voltage for every salt gradient but the dwell times decreased to ~ 2 ms at 180 mV for each gradient which is close to 1 ms cut-off criterion for event acceptance. The highest capture rate was obtained with 0.1 / 4 M KCl (*cis*/ *trans*) at 180 mV had the value of 116 ± 19.8 s^{-1}.

Unlike symmetrical 1 M KCl, where the dwell time was too long at voltages below 120 mV, hence dwell and interevent times could not be determined, under salt gradient conditions, the minimum voltage required for dehybridization of the DNA duplex was lower. For example, with the selected 8- fold gradient it was possible to achieve dehybridization for voltages in the range 100-180 mV. In this spectrum, the capture frequency increased exponentially with the voltage (Figure 5.9). The event frequency at 100 mV was only 1.03 ± 0.22 s^{-1} and the dwell time was 700 ms. An increase of only 20 mV reduced the dwell time 20-fold and increased the frequency by ~12 fold.

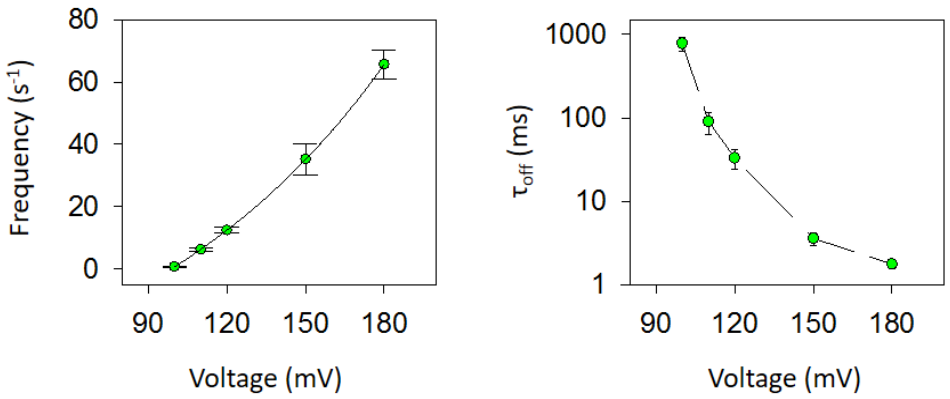

Figure 5.9. Event frequency increases exponentially with the applied voltage in the voltage range from 100-180 mV (Left panel). The dwell time (τ_{off}) decreased non -linearly with applied voltage.

At higher voltages, the dwell times were close to 1 ms cut-off acceptance criterion, 150 mV (3.6 ms) and 180 mV (1.78 ms). Therefore, the 120 mV was again selected as a voltage at which the quantification of miRNA-DNA duplex will be carried out in salt gradient conditions.

5.1.4 Residual amplitude of the DNA duplex resistive pulse under salt gradient conditions

The miDNA155-P155 duplex produced the specific electric signature consisting of three levels in every gradient. The resistive pulse signatures amplitudes produced by the miDNA155-P1555 duplex in various KCl salt gradients at 120 mV are shown in Table 5.6. The bimodal amplitude of level-1 was observed for every salt gradient. Levels 2 and 3 increased with the salt gradient magnitude. The residual current amplitude of level-2 increased from 0.54 ± 0.04 in 2/ 4 M KCl to 0.95 ± 0.03.

Table 5.6. Resistive pulse amplitude values for level 1, 2 and 3 obtained from single experiments under various $[KCl]_{cis}$ / $[KCl]_{trans}$ gradients at +120 mV (*trans* side positive).

	Level residual amplitude (I/I_0)			
$[KCl]_{cis}$ / $[KCl]_{trans}$	**1**		**2**	**3**
2 / 4	0.067 ± 0.003	0.102 ± 0.023	0.54 ± 0.04	0.05 ± 0.02
1 / 4	0.078 ± 0.003	0.11 ± 0.0025	0.65 ± 0.03	0.08 ± 0.015
0.5 / 4	0.096 ± 0.004	0.133 ± 0.004	0.72 ± 0.03	0.11 ± 0.001
0.2 / 4	0.12 ± 0.007	0.165 ±0.004	0.83 ± 0.02	0.13 ± 0.04
0.1 / 4	0.157 ± 0.011	0.197 ± 0.016	0.95 ± 0.03	0.15 ± 0.04

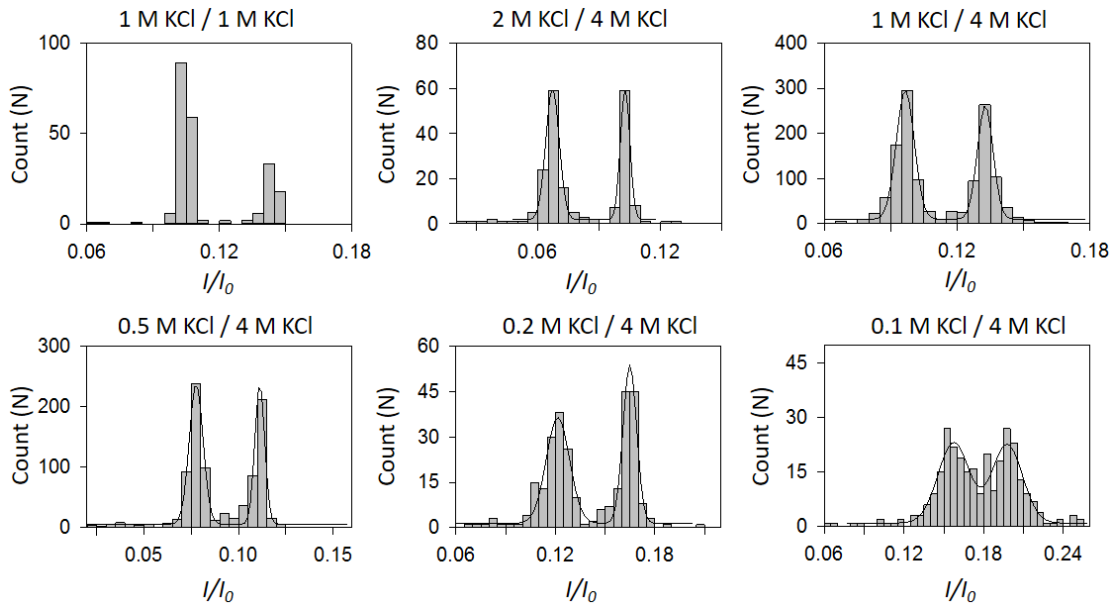

Figure 5.10. Histograms showing level 1 amplitude of miDNA155-P155 duplex under various KCl salt gradients. The voltage was set so the *trans* side was at +120 mV to the *cis* side. In all KCl salt conditions, the bimodal residual amplitude of level 1 was observed.

If we compare the event current histograms of miDNA155-P155 at 1M KCl with those obtained under salt gradients it is obvious that the number of events associated with 5'-entry is increased Figure 5.10.

The duration and number of events assigned to 5' and 3'-entries of the miDNA155-P155 were analysed for five independent experiments under 0.5 / 4 M KCl salt gradient at 120 mV (Figure 5.11). Based on histogram amplitude analysis of the 100 nM miDNA155-P155 duplex, the number of events assigned to 3' was similar to the one assigned to 5'-entry. The dwell time of miDNA155-P155 events assigned to 3'entry was found at 42.4 ms, 1.8 longer compared to the one of events assigned to 5' entry. (Figure 5.11 and Table 5.7).

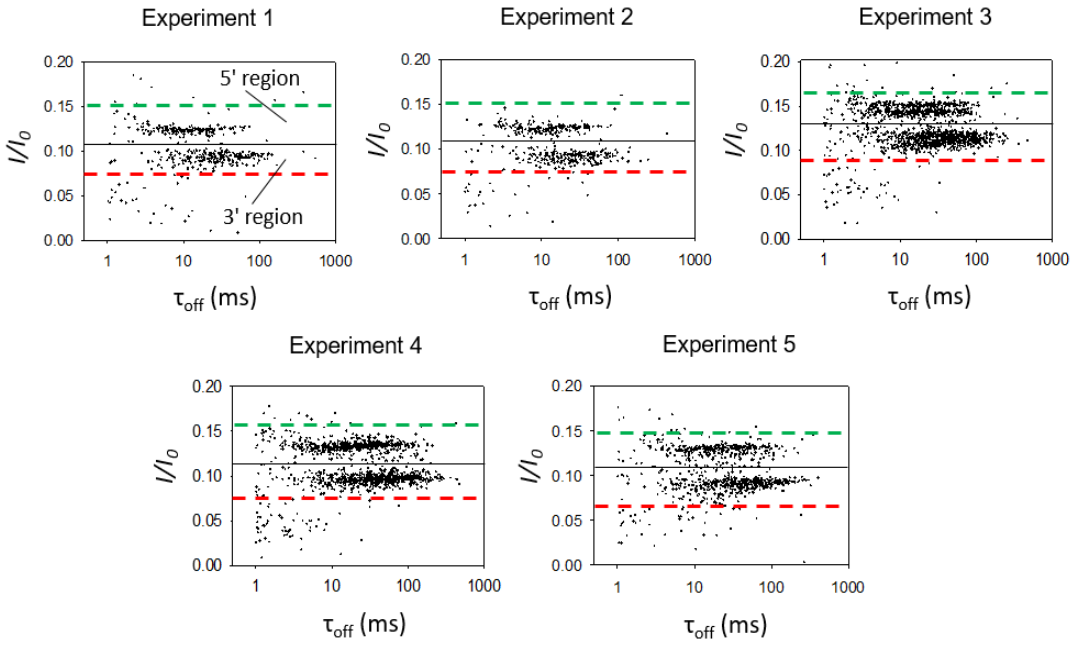

Figure 5.11. Amplitude vs dwell time distribution of 100 nM miDNA155-P155 duplex resistive pulses under *cis/ trans* 0.5 / 4 M KCl gradient at 120 mV. The region between solid black and dashed green line was assigned to 5' entry while regions between solid black and dashed red lines were assigned to 3' entry.

The duration and amplitudes of 5' and 3'-associated events are shown in Table 5.7

Table 5.7 Analysis of single experiments with 100 nM miDNA155-P155 duplex in asymmetrical 0.5 / 4 M KCl (*cis/trans*) KCl at 120 mV, with assignment of 5' and 3' -entry events.

N	I / I_0		Number of events			τ_{off} (ms)	
	3' entry	5' entry	Total	3' entry	5' entry	3' entry	5' entry
1	0.093	0.123	456	232 (54.2%)	196 (45.8%)	33.7	12.7
2	0.091	0.123	460	231 (52.9%)	206 (47.1%)	29.71	16
3	0.110	0.146	1411	763 (56.3%)	592 (43.7%)	41.5	24.4
4	0.097	0.133	1367	697 (54.7%)	577 (45.3%)	56.4	31.3
5	0.091	0.13	911	501 (57.5%)	370 (42.5%)	50.7	30.3
All	**0.096 ± 8.2%**	**0.131 ± 7%**	-	**55.1%**	**44.9%**	**42.4 ± 11.2**	**22.9 ± 8.4**

5.1.5 Dependence of level 1 bimodal amplitude on miDNA sequence

In order to test the influence of double level amplitude and different durations of 5' and 3'entrances, the miDNA21 target was annealed with corresponding probe P21 modified with the dC_{30}

overhang at both of its ends. The amplitude of level-1 block was again found to be bimodal in both asymmetric 0.5 / 4 M KCl and symmetric 1 / 1 M KCl experimental conditions. Similarly, to miDNA155-P155 the number of the blocks under the 3' end was higher than compared to 5' end. The duration of the events assigned to 3' region was 5 times longer compared to duration of events assigned to 5'-entry first.

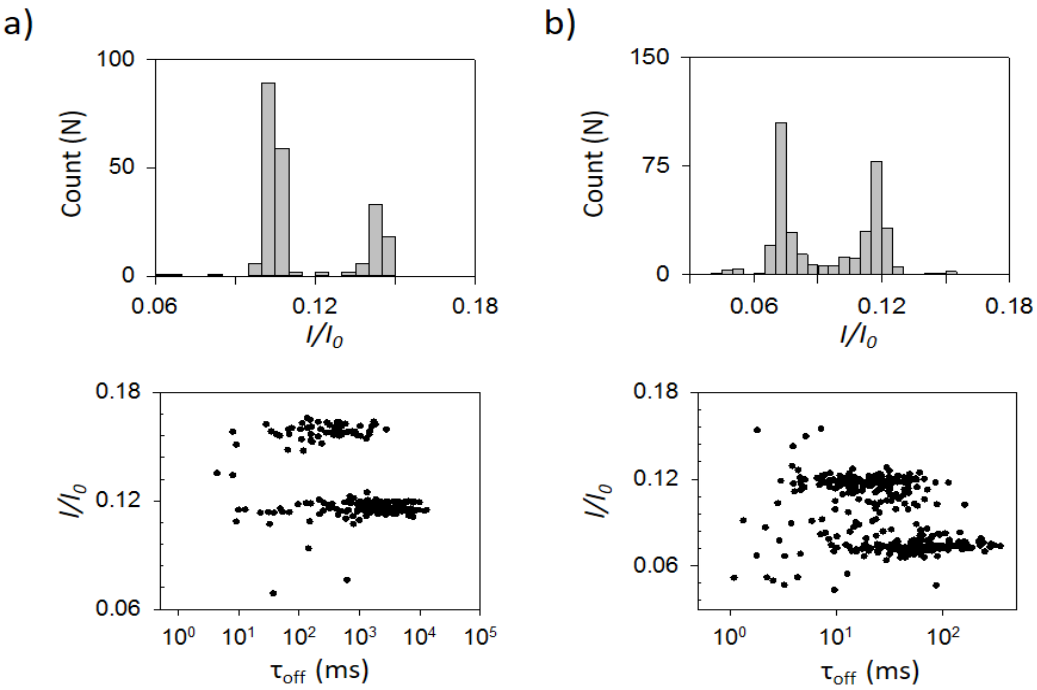

Figure 5.12. a) The histogram of level 1 amplitude distribution for 100 nM miDNA21-P21 for symmetrical *cis/trans* 1 M KCl conditions at 120 mV (upper panel). The distribution of level 1 I/I_0 and τ_{off} values for symmetrical *cis/trans* 1 M KCl conditions at 120 mV (lower panel). b) The histogram of level 1 amplitude distribution for 100 nM miDNA21-P21 for asymmetrical *cis/trans* 0.5 / 4 M KCl conditions at 120 mV (upper panel). The distribution of level 1 I/I_0 and τ_{off} values for asymmetrical *cis/trans* 0.5/ 4 M KCl conditions at 120 mV (lower panel).

The bimodal amplitude was again found just like for the miDNA155-P155 duplex with the probe elongated with poly $(dC)_{30}$ overhang from its both ends. From the Figure 5.12 it can be seen that the duration of the dwell times associated with 3'-first entry is longer compared to shallower 5'-first entry. The analysis of 100nM miDNA21-P21 duplex sidedness entrances in symmetrical 1 M KCl and asymmetrical 0.5 / 4M KCl *cis/trans* is given in Table 5.8.

Table 5.8. Analysis of single experiments with 100 nM miDNA21-P21 duplex in symmetrical 1 M KCl at 120 mV and asymmetrical *cis/trans* 0.5 / 4 M KCl at 120 mV, with the assignment of 5' and 3'-entry events.

Salt condition [*cis*] / [*trans*]	***I* / I_0**		**Number of events**			**τ_{off} (ms)**	
	3' entry	**5' entry**	**Total**	**3' entry**	**5' entry**	**3' entry**	**5' entry**
1 M/ 1 M	0.116	0.156	225	151 (70.9%)	62 (29.1%)	2134 ± 144	437 ± 216
0.5M / 4 M	0.073	0.118	372	182 (51.1%)	174 (48.9%)	67 ± 17	20.4 ± 4.7

The number of events assigned to deeper 3'-entry was again almost three times larger compared to 5'-first entry of miDNA21-P21 duplex in symmetrical 1 M KCl conditions. The duration of events associated with 3'-entry was ~ 5 times longer compared to 5'- entry.

In asymmetrical 0.5 / 4 M KCl the number of events associated with 3' and 5'-entries were almost identical (51.1% and 49.8%). The duration of events assigned to first 3' prime entry was three times longer compared to events associated with 5' prime end.

5.2 Influence of dC_{30} DNA probe extension on block amplitude and duration in salt gradient conditions

Analysis of resistive pulses of miDNA155-P155, miDNA21-P21 and miRNA155-P155 revealed the bimodal level-1 I/I_0 residual amplitude under all electrolyte and salt gradient conditions when P155 and P21 had poly $(dC)_{30}$ overhang attached at both ends. The experiments on miRNA155 and probes with single dC_{30} overhangs on 3' or 5' ends confirmed that the shallower block could be associated with the 5'-first entry, while the deeper amplitude corresponds to duplex entry from 3'-end. For both miDNA155-P155 and miDNA21-P21 duplexes, the number of level-1 events assigned with the 3'- entry was three times higher than the number of 5'-entry events when a low voltage was applied (< 120 mV) in 1 M KCl. The number of events associated with the 5'- entry significantly increased with the voltage in symmetrical 1 M KCl conditions for the miDNA155-P155 duplex and was almost the same as the number of 3'-entry events. A similar increase of the 5'- associated events was observed in salt gradient conditions.

In order to determine the influence of the probe modification with the dC_{30} on the DNA duplex parameters under salt gradient, the experiments with the single overhang probes: P155-5'-(dC_{30}) and P155-3'-(dC_{30}) were conducted in the 0.5 / 4 M KCl gradient at 120 mV.

5.2.1 DNA probe modified with dC_{30} at 5'-end

The resistive pulses produced under 100 nM of miDNA155-P155-5'-(dC_{30}) were collected at 120 mV in the 0.5 / 4 M KCl *cis/trans* gradient. The data analysis from a single experiment is shown in Figure 5.13. The results have been validated repeating the experiment 3 times, and the obtained parameters are shown in Table 5.9.

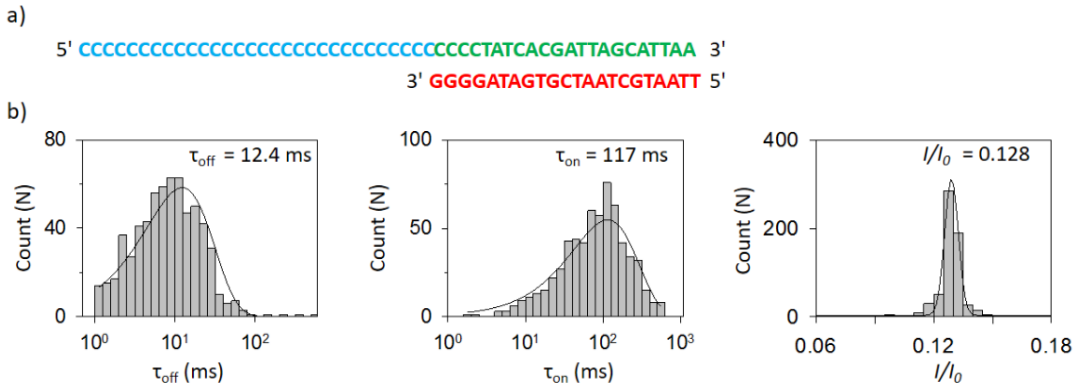

Figure 5.13. a) The miDNA155 (red) and P155-5'-(dC_{30}) probe sequences. b) The histogram of the dwell time (τ_{off}) and interevent time (τ_{on}) along with the current amplitude histogram obtained from collecting resistive pulses in the single experiment of 100 nM miDNA155-P155-5'-(dC_{30}) at 120 mV under 0.5 / 4 M KCl (*cis/trans*) conditions.

Table 5.9. The analysis of resistive pulse parameters from three independent experiments obtained with 100 nM miDNA155-P155-5'-(dC_{30}) probe at 120 mV in 0.5 / 4 M KCl.

N	I/I_0	τ_{off} (ms)	τ_{on} (ms)	f (s^{-1})
1	0.128	12.4 ± 2.7	117.0 ± 15.1	8.5 ± 1.1
2	0.128	11.8 ± 1.1	81.5 ± 9.2	12.3 ± 1.4
3	0.127	15.8 ± 3.7	116 ± 18	8.6 ± 1.3
Total	0.1276 ± 0.5 %	13.4 ± 2.1	104.8 ± 20.1	9.8 ± 2.1

5.2.2 DNA probe modified with dC_{30} at 3' end

Resistive pulses produced under 100 nM of miDNA155-P155-3'-($dC)_{30}$ were collected at the 120 mV in the 0.5 / 4 M KCl *cis/trans*. The data analysis from a single experiment is shown in Figure

5.14. The results have been validated repeating the experiment 3 times, and the obtained parameters are shown in Table 5.10.

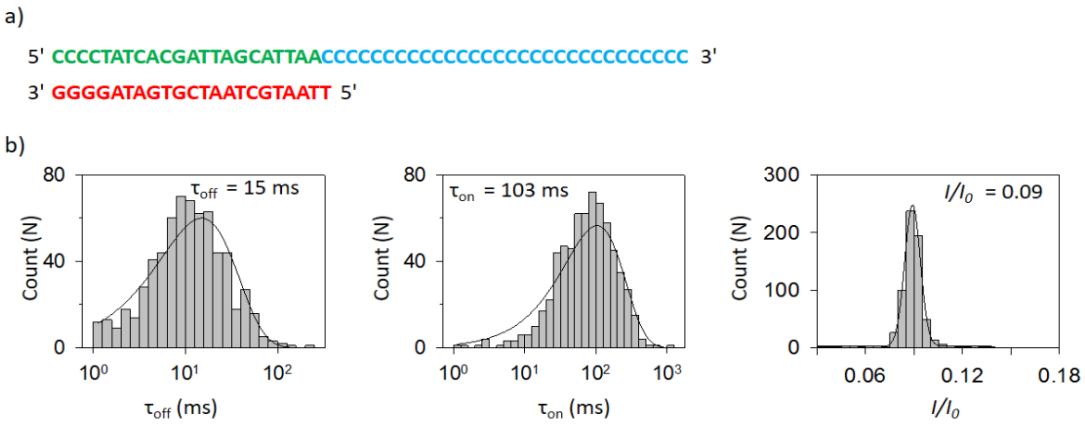

Figure 5.14. a) The miDNA155 (red) and P155-3'-(dC_{30}) probe sequences. b) The histogram of the dwell time (τ_{off}) and interevent time (τ_{on}) along with the current amplitude histogram obtained from collecting resistive pulses in a single experiment of 100 nM miDNA155-P155-3'-$(dC)_{30}$ at 120 mV under 0.5 / 4 M KCl (*cis/trans*) conditions.

Table 5.10. The resistive pulse parameters obtained with 100 nM miDNA155-P155-3'-$(dC)_{30}$ probe at 120 mV in 0.5 / 4 M KCl.

N	I/I_0	τ_{off} (ms)	τ_{on} (ms)	f (s^{-1})
1	0.09	15.0 ± 2.1	103.0 ± 14.3	9.7 ± 1.3
2	0.096	10.4 ± 2.3	77.0 ± 9.2	13 ± 1.6
3	0.096	13.6 ± 1.4	125.0 ± 11.5	8.0 ± 0.74
Total	0.094 ± 3.7 %	13.4 ± 2.1	102 ± 24	10.2 ± 2.5

Finally, in the presence of an equimolar 50 nM concentration of miDNA155-P155-3'-$(dC)_{30}$ and miRNA155-P155-5'-$(dC)_{30}$ in the *cis* chamber, the I/I_0 value of level- 1 adopted a bimodal distribution with I/I_0 values of 0.097 and 0.128 (Figure 5.15d)

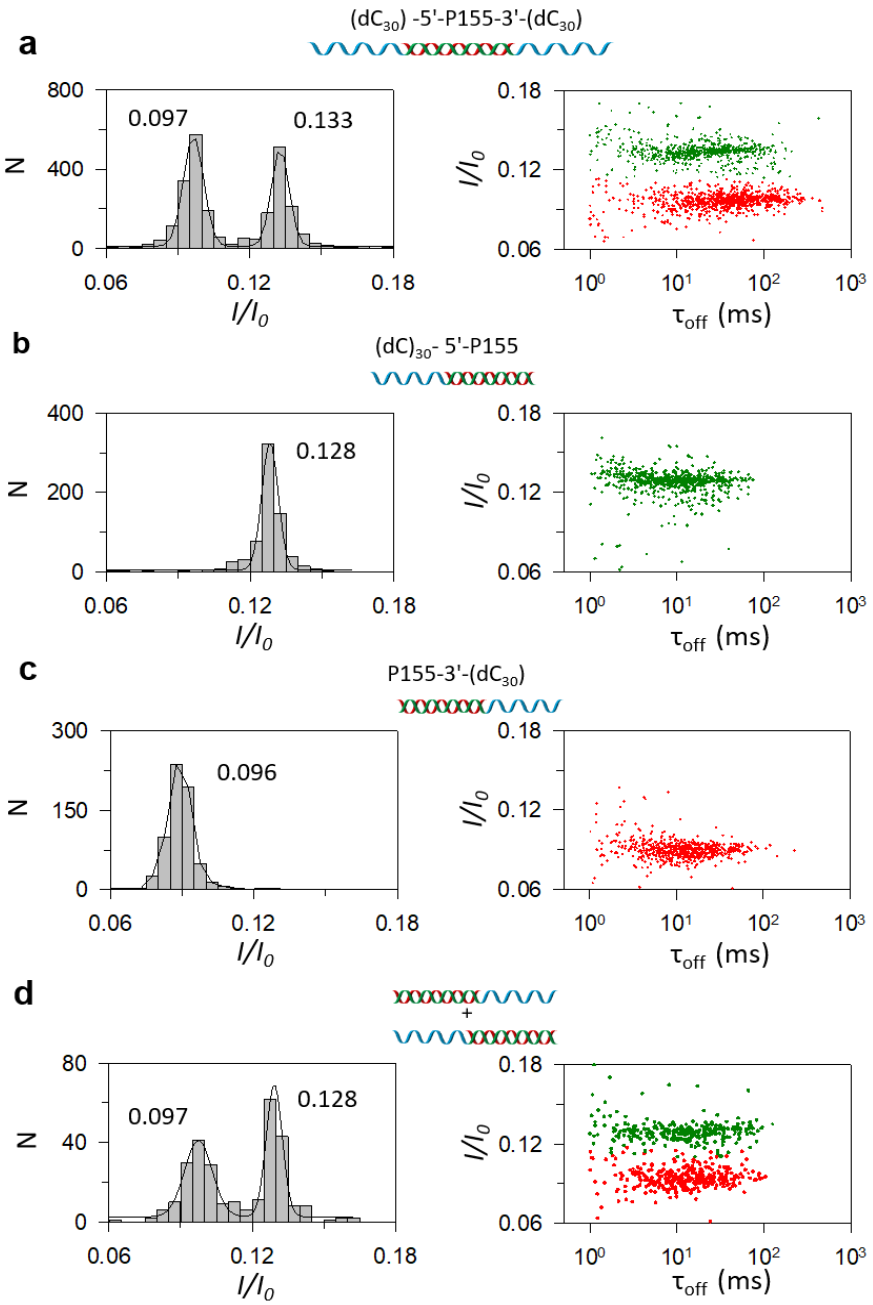

Figure 5.15. Level- 1 current block level and dwell time durations for miDNA155 hybridised with different probes. The events were collected in a single experiment at 120 mV in 0.5 / 4 M KCl *cis/trans*. a) The 100 nM miDNA155-P155 probe with double overhang gives bimodal distribution. Events with deeper residual amplitude (I/I_0= 0.096) had a mean dwell time of 56.4 ms, while shallower events (I/I_0= 0.133) had a dwell time of 31.3 ms. b) Duplexes with the P155-5'-$(dC)_{30}$ gave single amplitude level- 1 at 0.128 with the dwell time of 12.4 ms. c) duplexes with the P155-3'-$(dC)_{30}$ had single residual amplitude level at 0.096 I/I_0 and dwell time of 13.6 ms. d) A mixture of 50 nM miDNA155-P155-5'-$(dC)_{30}$ with 50 nM miDNA155-P155-3'-$(dC)_{30}$ had bimodal amplitude that is similar to miDNA155-P155 probe with double overhang

The experiments in asymmetrical 0.5 / 4 M KCl conditions with DNA probes with single capture overhangs confirmed that the deeper block amplitude observed for the miDNA-P155 probe with double overhang comes from the entry of duplex from its 3'- end first while shallower amplitude comes from the 5'- first entry. In symmetrical 1 M KCl solution at 120 mV the number of events assigned to 3'-entry first was three times higher compared to 5'-first entry. This was not the case

in the asymmetrical 0.5 / 4 M KCl salt gradient at 120 mV where the percentage of 5'-assigned events was 45% compared to 55% assigned to 3'-entry (Table 5.7). When the DNA probes with the singe overhang were used the similar capture frequencies were observed: ($9.8 \pm 2.1\ s^{-1}$) for P155-5'-$(dC)_{30}$ and $10.2 \pm 2.5\ s^{-1}$ for P155-3'-$(dC)_{30}$ in 0.5 / 4 M KCl gradient at 120 mV. These values are close to capture frequency of 12. 5 ± 1.1 observed with the double overhang P155 probe. However, the dwell times of duplexes with either 5' or 3'-end dC_{30} modification were about two times shorter than dwell time of miDNA155-155 duplex. Moreover, lack of the dC_{30} modification on either 5' or 3' end leaves one side of the duplex without extension (blunt end). In the next section, we will show that the duplex was not readily unzipped after it was captured from its blunt end with the αHL pore at 120 mV.

5.2.3 Resistive pulse signature of blunt-end DNA duplex

In the asymmetric 0.5 / 4 M KCl *cis/trans* at the 120 mV, the duplexes with miDNA155 hybridized to P155-5'-$(dC)_{30}$ and P155-3'-$(dC)_{30}$ produced specific level-1 signature upon traversing αHL pore. This specific signature comes from the duplex entry into the pore from its 'blunt' end [211, 221]. When blunt end entered the pore, the unzipping- associated level-1amplitude was rapidly fluctuating between two current stages (~ 20 and 50 pA), which is behaviour characteristic of the gating ion channel (Figure 5.17a,b). At the 120 mV, the deeper stage 1 had $I/I_0 = 0.11$, while the shallower stage 2 had $I/I_0 = 0.28$ (Figure 5.17b). The level-1 was followed by level-2 and level-3 that are characteristic for miDNA-DNA probe unzipping signature. Unfortunately, the unzipping duration of these rapidly fluctuating pulses was long > 5 s, so voltage reversal was applied in order to unclog the pore and continue recording (Figure 5.16a). At the higher voltages, unzipping of the DNA duplex from the blunt end was accelerated but the duration of blunt -end capture was about 100 times longer than ~ 2 ms duration of the overhang- end capture (Figure 5.16 bottom trace).

Although the capture frequencies for the duplexes with single overhangs was almost identical, the pore was frequently clogged by blunt end duplex entries. These blockages give an additional rise to the previously observed unspecific pore clogging in the salt gradient conditions and high voltages, which further complicates detection and analysis of the nanopore traces. In symmetrical 1 M KCl at 120 mV, the blunt-end blockages were not observed for either miRNA155- P155-5'-$(dC)_{30}$ or miRNA155- P155-3'-$(dC)_{30}$ duplexes, but the capture frequencies of these duplexes were significantly lower compared to the miRNA155-P155 duplex with a double overhang.

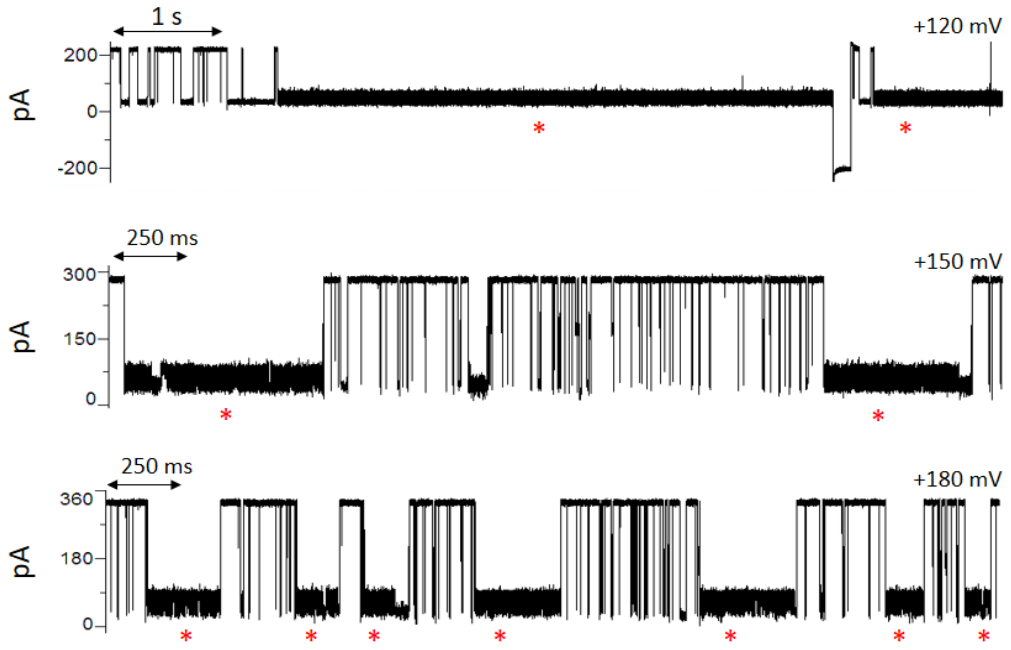

Figure 5.16. Current trace of the 100 nM miDNA155- P155-5'-$(dC)_{30}$ at the 0.5 / 4 M KCl salt gradient at the three different voltages. Blunt end translations through the pore are marked with red asterisks. At the low voltage (+ 120 mV), the level 1 block of blunt end DNA duplex entrance is long, hence the reverse polarity of potential was applied to re-establish current through the αHL pore. At the higher voltages >150 mV the unzipping of DNA duplex from the blunt end is more frequent and followed by level 2 and 3 current blocks characteristic for DNA duplex translocation.

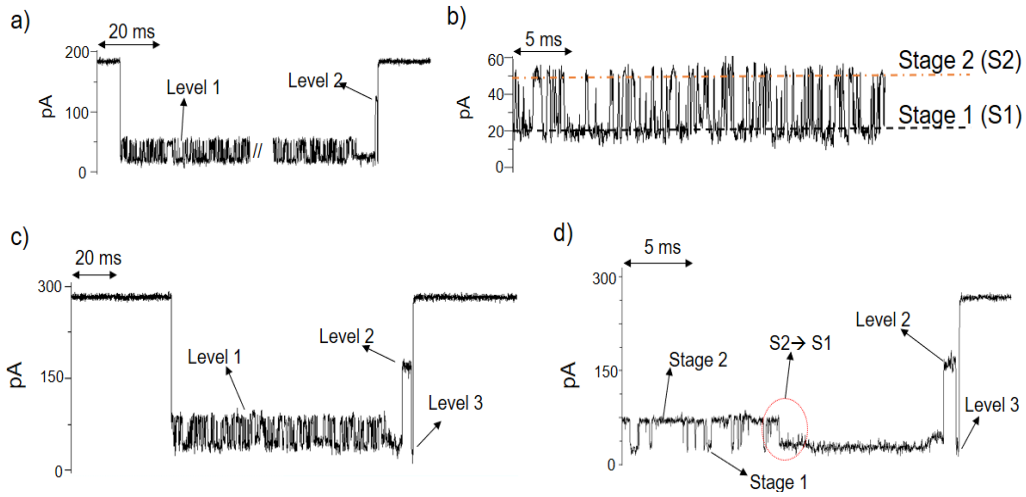

Figure 5.17. a) Blunt-end resistive pulse signature of the miDNA155- P155-5'-$(dC)_{30}$ duplex in 0.5 / 4 M KCl at 120 mV. b) The zoomed-in segment of blunt-end level 1. Current is fluctuating between stage 1 ~20 pA and stage 2 ~50 pA. c) Blunt end signature of miDNA155-(dC_{30}) -5'-P155 at +180 mV. Level 1 is followed by level 2 and level 3. d) The zoomed-in ending of the blunt-end capture event at +180 mV. Level-1 finishes with the transition of the shallower stage 2 to the deeper stage 1 (marked with the red circle) which is followed by level 2 and level 3.

5.3 Limit of the miDNA155-P155 duplex quantification under preferred salt conditions

After establishing 0.5 / 4 M KCl gradient, 120 mV as a preferred voltage and showing the importance of the double overhang extension of the DNA probe overhangs, the capture frequency of the miDNA155-P155 duplex was evaluated for a 10 pM to 100 nM range. The capture frequency for the 100 nM duplex at 120 mV was 12.5 s^{-1} that was 60- fold higher than in symmetrical 1 M KCl at 120 mv. This is a significant increase in sensitivity, which reduces the necessary time to collect a sufficient number of the resistive pulse events for a statistical analysis. However, the disadvantage of using salt gradient are frequent pore closures and bilayer instabilities. The unspecific pore blockages interrupt the continuous current recording and complicate detection of events. We estimated an average time between the necessity to apply voltage reversal to reopen the blocked pore in the presence of the 100 nM and 1 nM miDNA155-P155 duplex at 5.4 and 27 s respectively (Figure 5.18b). Hence, the resistive pulses were detected in individual open-pore segments. The interevent intervals from individual open-pore segments were then merged together for the determination of the mean interevent time and frequency. The detection of resistive pulses and the analysis of ~200 events was possible down to 10 nM where 801 resistive pulses in 692 seconds were detected in three individual experiments. For the lower duplex concentrations, the number of pulses per open pore episode was low to perform histogram analysis. The average number of resistive pulses for 1 nM, 500 pM and 100 pM duplex obtained from single experiments were 72, 20 and 10 respectively. Therefore, the capture frequencies for the duplex concentrations lower than a 10 nM were obtained by dividing the total number of pulses with a total open-time of the pore. Figure 5.19 shows concentration- frequency plot where capture frequencies for all concentrations were obtained by dividing the number of pulses with the total recording time. The capture frequency for 100 pM miDNA155-P155 duplex was 0.027 ± 0.0011 s^{-1}. The large error is due to a low number of events in single experiments. Only 29 events were detected during three experiments, which, combined, lasted for 1098 seconds. This number of events would be enough to estimate the time constant with the 30% of error if histogram detection was possible. For the lower concentrations, such is10 pM there were no resistive pulses observed for a couple of minutes of recording. The capture frequency was linearly dependent on duplex concentration over three orders of magnitude (Figure 5.18c). From the power fit of the data the expected frequency of 10 pM duplex is 1.96 x 10^{-3} s, suggesting one resistive pulse every ~500 s. This explains why for 10 pM of the miDNA155-P155 duplex there were no pulses observed over 5 min recording.

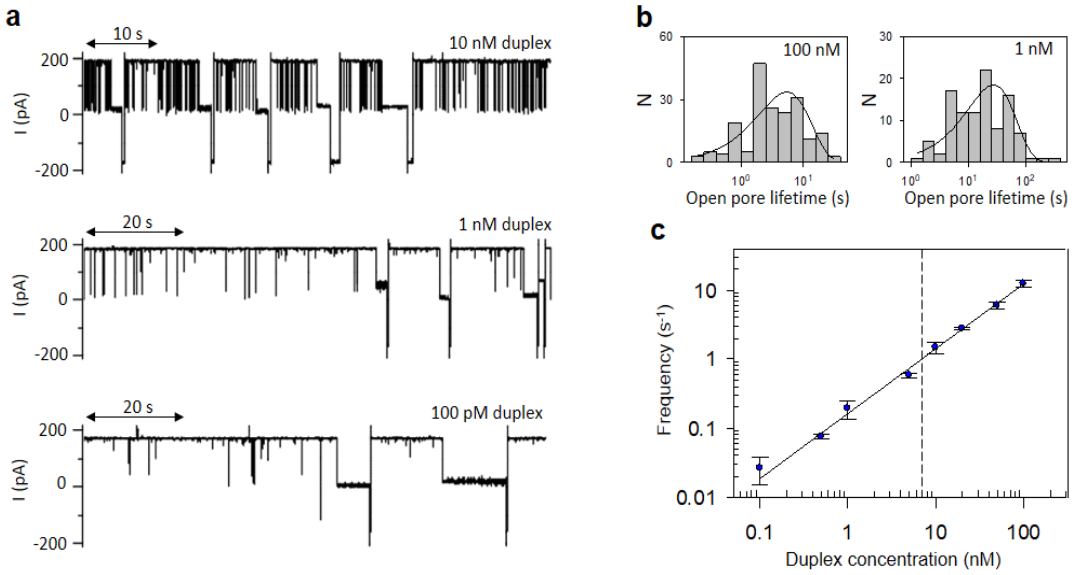

Figure 5.18. a) Representative nanopore current traces in 0.5 M / 4 M KCl (*cis/trans*) at 120 mV with the various concentrations of the miDNA155-P155 duplex. b) The average time between voltage reversal was applied in order to reopen the αHL pore in 0.5 M / 4 M KCl gradient at 120 mV at 100 nM and 1 nM. The mean value for 100 nM miDNA155-P155 concentration was found at 5.4 ± 2.6 and for 1 nM DNA duplex mean time was 27 ± 9.5 s. c) Dependence of event frequency versus duplex concentration shown as a log-log plot. The frequencies obtained by fitting interevent times histograms are separated with dash line from frequencies obtained by dividing the number of events with total recording time. The straight line presents power law fit ($y= ax^b$), R^2=0.988 with a and b coefficients of 0.156 and 0.95.

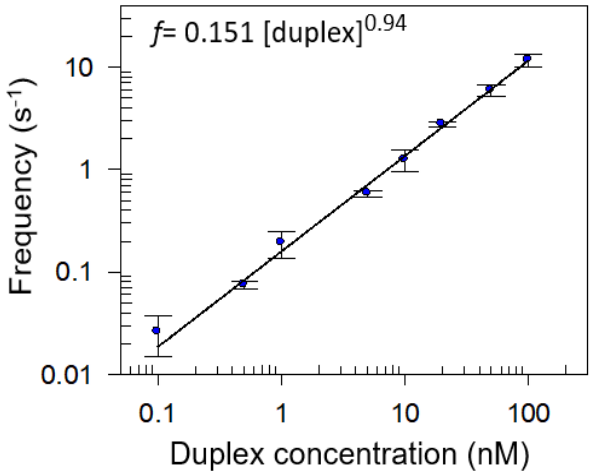

Figure 5.19. Event frequency as a function of miDNA155-P155 duplex concentration in the 0.5 / 4 M KCl at 120 mV. The frequencies were obtained by dividing the number of events with the recording time. Solid line presents power law fit ($y=ax^b$) and reported coefficients with R^2=0.9993.

.

5.4 Selectivity test in asymmetrical salt conditions

To test selectivity in the asymmetrical 0.5 M / 4 M KCl conditions, 100 nM miDNA 155 was mixed with an equimolar concentration of P21. Another sample was made by spiking in 20 nM

miDNA155-P155 duplex to 100 nM miDNA155 and 100 nM P21. The nucleotides were dispersed in the *cis* chamber and the voltage was set at 120 mV. For the sample made with 100 nM miDNA155 and 100 nM P21, the majority of events had ~200 µs duration, characteristic for the for single-stranded oligonucleotide translocations. However, various resistive pulses observed with some resembling the DNA duplex signatures (red asterisks in Figure 5.20 top trace) what was not observed in symmetrical 1 M KCl solution with 100 nM miDNA 155 with 100 nM P21. When the concentration of non-complementary miDNA155 and P21 was lowered to 10 nM, unspecific pore blockings reduced significantly (Figure 5.20 bottom trace).

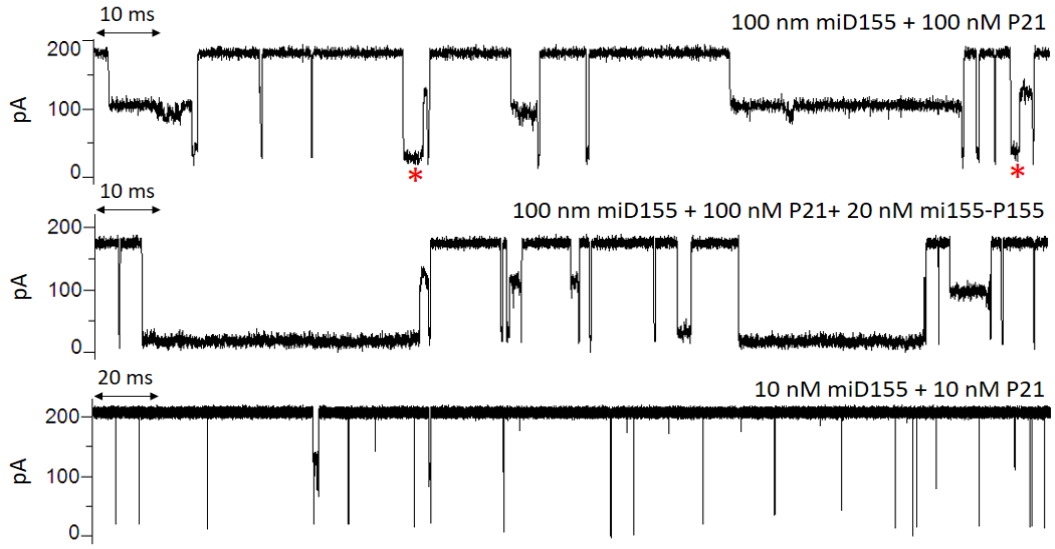

Figure 5.20. Representative traces of αHL pore under 120 mV in the 0.5 M / 4 M KCl (*cis/trans*) in the presence of the 100 nM miDNA155 and 100 nM P21 (top trace). The events resembling DNA duplex signature upon translocation through nanopore are marked with red asterisks. 100 nM miDNA155 and P21 with 20 nM of the pre-hybridised miDNA155-P155 duplex (middle trace). 10 nM miDNA155 and 10 nM P21 only short-lived events were recorded upon interacting with the αHL pore (bottom trace).

The frequency of the spiked-in 20 nM miDNA155-P155 duplex in the solution containing 100 nM P21 and 100 nM miDNA155 was 4.37 ± 0.95 s^{-1} what was a higher than frequency obtained with only 20 nM miDNA155-P155 duplex (2.95 ± 0.21 s^{-1}). The higher frequency probably comes from unspecific blockages, which were observed without the presence of miDNA155-P155 duplex with only 100 nM miDNA155 and 100 nM P21. The unspecific blockages might be filtered out with increasing cut-off criterion for the event acceptance. When cut-off was increased from 1 to 4 ms the capture frequency of 20 nM miDNA155-P155 in the presence of 100 nM P21 and 100 nM miDNA155 was 3.23 s^{-1} what is closer to 2.95 s^{-1} for 20 nM miDNA155-P155 duplex alone. This suggests that, at high concentration of background molecules, the capture frequency might increase due to unspecific interactions of background DNA/RNA molecules with the pore. The quantification can be improved by the increasing the cut-off criterion for event acceptance in order to remove the short nonspecific interactions.

5.5 miRNA155 and miRNA21 detection in the preferred KCl salt gradient

In Section 4.13 was shown that in symmetrical 1 M KCl, miDNA155-P155 duplex had seven times longer dwell time than miRNA155-P155 duplex at 120 mV. On the other hand, the capture frequency of the 100 nM miRNA155-P155 was similar to the one of 100 nM miDNA155-P155 duplex implying that the frequency is rather depended on DNA probe and its overhang extensions than on target molecule. In order to compare the resistive pulse characteristics between miRNA155 and miDNA155, the miRNA155-P155 duplex was investigated under preferred 8-fold 0.5 / 4 M KCl salt gradient at 120 mV. The representative αHL single-channel traces in the presence of 100 nM miRNA155 and 100 nM miRNA155-P155 duplex are shown in Figure 5.21.

Figure 5.21. Single-channel currents traces recorded at 120 mV in 0.5 / 4 M KCl *cis/trans* gradient in presence of 100 nM miRNA155 (top trace) and 100 nM miRNA155-P155 duplex (lower trace).

The single-stranded miRNA155 produces short-lived ~200 μs current pulses, can be easily separated from longer resistive pulses produced by the miRNA155-P155 duplex. Analysis of the miRNA155-P155 duplex signatures in 0.5 / 4 M KCl gradient at 120 mV is shown in Figure 5.22.

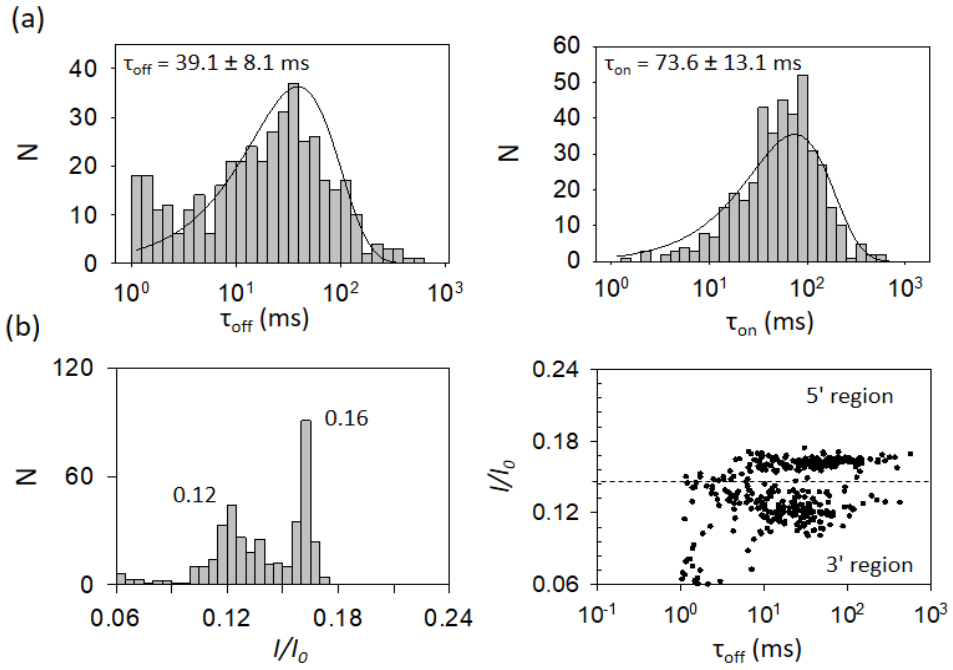

Figure 5.22. (a) Histograms of τ_{off} and τ_{on} distributions obtained with 100 nM miRNA155-P155 duplex in 0.5 / 4 M KCl (*cis/ trans*). The solid lines present fitted functions to histograms. (b) Distribution of level -1 and τ_{off} values for 100 nM miRNA155-P155 duplex in 0.5 / 4 M KCl at 120 mV. Events above the dashed line were assigned to 5' entry while events below the dashed line were assigned to 3'- entry.

The capture frequency of the 100 nM miRNA155-P155 duplex in 0.5 / 4 M KCl gradient at 120 mV was obtained at 13.6 ± 2.4 s^{-1} that is slightly higher than the frequency of 100 nM miDNA155-P155 duplex (12.5 s^{-1}) in the same experimental conditions and 45 times higher than the capture frequency of the miRNA155-P155 duplex (0.30 s^{-1}) at 120 mV in symmetrical 1 M KCl conditions. The dwell time of miRNA155-P155 duplex in 0.5 / 4 M KCl was 39.1 ± 8.1 ms, what is four times shorter compared to the dwell time in symmetrical 1 M KCl conditions at 120 mV. Moreover, the dwell time of the miRNA155-P155 in 0.5/ 4 M KCl was similar to the dwell time of the miDNA155-P155 duplex (33.5 ± 9 ms) in the same conditions. This observation was different from one in symmetrical 1 M KCl (*cis/ trans*) at 120 mV where the duration of miDNA155-P155 was 7 times longer compared to miRNA155-P155 duration.

In symmetrical 1 M KCl, the number of events assigned to 3'-first entry was two times higher than the number of the 5'-first entry (Section 4.11.3). This was not the case for the 0.5 / 4 M KCl gradient conditions where from the 418 detected miRNA155-P155 resistive pulses, 47.7% (199) events were assigned to 5'- first entry, while 52.3% (219) events were assigned to 3'-first entry of the duplex (Figure 5.22 b,c). This again supports the speculation that increased electrophoretic force is acting on the duplex in the salt gradient conditions.

The mean duration of 5'- first entry of miRNA155-P155 duplex was 49.4 ± 7.5 ms that was two times longer than the mean duration of 3'-first entry (24.4 ± 7.4 ms). This is in contrast with the miDNA155-P155 duplex where the duration of the 3'-first entry is two times longer than the

duration of 5'-entry (Table 5.7). The difference between the DNA-DNA and RNA-DNA duplexes upon translocation through the αHL pore was proposed to come from their different structure and diameters: DNA-DNA (B-form, 2 nm wide), RNA-DNA (A-form, ~2.4 nm) [211].

5.5.1 miRNA21-P21 resistive pulse parameters in asymmetrical 0.5 / 4 M KCl *cis/trans* gradient

In Chapter 6, the trial experiments with the total RNA extract from the blood serum samples taken from patients diagnosed with colorectal cancer have been conducted. In this type of cancer, the most common miRNA, for which upper regulated levels of expressions are reported is miRNA21 [222]. Therefore, the experiments with the synthetic miRNA 21 and its complementary probe P21 were conducted in the preferred 8- fold salt gradient. In order to describe the resistive pulse parameters of the miRNA21-P21 duplex, the pulses were collected in the presence of 100 nM miRNA21-P21 duplex at 120 mV. The statistical analysis of current blockages produced by 100 nM miRNA21-P21 duplex is shown in Figure 5.23.

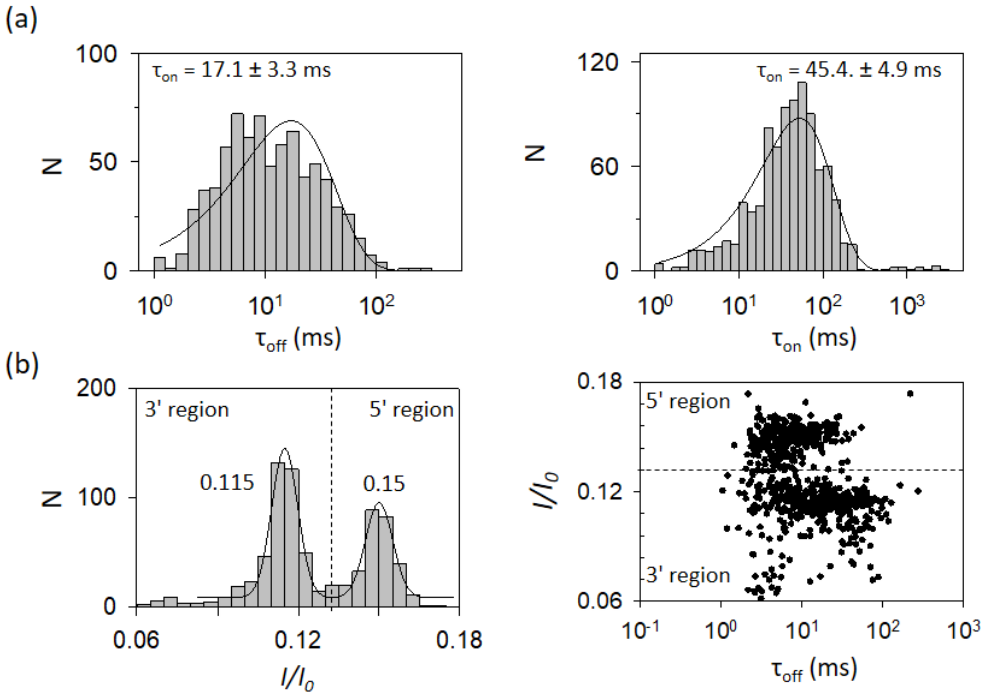

Figure 5.23. (a) Histograms of τ_{off} and τ_{on} distributions obtained with 100 nM miRNA21-P21 duplex in 0.5 / 4 M KCl (*cis/ trans*) at 120 mV. The solid lines present fitted functions to histograms. (b) Distribution of level -1 and τ_{off} values for 100 nM miRNA21-P21 duplex in 0.5 / 4 M KCl at 120 mV. Events above the dashed line were assigned to 5' entry while events below the dashed line were assigned to 3' entry.

The dwell time of miRNA21-P21 duplex was 17.1 ms, two times shorter than the mean dwell time of miRNA155-P155 duplex. The reason for the longer dwell time of miRNA155-P155 duplex compare to miRNA21-P21 might come from the higher G-C content in miRNA155

sequence compared to miRNA21 sequence (41% vs 36 %). The longer dwell time of duplexes containing G-C pairs upon translocating the αHL pore was observed by Liu *et al*. and Tian *et .al* [17, 223].

The capture frequency of 100 nM miRNA21-P21 was 19.1 s^{-1} what was ~1.5 times higher compared to miRNA155-P155 duplex. Bimodal I/I_0 level-1 distribution was observed when double dC_{30} overhang P21 was used (Figure 5.23 b). Based on earlier experiments on miDNA21-P21 the shallower amplitude was assigned to 5' entry while deeper 0.115 I/I_0 events were associated with 3' entry.

The total number of detected miRNA21-P21 pulses was 766 from which 311 (41%) were assigned to 5'- first entry with the mean duration of 8.74 ms, while 455 (59%) were assigned to 3'- entry with the mean duration of 22.45 ms.

5.5.2 miRNA21 quantification in 0.5 / 4 M KCl gradient

The capture frequency of miRNA21-P21 probe was determined for the four different duplex concentrations (100 nM, 10nM, 1 nM and 100pM) at 120 mV in 0.5 / 4 M KCl salt gradient.

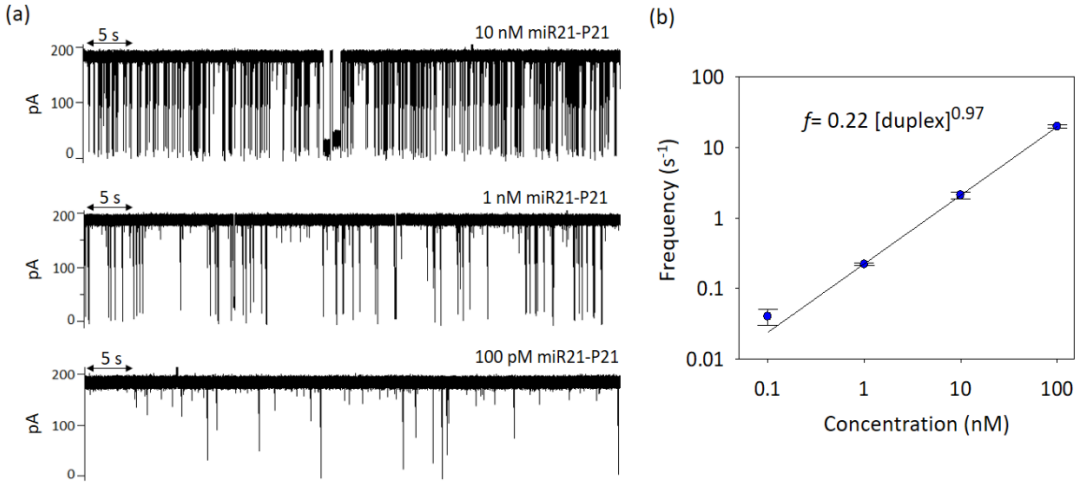

Figure 5.24. (a) Representative single-channel traces in 0.5 / 4 M KCl salt gradient at 120 mV in the presence of 10 nM, 1nM and 100 pM miRNA21-P21 duplex. (b) Log-log plot of capture frequency versus miRNA21-P21 duplex concentration. Capture frequencies of 100 nM and 10 nM were determined by histogram fitting while capture frequencies for 100 pM and 1 nM were determined by dividing the number of events with the total open pore recording time. The solid line presents the fit with power function ($y= ax^b$). Standard deviations are derived from three independent experiments except for 1 nM where the standard deviation was calculated from two independent experiments.

The linear dependence of duplex capture frequency on duplex concentration was found over three orders of magnitude (Figure 5.24). Capture frequencies for 100 nM (19.82 ± 1.1 s^{-1}) and 10 nM (2.11 ± 0.23 s^{-1}) were determined by fitting the interevent time histograms. The frequencies of 1 nM (0.22 ± 0.01 s^{-1}) and 100 pM (0.044 ± 0.01 s^{-1}) were obtained by dividing the number of pulses with the total recording time. For 1 nM duplex concentration, 292 resistive pulses were detected

in two independent experiments: 193 pulses in 904 seconds with one pore in first and 99 pulses in 438 seconds with one pore in the second experiment. For the 100 pM duplex concentration, 68 resistive pulses were obtained from three individual experiments: 46 pulses in 422 seconds with two pores, 14 events in 359 s with one nanopore and 8 pulses in 211 seconds with one nanopore. The capture frequencies for concentrations lower than 100 pM were not experimentally determined since the capture frequency for 100 pM was $0.044 s^{-1}$ (1 pulse ~every 25 s). The expected frequency of 10 pM concentration from the power fit is 2.5×10^{-3} s^{-1}, meaning pulse every ~400 s. Therefore we set 100 pM as a limit of quantification of miRNA under 0.5 / 4 M KCl at 120 mV.

Wang *et al.* reported the lower limit of miRNA quantification in 0.2 / 3 M KCl conditions at 120 mV [13]. The frequency for their miRNA155-P155 duplex in 0.2 / 3 M KCl was 0.04 s^{-1} what is similar to capture frequency of 0.04 s^{-1} observed with 100 pM of miRNA21-P21 duplex used in this work. The reported frequency for 0.1 pM duplex in their work was 0.01 s^{-1} meaning one resistive pulse every 100 s [13]. Xi *et al.* measured the capture frequency of~ 0.003 s^{-1} for the 100 pM let-7b- LNA-P_{b15} duplex in 0.5 / 3 M KCl at 100 mV [19]. However, none of the studies did present the number of detected pulses at low duplex concentrations that were used for the miRNA quantification. The resistive pulse parameters (dwell time and residual current amplitude) under salt gradient were not determined in these studies. Moreover, the influence of the salt gradient on a bilayer and pore stability was not discussed.

The experimental volume, where RNA extract is resuspended for the nanopore sensing, determines the final concentration of miRNA for the experiment. The amounts of individual miRNAs that can be extracted from ~1 mL of plasma are in 0.1 -1 fmol range [7, 215]. Hence, to achieve 100 pM of quantification limit, that amount should be resuspended in the volumes from 1- 10 µL, which is 100-1000 times smaller than our 1.1 mL chamber.

5.6 Asymmetrical salt gradient with different electrolytes

The 8-fold KCl gradient across the pore resulted in 60-fold enhancement of miDNA155 capture rate but the dwell time reduced more than 30 times. In the symmetrical salt conditions, it was shown that the dwell time of miDNA155-P155 duplex is ~ 20 times longer than in 1 M KCl. Therefore, the experiments with the different electrolyte gradients were conducted with the 100 nM of the miDNA155-P155 duplex.

When 0.5 / 4 M LiCl was used across the membrane, the dwell time of 100 nM miDNA155-P155 duplex was significantly longer (>5 s) compared to the average duration of 33.5 ms in same KCl gradient at 120 mV. When the voltage was increased to 150 mV, the dwell time was found at 102 ± 48 ms, that is 30 times longer compared to a dwell time of miDNA155-P155 in the same KCl

gradient at 150 mV (3.6 ± 0.6 ms). However, the capture rate decreased 4-fold to 8 s^{-1} compared to capture frequency in 0.5 / 4 M KCl at 150 mV.

Interestingly, in a mixed electrolyte gradient 0.5 M LiCl (*cis*) and 4 M KCl (t*rans*), the dwell time increased to 63.0 ± 7.5 ms, which is 2-fold higher compared to the dwell time of 33.5 ± 9 ms in 0.5 / 4 M KCl at 120 mV (Table 5.11). At the same time, capture frequency was 10.8 ± 1 s^{-1} that is not significant decrease compared to 12.5 s^{-1} in 0.5 / 4 M KCl. The reason for a longer dwell time of DNA duplex when the solution in a *cis* compartment 0.5 LiCl might be the result of the stronger binding affinity of lithium ions to DNA. The electrophoretic force acting on the DNA is proportional to the effective charge of DNA; hence, the stronger binding of Li^+ ions might reduce the effective charge of DNA and result in a longer translocation time through the pore [214]. In addition, Johnson *et al.* suggested that the stronger counterion binding of Li^+ to the neighbouring phosphate charges in a DNA duplex increases duplex stability and results in the prolonged duplex translocation time through αHL pore [213]. In their work on dsDNA translation through the αHL pore, the dwell time was the longest in LiCl where it was found at 714 ms, which reduced to 31.3 ms in 1 M KCl at 120 mV [213].

The maximum solubility of KCl in water at 20 °C is about 4.5 M. Therefore, to establish salt gradients with the higher salt concentration in *trans* chamber other salts might be better candidates. LiCl can be dissolved up to significantly higher concentrations (~20 M at 25 °C). However, in 0.5 / 4 M LiCl we showed that the miDNA155-P155 dwell time is too long (> 5s) and the capture frequency was not determined. CsCl can be dissolved up to 11 M at the room temperature that is 2.5 times higher than maximum solubility of KCl at the room temperature. In symmetrical 1 M conditions in section 4.14 we showed that the capture frequency and dwell times were similar for CsCl and KCl conditions at 120 mV.

The capture rate of 100 miDNA155-P155 in 0.5 / 4 M CsCl was 11.76 s^{-1} that is similar to 0.5 / 4 M KCl conditions. The dwell time was found at 44.5 ms, which is slightly longer than for 0.5 / 4 M KCl (Table 5.11). Unfortunately, bilayers were severely destabilized when the concentration of CsCl in *trans* chamber was increased to 6 M and no pore activities were observed. This should not be the problem for the solid-state nanopores which do not require the biological membrane and can withstand steeper salt gradients (0.2 / 4 M KCl) and higher voltages (>500 mV) [151].

Table 5.11. The dwell and interevent times duration of 100 nM miDNA155-P155 in various salt gradinets. The data are presented as a mean ± S.E. obtained from single experiemnt in all cases except for 0.5 (KCl, LiCl, NaCl) / 4 M KCl at 120 mV* where data are presented as mean ± S.D. from n independent experiments: n=5 (0.5 / 4 M KCl), n= 3 (0.5 LiCl / 4 M KCl) and n= 3 (0.5 M NaCl / 4 M KCl)

Salt gradient		**τ_{off} (ms)**			**τ_{on} (ms)**		
cis	***trans***	**120 mV**	**150 mV**	**180 mV**	**120 mV**	**150 mV**	**180 mV**
0.5 M KCl	4 M KCl	33.5 ± 9.0*	3.6 ± 0.6	1.78 ± 0.21	80.5 ± 7.0*	26 ± 2.4	14 ± 2.2
0.5 M LiCl	4 M LiCl	>5000	102 ± 48	38.8 ± 13.6	N.D.	121 ± 47	39 ± 13.6
0.5 M CsCl	4 M CsCl	44.5 ± 5.8	4.5 ± 1.4	2.24 ± 1.1	85 ± 17.7	51 ± 5.7	37 ± 4.9
0.5 M LiCl	4 M KCl	63.0 ± 7.5*	7.0 ± 2.5	2.1 ± 0.9	92.9 ± 8.8*	24 ± 4.9	13 ± 2.8
0.5 M NaCl	4 M KCl	51.5 ± 10.1*	N.D.	N.D.	88.9 ± 11.3*	N.D.	N.D.

5.7 Summary

This chapter systematically investigated salt gradients influence on nanopore translocation properties of various duplexes. The duplex capture frequency exponentially increased with the salt gradient, while the dwell time decreased in the same way. This observation indicates that the larger electrophoretic force is acting on a duplex near the pore entrance. The decrease of dwell time was in contrast with the results shown on silicon nitrate nanopores by Wanunu *et al.*, where the strong EOF was in the opposite direction of the DNA translocation through the pore [151].

In this work, the proposed transmembrane salt gradient was 0.5 / 4 M KCl (*cis / trans*) since the bilayers were not significantly destabilized and the pore current could be monitored for ~20 min when a voltage of 120 mV was applied. For this salt gradient, the capture frequency of the 100 nM miDNA155-P155 duplex increased 60-fold compared to symmetrical 1 M KCl conditions at 120 mV, while the mean dwell time was found at 33.5 ms which is ~30 times shorter compared to the dwell time in symmetrical 1 M KCl. However, the experiments in section 5.6 showed that the duplex dwell time can be increased by using a mixed electrolyte gradient by replacing the KCl solution in the donor cis compartment with NaCl or LiCl without excessive reduction of the capture frequency.

The 0.5 / 4 M KCl gradient enabled quantification of miDNA155-P155 and miRNA21-P21 duplexes in the range of 100 nM to 100 pM, which was a significant enhancement compared to symmetrical 1 M KCl where concentrations below 10 nM could not be quantified. It must be noted that under salt gradient conditions, the unspecific pore closures complicate the trace analysis and interevent time estimation, which is problematic for low concentration of the duplex

(<1 nM). In the presence of 1 nM miDNA155-P155, the pore stayed open for ~30 seconds before voltage reversal was needed to reopen the pore. Hence, the analysis was performed on multiple segments of the open pore duration.

As previously mentioned, the expected concentration of patho(physiological) miRNA extracted from 1 mL of plasma is in a range from 0.1-1 pM. Albeit the capture frequency of the miRNA-DNA duplex was vastly improved in salt gradient, the limit of miRNA quantification was still well above the desired 0.1-1 pM concentration. The most intuitive way to increase the concentration of miRNA in the sample would be to reduce the volume of the chamber where the total amount of miRNA is resuspended. For example, the same amount of miRNA extracted from 1 mL of plasma would have concertation from 0.1 – 1 nM if resuspended in volumes of 1-10 µL.

Although the salt gradient magnitude can be increased, high salt gradients (0.1 / 4 M KCl and 0.2 / 4 M KCl) resulted in frequent pore closures and pore-clogging, hence the voltage needed to be reversed in order to restore the pore current (Figure 5.8). Moreover, the lipid bilayer membrane was very unstable under those conditions and it was not possible to monitor the pore currents for longer than a couple of minutes. It is possible that the steep salt gradients generate osmotic pressure that can act as a destabilizing factor on the lipid membrane.

The influence of the probe design on the capture rate of the miDNA155-P155 duplex in the 0.5 / 4 M KCl salt gradient condition was evaluated in section 5.2. The experiments with single overhang probe confirmed, undoubtedly, that the deeper level-1 amplitude comes from an entry of the dC_{30} at the 3'-end of the probe, while the shallower level-1 amplitude comes from 5'-end entry. The capture rates of duplexes with miDNA155 hybridized to DNA probes with single overhang were almost the same, which was in contrast with the capture rates in 1 M KCl, where the capture frequency of probe modified with dC_{30} at the 3'-end was two times higher than capture frequency of probe modified with dC_{30} at the 5'-end. This could potentially reduce the cost of the DNA probe synthesis used for the miRNA detection. Unfortunately, duplexes with single dC_{30} overhang have one blunt end, which has a diameter of ~2 nm, typical for dsDNA. Once the blunt end was captured by the αHL nanopore, it underwent slow unzipping that was significantly longer (>5 s) and 'noisier' compared to the capture of the duplex with its overhang-extended end (Figure 5.17). Therefore, the main conclusion for DNA probes tested in transmembrane salt gradients was that the capture overhang dC_{30} is necessary at both probe ends to ensure maximum duplex capture rate and facilitate the duplex unzipping through the pore.

Although the transmembrane salt gradient was proposed as an enhancing mechanism for the capture frequency of miRNA-DNA probe duplex, it was not used for detection of miRNA in the biological sample in previous works form the literature. After the salt gradient of 0.5 / 4 M KCl cis / trans, the voltage of 120 mV, and the double dC_{30} probe modification were established as preferred parameters for the miRNA-DNA probe detection with the αHL nanopore, the trial

experiments with total RNA extract from clinical samples were conducted and described in Chapter 6.

Chapter 6: Clinical RNA extracts

This chapter describes the trial experiments with the total RNA extracted from the blood serum samples taken from patients with colorectal cancer. The samples were provided by prof. Alex Mirnezami and Mr Rahul Bhome (Faculty of Medicine, University of Southampton, UK). The first section will explore the influence of total RNA extract on the bilayer and pore stability. The detection of spiked-in duplex along with total RNA extract is described in section 6.2. Finally, in the last section, probe P21 was added to the sample in order to bind complementary miRNA21, since the expression levels of this miRNA were found increased for colorectal cancer.

6.1 The influence of total extract on bilayer pore stability under asymmetric and symmetric KCl conditions

To test the influence of total RNA extract on the bilayer/pore stability, the total RNA extract from 250 µL of serum sample was dispersed in the *cis* chamber. The RNA was extracted with the miRNeasy micro kit (Qiagen, CA), which is used for purifying the total RNA enriched with small RNAs, such are miRNAs. Briefly, blood serum samples were homogenized with QIAzol lysis reagent (solution of phenol and guanidine thiocyanate), which lyses tissues, and removes RNases and proteins from the sample. After addition of chloroform, the lysate was separated in an aqueous and an organic phases: the RNA partitions were in the upper aqueous phase, while the DNA partitions could be found in the organic-aqueous interphase. The upper phase was then extracted and, after ethanol addition (which causes the RNA molecules to precipitate), it was transferred to a spin column. Here RNAs were captured by a membrane, while other species were washed away. The total RNA extract enriched with short RNAs was then eluted in nuclease-free water. The concentration of RNA was estimated by measuring the absorbance at 260 nm with Nanodrop™ 1000 spectrophotometer (Thermo Scientific).

In order to test the stability of the bilayer and αHL pore in the presence of total RNA extract in asymmetric 0.5 / 4 M KCl conditions at 120 mV, 5.5 µg of total RNA extract was presented to the *cis* chamber containing 1.1 mL of 0.5 M KCl, hence the RNA concentration was 5 µg/mL. The current trace is shown in Figure 6.1.

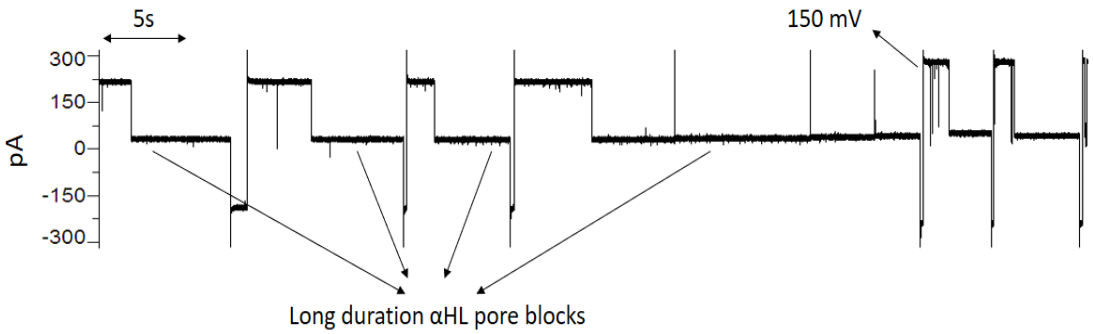

Figure 6.1. The representative nanopore current trace in 0.5 / 4 M KCl at 120 mV in the presence of 5 µg/mL of total RNA extract from the blood serum sample. Long-duration current-block events were observed even though there was no DNA probe present. The open-pore current could be restored by applying a negative potential. At the higher voltages >150 mV, short current blockages were observed just before pore clogging that can represent ssRNA translocation through the pore.

Unlike for synthetic oligonucleotides used in this work, the total RNA extract from the serum sample of the similar concentration of ~5 µg/mL produced long blocking of the αHL pore. However, the αHL pore current could be restored by reversing the voltage, which probably ejects stuck RNA molecule away from the pore entrance. The reason for the long blockages of the αHL pore might be the diversity of RNA molecules presented in the sample and other impurities that could still be presented along with RNA species such are proteins or DNA. At 150 mV, the short-lived current blockages were recorded before the pore was blocked which can represent transient collisions of RNA molecules with the pore mouth or translocation of short RNAs through the pore.

The same sample was used to investigate the influence of total RNA extract under symmetrical 1 M KCl *cis/trans* conditions. The 550 µL of 0.5 M KCl usually present in the *cis* chamber were replaced with 1.5 M KCl, in order to bring the concentration in *cis* chamber to 1 M KCl, while the 4 M KCl solution *trans* compartment was replaced by 1 M KCl. By doing so, the concentration of total RNA extract in *cis* chamber was 2.5 µg/mL. Figure 6.2 shows representative αHL current trace in 1 M KCl at two different voltages.

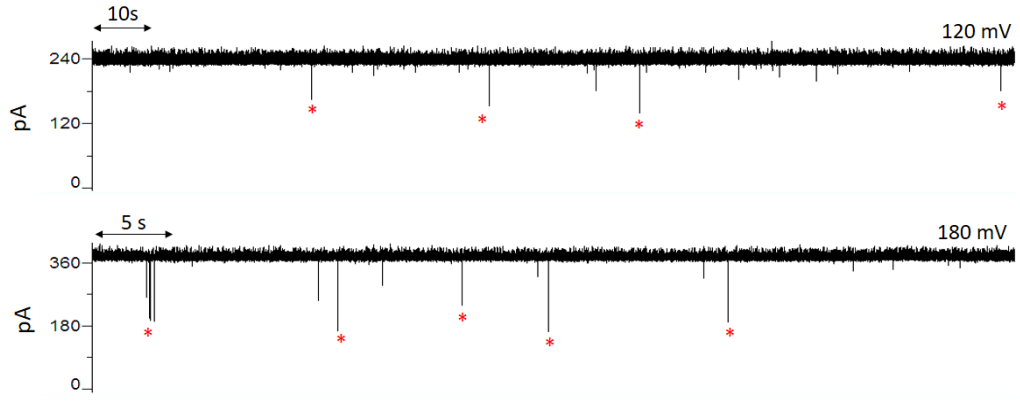

Figure 6.2. The representative current trace through two αHL pores in symmetrical 1 M KCl conditions at 120 mV (top trace) and 180 mV (bottom trace) in the presence of 2.5 µg/mL of total RNA extract from the blood serum sample. The possible RNA translocations are marked with red asterisks.

When compared to asymmetrical 0.5 / 4 M KCl conditions, the long blockages were not observed frequently at 120 and 180 mV. However, the concentration of total RNA extract used in symmetrical 1 M KCl solution was two times lower than for experiment with asymmetrical 0.5 / 4 M KCl.

These experiments show that RNA extract does not influence the bilayer stability. However, under the salt gradient conditions, the pore was constantly clogged by, presumably, various RNA fragments that can be found in the biological extract. Moreover, the estimated amount of total RNA in this particular sample was 5.5 µg. This is higher compared with the usual 0.1 – 1 µg amount extracted from the ~200 µL of plasma/serum samples [35, 224]. It is possible that this sample was containing some DNA or other impurities. The existence of additional nucleic acids in the solution might increase the number of the unspecific polymer-pore interactions.

6.2 Detection of spiked-in concentration of miDNA155 in the biological sample

The second experiment was performed by spiking-in miDNA155 to the total RNA extract from the second sample (0.3 µg of total RNA amount obtained from 250 µL of blood serum and resuspended in 13 µL of RNase free water). The concentration of miDNA155 was set to be 20 nM in the final 1.1 mL volume. Hence 2.2 µL of miDNA155 (10 mM stock solution) were mixed with 10 µL of P155 (10 mM stock solution), along with the sample extracted from blood serum and 25 µL of TE buffer (Sigma Aldrich). The solution in Eppendorf tube with RNA extract along with synthetic oligonucleotides was mixed with 50 µL of 1 M KCl, 10 mM Tris, 1 mM EDTA, pH=8. The solution was heated for 5 minutes at 90 °C to anneal the miDNA155 and P155 and left to cool down gradually to the room temperature and was added to 1 mL of 0.5 M KCl in the *cis* chamber. This lead to a concentration of miDNA155-P155 of 20 nM, with 0.27 µg/mL of total RNA extract in the *cis* chamber, while the KCl concentration in *trans* chamber was 4 M KCl.

Figure 6.3. The representative current trace of αHL pore for 0.5 / 4 M KCl gradient in the presence of 20 nM miDNA155, 100 nM P155 and 0.27 µg/mL of total RNA extract from blood serum sample

For this particular RNA extract, the blockages were not observed frequently. This was expected, since the amount of RNA in this sample was ~20 times lower compared to the amount used in the experiment previously described in section 6.1. This enabled detection of the specific miDNA155-P155 duplex resistive pulses with the Clampfit software. The frequency of 20 nM miDNA155-P155 duplex in the presence of 0.27 µg/mL of total RNA extract was 1.58 ± 0.30 s^{-1}, that was almost 2 times lower compared to the capture frequency of 20 nM miDNA155-P155 alone in solution. A possible reason for the lower capture frequency is that not all miDNA155 were hybridized with P155 in the presence of total RNA extract.

6.3 Detection of miRNA21 in clinical sample

High expression levels of miRNA21 have been correlated to colorectal cancer [225-227]. Therefore, its complementary probe P21 was added to the third RNA extract sample to hybridize with potential miRNA21 targets. The total amount of RNA extracted from this sample, obtained from 250 µL of blood serum, was estimated at 334.8 ng and resuspended in 12 µL of RNase-free water. In order to hybridize the miRNA21 targets in the sample, 2.2 µL of the probe P21 (50 µM) was added in the solution along with 36 µL of TE buffer (Sigma Aldrich) and 50 µL of 1 M KCl, 10 mM Tris and 1mM EDTA, pH=8. The solution was stirred and heated at 90 °C for 5 minutes and then left to cool down gradually to room temperature. Afterwards, the solution was mixed together with 1 mL of 0.5 M KCl, 10 mM Tris, 1 mM EDTA, pH =8 in the *cis* chamber. The solution in *trans* chamber was 4 M KCl, 10 mM Tris, 1mM EDTA, pH=8. The representative current trace of the αHL pore is shown in Figure 6.4.

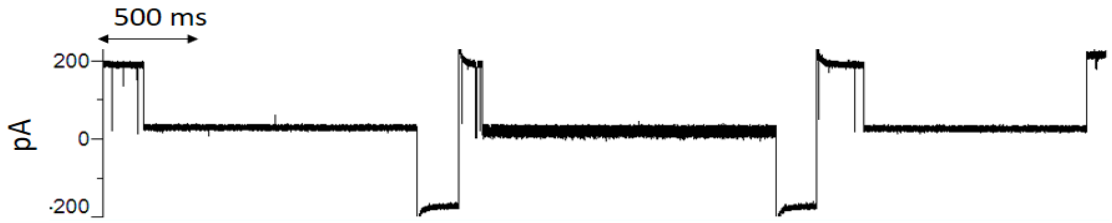

Figure 6.4. The representative αHL current trace for 0.5 / 4 M KCl *cis/trans* at 120 mV in the presence of 0.3 µg/mL RNA extract and 100 nM P21.

Long αHL pore blockages were observed again, despite the concentration of the total RNA extract being 0.3 µg/mL, ~20 times lower than the 5 µg/mL concentration used in section 6.1. This is a relatively low concentration even when compared to our experiments with the duplexes in Chapter 4 and Chapter 5. For example, 100 nM miRNA155 in our 1.1 mL chamber gave ~0.8 µg, an amount that is ~2.5 times higher compared to the 0.334 µg of total RNA extracted from this particular sample.

Long blockages were still observed after the bilayer was disrupted and reformed with another αHL pore, suggesting that pore was properly inserted, but the analytes in the sample were causing

its clogging. The salt gradient across the pore vastly enhanced the capture rate of duplexes used in this work. However, the samples described in Chapter 4 and 5 were only contained one miRNA/miDNA sequence hybridized to DNA probe. The enhanced electrical field near the pore entrance is nonselective on RNA/DNA analytes presented in the sample, which could result in many non-specific pore interactions.

For this reason, the same sample was tested in the symmetrical 1 M KCl *cis/trans* solution. The additional amount of 40 mg of KCl was dissolved in 0.5 M KCl *cis* compartment to achieve 1 M KCl. The 4 M KCl in *trans* side was replaced by 1 M KCl. The representative trace is shown in the Figure 6.5.

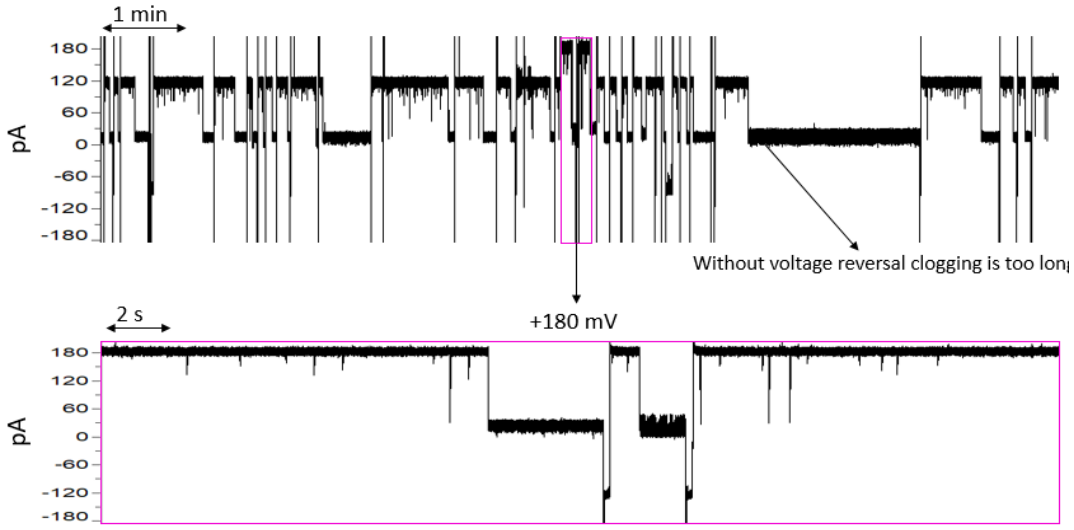

Figure 6.5. The representative αHL current trace in symmetrical 1 M KCl *cis/trans* at 120 mV in the presence of 0.3 µg/mL RNA extract and 100 nM P21. Bottom trace presents the occasion where the voltage was increased to 180 mV. However, long blockages (>1 s) were observed again.

From Figure 6.5 it can be seen that the pore was frequently clogged, even in the symmetrical 1 M KCl conditions in the presence of the same RNA extract. Those long blockages were not coming from duplex translocations, since their duration was too long compared to the ~0.1 -1 s dwell time durations of the duplexes in 1 M KCl at 120 mV investigated in this work. When the voltage reversal was not applied, the clogging durations were > 1 min long at 120 mV. Increasing the voltage to 180 mV did not help, since the blockages were longer than 2 seconds (significantly longer compared to the ~2-10 ms of dwell time observed for all duplexes in this work at 180 mV). These unspecific pore blockings complicate the nanopore recording and decrease the open pore time. For example, the duration of the total recording in Figure 6.5 (upper panel) is 11.5 min, but the pore stayed unclogged for only half of the total time.

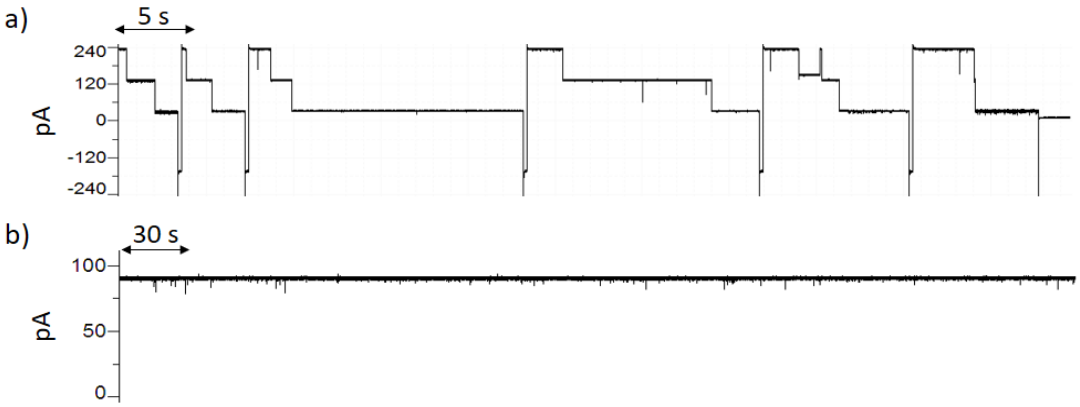

Figure 6.6. The representative αHL current trace for 1 M KCl *cis/trans* at 120 mV (top trace) and 50 mV (bottom trace) in the presence of 0.3 µg/mL RNA extract and 100 nM P21.

Figure 6.6 shows the current recording from two αHL pores in the presence of 0.3 µg/mL of the total RNA extract and 100 nM P21 in the symmetrical 1 M KCl *cis/trans* at 120 mV. It can be seen that both pores were frequently clogged when +120 mV was applied (Figure 6.6a). Interestingly, when the voltage was lowered to 50 mV, the blockages did not appear and two pores stayed simultaneously open for a couple of minutes (Figure 6.6 b). This suggests that long blockages have indeed resulted from RNA molecules stalling inside the nanopore.

The residual current amplitude of long blockages was found at I/I_0 = 0.13 ± 0.01, similar to amplitudes of level-1 observed in this work with various duplexes (see Table 4.5 and 4.7). Since in symmetrical 1 M KCl it was possible to monitor the pore current longer than in asymmetrical 0.5 / 4 M KCl conditions, a few complete resistive pulses in the presence of the P21 probe were observed (Figure 6.7). The frequently observed pulses were short ~200 µs long transient events that are probably representing P21 probe traversing the pore (first resistive pulse presented in Figure 6.7). The second resistive pulse in Figure 6.7 resembles a duplex signature. The deeper residual amplitude (I/I_0 = 0.2), similar to level-1, was followed by an increase of the current to the level with the I/I_0 = 0.49, which is similar to level-2 of the characteristic duplex signature in 1 M KCl at 120 mV. The last two pulses did not have a characteristic duplex signature upon translocating the αHL pore. The duration of these pulses was similar to miRNA155-P155 duration in 1 M KCl at 120 mV (~150 ms). Their residual current amplitudes were found at 0.1 and 0.06 respectively.

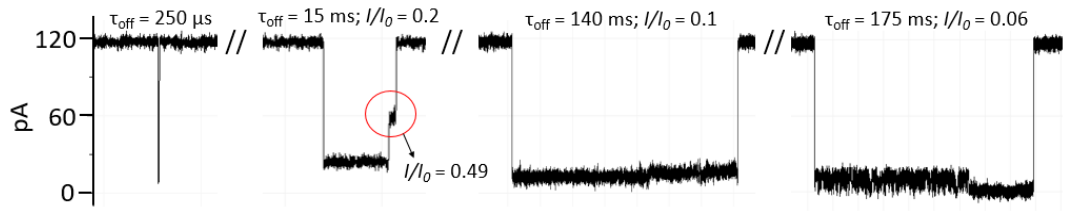

Figure 6.7. Various resistive pulse parameters collected from recordings with 1 M KCl, at 120 mV in the presence of 0.3 µg/mL RNA extract and 100 nM P21.

These three pulses were the only ones detected in the 1 M KCl at 120 mV during the recording time of ~20 min. Therefore, it is clear that any kind of statistical analysis and estimation of the concentration could not be performed on only three recorded resistive pulses. Moreover, the possibility that they represent the actual miRNA21-P21 duplex-pore interaction is extremely low, because they do not have the specific duplex signature. Only the second pulse could be considered as a duplex interaction with the pore. However, the 0.2 amplitude of level-1 observed for this pulse is higher than the one of those of level-1 observed for duplexes investigated in this work (Table 4.5 and Table 4.7).

6.4 Summary

This chapter describes the trial experiments with real biological RNA extracts obtained from blood serum of patients with colorectal cancer. miRNA21 is suspected to be upregulated in colorectal cancer, therefore it was selected as a target for the P21 probe. Experimental conditions of 0.5 / 4 M KCl and 120 mV, established in experiments with synthetic miRNA, were used in experiments with real RNA extract. It was immediately obvious that nanopore sensing is susceptible to the background interference. In the presence of biological extract, the αHL pore was permanently blocked so the pore current was hardly observed for more than a couple of seconds (Figure 6.1). The closures might come from various RNA molecules such are mRNA, rRNA, tRNA and short fragments presented in the sample that are able to fold in specific secondary structures and induce permanent pore clogging. The increased electrophoretic force due to salt gradient increases the capture rate of all RNA species in the solution and, as a result, frequent pore closures might be observed.

Due to the small number of performed experiments, it is unsure how the sample variation influences the nanopore recording in the salt gradient condition. For example, the pore clogging was not frequent when the miDNA 155 was presented to the total RNA extract along with 100 nM P155 in the 0.5 / 4 M KCl at 120 mV (section 6.2). After the hybridization step, the resistive pulses of the 20 nM miDNA155-P155 duplex were detected and analysed. The obtained frequency for 20 nM miDNA155-P155 duplex (1.58 ± 0.30 s^{-1}) in the presence of 0.27 µg/mL of the total RNA extract was lower than the one observed for only 20 nM miDNA155-P155 duplex in absence of the total RNA extract (2.95 ± 0.21 s^{-1}). It is possible that in the presence of total RNA, the hybridization of miDNA155 to the P155 was reduced. Moreover, the volume of 100 µL where the miDNA155 and P155 were hybridized in the presence of the RNA extract was maybe too large, since the final concentration of miDNA155 was 0.22 µM that is 10 times lower compared to the concentration used in experiments in Chapter 4 and Chapter 5.

In the experiments in section 6.3, the amount of total RNA extract from blood serum enriched with small RNAs (0.334 µg) was almost the same as the amount used in section 6.2 (0.3 µg). The

Probe 21 was added to hybridize to miRNA21, whose levels of expression are higher in colorectal cancer [225-227]. Unfortunately, the RNA extract in the presence of P21 induced frequent long pore blockages, that were not observed in the experiment with spiked-in miDNA155 and P155 probe in section 6.2 with a similar amount of RNA extract.

MiRNeasy Micro Kit (Qiagen) was used for the RNA extraction from clinical samples. This particular kit is designed for extracting the total RNA including small RNAs such are miRNAs from the cells and tissue samples. For the further purification of the RNAs shorter than 200 nt another kit - RNeasy MinElute Cleanup Kit (Qiagen) is recommended for use. It would be desirable to investigate whether this additional purification step would benefit, giving a reduction of pore-clogging observed in the presence of the total RNA extract.

The preferred amount of plasma/serum for a single RNA extraction is ~200-400 mL. The average yield of total RNA that can be extracted from this volume varies between 0.1-1 μg [35]. miRNAs constitute only 0.01 % of the total RNA. Therefore, multiple extractions might be necessary in order to bring the concentration of a certain miRNA to the detection limit of the nanopore device. Alternatively, miRNA nanopore sensing detection of other biological samples might be carried on. For example, cells and tissues contain higher amounts of miRNA material compared to the plasma/serum and might therefore be better candidates for the nanopore detection.

Chapter 7: Conclusion

This final Chapter summarizes the main conclusions and presents recommendations for future investigations on microRNA nanopore analytics. A list of publications arising from the project is also included.

7.1 Summary

Nanopore resistive pulse sensing is a novel analytical technique with the potential to detect and quantify cancer-related miRNAs in solution without labelling or amplification. For the detection with αHL nanopore of a specific miRNA, the only requirement is the hybridization with a complementary DNA probe [12, 13, 228]. MiRNA-DNA duplexes produce a longer, multilevel resistive current pulse compared to free miRNA molecules [13], i.e. the specificity of the nanopore assay is based on the interaction of a DNA probe with a particular miRNA species. For miRNA detection with αHL nanopores, the concentration of miRNA-DNA duplex was shown to be linearly correlated with the nanopore capture frequency [13, 17, 19]. Because of the stochastic nature of duplex-pore interactions, the number of detected events should be ~200 for histogram analysis (Section 4.4.2). In general, to obtain an accurate capture frequency, the number of resistive pulses for individual experiments should be as high as possible.

Therefore, the main challenge of nanopore resistive pulse sensing of miRNA is to increase the number of events. Various methods for increasing the capture frequency have been suggested, including DNA probe modification, bioengineering of the αHL pore, increasing the applied potential, and the use of salt gradients [13, 19, 158]. The latter approach showed promising results for both solid-state pores [151] and for the bilayer-embedded αHL pore [13, 19]. However, because the αHL studies only provided an average pulse frequency for one particular salt gradient, the potential of salt gradient enhancement of αHL, or more generally bilayer-embedded porins, nanopore sensing of miRNA remained an open question. Hence, the main aim of this thesis was to establish the optimal conditions and limitations of miRNA nanopore sensing by systematically investigating a range of experimental parameters, with a focus on electrolyte gradients over the αHL pore.

As a reference point, experiments with symmetrical 1 M electrolytes (Chapter 4) demonstrated that it was possible to detect and analyse multilevel current signatures produced with the investigated duplexes. The results for the current amplitudes and the interevent times were in agreement with previous reports [13, 16]. Additionally, this work showed that miRNA-DNA duplex pulses exhibit a bimodal amplitude of level-1, which was postulated to relate to the probe terminus with which the duplex enters the pore (5' or 3'-first). Previous data demonstrated that

probes with dC_{30} at the 3' end had a 20-fold higher capture frequency compared to probes modified with dC_{30} at the 5' end [13]. In the present work was observed that the capture rate of the 5' end increased with voltage. At +180 mV the capture rates of probes modified with single dC_{30} overhangs at the 3' or 5' end were almost identical (Section 4.10), indicating that with a stronger electrophoretic force subtle differences in probe-pore interactions become less important.

It was demonstrated that the frequency of the pulses increased with voltage, but at the expense of shorter dwell times and frequent pore clogging when compared to lower voltages. For example, the capture frequency of the 100 nM miRNA155-P155 duplex increased from 0.31 ± 0.04 s^{-1} at 120 mV to 3.95 ± 0.56 s^{-1} at 180 mV. However, the dwell time decreased from 174 ms to 10.0 ± 2.2 ms (Section 4.10.2). The high voltage (180 mV) was unfavourable for miRNA155 detection with the single-overhang probes because pore clogging frequently occurred. In fact, blunt-end-first entry of the duplex into the pore vestibule made the duplex unzipping problematic. Therefore, the quantification of miRNA155 in 1 M KCl was performed with a P155 probe that was elongated with poly dC_{30} at both ends and at 120 mV potential. Under these conditions, the frequency of the pulses was found to be linearly correlated with duplex concentration, in agreement with previous studies. The limit of quantification was found at 10 nM of the miRNA155-P155 duplex. The capture frequencies for 50 and 10 nM in 1 M KCl could not be determined by histogram analysis because of the low number of events. Therefore, two pores were used for the detection of the miRNA155-P155 duplex. Lower concentrations were not explored since the event frequency for 10 nM duplex was too low (~0.034 events s^{-1}).

This work showed for the first time that lithium chloride has advantages for NRPS experiments for the detection of miRNA molecules at higher voltages (180 mV). It was established that the translocation rate is about two times higher and the dwell time is 17 times longer when compared with potassium chloride (Section 4.13). The effective charge of DNA might be reduced due to a stronger interaction with lithium ions [214], which could prolong the dwell time of the analyte-probe DNA duplex by the αHL pore. Moreover, the negatively charged amino acids (D127 and D128) at the *trans* entrance of the αHL pore could be neutralized by the lithium ions, which show the highest affinity to bind to negative pore charges [155]. These amino acids are responsible for the current asymmetry of the αHL nanopore [153, 155, 156]. Their neutralization by protonation or by binding Li ions results in a decrease of the current asymmetry ratio [152, 153, 155]. In the present work, the current asymmetries of the αHL nanopore in various electrolytes with different cation species were measured (Section 4.13). The lowest current asymmetry ratio (1.14) was found for 1 M LiCl, while the highest ratios were for CsCl and KCl (~1.4), suggesting that the strongest shielding of negatively charged amino acids can be obtained in LiCl. The neutralization of negative pore charge would result in a weaker electrostatic pore-DNA repulsion and would thus enhance the capture rate of a DNA duplex.

The resistive pulse parameters of three different duplexes were determined for a range of salt gradients across the αHL pore. In Chapter 5 was demonstrated that the rate of pore entry of the 100 nM miDNA155-P155 duplex increased exponentially with a larger salt gradient and voltage (Section 5.1). For example, with a 0.1 / 4 M KCl gradient the interevent time was 27 ms, almost 200 times shorter than in symmetrical 1 M KCl. Moreover, the dwell time decreased with a larger salt gradient. At 0.1 / 4 M KCl the dwell time was about 200 times shorter than in symmetrical 1 M KCl solution. This example highlights a significant difference between solid-state nanopores and αHL, since Wanunu and co-workers reported that for a solid-state nanopore the dwell time is longer in asymmetric salt conditions than in symmetric 1 M KCl solution [151]. In silicon nitride nanopores, the uniformly distributed negative charge of the pore wall together with a salt gradient results in a considerable EOF in the opposite direction of the DNA translocation [151, 159]. However, the αHL pore has a heterogeneous charge distribution and a much smaller diameter and for this reason the EOF influence on charged polymer translocation properties is suspected to be minor [165, 219].

Unfortunately, 20-fold (0.2 / 4 M KCl) and 40-fold (0.1 / 4 M KCl) gradients were shown to destabilize both the αHL pore and the aperture-suspended bilayers. Consequently, nanopore recordings could not be performed for long periods of time, limiting the total number of recorded pulses. For this reason, salt gradients with a low salt concentration (< 0.2 M) in the *cis* compartment are not recommended. This work proposed the 8-fold gradient (0.5 / 4 M KCl) as the optimal compromise between increasing event frequency and reducing bilayer and pore stability, enabling monitoring of the pore current for ~20 minutes. This 8-fold gradient was used for the quantification of miDNA155-P155 and miRNA21-P21 duplexes. The capture frequency was found to be linearly correlated with the duplex concentration over three orders of magnitude at 120 mV. Unlike 1 M KCl, where the limit of quantification was found at 10 nM, the limit of quantification in 0.5 / 4 M KCl was found to be 100 pM for both duplexes. The histogram analysis with 0.5 / 4 M KCl was possible down to 10 nM, while for lower concentrations (1 nM - 100 pM) the frequency could only be obtained by dividing the number of pulses by the recording time.

It was also established that the double-overhang design of the DNA probe is even more important when salt gradients are applied over the nanopore. Blunt-end duplex entry was much more frequent compared to symmetrical 1 M KCl electrolyte. These long-lived blockages complicated the analysis of the traces. Therefore, the double capture overhang is crucial for miRNA nanopore sensing under salt gradient conditions.

This work showed the fascinating ability of the αHL to discriminate between the miRNA155-P155 and miDNA155 resistive pulse parameters. MiRNA155-P155 duplexes exhibited a ~7 times shorter dwell time at +120 mV than miDNA155-P155 duplexes (Section 4.12). However, interestingly, at +180 mV the opposite behaviour was observed, where miRNA155-P155

duplexes had a ~5 times longer dwell time than miDNA155-P155 duplexes (10.0 ms vs 2.4 ms). Moreover, the duration of 5'-entry assigned pulses in 1 M KCl at 120 mV of the miDNA155-P155 duplex was two times shorter than the duration of 3'-entry pulses (Section 4.7), while for miRNA155-P155 duplexes the duration of 5'-entry pulses was 4 times longer than 3'-assigned pulses (Section 4.11).

Finally, the experiments performed with total RNA extract enriched with short RNA molecules from clinical samples (Chapter 6) showed how sensitive the nanopore sensing technique is when a large number of different molecules is present in the solution. The RNA extract did not influence the bilayer formation and stability, but when a salt gradient was applied across the membrane the pore became permanently clogged, probably with various longer RNA molecules and fragments present in the sample, which could adopt a secondary structure, which prevents pore translocations. This pore clogging was less prominent when symmetrical 1 M KCl was used, probably because of a reduced pore capture rate. These experiments pointed out the importance of the preparation of the biological sample, suggesting that RNA extracts containing mostly very short RNA sequences (such are miRNAs), which can be obtained by a double precipitation protocol with commercial extraction kits, should be preferred to RNA extract samples that also contain longer sequences. For example with the commercially available mirVana™ kit, miRNAs are isolated by binding to the glass-fibre filter under optimized ethanol washing steps and binding conditions. The longer RNA molecules (>200 nt) can be filtered out, leaving a miRNA-enriched extract. It is important to note that Wang *et al.* used this miRNA extraction kit while Wanunu *et al.* purified probe-hybridized miRNA with a viral p19 protein, which could explain why pore clogging was not reported in these seminal studies [13, 190]. However, in cases where miRNAs are extracted along with the total RNA from a biological sample, a possible solution for the background RNA interference problem is to design a polycationic probe and use anti-field miRNA capture, as proposed by Tian *et al.*[158, 229].

7.2 Recommendations for future work

The main challenge for the miRNA quantification with the nanopore technology is increasing the capture frequency of these short target molecules by the nanopore. The capture rate of DNA can be enhanced with a voltage increase, but the lipid bilayer in which biological pores are self-assembled cannot withstand high voltages. The voltage used for miRNA quantification with the αHL nanopore in the literature does not exceed 100 mV [13, 17]. An alternative way to increase capture frequency of duplex is by establishing a salt gradient across the membrane. Although the salt gradient conditions increased the capture frequency of miRNA-DNA duplexes, miRNA concentrations lower than 100 pM could not be measured. The amount of pathophysiological miRNA that can be extracted from 1 mL of plasma is in the 0.1-1 fmol range [7]; if this quantity is present in 1 mL chamber used in this work, it gives final concentrations of 0.1-1 pM, that is 2-

3 orders of magnitude below the limit of detection (100 pM). Therefore, to have a final concentration of 100 pM, the RNA extract should be resuspended in a 100-1000 times smaller volume. A possible way to achieve this is to form lipid bilayers having two adjacent aqueous droplets in an oil system [230, 231]. This would reduce the working volume to microliters. Alternatively, the miRNA sample could be measured by a small volume nanopore chip containing multiple electrically independent nanopores [232].

The main limitations of nanopore sensing with a biological pore come from the fragility of the lipid bilayer in which biological pores self-assemble. Considerably less stable lipid bilayers were observed for high voltages (>150 mV) and under salt gradient conditions (*cis/trans* 0.2 / 4 M KCl, 0.1 / 4 M KCl) compared with symmetrical salt conditions and a potential of 120 mV. It is possible that an osmotic pressure, created by salt gradients, destabilizes the bilayer. It would hence be interesting to explore the bilayer stability, without the αHL pore, by increasing the osmolarity of the low concentration salt compartment by use of uncharged polymers [233]. The osmotic pressure was proposed as a contributor to increased capture frequency of dT_{20} with the αHL pore in the presence of the salt gradient [191]. However, once the pore is presented in the bilayer there should not be osmotic flow because the pore is also permeable to salt. Therefore, it would be interesting to compare the capture frequencies of duplexes for the electrolyte solutions in the *cis* compartment with and without the presence of uncharged polymers.

In this work, the influence of the origin of biological samples was not investigated, hence the RNA extraction protocol has not been optimized. Therefore, it would be necessary to test the performance of the nanopore technique on RNA extracts from various sources, such are plasma, blood, cells or tissue. The total RNA extract and miRNA extract from biological samples could be compared as well. This should be possible since RNA kits specialized for miRNA extraction kits are commercially available.

Furthermore, the DNA probe could be modified with overhangs having different nucleotide composition, for example poly (dA) and poly (dT) instead of the familiar (dC). The possible difference in amplitude block could be employed for multiplex detection of miRNA molecules.

7.3 Publications arising from this work

Poster presentations:

Josip Ivica, Philip T. F. Williamson and Maurits R. R. de Planque (2016) Quantification of microRNA with α-hemolysin nanopores. Poster presentation at *Membrane Pores: from Structure and Assembly to Medicine and Technology (The Royal Society)*, London, United Kingdom, 27 - 28 June 2016.

Josip Ivica, Philip T. F. Williamson and Maurits R. R. de Planque (2016) Optimization of parameters for nanopore resistive pulse sensing of microRNA. Poster presentation at the *60th Annual Meeting of the Biophysical Society*, Los Angeles, United States, 27 February - 02 March 2016.

Journal publication:

Josip Ivica, Philip T.F. Williamson and Maurits R.R. de Planque (2017) Salt gradient modulation of microRNA translocation through a biological nanopore. *Analytical Chemistry*, 89, 8822-8829.

List of References

1. Nagy Z, Igaz P. Introduction to microRNAs: Biogenesis, action, relevance of tissue micrornas in disease pathogenesis, diagnosis and therapy—the concept of circulating microRNAs. In: Igaz P, editor. Circulating microRNAs in disease diagnostics and their potential biological relevance. Basel: Springer Basel; 2015. p. 3-30.

2. Pritchard CC, Cheng HH, Tewari M. MicroRNA profiling: Approaches and considerations. Nature Reviews Genetics. 2012, 13, 358-369.

3. Lu J, Getz G, Miska EA, Alvarez-Saavedra E, Lamb J, Peck D, Sweet-Cordero A, Ebert BL, Mak RH, Ferrando AA, et al. MicroRNA expression profiles classify human cancers. Nature. 2005, 435, 834-838.

4. Lan HY, Lu HQ, Wang X, Jin HC. MicroRNAs as potential biomarkers in cancer: Opportunities and challenges. Biomed Research International. 2015.

5. Wang J, Chen J, Sen S. MicroRNA as biomarkers and diagnostics. Journal of Cellular Physiology. 2016, 231, 25-30.

6. Schmittgen TD, Lee EJ, Jiang J, Sarkar A, Yang L, Elton TS, Chen C. Real-time PCR quantification of precursor and mature microRNA. Methods. 2008, 44, 31-38.

7. Mitchell PS, Parkin RK, Kroh EM, Fritz BR, Wyman SK, Pogosova-Agadjanyan EL, Peterson A, Noteboom J, O'Briant KC, Allen A, et al. Circulating microRNAs as stable blood-based markers for cancer detection. Proc Natl Acad Sci U S A. 2008, 105, 10513-10518.

8. Shingara J, Keiger K, Shelton J, Laosinchai-Wolf W, Powers P, Conrad R, Brown D, Labourier E. An optimized isolation and labeling platform for accurate microRNA expression profiling. RNA. 2005, 11, 1461-1470.

9. Keshavarz M, Behpour M, Rafiee-pour H-A. Recent trends in electrochemical microRNA biosensors for early detection of cancer. RSC Advances. 2015, 5, 35651-35660.

10. Graybill RM, Bailey RC. Emerging biosensing approaches for microRNA analysis. Analytical Chemistry. 2016, 88, 431-450.

11. Johnson BN, Mutharasan R. Biosensor-based microRNA detection: Techniques, design, performance, and challenges. Analyst. 2014, 139, 1576-1588.

12. Gu LQ, Wanunu M, Wang MX, McReynolds L, Wang Y. Detection of miRNAs with a nanopore single-molecule counter. Expert Review of Molecular Diagnostics. 2012, 12, 573-584.

13. Wang Y, Zheng D, Tan Q, Wang MX, Gu LQ. Nanopore-based detection of circulating microRNAs in lung cancer patients. Nature Nanotechnology. 2011, 6, 668-674.

14. Feng Y, Zhang Y, Ying C, Wang D, Du C. Nanopore-based fourth-generation DNA sequencing technology. Genomics Proteomics Bioinformatics. 2015, 13, 4-16.

15. Song L, Hobaugh MR, Shustak C, Cheley S, Bayley H, Gouaux JE. Structure of staphylococcal alpha-hemolysin, a heptameric transmembrane pore. Science. 1996, 274, 1859-1866.

16. Wang Y, Tian K, Hunter LL, Ritzo B, Gu LQ. Probing molecular pathways for DNA orientational trapping, unzipping and translocation in nanopores by using a tunable overhang sensor. Nanoscale. 2014, 6, 11372-11379.

17. Zhang X, Wang Y, Fricke BL, Gu LQ. Programming nanopore ion flow for encoded multiplex microRNA detection. ACS Nano. 2014, 8, 3444-3450.

18. Maglia G, Restrepo MR, Mikhailova E, Bayley H. Enhanced translocation of single DNA molecules through alpha-hemolysin nanopores by manipulation of internal charge. Proc Natl Acad Sci U S A. 2008, 105, 19720-19725.

19. Xi D, Shang J, Fan E, You J, Zhang S, Wang H. Nanopore-based selective discrimination of microRNAs with single-nucleotide difference using locked nucleic acid-modified probes. Analytical Chemistry. 2016, 88, 10540-10546.

20. Gurtan AM, Sharp PA. The role of miRNAs in regulating gene expression networks. Journal of Molecular Biology. 2013, 425, 3582-3600.

21. Bartel DP. MicroRNAs: Genomics, biogenesis, mechanism, and function. Cell. 2004, 116, 281-297.

22. Calin GA, Dumitru CD, Shimizu M, Bichi R, Zupo S, Noch E, Aldler H, Rattan S, Keating M, Rai K, et al. Frequent deletions and down-regulation of micro- RNA genes mir15 and mir16 at 13q14 in chronic lymphocytic leukemia. Proc Natl Acad Sci U S A. 2002, 99, 15524-15529.

23. Xu LF, Wu ZP, Chen Y, Zhu QS, Hamidi S, Navab R. MicroRNA-21 (mir-21) regulates cellular proliferation, invasion, migration, and apoptosis by targeting pten, reck and bcl-2 in lung squamous carcinoma, gejiu city, china. PLoS One. 2014, 9, e103698.

24. Li C, Zhao L, Chen Y, He T, Chen X, Mao J, Li C, Lyu J, Meng QH. MicroRNA-21 promotes proliferation, migration, and invasion of colorectal cancer, and tumor growth associated with down-regulation of sec23a expression. BMC Cancer. 2016, 16, 605.

25. Meng F, Henson R, Wehbe-Janek H, Ghoshal K, Jacob ST, Patel T. MicroRNA-21 regulates expression of the pten tumor suppressor gene in human hepatocellular cancer. Gastroenterology. 2007, 133, 647-658.

26. Chan SH, Wu CW, Li AF, Chi CW, Lin WC. Mir-21 microRNA expression in human gastric carcinomas and its clinical association. Anticancer Research. 2008, 28, 907-911.

27. Yan LX, Huang XF, Shao Q, Huang MY, Deng L, Wu QL, Zeng YX, Shao JY. MicroRNA mir-21 overexpression in human breast cancer is associated with advanced clinical stage, lymph node metastasis and patient poor prognosis. RNA. 2008, 14, 2348-2360.

28. Robb T, Reid G, Blenkiron C. Exploiting microRNAs as cancer therapeutics. Targeted Oncology. 2017.

29. Di Leva G, Croce CM. Roles of small RNAs in tumor formation. Trends in Molecular Medicine. 2010, 16, 257-267.

30. Volinia S, Calin GA, Liu CG, Ambs S, Cimmino A, Petrocca F, Visone R, Iorio M, Roldo C, Ferracin M, et al. A microRNA expression signature of human solid tumors defines cancer gene targets. Proc Natl Acad Sci U S A. 2006, 103, 2257-2261.

31. Coenen-Stass AML, Mäger I, Wood MJA. Extracellular microRNAs in membrane vesicles and non-vesicular carriers. In: Igaz P, editor. Circulating microRNAs in disease diagnostics and their potential biological relevance. Basel: Springer Basel; 2015. p. 31-53.

32. Weber JA, Baxter DH, Zhang S, Huang DY, Huang KH, Lee MJ, Galas DJ, Wang K. The microRNA spectrum in 12 body fluids. Clinical Chemistry. 2010, 56, 1733-1741.

33. Schwarzenbach H, Nishida N, Calin GA, Pantel K. Clinical relevance of circulating cell-free microRNAs in cancer. Nature Reviews Clinical Oncology. 2014, 11, 145-156.

34. Khoury S, Tran N. Circulating microRNAs: Potential biomarkers for common malignancies. Biomarkers in Medicine. 2015, 9, 131-151.

35. Fiammengo R. Can nanotechnology improve cancer diagnosis through miRNA detection? Biomarkers in Medicine. 2017, 11, 69-86.

36. Lautner G, Gyurcsanyi RE. Electrochemical detection of miRNAs. Electroanalysis. 2014, 26, 1224-1235.

37. Planell-Saguer M, Rodicio MC. Detection methods for microRNAs in clinic practice. Clinical Biochemistry. 2013, 46, 869-878.

38. Holland PM, Abramson RD, Watson R, Gelfand DH. Detection of specific polymerase chain reaction product by utilizing the 5'----3' exonuclease activity of thermus aquaticus DNA polymerase. Proc Natl Acad Sci U S A. 1991, 88, 7276-7280.

39. Benes V, Castoldi M. Expression profiling of microRNA using real-time quantitative PCR, how to use it and what is available. Methods. 2010, 50, 244-249.

40. Yan J, Zhang N, Qi C, Liu X, Shangguan D. One-step real time RT-PCR for detection of microRNAs. Talanta. 2013, 110, 190-195.

41. Flowers E, Froelicher ES, Aouizerat BE. Measurement of microRNA: A regulator of gene expression. Biological Research for Nursing. 2013, 15, 167-178.

42. Nolan T, Hands RE, Bustin SA. Quantification of mRNA using real-time RT-PCR. Nature Protocols. 2006, 1, 1559-1582.

43. Hunt EA, Broyles D, Head T, Deo SK. MicroRNA detection: Current technology and research strategies. Annual Review of Analytical Chemistry. 2015, 8, 217-237.

44. Li W, Ruan K. MicroRNA detection by microarray. Analytical and Bioanalytical Chemistry. 2009, 394, 1117-1124.

45. Castoldi M, Schmidt S, Benes V, Noerholm M, Kulozik AE, Hentze MW, Muckenthaler MU. A sensitive array for microRNA expression profiling (michip) based on locked nucleic acids (lna). RNA. 2006, 12, 913-920.

46. Ueno T, Funatsu T. Label-free quantification of microRNAs using ligase-assisted sandwich hybridization on a DNA microarray. PLoS One. 2014, 9, e90920.

47. Mardis ER. Next-generation sequencing platforms. Annual Review of Analytical Chemistry. 2013, 6, 287-303.

48. Metzker ML. Sequencing technologies - the next generation. Nature Reviews Genetics. 2010, 11, 31-46.

49. Motameny S, Wolters S, Nurnberg P, Schumacher B. Next generation sequencing of miRNAs - strategies, resources and methods. Genes (Basel). 2010, 1, 70-84.

50. Fracchiolla NS, Artuso S, Cortelezzi A. Biosensors in clinical practice: Focus on oncohematology. Sensors (Basel). 2013, 13, 6423-6447.

51. Wu P, Tu Y, Qian Y, Zhang H, Cai C. DNA strand-displacement-induced fluorescence enhancement for highly sensitive and selective assay of multiple microRNA in cancer cells. Chemical Communications. 2014, 50, 1012-1014.

52. Larkey NE, Almlie CK, Tran V, Egan M, Burrows SM. Detection of miRNA using a double-strand displacement biosensor with a self-complementary fluorescent reporter. Analytical Chemistry. 2014, 86, 1853-1863.

53. Tu Y, Li W, Wu P, Zhang H, Cai C. Fluorescence quenching of graphene oxide integrating with the site-specific cleavage of the endonuclease for sensitive and selective microRNA detection. Analytical Chemistry. 2013, 85, 2536-2542.

54. Liu W, Zhou X, Xing D. Rapid and reliable microRNA detection by stacking hybridization on electrochemiluminescent chip system. Biosensors & Bioelectronics. 2014, 58, 388-394.

55. Hao N, Dai PP, Yu T, Xu JJ, Chen HY. A dual target-recycling amplification strategy for sensitive detection of microRNAs based on duplex-specific nuclease and catalytic hairpin assembly. Chemical Communications. 2015, 51, 13504-13507.

56. Chen A, Gui GF, Zhuo Y, Chai YQ, Xiang Y, Yuan R. Signal-off electrochemiluminescence biosensor based on phi29 DNA polymerase mediated strand displacement amplification for microRNA detection. Analytical Chemistry. 2015, 87, 6328-6334.

57. Qiu X, Liu X, Zhang W, Zhang H, Jiang T, Fan D, Luo Y. Dynamic monitoring of microRNA-DNA hybridization using dnaase-triggered signal amplification. Analytical Chemistry. 2015, 87, 6303-6310.

58. Fan Y, Chen X, Trigg AD, Tung CH, Kong J, Gao Z. Detection of microRNAs using target-guided formation of conducting polymer nanowires in nanogaps. J Am Chem Soc. 2007, 129, 5437-5443.

59. Zhang GJ, Chua JH, Chee RE, Agarwal A, Wong SM. Label-free direct detection of miRNAs with silicon nanowire biosensors. Biosensors & Bioelectronics. 2009, 24, 2504-2508.

60. Ren Y, Deng H, Shen W, Gao Z. A highly sensitive and selective electrochemical biosensor for direct detection of microRNAs in serum. Analytical Chemistry. 2013, 85, 4784-4789.

61. Shen W, Deng H, Ren Y, Gao Z. A label-free microRNA biosensor based on dnazyme-catalyzed and microRNA-guided formation of a thin insulating polymer film. Biosensors & Bioelectronics. 2013, 44, 171-176.

62. Lusi EA, Passamano M, Guarascio P, Scarpa A, Schiavo L. Innovative electrochemical approach for an early detection of microRNAs. Analytical Chemistry. 2009, 81, 2819-2822.

63. Labib M, Khan N, Ghobadloo SM, Cheng J, Pezacki JP, Berezovski MV. Three-mode electrochemical sensing of ultralow microRNA levels. J Am Chem Soc. 2013, 135, 3027-3038.

64. Azimzadeh M, Rahaie M, Nasirizadeh N, Daneshpour M, Naderi-Manesh H. Electrochemical miRNA biosensors: The benefits of nanotechnology. Nanomedicine Research Journal. 2017, 2, 36-48.

65. Miao X, Wang W, Kang T, Liu J, Shiu KK, Leung CH, Ma DL. Ultrasensitive electrochemical detection of miRNA-21 by using an iridium(iii) complex as catalyst. Biosensors & Bioelectronics. 2016, 86, 454-458.

66. Li F, Peng J, Wang J, Tang H, Tan L, Xie Q, Yao S. Carbon nanotube-based label-free electrochemical biosensor for sensitive detection of miRNA-24. Biosensors & Bioelectronics. 2014, 54, 158-164.

67. Tran HV, Piro B, Reisberg S, Anquetin G, Duc HT, Pham MC. An innovative strategy for direct electrochemical detection of microRNA biomarkers. Analytical and Bioanalytical Chemistry. 2014, 406, 1241-1244.

68. Cheng FF, He TT, Miao HT, Shi JJ, Jiang LP, Zhu JJ. Electron transfer mediated electrochemical biosensor for microRNAs detection based on metal ion functionalized titanium phosphate nanospheres at attomole level. ACS Applied Materials & Interfaces. 2015, 7, 2979-2985.

69. H CW. Means for counting particles suspended in a fluid. US patent 2,656,508 (1953); 1953.

70. Henriquez RR, Ito T, Sun L, Crooks RM. The resurgence of coulter counting for analyzing nanoscale objects. Analyst. 2004, 129, 478-482.

71. Wanunu M. Nanopores: A journey towards DNA sequencing. Physics of Life Reviews. 2012, 9, 125-158.

72. Schmidt J. Membrane platforms for biological nanopore sensing and sequencing. Current Opinion in Biotechnology. 2016, 39, 17-27.

73. Howorka S, Siwy Z. Nanopore analytics: Sensing of single molecules. Chemical Society Reviews. 2009, 38, 2360-2384.

74. Ying Y-L, Cao C, Long Y-T. Single molecule analysis by biological nanopore sensors. Analyst. 2014, 139, 3826-3835.

75. Liu L, Wu H-C. DNA-based nanopore sensing. Angewandte Chemie International Edition. 2016, 55, 15216-15222.

76. Reiner JE, Balijepalli A, Robertson JW, Campbell J, Suehle J, Kasianowicz JJ. Disease detection and management via single nanopore-based sensors. Chemical Reviews. 2012, 112, 6431-6451.

77. Gu LQ, Shim JW. Single molecule sensing by nanopores and nanopore devices. Analyst. 2010, 135, 441-451.

78. Ma L, Cockroft SL. Biological nanopores for single-molecule biophysics. Chembiochem : a European Journal of Chemical Biology. 2010, 11, 25-34.

79. Kasianowicz JJ, Balijepalli AK, Ettedgui J, Forstater JH, Wang H, Zhang H, Robertson JW. Analytical applications for pore-forming proteins. Biochimica et Biophysica Acta. 2016, 1858, 593-606.

80. Denise W, Tae-Joon J, Jacob S. Single molecule measurements of channel proteins incorporated into biomimetic polymer membranes. Nanotechnology. 2006, 17, 3710.

81. Zakharian E. Recording of ion channel activity in planar lipid bilayer experiments. Methods in molecular biology (Clifton, NJ). 2013, 998, 109-118.

82. Gutsmann T, Heimburg T, Keyser U, Mahendran KR, Winterhalter M. Protein reconstitution into freestanding planar lipid membranes for electrophysiological characterization. Nature Protocols. 2015, 10, 188-198.

83. Majd S, Yusko EC, Billeh YN, Macrae MX, Yang J, Mayer M. Applications of biological pores in nanomedicine, sensing, and nanoelectronics. Current Opinion in Biotechnology. 2010, 21, 439-476.

84. Shi W, Friedman AK, Baker LA. Nanopore sensing. Analytical Chemistry. 2017, 89, 157-188.

85. Menestrina G, Dalla Serra M, Comai M, Coraiola M, Viero G, Werner S, Colin DA, Monteil H, Prevost G. Ion channels and bacterial infection: The case of beta-barrel pore-forming protein toxins of staphylococcus aureus. FEBS Letters. 2003, 552, 54-60.

86. Bhakdi S, Tranum-Jensen J. Alpha-toxin of staphylococcus aureus. Microbiological Reviews. 1991, 55, 733-751.

87. Berube BJ, Bubeck Wardenburg J. Staphylococcus aureus α-toxin: Nearly a century of intrigue. Toxins. 2013, 5, 1140-1166.

88. Drew HR, Wing RM, Takano T, Broka C, Tanaka S, Itakura K, Dickerson RE. Structure of a b-DNA dodecamer: Conformation and dynamics. Proc Natl Acad Sci U S A. 1981, 78, 2179-2183.

89. Bayley H, Cremer PS. Stochastic sensors inspired by biology. Nature. 2001, 413, 226-230.

90. Kang XF, Gu LQ, Cheley S, Bayley H. Single protein pores containing molecular adapters at high temperatures. Angewandte Chemie International Edition. 2005, 44, 1495-1499.

91. Gu LQ, Bayley H. Interaction of the noncovalent molecular adapter, beta-cyclodextrin, with the staphylococcal alpha-hemolysin pore. Biophysical Journal. 2000, 79, 1967-1975.

92. Maglia G, Heron AJ, Stoddart D, Japrung D, Bayley H. Analysis of single nucleic acid molecules with protein nanopores. Methods in Enzymology. 2010, 475, 591-623.

93. Derrington IM, Butler TZ, Collins MD, Manrao E, Pavlenok M, Niederweis M, Gundlach JH. Nanopore DNA sequencing with mspa. Proceedings of the National Academy of Sciences. 2010, 107, 16060-16065.

94. Manrao EA, Derrington IM, Pavlenok M, Niederweis M, Gundlach JH. Nucleotide discrimination with DNA immobilized in the mspa nanopore. PLoS One. 2011, 6, e25723.

95. Wendell D, Jing P, Geng J, Subramaniam V, Lee TJ, Montemagno C, Guo P. Translocation of double stranded DNA through membrane adapted phi29 motor protein nanopore. Nature Nanotechnology. 2009, 4, 765-772.

96. Haque F, Wang S, Stites C, Chen L, Wang C, Guo P. Single pore translocation of folded, double-stranded, and tetra-stranded DNA through channel of bacteriophage phi29 DNA packaging motor. Biomaterials. 2015, 53, 744-752.

97. Soskine M, Biesemans A, Maglia G. Single-molecule analyte recognition with clya nanopores equipped with internal protein adaptors. J Am Chem Soc. 2015, 137, 5793-5797.

98. Soskine M, Biesemans A, De Maeyer M, Maglia G. Tuning the size and properties of clya nanopores assisted by directed evolution. J Am Chem Soc. 2013, 135, 13456-13463.

99. Soskine M, Biesemans A, Moeyaert B, Cheley S, Bayley H, Maglia G. An engineered clya nanopore detects folded target proteins by selective external association and pore entry. Nano Letters. 2012, 12, 4895-4900.

100. Franceschini L, Brouns T, Willems K, Carlon E, Maglia G. DNA translocation through clya nanopores at physiological ionic strengths requires precise nanoscale engineering. ACS Nano. 2016, 10, 8394-8402.

101. Degiacomi MT, Iacovache I, Pernot L, Chami M, Kudryashev M, Stahlberg H, van der Goot FG, Dal Peraro M. Molecular assembly of the aerolysin pore reveals a swirling membrane-insertion mechanism. Nat Chem Biol. 2013, 9, 623-629.

102. Stefureac R, Long Y-t, Kraatz H-B, Howard P, Lee JS. Transport of α-helical peptides through α-hemolysin and aerolysin pores. Biochemistry. 2006, 45, 9172-9179.

103. Wang Y, Montana V, Grubišić V, Stout RF, Parpura V, Gu L-Q. Nanopore sensing of botulinum toxin type b by discriminating an enzymatically cleaved peptide from a synaptic protein synaptobrevin 2 derivative. ACS Applied Materials & Interfaces. 2015, 7, 184-192.

104. Cao C, Ying Y-L, Hu Z-L, Liao D-F, Tian H, Long Y-T. Discrimination of oligonucleotides of different lengths with a wild-type aerolysin nanopore. Nature Nanotechnology. 2016, 11, 713-718.

105. Baaken G, Halimeh I, Bacri L, Pelta J, Oukhaled A, Behrends JC. High-resolution size-discrimination of single nonionic synthetic polymers with a highly charged biological nanopore. ACS Nano. 2015, 9, 6443-6449.

106. Subbarao GV, van den Berg B. Crystal structure of the monomeric porin ompg. Journal of Molecular Biology. 2006, 360, 750-759.

107. Fahie MA, Yang B, Mullis M, Holden MA, Chen M. Selective detection of protein homologues in serum using an ompg nanopore. Analytical Chemistry. 2015, 87, 11143-11149.

108. Fahie MA, Yang B, Pham B, Chen M. Tuning the selectivity and sensitivity of an ompg nanopore sensor by adjusting ligand tether length. Acs Sensors. 2016, 1, 614-622.

109. Venkatesan BM, Bashir R. Nanopore sensors for nucleic acid analysis. Nature Nanotechnology. 2011, 6, 615-624.

110. Dekker C. Solid-state nanopores. Nature Nanotechnology. 2007, 2, 209-215.

111. Haque F, Li J, Wu HC, Liang XJ, Guo P. Solid-state and biological nanopore for real-time sensing of single chemical and sequencing of DNA. Nano Today. 2013, 8, 56-74.

112. Kim MJ, Wanunu M, Bell DC, Meller A. Rapid fabrication of uniformly sized nanopores and nanopore arrays for parallel DNA analysis. Advanced Materials. 2006, 18, 3149-+.

113. Venkatesan BM, Shah AB, Zuo JM, Bashir R. DNA sensing using nano-crystalline surface enhanced al(2)o(3) nanopore sensors. Advanced Functional Materials. 2010, 20, 1266-1275.

114. Fischbein MD, Drndic M. Electron beam nanosculpting of suspended graphene sheets. Applied Physics Letters. 2008, 93.

115. Schneider GF, Kowalczyk SW, Calado VE, Pandraud G, Zandbergen HW, Vandersypen LMK, Dekker C. DNA translocation through graphene nanopores. Nano Letters. 2010, 10, 3163-3167.

116. Garaj S, Hubbard W, Reina A, Kong J, Branton D, Golovchenko JA. Graphene as a subnanometre trans-electrode membrane. Nature. 2010, 467, 190-U173.

117. Feng Y, Zhang Y, Ying C, Wang D, Du C. Nanopore-based fourth-generation DNA sequencing technology. Genomics Proteomics Bioinformatics. 2015, 13, 4-16.

118. Fologea D, Uplinger J, Thomas B, McNabb DS, Li J. Slowing DNA translocation in a solid-state nanopore. Nano Letters. 2005, 5, 1734-1737.

119. Chen P, Gu J, Brandin E, Kim YR, Wang Q, Branton D. Probing single DNA molecule transport using fabricated nanopores. Nano Letters. 2004, 4, 2293-2298.

120. Goodwin S, McPherson JD, McCombie WR. Coming of age: Ten years of next-generation sequencing technologies. Nature Reviews Genetics. 2016, 17, 333-351.

121. International Human Genome Sequencing C. Initial sequencing and analysis of the human genome. Nature. 2001, 409, 860.

122. Venter JC, Adams MD, Myers EW, Li PW, Mural RJ, Sutton GG, Smith HO, Yandell M, Evans CA, Holt RA, et al. The sequence of the human genome. Science. 2001, 291, 1304.

123. Christensen KD, Dukhovny D, Siebert U, Green RC. Assessing the costs and cost-effectiveness of genomic sequencing. Journal of Personalized Medicine. 2015, 5, 470-486.

124. Agah S, Zheng M, Pasquali M, Kolomeisky AB. DNA sequencing by nanopores: Advances and challenges. Journal of Physics D-Applied Physics. 2016, 49.

125. Clarke J, Wu HC, Jayasinghe L, Patel A, Reid S, Bayley H. Continuous base identification for single-molecule nanopore DNA sequencing. Nature Nanotechnology. 2009, 4, 265-270.

126. Kasianowicz JJ, Brandin E, Branton D, Deamer DW. Characterization of individual polynucleotide molecules using a membrane channel. Proc Natl Acad Sci U S A. 1996, 93, 13770-13773.

127. Akeson M, Branton D, Kasianowicz JJ, Brandin E, Deamer DW. Microsecond time-scale discrimination among polycytidylic acid, polyadenylic acid, and polyuridylic acid as homopolymers or as segments within single RNA molecules. Biophysical Journal. 1999, 77, 3227-3233.

128. Branton D, Deamer DW, Marziali A, Bayley H, Benner SA, Butler T, Di Ventra M, Garaj S, Hibbs A, Huang X, et al. The potential and challenges of nanopore sequencing. Nature Biotechnology. 2008, 26, 1146-1153.

129. Henley RY, Carson S, Wanunu M. Studies of RNA sequence and structure using nanopores. Progress in molecular biology and translational science. 2016, 139, 73-99.

130. Deamer DW, Branton D. Characterization of nucleic acids by nanopore analysis. Accounts of Chemical Research. 2002, 35, 817-825.

131. Kasianowicz JJ, Reiner JE, Robertson JWF, Henrickson SE, Rodrigues C, Krasilnikov OV. Detecting and characterizing individual molecules with single nanopores. In: Gracheva ME, editor. Nanopore-based technology. Totowa, NJ: Humana Press; 2012. p. 3-20.

132. Mathe J, Aksimentiev A, Nelson DR, Schulten K, Meller A. Orientation discrimination of single-stranded DNA inside the alpha-hemolysin membrane channel. Proc Natl Acad Sci U S A. 2005, 102, 12377-12382.

133. Purnell RF, Mehta KK, Schmidt JJ. Nucleotide identification and orientation discrimination of DNA homopolymers immobilized in a protein nanopore. Nano Letters. 2008, 8, 3029-3034.

134. Muzard J, Martinho M, Mathe J, Bockelmann U, Viasnoff V. DNA translocation and unzipping through a nanopore: Some geometrical effects. Biophysical Journal. 2010, 98, 2170-2178.

135. Meller A, Nivon L, Branton D. Voltage-driven DNA translocations through a nanopore. Physical Review Letters. 2001, 86, 3435-3438.

136. Stoddart D, Heron AJ, Mikhailova E, Maglia G, Bayley H. Single-nucleotide discrimination in immobilized DNA oligonucleotides with a biological nanopore. Proc Natl Acad Sci U S A. 2009, 106, 7702-7707.

137. Stoddart D, Heron AJ, Klingelhoefer J, Mikhailova E, Maglia G, Bayley H. Nucleobase recognition in ssdna at the central constriction of the α-hemolysin pore. Nano Letters. 2010, 10, 3633-3637.

138. Cherf GM, Lieberman KR, Rashid H, Lam CE, Karplus K, Akeson M. Automated forward and reverse ratcheting of DNA in a nanopore at 5-angstrom precision. Nature Biotechnology. 2012, 30, 344-348.

139. Manrao EA, Derrington IM, Laszlo AH, Langford KW, Hopper MK, Gillgren N, Pavlenok M, Niederweis M, Gundlach JH. Reading DNA at single-nucleotide resolution with a mutant mspa nanopore and phi29 DNA polymerase. Nature Biotechnology. 2012, 30, 349-U174.

140. Deamer D, Akeson M, Branton D. Three decades of nanopore sequencing. Nature Biotechnology. 2016, 34, 518-524.

141. Lu HY, Giordano F, Ning ZM. A3 oxford nanopore minion sequencing and genome assembly. Genomics Proteomics & Bioinformatics. 2016, 14, 265-279.

142. Loman NJ, Quick J, Simpson JT. A complete bacterial genome assembled de novo using only nanopore sequencing data. Nature Methods. 2015, 12, 733-U751.

143. Quick J, Loman NJ, Duraffour S, Simpson JT, Ettore S, Cowley L, Bore JA, Koundouno R, Dudas G, Mikhail A, et al. Real-time, portable genome sequencing for ebola surveillance. Nature. 2016, 530, 228-+.

144. Meller A. Dynamics of polynucleotide transport through nanometre-scale pores. Journal of Physics-Condensed Matter. 2003, 15, R581-R607.

145. Henrickson SE, Misakian M, Robertson B, Kasianowicz JJ. Driven DNA transport into an asymmetric nanometer-scale pore. Physical Review Letters. 2000, 85, 3057-3060.

146. Sauer-Budge AF, Nyamwanda JA, Lubensky DK, Branton D. Unzipping kinetics of double-stranded DNA in a nanopore. Physical Review Letters. 2003, 90, 238101.

147. Mathé J, Visram H, Viasnoff V, Rabin Y, Meller A. Nanopore unzipping of individual DNA hairpin molecules. Biophysical Journal. 2004, 87, 3205-3212.

148. Meller A, Branton D. Single molecule measurements of DNA transport through a nanopore. Electrophoresis. 2002, 23, 2583-2591.

149. Nakane J, Akeson M, Marziali A. Evaluation of nanopores as candidates for electronic analyte detection. Electrophoresis. 2002, 23, 2592-2601.

150. Grosberg AY, Rabin Y. DNA capture into a nanopore: Interplay of diffusion and electrohydrodynamics. Journal of Chemical Physics. 2010, 133.

151. Wanunu M, Morrison W, Rabin Y, Grosberg AY, Meller A. Electrostatic focusing of unlabelled DNA into nanoscale pores using a salt gradient. Nature Nanotechnology. 2010, 5, 160-165.

152. Wong CT, Muthukumar M. Polymer translocation through alpha-hemolysin pore with tunable polymer-pore electrostatic interaction. The Journal of Chemical Physics. 2010, 133, 045101.

153. Misakian M, Kasianowicz JJ. Electrostatic influence on ion transport through the alphahl channel. The Journal of Membrane Biology. 2003, 195, 137-146.

154. Noskov SY, Im W, Roux B. Ion permeation through the alpha-hemolysin channel: Theoretical studies based on brownian dynamics and poisson-nernst-plank electrodiffusion theory. Biophysical Journal. 2004, 87, 2299-2309.

155. Bhattacharya S, Muzard L, Payet L, Mathe J, Bockelmann U, Aksimentiev A, Viasnoff V. Rectification of the current in alpha-hemolysin pore depends on the cation type: The alkali series probed by md simulations and experiments. The Journal of Physical Chemistry C. 2011, 115, 4255-4264.

156. Merzlyak PG, Capistrano MF, Valeva A, Kasianowicz JJ, Krasilnikov OV. Conductance and ion selectivity of a mesoscopic protein nanopore probed with cysteine scanning mutagenesis. Biophysical Journal. 2005, 89, 3059-3070.

157. Krasilnikov OV, Merzlyak PG, Yuldasheva LN, Capistrano MF. Protein electrostriction: A possibility of elastic deformation of the alpha-hemolysin channel by the applied field. Eur Biophys J. 2005, 34, 997-1006.

158. Tian K, He Z, Wang Y, Chen SJ, Gu LQ. Designing a polycationic probe for simultaneous enrichment and detection of microRNAs in a nanopore. ACS Nano. 2013, 7, 3962-3969.

159. He YH, Tsutsui M, Scheicher RH, Fan C, Taniguchi M, Kawai T. Mechanism of how salt-gradient-induced charges affect the translocation of DNA molecules through a nanopore. Biophysical Journal. 2013, 105, 776-782.

160. Hoogerheide DP, Garaj S, Golovchenko JA. Probing surface charge fluctuations with solid-state nanopores. Physical Review Letters. 2009, 102, 256804.

161. Lin CY, Yeh LH, Hsu JP, Tseng S. Regulating current rectification and nanoparticle transport through a salt gradient in bipolar nanopores. Small. 2015, 11, 4594-4602.

162. Ghosal S. Effect of salt concentration on the electrophoretic speed of a polyelectrolyte through a nanopore. Physical Review Letters. 2007, 98, 238104.

163. Smeets RM, Keyser UF, Krapf D, Wu MY, Dekker NH, Dekker C. Salt dependence of ion transport and DNA translocation through solid-state nanopores. Nano Letters. 2006, 6, 89-95.

164. Shim J, Banerjee S, Qiu H, Smithe KKH, Estrada D, Bello J, Pop E, Schulten K, Bashir R. Detection of methylation on dsdna using nanopores in a mos2 membrane. Nanoscale. 2017, 9, 14836-14845.

165. Jeon BJ, Muthukumar M. Polymer capture by alpha-hemolysin pore upon salt concentration gradient. Journal of Chemical Physics. 2014, 140.

166. Jeon BJ, Muthukumar M. Electrostatic control of polymer translocation speed through alpha-hemolysin protein pore. Macromolecules. 2016, 49, 9132-9138.

167. Gu L-Q, Cheley S, Bayley H. Electroosmotic enhancement of the binding of a neutral molecule to a transmembrane pore. Proc Natl Acad Sci U S A. 2003, 100, 15498-15503.

168. Mereuta L, Roy M, Asandei A, Lee JK, Park Y, Andricioaei I, Luchian T. Slowing down single-molecule trafficking through a protein nanopore reveals intermediates for peptide translocation. Scientific Reports. 2014, 4.

169. Robertson JWF, Rodrigues CG, Stanford VM, Rubinson KA, Krasilnikov OV, Kasianowicz JJ. Single-molecule mass spectrometry in solution using a solitary nanopore. Proceedings of the National Academy of Sciences. 2007, 104, 8207-8211.

170. Baaken G, Ankri N, Schuler A-K, Rühe J, Behrends JC. Nanopore-based single-molecule mass spectrometry on a lipid membrane microarray. ACS Nano. 2011, 5, 8080-8088.

171. Baaken G, Halimeh I, Bacri L, Pelta J, Oukhaled A, Behrends JC. High-resolution size-discrimination of single nonionic synthetic polymers with a highly charged biological nanopore. ACS Nano. 2015, 9, 6443-6449.

172. Movileanu L. Interrogating single proteins through nanopores: Challenges and opportunities. Trends in Biotechnology. 2009, 27, 333-341.

173. Goodrich CP, Kirmizialtin S, Huyghues-Despointes BM, Zhu A, Scholtz JM, Makarov DE, Movileanu L. Single-molecule electrophoresis of beta-hairpin peptides by electrical recordings and langevin dynamics simulations. The Journal of Physical Chemistry B. 2007, 111, 3332-3335.

174. Oukhaled G, Mathe J, Biance AL, Bacri L, Betton JM, Lairez D, Pelta J, Auvray L. Unfolding of proteins and long transient conformations detected by single nanopore recording. Physical Review Letters. 2007, 98, 158101.

175. Movileanu L, Howorka S, Braha O, Bayley H. Detecting protein analytes that modulate transmembrane movement of a polymer chain within a single protein pore. Nature Biotechnology. 2000, 18, 1091-1095.

176. Wolfe AJ, Mohammad MM, Cheley S, Bayley H, Movileanu L. Catalyzing the translocation of polypeptides through attractive interactions. J Am Chem Soc. 2007, 129, 14034-14041.

177. Talaga DS, Li J. Single-molecule protein unfolding in solid state nanopores. J Am Chem Soc. 2009, 131, 9287-9297.

178. Yusko EC, Johnson JM, Majd S, Prangkio P, Rollings RC, Li J, Yang J, Mayer M. Controlling protein translocation through nanopores with bio-inspired fluid walls. Nature Nanotechnology. 2011, 6, 253-260.

179. Freedman KJ, Haq SR, Edel JB, Jemth P, Kim MJ. Single molecule unfolding and stretching of protein domains inside a solid-state nanopore by electric field. Scientific Reports. 2013, 3, 1638.

180. An N, Fleming AM, White HS, Burrows CJ. Crown ether-electrolyte interactions permit nanopore detection of individual DNA abasic sites in single molecules. Proc Natl Acad Sci U S A. 2012, 109, 11504-11509.

181. An N, Fleming AM, White HS, Burrows CJ. Nanopore detection of 8-oxoguanine in the human telomere repeat sequence. ACS Nano. 2015, 9, 4296-4307.

182. Johnson RP, Fleming AM, Beuth LR, Burrows CJ, White HS. Base flipping within the a-hemolysin latch allows single-molecule identification of mismatches in DNA. J Am Chem Soc. 2016, 138, 594-603.

183. Kawano R, Osaki T, Sasaki H, Takinoue M, Yoshizawa S, Takeuchi S. Rapid detection of a cocaine-binding aptamer using biological nanopores on a chip. J Am Chem Soc. 2011, 133, 8474-8477.

184. Yang C, Liu L, Zeng T, Yang D, Yao Z, Zhao Y, Wu HC. Highly sensitive simultaneous detection of lead(ii) and barium(ii) with g-quadruplex DNA in alpha-hemolysin nanopore. Analytical Chemistry. 2013, 85, 7302-7307.

185. Zeng T, Li T, Li Y, Liu L, Wang X, Liu Q, Zhao Y, Wu H-C. DNA-based detection of mercury(ii) ions through characteristic current signals in nanopores with high sensitivity and selectivity. Nanoscale. 2014, 6, 8579-8584.

186. Wang Y, Gu L-q. Biomedical diagnosis perspective of epigenetic detections using alpha-hemolysin nanopore. AIMS Materials Science. 2015, 4, 448-472.

187. Meller A, Nivon L, Brandin E, Golovchenko J, Branton D. Rapid nanopore discrimination between single polynucleotide molecules. Proc Natl Acad Sci U S A. 2000, 97, 1079-1084.

188. Vercoutere W, Winters-Hilt S, Olsen H, Deamer D, Haussler D, Akeson M. Rapid discrimination among individual DNA hairpin molecules at single-nucleotide resolution using an ion channel. Nat Biotechnol. 2001, 19, 248-252.

189. Howorka S, Movileanu L, Braha O, Bayley H. Kinetics of duplex formation for individual DNA strands within a single protein nanopore. Proc Natl Acad Sci U S A. 2001, 98, 12996-13001.

190. Wanunu M, Dadosh T, Ray V, Jin J, McReynolds L, Drndic M. Rapid electronic detection of probe-specific microRNAs using thin nanopore sensors. Nature Nanotechnology. 2010, 5, 807-814.

191. Zhang HL, Hiratani M, Nagaoka K, Kawano R. MicroRNA detection at femtomolar concentrations with isothermal amplification and a biological nanopore. Nanoscale. 2017, 9, 16124-16127.

192. Zahid OK, Wang F, Ruzicka JA, Taylor EW, Hall AR. Sequence-specific recognition of microRNAs and other short nucleic acids with solid-state nanopores. Nano Letters. 2016, 16, 2033-2039.

193. Maglia G, Heron AJ, Stoddart D, Japrung D, Bayley H. Analysis of single nucleic acid molecules with protein nanopores. Methods Enzymol. 2010, 475, 591-623.

194. Gold R. The axon guide for electrophysiology & biophysics laboratory techniques2007.

195. Wonderlin WF, Finkel A, French RJ. Optimizing planar lipid bilayer single-channel recordings for high resolution with rapid voltage steps. Biophysical Journal. 1990, 58, 289-297.

196. Mayer M, Kriebel JK, Tosteson MT, Whitesides GM. Microfabricated teflon membranes for low-noise recordings of ion channels in planar lipid bilayers. Biophysical Journal. 2003, 85, 2684-2695.

197. Sandison ME, Morgan H. Rapid fabrication of polymer microfluidic systems for the production of artificial lipid bilayers. Journal of Micromechanics and Microengineering. 2005, 15, S139.

198. O'Shaughnessy TJ, Hu JE, Kulp JL, Daly SM, Ligler FS. Laser ablation of micropores for formation of artificial planar lipid bilayers. Biomedical Microdevices. 2007, 9, 863-868.

199. Hansen JS, Perry M, Vogel J, Vissing T, Hansen CR, Geschke O, Emnéus J, Nielsen CH. Development of an automation technique for the establishment of functional lipid bilayer arrays. Journal of Micromechanics and Microengineering. 2009, 19, 025014.

200. Andrey P, Boudier T. Adaptive active contours (snakes) for the segmentation of complex structures in biological images2010.

201. Montal M, Mueller P. Formation of bimolecular membranes from lipid monolayers and a study of their electrical properties. Proc Natl Acad Sci U S A. 1972, 69, 3561-3566.

202. Oiki S. Planar lipid bilayer method for studying channel molecules. In: Okada Y, editor. Patch clamp techniques: From beginning to advanced protocols. Tokyo: Springer Japan; 2012. p. 229-275.

203. White SH, Petersen DC, Simon S, Masaoyafuso. Formation of planar bilayer membranes from lipid monolayers - critique. Biophysical Journal. 1976, 16, 481-489.

204. Kalsi S, Powl AM, Wallace BA, Morgan H, de Planque MR. Shaped apertures in photoresist films enhance the lifetime and mechanical stability of suspended lipid bilayers. Biophysical Journal. 2014, 106, 1650-1659.

205. Butler TZ, Gundlach JH, Troll MA. Determination of RNA orientation during translocation through a biological nanopore. Biophysical Journal. 2006, 90, 190-199.

206. Japrung D, Henricus M, Li QH, Maglia G, Bayley H. Urea facilitates the translocation of single-stranded DNA and RNA through the alpha-hemolysin nanopore. Biophysical Journal. 2010, 98, 1856-1863.

207. Colquhoun D, Hawkes AG. The principles of the stochastic interpretation of ion-channel mechanisms. In: Sakmann B, Neher E, editors. Single-channel recording. Boston, MA: Springer US; 1995. p. 397-482.

208. Landowne D, Yuan B, Magleby Karl L. Exponential sum-fitting of dwell-time distributions without specifying starting parameters. Biophysical Journal. 2013, 104, 2383-2391.

209. Sigworth FJ, Sine SM. Data transformations for improved display and fitting of single-channel dwell time histograms. Biophysical Journal. 1987, 52, 1047-1054.

210. Butler TZ, Gundlach JH, Troll M. Ionic current blockades from DNA and RNA molecules in the alpha-hemolysin nanopore. Biophysical Journal. 2007, 93, 3229-3240.

211. Perera RT, Fleming AM, Peterson AM, Heemstra JM, Burrows CJ, White HS. Unzipping of a-form DNA-RNA, a-form DNA-pna, and b-form DNA-DNA in the alpha-hemolysin nanopore. Biophysical Journal. 2016, 110, 306-314.

212. Arias-Gonzalez JR. Single-molecule portrait of DNA and RNA double helices. Integrative Biology. 2014, 6, 904-925.

213. Johnson RP, Fleming AM, Burrows CJ, White HS. Effect of an electrolyte cation on detecting DNA damage with the latch constriction of alpha-hemolysin. Journal of Physical Chemistry Letters. 2014, 5, 3781-3786.

214. Kowalczyk SW, Wells DB, Aksimentiev A, Dekker C. Slowing down DNA translocation through a nanopore in lithium chloride. Nano Letters. 2012, 12, 1038-1044.

215. Wang J, Yi X, Tang H, Han H, Wu M, Zhou F. Direct quantification of microRNA at low picomolar level in sera of glioma patients using a competitive hybridization followed by amplified voltammetric detection. Analyitical Chemistry. 2012, 84, 6400-6406.

216. Yeh LH, Hughes C, Zeng Z, Qian S. Tuning ion transport and selectivity by a salt gradient in a charged nanopore. Analytical Chemistry. 2014, 86, 2681-2686.

217. He YH, Tsutsui M, Scheicher RH, Miao XS, Taniguchi M. Salt-gradient approach for regulating capture-to-translocation dynamics of DNA with nanochannel sensors. Acs Sensors. 2016, 1, 807-816.

218. Lu B, Hoogerheide DP, Zhao Q, Yu D. Effective driving force applied on DNA inside a solid-state nanopore. Physical Review E, Statistical, Nonlinear, and Soft Matter Physics. 2012, 86, 011921.

219. Boukhet M, Piguet F, Ouldali H, Pastoriza-Gallego M, Pelta J, Oukhaled A. Probing driving forces in aerolysin and alpha-hemolysin biological nanopores: Electrophoresis versus electroosmosis. Nanoscale. 2016, 8, 18352-18359.

220. Mohammad MM, Movileanu L. Impact of distant charge reversals within a robust β-barrel protein pore(&). The Journal of Physical Chemistry B. 2010, 114, 8750-8759.

221. Zhang X, Price NE, Fang X, Yang Z, Gu LQ, Gates KS. Characterization of interstrand DNA-DNA cross-links using the alpha-hemolysin protein nanopore. ACS Nano. 2015, 9, 11812-11819.

222. Mazeh H, Mizrahi I, Ilyayev N, Halle D, Brücher BLDM, Bilchik A, Protic M, Daumer M, Stojadinovic A, Avital I, Nissan A. The diagnostic and prognostic role of microRNA in colorectal cancer - a comprehensive review. Journal of Cancer. 2013, 4, 281-295.

223. Liu A, Zhao Q, Krishantha DM, Guan X. Unzipping of double-stranded DNA in engineered alpha-hemolysin pores. The Journal of Physical Chemistry Letters. 2011, 2, 1372-1376.

224. Li Y, Kowdley KV. Method for microRNA isolation from clinical serum samples. Anal Biochem. 2012, 431, 69-75.

225. Kanaan Z, Rai SN, Eichenberger MR, Roberts H, Keskey B, Pan J, Galandiuk S. Plasma mir-21: A potential diagnostic marker of colorectal cancer. Ann Surg. 2012, 256, 544-551.

226. Yu WEI, Wang Z, Shen LI, Wei Q. Circulating microRNA-21 as a potential diagnostic marker for colorectal cancer: A meta-analysis. Molecular and Clinical Oncology. 2016, 4, 237-244.

227. Li C, Zhao L, Chen Y, He T, Chen X, Mao J, Li C, Lyu J, Meng QH. MicroRNA-21 promotes proliferation, migration, and invasion of colorectal cancer, and tumor growth associated with down-regulation of sec23a expression. BMC Cancer. 2016, 16, 605.

228. Gu LQ, Wang Y. Nanopore single-molecule detection of circulating microRNAs. Methods in molecular biology (Clifton, NJ). 2013, 1024, 255-268.

229. Tian K, Decker K, Aksimentiev A, Gu LQ. Interference-free detection of genetic biomarkers using synthetic dipole-facilitated nanopore dielectrophoresis. ACS Nano. 2017, 11, 1204-1213.

230. Friddin MS, Smithers NP, Beaugrand M, Marcotte I, Williamson PT, Morgan H, de Planque MR. Single-channel electrophysiology of cell-free expressed ion channels by direct incorporation in lipid bilayers. Analyst. 2013, 138, 7294-7298.

231. Bayley H, Cronin B, Heron A, Holden MA, Hwang W, Syeda R, Thompson J, Wallace M. Droplet interface bilayers. Molecular BioSystems. 2008, 4, 1191-1208.

232. Baaken G, Sondermann M, Schlemmer C, Ruhe J, Behrends JC. Planar microelectrode-cavity array for high-resolution and parallel electrical recording of membrane ionic currents. Lab on a Chip. 2008, 8, 938-944.

233. Money NP. Osmotic pressure of aqueous polyethylene glycols : Relationship between molecular weight and vapor pressure deficit. Plant Physiology. 1989, 91, 766-769.